Department of Pharmaceutical Technology
Poznań University of Medical Sciences

CHARACTERISATION OF VALSARTAN AND ITS COMPATIBILITY WITH BISOPROLOL STUDIED BY DIFFERENTIAL SCANNING CALORIMETRY AND SOLID-STATE NUCLEAR MAGNETIC RESONANCE

CHARAKTERYSTYKA WALSARTANU ORAZ BADANIE JEGO ZGODNOŚCI FIZYKOCHEMICZNEJ Z BISOPROLOLEM Z WYKORZYSTANIEM RÓŻNICOWEJ KALORYMETRII SKANINGOWEJ I MAGNETYCZNEGO REZONANSU JĄDROWEGO W FAZIE STAŁEJ

Marcin SKOTNICKI

Doctoral dissertation

Supervisor:
Marek PYDA, PhD, Prof. RUT

Poznań 2014

Key words: valsartan; bisoprolol; solid state; amorphous state; glass transition; compatibility; differential scanning calorimetry; solid-state nuclear magnetic resonance; thermal methods

Słowa kluczowe: walsartan; bisoprolol; stan stały; stan amorficzny; przejście szkliste; zgodność fizykochemiczna; różnicowa kalorymetria skaningowa; magnetyczny rezonans jądrowy w fazie stałej; metody termiczne

ACKNOWLEDGMENTS

The research was conducted mainly at the Department of Pharmaceutical Technology, Faculty of Pharmacy, Poznań University of Medical Sciences (Poland), Department of Chemistry, University of Durham (United Kingdom) and also at the Department of Chemistry, Rzeszów University of Technology (Poland).

First of all I would like to thank my supervisor Prof. Marek Pyda (Rzeszów University of Technology and formerly Poznań University of Medical Sciences) for generous support, guidance and encouragement throughout this project.

I would like to express my sincere gratitude to Dr Paul Hodgkinson, who was my supervisor at Durham University, for the great opportunity to work in his group, learn solid-state NMR and his constant support and interest.

I am also indebted to Prof. Janina Lulek, Head of the Pharmaceutical Technology Department (Poznań University of Medical Sciences), for the opportunity to work on this project, for reviewing this thesis and all valuable help provided during the time I have worked at the Pharmaceutical Technology Department.

Dr Juan Aguilar from the Solution-state NMR Service (Durham University) is sincerely acknowledged for performing experiments and sharing his expertise on solution-state NMR. Special acknowledgement is given to Dr David C. Apperley from the EPSRC UK National Solid-state NMR Service (Durham University), and Dr Hodgkinson's research group members: Dr Martin Dračínský and Dr Ilya Frantsuzov for all the help with solid-state NMR. I am also grateful to Dr Catherine E. Nicholson (Durham University) for her assistance with XRPD experiments and Dr Beata Łukasiewicz and Dr Iwona Zarzyka (Rzeszów University of Technology) for their assistance with FT-IR experiments. Also I would like to thank co-author of the publication based on this thesis Prof. Peggy Cebe (Tufts University).

Finally help of all colleagues from Poznań University of Medical Sciences is greatly acknowledged. Special thanks go to Dr Bartłomiej Milanowski for his help with dissolution studies and long valuable discussions out of the hours in the Office and to Dr Paweł Grobelny (presently University of Connecticut) for advice and comments provided on this thesis. Moreover, I thank Ms Kinga Hyla and Mr Łukasz Grobelny for help with performing dissolution and DSC experiments.

I also acknowledge Biofarm Sp. z o.o. (Poznań, Poland) for supplying bisoprolol fumarate and Polpharma SA Company (Starogard Gdański, Poland) for supplying valsartan used in this study.

Niniejszą pracę dedykuję mojej Żonie

CONTENTS

1 ABBREVIATIONS 9

2 INTRODUCTION 11

3 THEORETICAL PART 15

3.1 Introduction 15

3.2 Valsartan 15

3.2.1 Chemical structure and physicochemical properties 15

3.2.2 Mechanism of action 17

3.2.3 Pharmacokinetic properties 18

3.2.4 Pharmacological properties 18

3.2.5 Available valsartan preparations 19

3.3 Bisoprolol 19

3.3.1 Chemical structure and physicochemical properties 19

3.3.2 Mechanism of action 20

3.3.3 Pharmacokinetic properties 20

3.3.4 Pharmacological properties 20

3.3.5 Available bisoprolol preparations 20

3.4 Solid state forms of active pharmaceutical ingredients 21

3.4.1 Introduction 21

3.4.2 Crystalline and amorphous state 21

3.5 Selected techniques of solid state characterisation 28

3.5.1 Introduction 28

3.5.2 Thermal analysis 29

3.5.3 Spectroscopic techniques 30

3.5.4 X-ray diffraction 31

3.5.5 Microscopy 32

3.5.6 Measurement of solubility and dissolution rate 33

3.5.7 Differential scanning calorimetry 35

3.5.7.1 Standard differential scanning calorimetry 36

3.5.7.2 Temperature-modulated differential scanning calorimetry 38

3.5.7.3 Pharmaceutical applications of differential scanning calorimetry 41

3.5.8 Nuclear magnetic resonance 44
3.5.8.1 Basic theory of NMR spectroscopy 44
3.5.8.2 Solid-state NMR....45
3.5.8.2.1 Dipole-dipole interactions....45
3.5.8.2.2 Chemical shift anisotropy 47
3.5.8.2.3 Magic-angle spinning and high-power proton decoupling....47
3.5.8.2.4 Relaxation times....50
3.5.8.3 Solid-state NMR experiments....51
3.5.8.3.1 Direct excitation....51
3.5.8.3.2 Cross-polarisation 51
3.5.8.3.3 Dipolar dephasing 52
3.5.8.3.4 Inversion-recovery 53
3.5.8.3.5 Spin–lattice relaxation time experiments 54
3.5.8.3.6 Spin–lattice relaxation time in the rotating frame experiments 55
3.5.8.3.7 Heteronuclear correlation experiments 57
3.5.8.4 Pharmaceutical applications of solid-state NMR 58
3.6 Solid state drug-drug compatibility testing....61
4 RESEARCH OBJECTIVES 64
5 EXPERIMENTAL PART 65
5.1 Materials 65
5.2 Methods 66
5.2.1 Particle size and shape measurements....66
5.2.2 Thermogravimetric analysis....68
5.2.3 Hot-stage microscopy....68
5.2.4 Differential scanning calorimetry....68
5.2.5 Fourier transform infra-red measurements....69
5.2.6 Solution-state nuclear magnetic resonance 69
5.2.7 Solid-state nuclear magnetic resonance 70
5.2.8 First-principles computation 72
5.2.9 Powder X-ray diffractometry 72

5.2.10 Intrinsic and apparent dissolution testing....72
5.3 Results....74
5.3.1 Valsartan....74
5.3.1.1 Particle size and shape analysis....74
5.3.1.2 Thermal analysis....75
5.3.1.3 X-ray powder diffractometry....81
5.3.1.4 Fourier transform infra-red spectroscopy....82
5.3.1.5 NMR analyses....83
5.3.1.5.1 Carbon-13 solid-state NMR....83
5.3.1.5.2 Proton solid-state NMR....87
5.3.1.5.3 Proton–carbon-13 heteronuclear correlation solid-state NMR....89
5.3.1.5.4 Nitrogen-15 solid-state NMR....90
5.3.1.6 Molecular mobility....93
5.3.1.6.1 Spin–lattice relaxation time....94
5.3.1.6.2 Spin–lattice relaxation time in the rotating frame....97
5.3.1.7 Molecular mobility in the annealed fully amorphous valsartan....98
5.3.1.7.1 Temperature-modulated differential scanning calorimetry....98
5.3.1.7.2 The effect of annealing on the NMR relaxation times....100
5.3.1.8 Intrinsic and apparent dissolution rate measurements....101
5.3.2 Valsartan and bisoprolol compatibility studies....102
5.3.2.1 Thermal analysis....102
5.3.2.2 NMR, Fourier transform infra-red and X-ray powder diffraction analyses108
5.4 Discussion....123
5.4.1 Valsartan....123
5.4.2 Valsartan and bisoprolol compatibility....128
5.5 Conclusions....131
6 LIST OF FIGURES AND TABLES....133
6.1 Figures....133
6.1.1 Main text....133

6.1.2 Extended abstract in Polish 137
6.1.3 Appendices 138
6.2 Tables 138
6.2.1 Main text 138
6.2.2 Appendices 138
7 LIST OF PUBLICATIONS AND PRESENTATIONS 139
7.1 Journal publications 139
7.2 Conference presentations 139
8 ABSTRACT 141
9 EXTENDED ABSTRACT IN POLISH 145
10 REFERENCES 160
11 APPENDICES 169
11.1 2D solution-state NMR spectra of valsartan 169
11.2 Relaxation times for valsartan forms 172
11.3 2D solution-state NMR spectra of bisoprolol 173
12 OŚWIADCZENIA 176

1 ABBREVIATIONS

ACE	Angiotensin-converting enzyme
ADR	Apparent dissolution rate
AM form	Fully amorphous valsartan form
API	Active pharmaceutical ingredient
ARB	Angiotensin receptor blocker
AR form	As-received valsartan form
AT_1	Angiotensin II type 1 receptor
AT_2	Angiotensin II type 2 receptor
BCS	Biopharmaceutics classification system
BISO	Bisoprolol fumarate
CE	Circle equivalent
COSY	Correlated spectroscopy
CP	Cross-polarisation
CSA	Chemical shift anisotropy
CT	Contact time
CW	Continuous-wave
CVD	Cardiovascular disease
DD	Dipolar dephasing
DBPPSTE	DOSY bipolar gradient pulses stimulated echo sequence
DE	Direct excitation
DP	Direct polarisation
DOSY	Diffusion ordered spectroscopy
DSC	Differential scanning calorimetry
FDA	US Food and Drug Administration
FDC	Fixed-dose combination
FID	Free-induction decay
FSLG	Frequency switched Lee-Goldburg
FT-IR	Fourier transform infra-red spectroscopy
HETCOR	Heteronuclear correlation
HMBC	Heteronuclear multiple bond correlation
HPPD	High-power proton decoupling
HS	High sensitivity
HSM	Hot-stage microscopy
HSQC	Heteronuclear single quantum correlation
IDR	Intrinsic dissolution rate
IM	Isothermal microcalorimetry
IR	Inversion recovery
LM	Light microscopy
LRO	Long-range order
MAS	Magic-angle spinning
MCCP	Multicomponent cardiovascular pill
NQS	Non-quaternary suppression
NDA	New drug application
PLA	Poly(lactic acid)
PVP	Polyvinylpyrrolidone
PVP-CL	Cross-linked polyvinylpyrrolidone
Qi-TMDSC	Quasi-isothermal temperature-modulated DSC
RAS	Rennin angiotensin system
RF	Radiofrequency

SCXRD	Single-crystal X-ray diffractometry
SEM	Scanning electron microscopy
SPE	Single-pulse excitation
SRO	Short-range order
SSNMR	Solid-state nuclear magnetic resonance
StDSC	Standard DSC
TGA	Thermogravimetric analysis
TG	Thermogravimetry
TMDSC	Temperature-modulated DSC
TOSS	Total suppression of spinning sidebands
TPPM	Two-pulse phase-modulated
USP	United States Pharmacopeia
VAL	Valsartan
VT	Variable-temperature
XRPD	X-ray powder diffractometry

2 INTRODUCTION

Oral administration of drugs is usually the preferred and also the most common route of drug delivery. It is estimated that 80–90% of the active pharmaceutical ingredients (APIs) is formulated into solid dosage forms [1] and majority of these dosage forms are tablets or capsules. A solid active pharmaceutical ingredient used in a solid dosage form can exist in crystalline or amorphous state. Amorphous solids differ from their crystalline counterparts in the order of the molecular network i.e. they have no long-range order but some short-range order might exist [2, 3]. Amorphous active pharmaceutical ingredients have been used in the development of pharmaceutical solid formulations due to their advantages over crystalline forms such as increased solubility and dissolution rate [4-6]. However, amorphous APIs are usually less stable than their crystalline counterparts. For example the blockbuster, lipid-regulating drug, atorvastatin, was initially formulated as an amorphous salt, however, it was observed during the phase III clinical trials that drug had crystallized and as a result its physicochemical properties had changed causing the delay in lunching drug onto the market [7]. Understanding why particular amorphous APIs are stable and other re-crystallize is of paramount importance. The occurrence of polymorphism in crystal pharmaceuticals and its impact on physicochemical properties on API is well documented in the pharmaceutical literature [8-11]. It is known that amorphous materials can have different physicochemical properties depending on previous thermal history and time of storage, thus from the kinetic perspective it can be said that amorphous glasses can exist in different kinetic states, the term pseudopolyamorphism or relaxation polyamorphism has been used to describe this phenomenon [2]. Furthermore, differences in amorphous forms regarding stability and physicochemical properties, obtained by various preparation techniques have been reported for certain APIs [12-15]. Polyamorphism, the possible existence of two or more distinct amorphous forms of the same compound separated by a clear phase transition has been reported for inorganic compounds [16-18] and discussed in the context of pharmaceuticals in the literature [2, 11, 19]. However, it is believed that, there is no example of true polyamorphism in pharmaceutics and investigation into the existence of polyamorphism in organic APIs is crucial. The amorphous APIs have been studied intensively during the past years and there have been a few drug products with amorphous API on the market. For example, an angiotensin-converting enzyme (ACE) inhibitor, quinapril hydrochloride, a leukotriene receptor agonist, zafirlukast or an antiretroviral drug, lopinavir [8].

Despite a wide variety of analytical techniques available to characterise solid state such as differential scanning calorimetry (DSC), Fourier transform infrared spectroscopy (FT-IR),

Raman spectroscopy, solid-state nuclear magnetic resonance (SSNMR) or X-ray powder diffractometry (XRPD), the structural characterisation of subtle differences between different amorphous forms of active pharmaceutical ingredients continues to be a challenge. The physicochemical properties of a solid API are strongly related not only to its structural features but also to its molecular dynamics [20, 21]. It is important to understand the dynamic of molecular motion occurring in an amorphous APIs, because molecular relaxation takes place during storage of formulated amorphous drug.

Valsartan is an antihypertensive drug belonging to angiotensin II receptor antagonists class called sartans [22]. Valsartan is marketed in the non-crystalline form. Various analytical methods have been used to characterise solid state of valsartan. Tran *et al*. studied the influence of various types of solvents on the polymorphic crystallization behaviours and dissolution rates of two sources of valsartan by scanning electron microscopy (SEM), DSC and XRPD [23]. Although authors regarded obtained solid forms as crystalline polymorphic forms, XRPD data suggest that most of the forms existed in the amorphous state with different level of structure arrangement rather than in the crystalline state and/or as a mixture of amorphous and crystalline materials. Shrivastava and co-workers [24] reported DSC thermogram of valsartan showing a single endotherm which was ascribed to melting of the drug, however they presented powder X-ray diffraction pattern of valsartan indicating its amorphous nature. The crystal structure of a highly crystalline valsartan has been relatively recently patented [25], published [26] and characterised by selected solid-state techniques. SSNMR was not used to characterise the valsartan solid state, however was successfully employed to characterise different polymorphic and amorphous forms of other sartans (candesartan, irbesartan and losartan) [27-29].

Valsartan can be used alone or in combination with other antihypertensive agents. Combining drugs with synergistic mechanism of action in one dosage form (fixed-dose combination, FDC) has potential benefits, such as improved efficacy, reduced dosing, lower cost or enhanced patient compliance [30]. Bisoprolol fumarate is a $beta_1$-selective (cardioselective) adrenoceptor blocking agent [31]. Both valsartan and bisoprolol are used concomitantly in the treatment of cardiovascular diseases (CVDs), however, there is no single dosage form currently on the market containing both agents. Although, it is worth noting that the New Drug Application (NDA) to the FDA (*US Food and Drug Administration*) for an fixed-dose combination of valsartan and other beta-blocker, nebivolol, has been recently submitted by Forest Laboratories Inc. [32]

The multi-ingredient drug products offer many benefits over the single ingredient drug products. It has been especially investigated in the case of CVD treatments. Combination therapy has been shown to reduce CVD complications by more than 80% [30], and strong

interest has been expressed by the pharmaceutical industry to develop an all-in-one pill (multicomponent cardiovascular pill, MCCP or polypill) containing an angiotensin-converting enzyme inhibitor, beta-blocker, aspirin and statin [33].

The simplest and the most economic approach to formulating a multi-ingredient dosage form is a blend or granulation containing all the active pharmaceutical ingredients. The combination of different agents in a single dosage form can, however, lead to interactions between APIs, potentially affecting the stability and bioavailability of either component [34-40]. Such interactions, termed incompatibilities, can be either physical or chemical in nature. Chemical interactions between APIs are well documented for FDCs intended for the treatment of tuberculosis, malaria or CVDs, conditions which usually require combination therapy [38-43]. Even in the absence of chemical reactions between components, the combination of two or more compounds (API-API or API-excipient) can result in physical interactions such as polymorphic transitions [44], amorphisation [45] or the formation of eutectic mixtures [46, 47]. These can cause problems during manufacturing [47, 48], with shelf life [49] or bioavailability [50].

The identification of possible interactions between APIs is extremely important at an early stage of drug development process. Thermal analysis is frequently used to study the physicochemical properties of APIs and compatibilities between drug-drug and drug-excipient [41, 47, 51, 52]. DSC quickly provides information about possible interactions among the formulation components, according to the appearance, shift or disappearance of phase transition peaks and/or variations in the corresponding enthalpy or heat capacity values in thermal curves of drug-drug/excipient in physical mixtures [53, 54]. However, the interpretation of the thermal data is not always trivial, and the interactions observed at high temperatures may not always be relevant to ambient conditions. Therefore, the use of complementary analytical techniques is advisable [55-57]. Solid-state nuclear magnetic resonance is another technique used to characterise pharmaceuticals [58, 59] and study physical or chemical interactions between APIs and excipients. It has been successfully used for characterising the physical interactions occurring between API and polymers [60-63], between API and β-cyclodextrin [64], and acid-base reactions between API and excipients [65-67], but SSNMR has not been widely used, however, in API–API compatibility studies.

The ambiguous reports regarding solid state forms of valsartan raised the question if the solid state of commercially available valsartan is truly amorphous. In this dissertation differential scanning calorimetry and solid-state NMR were used to characterise solid state of two valsartan forms and two forms of bisoprolol fumarate and to evaluate their compatibility. The main analytical techniques were supported by, where appropriate, particle size and shape

analysis, hot-stage microscopy (HSM), TGA, solution-state NMR, FT-IR, XRPD, and dissolution studies.

3 THEORETICAL PART

3.1 Introduction

Cardiovascular diseases (CVDs) are the disorders of heart and blood vessels and include coronary heart disease, cerebrovascular disease, peripheral artery disease, congenital heart disease, heart failure and hypertension. CVDs are one of the major causes of death in both developed and undeveloped countries [68, 69]. It is estimated that 23.3 million people will die from CVDs by 2030 [69, 70]. Hypertension is a significant factor increasing the incidence of stroke and coronary heart disease. Despite the advances in the hypertension treatment in the last few decades and availability of a wide variety of effective antihypertensive agents in many patients the hypertension is still not adequately controlled.

Angiotensin II type 1 receptor antagonists (AT_1 blockers, angiotensin receptor blockers, ARBs or sartans) have been successfully used in the treatment of hypertension for nearly two decades. The first sartan, losartan, was approved by the FDA (*US Food and Drug Administration*) in 1995. In 2011 the new ARB, azilsartan, was approved by the FDA and introduced into the pharmaceutical market. Currently there have been 8 ARBs available in the US and EU pharmaceutical markets, i.e.: azilsartan, candesartan, eprosartan, irbesartan, losartan, olmesartan, telmisartan and valsartan. Azilsartan and olmesartan have not been approved for marketing in Poland yet. Valsartan was approved by the FDA in 1997. It was discovered and initially manufactured by Ciba-Geigy.

Beta-adrenoreceptor blocking agents (beta-blockers) are another class of drugs used in the management of cardiovascular disorders. They have been used in the clinical practice since the 60’s of the 20th century. Currently there has been more than 30 beta-blockers available in the US and EU pharmaceutical markets. Bisoprolol was approved by the FDA as a new molecular entity in 1992 and manufactured by Duramed Pharmaceuticals Inc.

3.2 Valsartan

3.2.1 Chemical structure and physicochemical properties

Valsartan, Figure 1, as most of the sartans, contains in its structure biphenyl component and a tetrazole substituent, which was initially considered to be essential for a pharmacological activity [71]. Valsartan molecule contains chiral centre and only pure (*S*)-enantiomer (or L) is used as an (*R*)-enantiomer (or D) has much lower pharmacological activity [72]. Valsartan is marketed as a free acid.

Valsartan is a white amorphous powder and belongs to class II Biopharmaceutics Classification System (BCS; low solubility and high permeability). Different polymorphic, amorphous and partially amorphous forms were reported in the patent literature [73-76], however, the crystal structure of highly crystalline valsartan form has been relatively recently patented [25] and published [26].

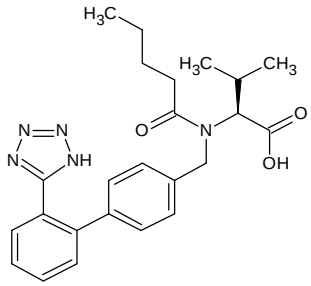

Figure 1. Chemical structure of valsartan, *N*-[*p*-(*o*-1*H*-tetrazol-5-ylphenyl)benzyl]-*N*-valeryl-L-valine (M = 435.52 g mol^{-1}).

Various analytical methods have been used to characterise solid state of valsartan. Tran *et al*. studied the influence of various types of solvents on the polymorphic crystallization behaviours and dissolution rates of two sources of valsartan by SEM, DSC and XRPD [23]. Although authors regarded obtained solid forms as crystalline polymorphic forms, XRPD data suggest that most of the forms exist in the amorphous state with different level of structure arrangement and/or as a mixture of amorphous and crystalline materials rather than in the truly crystalline state. They found significant differences in morphology, structure and dissolution rates among re-crystallized samples. Shrivastava and co-workers [24] reported DSC thermogram of valsartan showing a single endotherm at 108 °C which was ascribed to melting of the drug, however, they presented powder X-ray diffraction pattern of valsartan indicating its amorphous nature. The crystal structure of highly crystalline valsartan and its ethanol solvate have been relatively recently published [26], characterised by solid-state techniques (thermal methods, Raman spectroscopy, FT-IR, XRPD, single crystal X-ray diffraction and dynamic vapour sorption) and compared to commercially available non-crystalline form. Valsartan crystallizes in an orthorhombic space group $P2_12_12_1$. The unit cell contains one molecule of valsartan in an asymmetric unit (Z = 4). The molecules of valsartan are connected via two hydrogen bonds associated with tetrazole ring, Figure 2. The molecules of valsartan in the crystal structure occurs in a *trans* conformation in regard to the C(O)–N peptide bond.

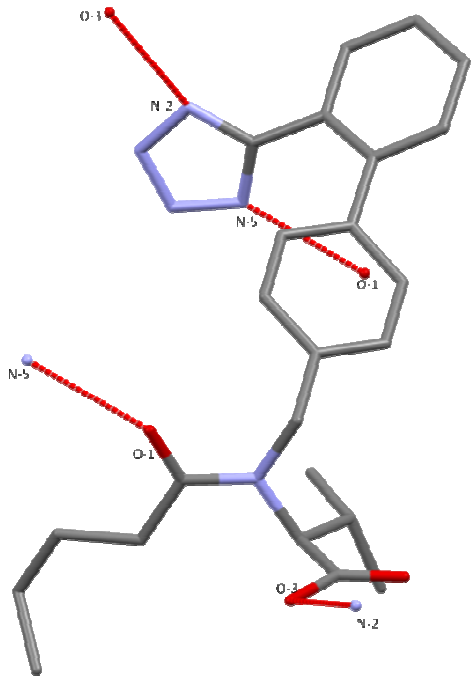

Figure 2. The structure and hydrogen bonding of (*S*)-*trans* valsartan isomer adapted from Ref. [26]. Hydrogens are omitted for clarity.

It was reported that in a solution valsartan exists in two conformations (*cis–trans*) due to interchange via rotation around the C(O)–N peptide bond [77, 78].

3.2.2 Mechanism of action

A rennin angiotensin system (RAS) plays an important role in the in the regulation of fluid balance and arterial blood pressure. A proteinase enzyme, rennin, cleavages angiotensinogen to inactive decapeptide angiotensin I. Then, angiotensin I is converted by angiotensin-converting enzyme (ACE) into angiotensin II. The final step of the RAS cascade is the activation of an angiotensin II receptors AT_1 and AT_2 by angiotensin II [79, 80]. Activation of the AT_1 receptors promote aldosterone secretion and sodium retention, resulting in elevated blood pressure due to vasoconstriction. The functional role of the AT_2 receptors still remains unclear, however, there is some evidence that simulation of AT_2 receptors causes vasodilatation thus counteracting the vasoconstriction caused by the stimulation of the AT_1 receptors [80-82]. The sartans are highly selective blockers for the AT_1 receptors. The affinity for AT_1 receptor is 10 000–20 000 times higher than for the AT_2 receptor [81]. The rennin angiotensin cascade with the drugs targets is shown in Figure 3.

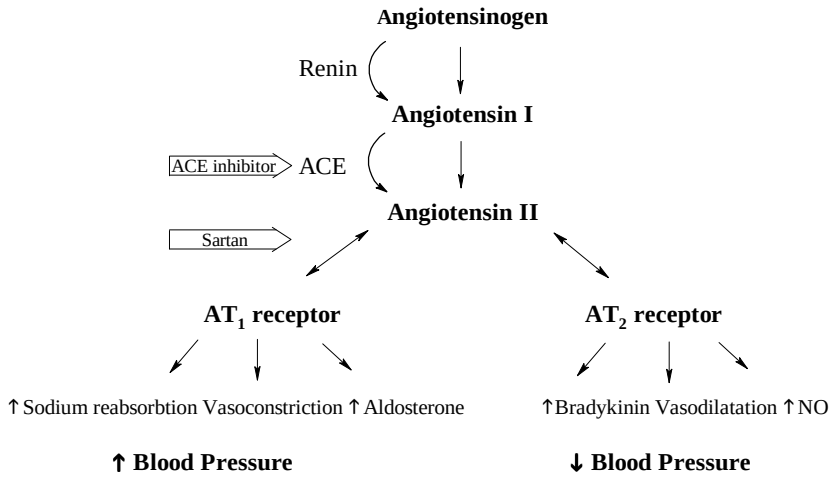

Figure 3. The rennin angiotensin system with sites of blockade by ACE inhibitors and sartans. Modified from Ref. [82]

3.2.3 Pharmacokinetic properties

The pharmacokinetic properties of various sartans are generally similar. After oral administration valsartan is readily absorbed and displays the pharmacological action after a few hours [83]. The oral bioavailability is low (25%). Valsartan has a long duration of action which allows for once daily administration and control of blood pressure for 24 h. Valsartan highly bounds to plasma proteins with volume of distribution of 17 L. Valsartan is mainly metabolised in the liver and eliminated by the bile or kidney as faeces and urine, respectively.

3.2.4 Pharmacological properties

Valsartan is mainly used in the treatment of hypertension as an alternative for ACE inhibitors for patients who have to discontinue use of ACE inhibitors due to side-effect (dry cough) caused by them. The ARBs unlike the ACEis do not inhibit the breakdown of bradikinin and other kinins, and thus are less likely to cause dry cough as a result of this inhibition [80, 84]. Other indications include the management of heart failure, diabetic nephropathy and also may be used after myocardial infarction and for renal dysfunction and/or microalbuminuria [80-82]. Furthermore, there are some studies indicating possible future usage of the ARBs in the treatment of the following conditions: diabetes mellitus, diabetic proliferative retinopathy, glaucoma, atherosclerosis, cancer and lung diseases [80]. Usual dose of valsartan is 80 to 320 mg orally as a single daily dose.

Valsartan is usually well tolerated and hypersensivity is rare. Caution is advised for patients with renal artery stenosis, primary aldosteronism or hepatic impairment. ARBs should

be avoided during pregnancy and lactation. The side-effects are comparable with placebo. Symptomatic hypertension may occur particularly in patient taking high dose diuretics. ARBs appear less likely than ACE inhibitors to cause cough. Hyperkalaemia may occur, especially when used with potassium-sparing diuretics. Angioneurotic oedema has also been reported.

3.2.5 Available valsartan preparations

Valsartan is formulated as tablets, capsules or oral solution (Diovan®, Novartis Pharmaceuticals Corp.). The generic formulations are also marketed. Apart of single-ingredient formulations, multi-ingredient preparations are also available. Available valsartan fixed-dose combinations contain diuretic (hydrochlorothiazide, Co-Diovan®, Novartis Pharmaceuticals Corp.), calcium channel blocker (amlodipine besilate, Exforge®, Novartis Pharmaceuticals Corp.), both agents together (Exforge HCT®, Novartis Pharmaceuticals Corp.) or rennin inhibitor (aliskiren, Valturna®, Novartis Pharmaceuticals Corp.). Valturna® was discontinued due to adverse events. Recently, New Drug Application (NDA) to the FDA for an fixed-dose combination of valsartan and beta-blocker, nebivolol, has been submitted by Forest Laboratories Inc. [32].

3.3 Bisoprolol

3.3.1 Chemical structure and physicochemical properties

Most of the beta-adrenoreceptor blocking agents are derivatives of aryloxypropanolamines. The chemical structure of bisoprolol is shown in Figure 4. High cardioselectivity of bisoprolol resulting from the *para* substituent in the aromatic ring [85]. The hydroxyl group, which appears to be essential for activity, confers on the compounds their optical activity. Bisoprolol is marketed as a racemic mixture as a fumarate salt. Although, the activity of the (*S*)-enantiomer is about 30–80 times higher than that of the (*R*)-enantiomer [86]. Bisoprolol fumarate is a white crystalline powder and belongs to class I of the BCS (high solubility and high permeability) and is marketed in its crystalline form [87]. The European Pharmacopeia states that bisoprolol fumarate exhibits polymorphism [88], however, references to polymorphic forms could not be found in the literature.

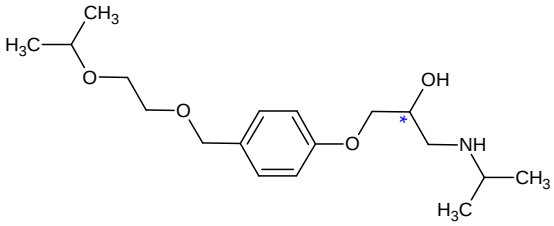

Figure 4. Chemical structure of bisoprolol base, ((*RS*)-1-((alpha-(2-isopropoxyethoxy)-p-tolyl)oxy)-3-(isopropylamino)-2-propanol), with chiral centre denoted by asterisk (*) (M = 325.44 g mol^{-1}).

3.3.2 Mechanism of action

Beta-adrenoceptor blocking drugs block the beta-adrenoreceptors in the heart, peripheral vasculature, bronchi, pancreas, and liver thus decreasing the excitability of the heart, decreasing cardiac output and oxygen consumption, decreasing the release of renin from the kidney, and finally lowering blood pressure. Bisoprolol highly selectively blocks β_1 receptors and does not have any intrinsic sympathomimetic (partial agonist) or membrane stabilising activity [89].

3.3.3 Pharmacokinetic properties

Bisoprolol is well absorbed from the gastrointestinal tract and oral bioavailability is about 90%. Peak plasma bisoprolol concentrations are reached 2 to 4 h after administration. Bisoprolol is about 30% bound to plasma proteins with an apparent volume of distribution of 3.5 L kg $^{-1}$. The plasma elimination half-life is about 10 to 12 h. Bisoprolol is moderately lipid-soluble. It is metabolised in the liver and excreted in urine, about 50% as unchanged drug and 50% as metabolites [89].

3.3.4 Pharmacological properties

Bisoprolol is used in the management of hypertension and angina pectoris and as an adjunct to standard therapy in patients with stable chronic heart failure [90]. It is generally well tolerated and most adverse effects are mild and transient. The major side-effects include: bronchospasm, gastro-intestinal disturbances, bradycardia, sleep disturbances, fatigue or headache. Bisoprolol has less effect on the β_2 (brionchal) receptors and is relatively cardioselective but not cardiospecific and therefore it has lesser effect on airways resistance but it is not free of this side-effect. The usual dose of bisoprolol fumarate is 5 to 10 mg orally as a single daily dose.

3.3.5 Available bisoprolol preparations

Bisoprolol is marketed as a single-ingredient tablet formulation (Zebeta®, Duramed Pharmaceuticals Inc.). Also, multi-ingredient formulation is available. The FDC contains

diuretic – hydrochlorothiazide (Ziac®, Duramed Pharmaceuticals Inc.). The generic formulations of bisoprolol and its FDC are also marketed. Moreover, FDC of bisoprolol fumarate and amlodipine besilate in the treatment of hypertension, sponsored by Merck KGaA, is in the phase 3 of the clinical trial [91].

3.4 Solid state forms of active pharmaceutical ingredients

3.4.1 Introduction

Oral administration of drugs is usually the preferred and also the most common route of drug delivery. It is the most convenient route of administration for the patient and results in improved compliance. It is estimated that approximately 80–90% of the active pharmaceutical ingredients is formulated into solid dosage forms [1] and majority of these solid dosage forms are tablets or capsules. The solid oral dosage forms offer some advantages over the other forms. The shelf-life is longer than that for liquid forms as the reactions in a solid state are usually slower than that in the solution. Moreover, tablets and capsules are easy to handle, store and transport, and also they are the most economic solid dosage forms to manufacture.

The oral solid dosage form is usually composed of two components: active pharmaceutical ingredient and inactive adjuvant substances known as excipients. Both APIs and excipients may exist in a different solid state. The solid state can be classified into two major categories: crystalline state and amorphous state [8, 92-95]. If a solid exhibits long-range, regularly repeating units, it is classified as the crystalline materials. The crystalline materials exhibit both long-range order (LRO, over ~10^3 to ~10^{20} atoms) and short-range order (SRO, over a few atoms) in a crystal lattice. The disordered solids which do not exhibit LRO, but may possess some SRO are classified as amorphous materials. Since the different solid state forms may feature different physicochemical properties, the solid state characterisation of pharmaceuticals is a very important matter from the pharmaceutical sciences and industry point of view [8, 94, 96].

3.4.2 Crystalline and amorphous state

Crystals and crystal structures can be described in two terms: *habit* and *form* [95]. The *habit* describes the overall external shape of a particular crystal. The crystal shape is a kinetically controlled phenomenon and is influenced by the crystallization conditions [95]. Examples of a crystal habit include: aciruclar (needle-like), prismatic, pyramidal, tabular, equant, columnar and lamellar types. The crystal habit may have an impact on the physicochemical properties and

thus may have significance from both biopharmaceutical and technological point of view [97-101].

The term *form* refers to the internal crystal structure and derives from the Greek *morph*. Hence, the term *polymorphism* is defined as crystalline materials with the same chemical composition, different lattice structures and/or different molecular conformations [8, 11, 94, 95, 102]. The difference in crystal structure is mostly a function of thermodynamics. It has to be noted that the differences in a habit or crystal morphology may not indicate different polymorphic crystal structure [95]. As implied by the definition, polymorphism can be divided into two categories: packing and conformational polymorphism [11, 95, 96, 103]. In the *packing polymorphism* conformationally rigid molecules adopt different packing arrangements [96]. For instance, packing polymorphism can be observed in an anti-inflammatory drug, nabumetone, where two forms (I and II) adopt similar molecular conformations but different arrangements in the lattice. Form I assembles in head-to-tail manner whereas form II packs in tail-to-tail head-to-head fashion. The two arrangements occur due two weak intermolecular interactions especially C–H···O (form I) and C–H··π (form II) [104]. In the *conformational polymorphism* molecules adopt more than one conformation in the solid state [103]. For example an antypsychotic drug, olanzapine, is known to exhibit conformational polymorphism. It was found that olanzapine can exists in three polymorphic forms [105]. If the solid state is composed from the molecules with the different configurations such as geometric isomers or tautomers the term *configurational polymorphism* is used [94, 96]. However, because isomers are essentially different molecules, the term polymorphism should not be applied in these cases and is sometimes refers to as *parapolymorphism* [94]. An example of configurational polymorphism is a desmotropy (the existence of crystals of a compound in two different tautomers) [106]. A well-known example is AT_1 blocker, irbesartan, where two crystal forms due to tautomerism in the tetrazole ring were obtained [27]. The crystalline solids where solvent molecules are incorporated into the crystal lattice in a stoichiometric or non-stoichiometric way are termed *solvates* (*hydrates* where the solvent is water), *solvatomorphs* or *pseudopolymorphs* [8, 11, 94, 96, 102]. It is generally not advisable to use the latter term [107]. The well-known example of active molecules formulated as hydrates are, for instance, a drug used in the dyslipidemia treatment, atorvastatine calcium trihydrate [108] or a proton pump inhibitor, pantoprazole sodium sesquihydrate [109]. If in the crystalline solid non-volatile molecule is incorporated then the solid is termed as *co-crystal* [94, 110-112]. There have been many examples of pharmaceutical co-crystals in the scientific literature [112], however, there is only a few co-crystals APIs approved by FDA, for example, a drug used in epilepsy treatment – Depakote® (the valproic acid cocrystal of sodium valproate) [113]. When an active compound is

an acidic or basic it is possible to create a salt. About half of all APIs are marketed as salts [114]. The main difference between crystalline salts and co-crystals is that in salts proton is transferred from acidic to basic functionality of the crystallization partner or vice versa, whereas in co-crystals no such transfer occurs [115]. Solvates, co-crystals and salts can exist as different polymorphs. The schematic representation of different solid state forms of APIs is shown in Figure 5.

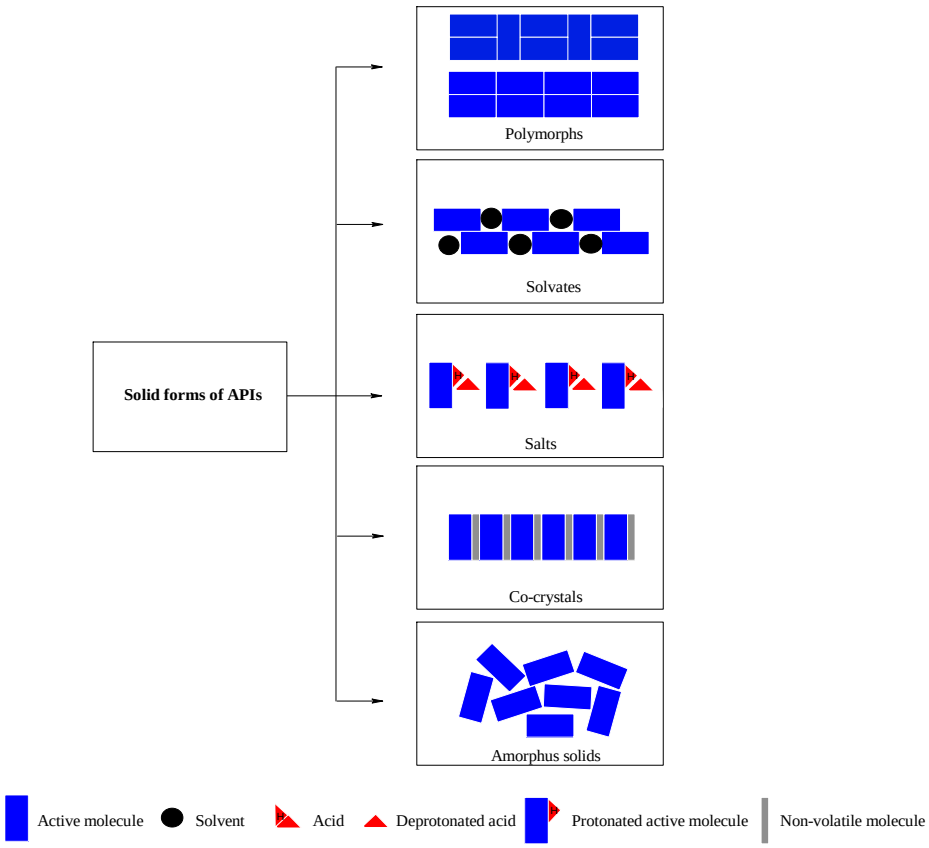

Figure 5. Schematic representation of APIs solid forms. Modified from Refs. [94, 116].

Amorphous solids differ from their crystalline counterparts in the order of the molecular network i.e. they have no LRO but some SRO might exist [2, 3, 49]. Amorphous materials are non-equilibrium systems and possess higher energy than their crystalline counterparts. Amorphous active pharmaceutical ingredients have been used in the development of pharmaceutical solid formulations due to their advantages over crystalline forms such as increased solubility, dissolution rate and as a consequence higher bioavailability [4-6, 117], some mechanical properties of amorphous materials may also be an advantage [117-120]. However, the drawback is that amorphous APIs are usually less stable than their crystalline counterparts [21, 49, 117]. Some amorphous excipients and active pharmaceutical materials are used in licensed drug products. The widely used in amorphous state excipients are, for example,

polyvinylpyrrolidone (PVP), poly(DL-lactic acid) or colloidal silicon dioxide [121]. A well-known marketed amorphous APIs include: an ACE inhibitor, quinapril hydrochloride, a leukotriene receptor agonist, zafirlukast or an antiretroviral drug, lopinavir [8]. Mostly, the reasons for employing the amorphous APIs in licensed products, are the increased bioavailability, instability of crystalline material or inability to crystallize the API [8].

One of the important differences in the physical properties between crystalline and amorphous materials is that the disordered material does not melt and hence there is no sharply-defined melting temperature. Instead, the amorphous solids undergo a unique transition over a temperature interval. The transition from the rigid glassy state to a more flexible and more viscous form is termed as a *glass transition* and the temperature over which this change occurs is known as the *glass transition temperature* (T_g) [8, 122].

Amorphous solid below T_g is called a glass or amorphous solid and above an amorphous liquid or supercooled liquid. The process occurs during heating the glass or cooling supercooled liquid. T_g is typically approximately 2/3 of the melting temperatures expressed in Kelvin (K) [123]. There are significant differences in the macroscopic and thermodynamic properties such as viscosity, mechanical strength, enthalpy, entropy and volume, below and above the glass transition [49, 117]. These changes are of the results of different molecular mobility below and above the glass transition [124].

The important issue related to the crystalline polymorphic and amorphous materials is their thermodynamic stability. The relative thermodynamic stability of solid materials for a transformation at constant temperature and pressure is related to their Gibbs free energy (G) and determined by the ΔG:

$$\Delta G = \Delta H - T\Delta S \quad (1)$$

where ΔH is the enthalpy difference between the forms, reflecting the lattice or structural energy differences, ΔS is the entropy difference between the forms, reflecting the disorder and mostly lattice vibrations [11, 116]. Knowing the algebraic sign of Gibbs free energy allows for stability prediction of a solid form i.e.: when $\Delta G < 0$ the transformation can occur spontaneously, when $\Delta G = 0$ the system is in the equilibrium and when $\Delta G > 0$ the spontaneous transformation is not possible under the specific conditions. The differences between single component system that exists in different solid states in terms of Gibbs free energy are shown in Figure 6.

Polymorphs can be classified as *monotropes,* where one form is more stable than other at temperatures below the melting temperatures of the system (for example, crystal A or C in Figure 6), or *enantiotrops,* where the transition occurs below the melting temperatures of the system (for example, crystal A or B in Figure 6).

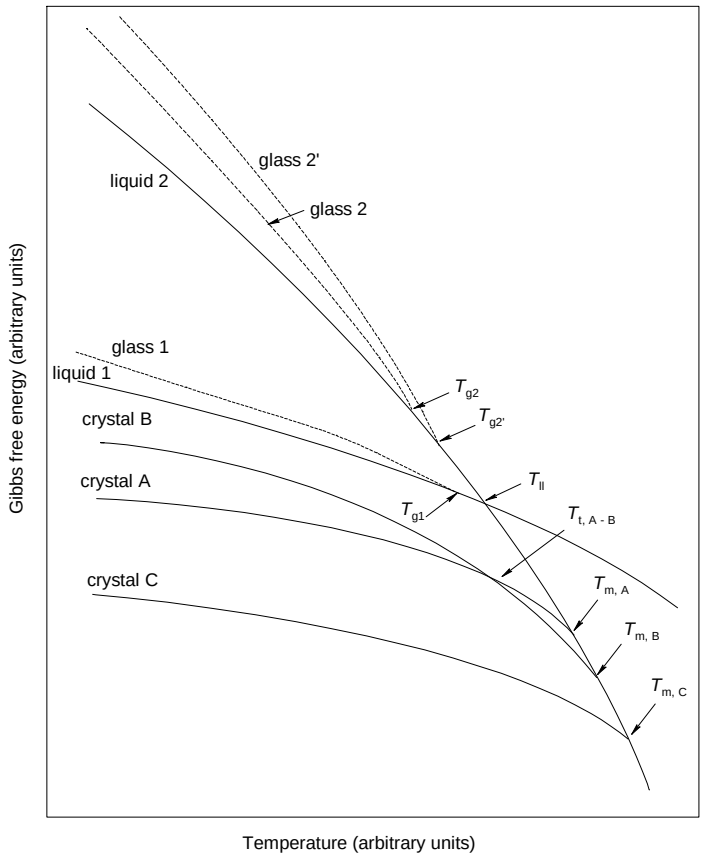

Figure 6. Schematic Gibbs free energy curves for a hypothetical single-component system that exhibits polymorphism, pseudopolyamorphism and polyamorphism. Crystals A, B and C correspond to polymorphs with melting temperatures, $T_{m, A}$, $T_{m, B}$ and $T_{m, C}$, respectively, and with a solid-solid polymorphic transition temperature ($T_{t, A-B}$). Liquid 1 and liquid 2 correspond to two liquids with first-order liquid-liquid true polyamorphic transition temperature (T_{ll}) with polyamorphs glass 1 and glass 2 with glass transitions temperatures, T_{g1} and T_{g2}, respectively. Glass 2 and 2′ describe glasses with different processing and/or storage history showing different glass transition temperatures, T_{g2} and $T_{g2'}$, respectively (pseudopolyamorphs). Modified from Refs. [2, 11].

Polymorphic transitions and crystal-liquid phase transitions are classified as *first-order phase transitions*. The first-order phase transition is a process whereby the first derivative of the change in Gibbs free energy with respect to temperature is not equal zero [125, 126], i.e.:

$$\frac{\delta \Delta G}{\delta T} = (-\Delta S) \neq 0 \tag{2}$$

In the first order transitions the first derivatives of free energy are discontinuous at the phase transition. The discontinuity of entropy, ΔS, leads to an associated exchange of heat, called the enthalpy of transition:

$$\Delta H = T\Delta S \tag{3}$$

This enthalpy of transition is also called "*latent heat*" since a small amount of heat exchanged at the transition point does not induce any change in the temperature of the system. In practice the

first-order transition will occur at the DSC experiment at a specific temperature and will be independent of heating or cooling rate, although instrumental factors might result in an apparent rate dependence [125]. A *second-order phase transition* is a process whereby the first derivative of the change in Gibbs free energy with respect to the temperature is equal zero but the second-order derivative is non-zero [125, 126], i.e.:

$$\frac{\delta^2 \Delta G}{\delta T^2} = \left(-\frac{\Delta C_\mathrm{p}}{T}\right) \neq 0 \tag{4}$$

There is no enthalpy of transition associated with these phase transitions because the entropy does not show discontinuity. The transition is defined as a step change in the heat capacity (ΔC_p) of a material as a function of temperature. The important transition that is by some authors considered as the second-order transition is the glass transition [125, 127]. Although, it does not follow exact definition of the second-order transition as the transition is gradual and occurs over about 10 °C or more. In practice the location of the glass transition temperature determined by DSC is a function of the experimental cooling or heating rate which reveals that it is also a kinetic phenomenon; hence, again, the process does not fit the strict definition of a second-order transition definition [125, 128]. Hence, the glass transition process is better ascribed by the term *second-order-like transition* [129]. The changes of thermodynamic quantities at first- and second-order transitions are shown in Figure 7.

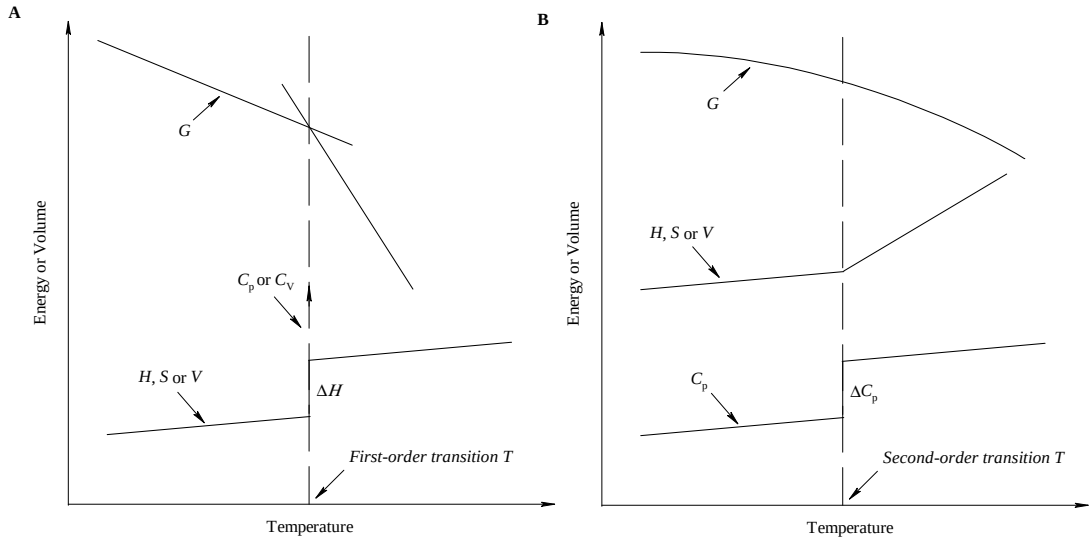

Figure 7. Changes of Gibbs free energy (*G*), enthalpy (*H*), entropy (*S*), volume (*V*) and heat capacity at constant pressure or volume (C_p and C_v) at (A) first- and (B) second-order phase transitions. The heat capacity has an infinite value at first-order phase transition temperature whereas at second-order phase transition, there is no discontinuity in *H, S, V* but a "jump" in the heat capacity is observed. Adapted from Ref. [127].

Several methods of determining T_g by DSC are used. The most common choice is either the onset or the point where half the change in C_p between the level of C_p(liquid) and C_p(solid) at T_g

has been reached. These are useful characteristic temperatures although both depend on experimental conditions and there might be a significant difference for aged and unaged amorphous materials. A fictive temperature (T_f) is used to characterise T_g of aged materials. T_f has a thermodynamic basis in that it represents the point of intersection of enthalpy curves for the glassy and liquid states [122, 130, 131]. The enthalpy of a glass depends on the method of glass formation, a fresh, unaged (non-stored) glass has a higher enthalpy than an aged (stored) one, and thus T_f shows no dependence on heating rate.

The physical ageing or annealing in the amorphous material i.e. structural relaxation towards thermodynamic equilibrium as a function of time [132] is also of a great importance from pharmaceutical sciences and industry point of view [133, 134]. The sample stored below T_g, non-equilibrium state, undergoes physical ageing. At low temperatures apparent equilibrium is difficult to achieve as the molecular mobility is low thus the time for observing physical ageing may be long [132]. Different apparent equilibria may exist below T_g depending on thermal history and storage of amorphous material and thus material might have different physicochemical properties. At the temperature above T_g no physical ageing is observed as molecular mobility is high and equilibrium is achieved rapidly.

The occurrence of polymorphism in the crystalline pharmaceuticals and its impact on physicochemical properties on API is well documented in the pharmaceutical literature [8-11]. It is known that amorphous materials can have different physicochemical properties depending on previous thermal history and time of storage, thus from the kinetic perspective it can be said that amorphous glasses can exists in the different kinetic states, the term *pseudopolyamorphism* or *relaxation polyamorphism* has been used to describe this phenomenon [2]. Furthermore, differences in the amorphous forms regarding stability and physicochemical properties, obtained by various preparation techniques have been reported for APIs [12-15]. *Polyamorphism*, the possible existence of two or more distinct amorphous forms of the same compound separated by a clear first-order phase transition has been reported for inorganic compounds [16-18, 135] and discussed in the context of pharmaceuticals in the literature [2, 11, 19], however, there is no example of true polyamorphism in pharmaceutics. The differences between polyamorphs and pseudopolyamorphs in terms of Gibbs free energy are shown in Figure 6. The relaxation polyamorphism is describes by curves “glass 2” and “glass 2′” (second-order transitions) and the true polyamorphism between two amorphous phases in the supercooled or equilibrium liquid state is described by “liquid 1” and “liquid 2” where liquid-liquid first-order transition occurs at the temperature transition (T_{ll}). Similarly to the crystalline state, amorphous materials may exist as solvates, salts, co-amorphous systems or non-stoichiometric amorphous polymer solid dispersions [136-140].

3.5 Selected techniques of solid state characterisation

3.5.1 Introduction

The solid form of an API or excipient can have a significant impact on the properties of the final dosage form. When the active agent is under developing process it is important to produce it in a desired solid form in a consistent, pure and reproducible manner. Furthermore, during the formulation process the drug can change solid form forming other polymorph, solvate or amorphous state [9, 141]. The scheme of critical manufacturing steps leading to a final dosage form in which a solid state change might occur is shown in Figure 8.

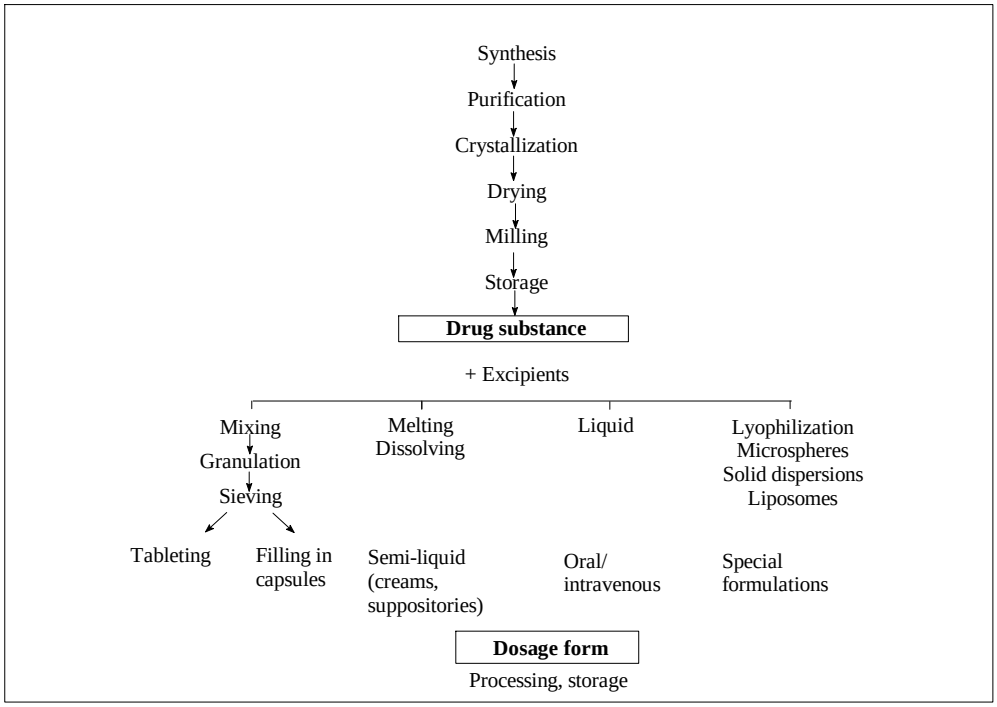

Figure 8. Scheme of the critical manufacturing steps leading to final dosage formulation in which a solid state change might occur. Adapted from Ref. [141].

Hence, the detailed characterisation of solid state is of a paramount importance. The suitable and the most common techniques used to characterise solid state of pharmaceuticals include [93, 94]:

- thermal analysis:
    - thermogravimetric analysis (TGA),
    - differential scanning calorimetry (DSC),
    - temperature-modulated differential scanning calorimetry (TMDSC),
    - hot-stage microscopy (HSM);
- spectroscopic techniques:

  - Fourier transform infrared spectroscopy (FT-IR),
  - Raman spectroscopy,
  - solid-state nuclear magnetic resonance (SSNMR);
- X-ray diffraction techniques:
  - single-crystal X-ray diffractometry (SCXRD),
  - X-ray powder diffractometry (XRPD);
- microscopic techniques:
  - light microscopy (LM),
  - scanning electron microscopy (SEM);
- measurement of other physical properties:
  - solubility measurements,
  - dissolution rate measurements.

3.5.2 Thermal analysis

Thermal analysis is a group of techniques in which one (or more) property of a sample is studied while the sample is subjected to a controlled temperature programme [142]. The properties studied might include almost every physical or chemical property of the sample, or its product.

Thermogravimetric analysis (TGA) or thermogravimetry (TG) defines any experimental methods where changes in mass are used to detect and to measure the chemical or, less frequently, the physical processes that occur on heating the sample [125]. In the pharmaceutical analysis TGA is used for the determination of stoichiometry of solvates and may also provide information about the type of binding involved, on the basis of the temperature at which the solvent is lost. Another important application of the technique is investigation of the reaction kinetic. The TGA is also employed before any other thermal methods are used, to determine a thermal degradation point of the sample. A weakness of this technique is that it does not provide information on the nature of the substance being lost or less frequently bonded during heating, only the mass changes are known. Therefore TG is commonly coupled with other analytical techniques such as mass spectroscopy or infrared spectroscopy to allow chemical identification of lost material [143].

Hot-stage microscopy (HSM) or thermomicroscopy is a technique in which an optical property of a sample is monitored, against the temperature or time, while the temperature of the sample, in a specified atmosphere, is programmed [125]. The observation is usually conducted by using polarised light microscope. Diagnostic properties that can be determined employing HSM include: melting point, crystallization, cold crystallization, polymorphic transitions,

decomposition, assessment of purity, desolvation, sublimation, and it can be used as a rapid and easy way to establish the thermodynamic relationship between metastable polymorphs. In the pharmaceutical sciences the HSM is usually used for the visual confirmation of transitions observed by other techniques such as TGA or DSC. The HSM is widely used to characterise polymorphic forms and transitions of pharmaceuticals by identifying changes in crystal habit or changes in light transmission or reflection associated with transition [94]. As a multi-technique approach is needed for comprehensive characterisation of pharmaceutical solids' physical properties, the thermomicroscopy is a valuable complementary technique for a development of new APIs.

As the DSC and TMDSC are the main solid state characterisation tools used in this work, both techniques are discussed in greater details in the section 3.5.7.

3.5.3 Spectroscopic techniques

In the 1940s the first spectroscopic technique, infrared spectroscopy (IR), was introduced for the physical characterisation of pharmaceutical solids. More recently, Raman and solid-state nuclear magnetic resonance spectroscopy have been applied for the solid state characterisation of pharmaceuticals [93, 94, 144-146]. Infrared and Raman spectroscopy belongs to vibrational spectroscopy techniques. They typically encompass the wavelength range from 400–4000 cm^{-1} for IR and 3600–10 cm^{-1} for Raman spectroscopy. The IR region corresponds to the fundamental vibrations of the molecular species, and therefore many of the spectrum regions can be assigned to the specific functional groups. Raman spectroscopy involves measuring the inelastic scattering of a coherent source of monochromatic radiation by the sample. Because both IR and Raman probe the fundamental vibrational frequencies of the molecules, there is some chemical information that can be obtained from spectra. The spectra are acquired using either a dispersive (not common for IR) or Fourier transform (FT) instrument. FT-IR is usually employed to characterise polymorphs, amorphous forms and solvates/hydrates [93, 94, 144, 145]. The technique has also been applied to study the interactions between the components of a formulation [93, 145, 147]. There are several advantages for using Raman spectroscopy for characterisation of pharmaceutical solids. One important advantage is that this technique can probe the lattice vibrations that are associated with a molecule in the crystalline form. Lattice vibrations corresponds to the translator and rotator motion of the molecule within the crystalline lattice which are typically in the 400–10 cm^{-1} region of the vibrational spectrum [144]. Although these modes can be covered by both IR and Raman spectroscopy, these bands are easier to study by Raman spectroscopy. Another advantage of Raman over IR spectroscopy is a minimum or no sample preparation. Also Raman measurements can be conducted on solids in

an aqueous environment since water is a weak Raman scatterer. Raman spectroscopy has been used to characterise polymorphic and amorphous forms of APIs and also to study interactions and compatibility between APIs and excipients [144-148]. Raman and IR spectroscopy are complementary techniques.

As the SSNMR is the main solid state characterisation tool used in this work, the technique is discussed in greater details in the section 3.5.8.

3.5.4 X-ray diffraction

X-ray diffraction and X-ray crystallography have often been referred to as the gold standard in the characterisation of pharmaceuticals in the solid state [93]. X-ray diffraction is the most common tool for the elucidation of three-dimensional structure of solid state and it is also employed for fingerprinting and quantitative analysis because it is very sensitive to small chemical changes. A crystal structure provides information regarding crystal packing, hydrogen bonding and structural conformation and therefore provides information necessary to understand the physical properties of the solid state.

Diffraction describes the scattering of waves (electromagnetic radiation with wavelengths between 10^{-7} and 10^{-11} m) by an object. The diffraction occurs at angles corresponding to Bragg's law equation:

$$n\lambda = 2d \sin\theta \quad (5)$$

where n is an integer, λ is the wavelength of the radiation, θ is the angle through which the radiation is diffracted and d represents the characteristic spacing distance of the lattice. The obtained data allow for solving of the three-dimensional arrangement of atoms in the unit cell. Single-crystal XRD (SCXRD) is one of the most powerful techniques to determine the structure of the molecule in a crystal. It provides information about molecular conformation and packing, hydrogen bonding, presence of channels and solvent location. In the pharmaceutical science it is one of the most definitive technique for identification of polymorphs as each crystalline form must have different conformation and/or arrangement of the molecules in the crystal lattice [94]. The drawback of the SCXRD is that a crystal of sufficient size must be grown to determine the crystal structure what is not always possible in practice.

The general principles for XRPD and SCXRD are the same, except that the material for XRPD is in the powder form. Since the majority of pharmaceuticals are obtained as microcrystalline powders, the powder pattern of these substances is often used as a readily obtainable fingerprint for determination of its structural form and is one of the most common techniques used for this purpose in the pharmaceutical sciences and industry. One of the advantages of XRPD over other techniques is that it can differentiate compounds that may be

very similar chemically, for example, may have very similar Raman spectra, but XRPD pattern will exhibit significantly different powder pattern. Other common applications include quantitative analysis of polymorphic mixtures, calculation of degree of crystallinity, determination of the size of crystallites by measuring peak widths and, also, crystal structure may be obtained using powder data [93, 94, 149]. Less commonly the XRPD is employed to study interactions and compatibility between API and excipients [147]. Variable-temperature XRPD (VT XRPD) is a very useful, supporting technique for determination of phase transitions (crystallization, polymorphic transition, amorphisation) or desolvatation during heating or cooling examined material. VT XRPD can also be used to study accelerated stability of formulated product [149]. VT XRPD is invaluable complementary method to TGA and DSC analyses.

3.5.5 Microscopy

The microscopy has been widely applied for characterisation of pharmaceutical solids [93, 94, 150-153]. The main applications of microscopy in the pharmaceutical sciences and industry include: solid state form analysis, particle size and shape analysis and identification of contaminants [151-153]. A particle size and shape are important properties of solid APIs and may have an impact on dissolution behaviour and in consequence bioavailability [154, 155]. The microscopic methods can be divided into two categories: an optical microscopy and electron microscopy. The first method probe the sample features on the order of a micron or larger and the latter on the order of sub-micron level. The two methods are complementary and can confirm the information provided by other solid state analytical techniques.

The optical microscopy often referred to as the light microscopy (LM). LM uses visible light to examine the material. The microscope is usually combined with polarizing filter to analyse birefringence of the material. Optical microscopy can provide information about physical properties of different solid state forms such as refractive index, colour or extinction angle. Other phenomena readily observable by LM include particle size and shape, presence of inclusion, twinning, crystal growth and dissolution or mechanical behaviour and mesomorphism [94]. For example the polarised LM can be employed to rapidly distinguish between crystalline and amorphous state as the amorphous state will not display birefringence. Also, LM is the technique of choice for quick assessment of particle size, because the sample preparation is quick and simple. However, it has to be noted that nonrepresentative sample will give nonrepresentative results. Thus, the sample preparation is the critical step for proper image analysis. The sample must contain sufficient number of particles to represent the size distribution of the bulk powder. The reproducibility dispersion of particles in the powder is a

major challenge for image analysis. To overcome dispersion reproducibility problem the fully automated, light-microscope based image analyser system (the Morphologi® G3, Malvern Instruments Ltd.) with a dry powder dispersing unit has been relatively recently developed [156, 157]. The analyser detects, lists and classifies particles by size and shape and is fully automated thus no advanced knowledge and training is required to operate the instrument.

A disadvantage of light microscopy is that it does not provide chemical information about the investigated material. This drawback can be overcome by combining LM with IR or Raman spectroscopy [151-153].

The scanning electron microscopy (SEM) allows the examination of the sample at much higher magnification and resolution than it is possible by LM. The major benefits of using SEM, which cannot be achieved by using LM include: an upper magnification (about 250 000X compared to about 1000X for LM), a large depth of field (resulting in 3D image) and lateral spatial resolution better than 3 nm (for LM 200 nm). SEM provides detailed information about the morphology and the surface of the specimens. The application of SEM in the pharmaceutical sciences and industry is a routine and SEM is employed for examination of both APIs and excipients in preformulation studies of single materials and during the technological processes in bulk materials such as tablets, pellets or spry-dried powders [151-153].

3.5.6 Measurement of solubility and dissolution rate

One of the most important physical properties of solid pharmaceuticals is solubility. The solubility, i.e. the concentration of the dissolved solid (the solute) in the solvent medium (the saturated solution), which is in equilibrium with the solid at defined temperature and pressure, depends on the solid physical form, the nature and composition of the solvent medium, the temperature, and the pressure [150, 158]. The solubility of an API has direct impact on the bioavailability of the formulated drug. Thus the solubility of an API in a relevant solvent medium is an important characteristic. There are three major methods to determine solubility: “shake-flask” or batch agitation method, flow column (generator column) method and the synthetic method [150, 158, 159]. The solubility of a substance may be expressed in a variety of ways i.e.: in terms of molality, normality, molarity, percentage or parts of solvent required for one part of the solute. The latter one is used by the *United States Pharmacopeia* (*USP*) [160].

The dissolution rate is another important physical property of a solid state. The dissolution rate can be defined as the rate at which the thermodynamic equilibrium (thermodynamic solubility) is achieved. Thus the dissolution rate is directly proportional to its solubility and can be expressed by the modified Noyes-Whitney equation:

$$\text{Dissolution rate} = \frac{\mathrm{d}m}{\mathrm{d}t} = \frac{DA}{h}\,(C_s - C_t) \tag{6}$$

where: d*m*/d*t* is the rate of mass transfer, *D* is the diffusion coefficient, *A* is the surface area of the drug, *h* is the static boundary layer, C_s is the saturation solubility of the drug C_t is the concentration of the drug at time (*t*) [161, 162]. Solid state form (polymorphs, solvates, amorphous state) is the major factor determining dissolution rate, however, other important factors influencing the dissolution rate can be listed: particle size, pH, viscosity or wettability [162].

Dissolution testing is extremely important during preformulation, formulation and quality control of both pure APIs and formulated solid dosage forms [163]. The methods can be categorised as the flow-through column method (or the continuous-flow method; Figure 9) and the stirred-vessel method (or the batch-type method; Figure 10) [150, 163]. In the stirred-type, agitation is provided by some kind of paddle or rotating disc whereas in the column method the solvent flows over the analysed sample. Two major methods of dissolution testing for determination of APIs dissolution rate exist: apparent dissolution testing and intrinsic dissolution testing [88, 150, 160, 163].

Apparent dissolution testing is mainly used to determine the apparent dissolution rate (ADR) of pure solid APIs or APIs in solid dosage forms such as powders or granules [88]. The flow-through apparatus used for ADR testing is shown in Figure 9. Tests are performed in an appropriate dissolution medium at constant flow rate, temperature, ionic strength and pH. As the final concentration measured using powdered sample is the equilibrium solubility, and the initial stages of dissolution are strongly affected by the particle size and surface area of the dissolving API, intrinsic dissolution testing was introduced.

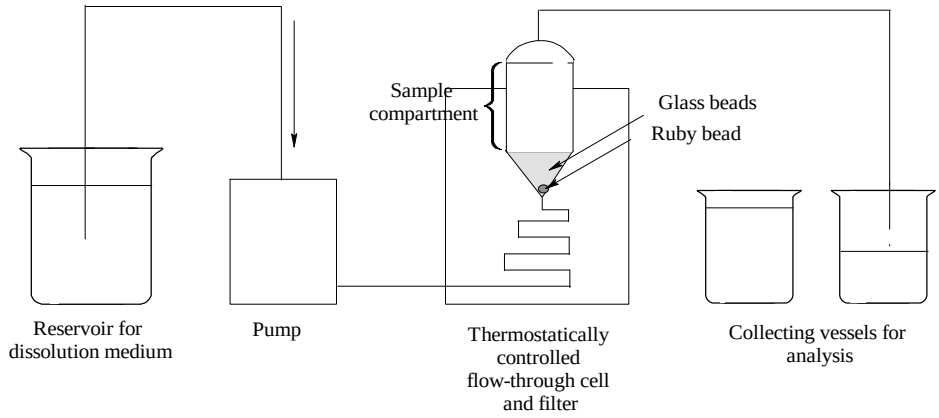

Figure 9. Diagram of a flow-through apparatus used for determination of ADR. Modified from Refs. [88, 150, 164].

The intrinsic dissolution testing is used to determine the intrinsic dissolution rate (IDR) of pure solid API following compaction [88]. The formulation of the disc allows for exclusion of impact of the particle size on the dissolution rate. The test is carried out under specified experimental conditions where the area of exposed sample is known. The IDR is expressed in terms of dissolved mass of

substance per time and exposed area usually in milligrams or micrograms per minute per square centimetre. Tests are performed by exposing a constant area of API disc to an appropriate dissolution medium at constant stirring rate, temperature, ionic strength and pH [88, 165]. The IDR can be determined using a following equation [166]:

$$\text{IDR} = \frac{C}{t}\frac{V}{S} = kC_s \tag{7}$$

where C is the drug concentration at time t, V is the volume of the test solution, S is the surface area of the disc, k is the intrinsic dissolution rate constant, and C_s is the saturation solubility of the drug. The batch-type apparatus used for IDR testing is shown in Figure 10.

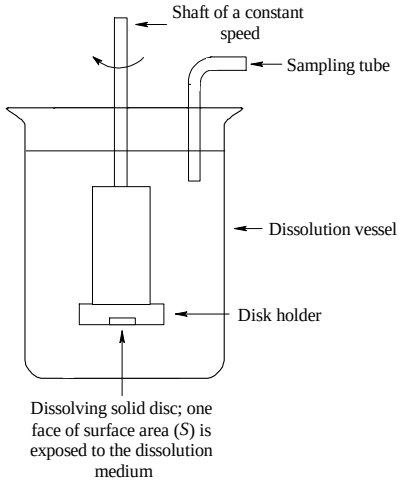

Figure 10. Diagram of rotating disc batch-type apparatus for determination of IDR. Modified from Refs. [88, 150, 165].

3.5.7 Differential scanning calorimetry

Differential scanning calorimetry (DSC) is the most widely used of all thermal analysis techniques. The earliest calorimetric studies were carried out by Black, Place and Lavoisier in the 18th century on a water-ice system and also on guinea pigs to determine the thermal effects of living animals [142, 167]. The first commercial calorimeter was introduced in the early 1960s [168]. Modern calorimetry has found many useful applications mainly in the field of polymer sciences, material sciences and pharmacy but physic, chemistry, biochemistry, biology, or food sciences have also significantly benefited from the existence of DSC [125, 142, 167, 169-171].

3.5.7.1 Standard differential scanning calorimetry

DSC is a technique in which the heat-flow rate difference into a substance and a reference is measured as a function of temperature or time, while the sample is subjected to a controlled temperature program [172]. The temperature program may be in the form of heating, cooling or isothermal mode. The heating/cooling linear program is mostly used, given by equation:

$$T = T_0 + \beta t \tag{8}$$

where T_0 is the starting temperature, t time and $+\beta$ the heating rate or $-\beta$ the cooling rate.

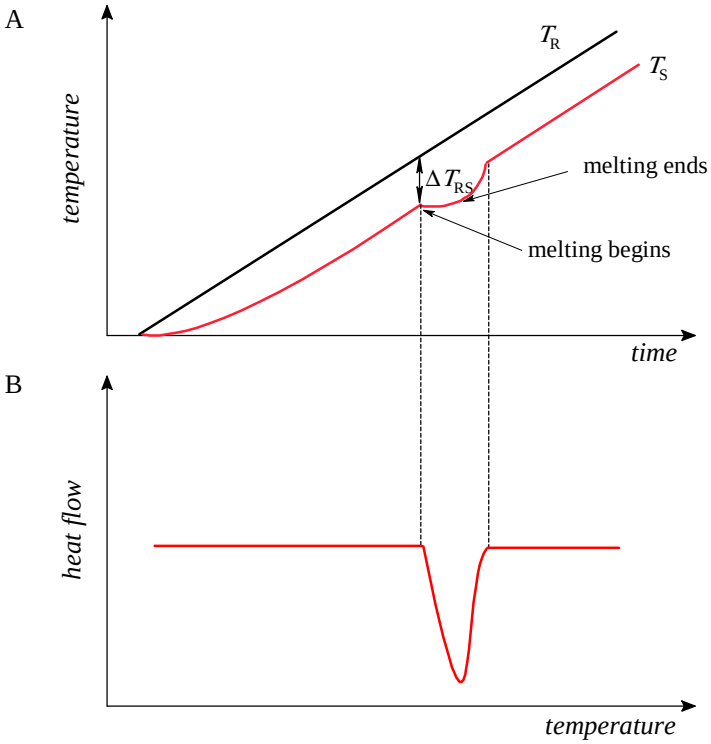

Figure 11. Plots showing (A) temperatures of sample (S) and reference (R) as a function of time in DSC experiment and (B) resulting from it changes of heat-flow rate as a function of temperature. Modified from Refs. [125, 167].

As no heat flow meter exists that could directly measure the heat flowing into or out of the sample, differential scanning calorimetry uses the temperature difference (ΔT_{RS}) developed between the sample (T_S), and a inert reference (T_R) for calculation of the heat-flow rate ($\Delta \Phi_{RS}$) according to the equation:

$$\Delta \Phi_{RS} = \frac{dQ}{dt} = K \Delta T_{RS} \tag{9}$$

where, Q is the heat, t is the time and K is the Newton's law constant. The typical DSC response to melting event is shown in Figure 11. Before the thermal event occurs, curve shows a baseline

indicates the heat-flow rate (power) required to raise the temperature of the sample in order to follow with the programmed temperature mode, Figure 11B. The thermal property of the sample is described by its heat capacity (C_p) and as the C_p represents the energy required to raise a one unit of the material by 1 K usually expressed in J g K^{-1}, the heat-flow rate is a function of a heat capacity and can be described by equation:

$$\Delta\Phi = \frac{dQ}{dt} = C_p \frac{dT}{dt} \tag{10}$$

where, dQ/dt is the heat-flow rate and dT/dt is the heating rate (β). This equation shows the simple relationship between measured by DSC heat-flow rate and the quantity describing thermal property of the examined material – heat capacity. In practice, the baseline dose not correspond to heat capacity due to some factors which contribute to the baseline heat-flow rate, thus proper calibration is necessary to measure "true" heat capacity of the sample.

There are two different types of DSC instruments: heat flux and power compensation. The scheme of the heat flux DSC is shown in Figure 12A. The reference (R) and sample (S) materials are placed symmetrically within a furnace with thermocouples placed in close contact to each other. The furnace-control thermocouple checks the furnace (block) temperature, T_b, against the program temperature. Any difference is used to adjust the power to the heater. The reference and sample should have the same heat flux for the same temperature difference from the furnace $T_b - T_R$ and $T_b - T_S$, hence, $\Delta T_{RS} = T_R - T_S$, proportional to the differential heat-flow rate ($\Delta\Phi_{RS}$), i.e.:

$$\Delta\Phi_{RS} = \frac{dQ}{dt} = \Delta T_{RS} R^{-1} \tag{11}$$

where, Q is the heat, t the time and R the thermal resistance between the furnace and the crucible [125, 167].

In the heat flux type DSC, the furnace is subjected to the temperature program, thus the temperature profile experienced by the sample is not known in advance, but is measured and is determined after the experiment.

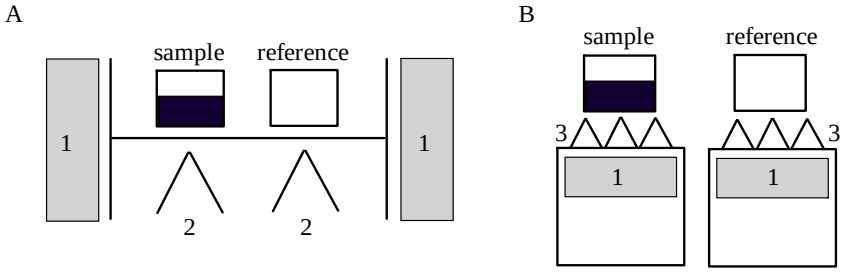

Figure 12. Scheme of two types of DSC instruments: (A) heat flux DSC and (B) power compensation DSC.
1 = furnaces, 2 = thermocouple and 3 = platinum resistance thermometers. Modified from Ref. [125].

The scheme of the power compensation DSC is shown in Figure 12B. This type of calorimeter uses two separate furnaces one for sample and one for reference. Both furnaces are programmed to go through the same temperature mode and the difference in electrical power supplied to both furnaces is measured. In comparison to the heat flux instrument, in this approach, the sample temperature is programmed and should follow exactly selected programme mode and thus the power compensation calorimeters should provide for a better-defined experiments [167].

In practice, both types of instruments are widely used and the performance in terms of sensitivity and accuracy is very similar. As the power compensation calorimeters have smaller furnaces the higher heating and cooling rates can be achieved, which can be an advantage in some experiments. The heat flux calorimeters may have better baseline stability as the single furnace tends to be more robust than those in power compensation instruments.

Using standard DSC all phase transitions thermal effects can be measured, both endothermic (melting, chemical reactions) and exothermic (crystallization, cold crystallization, re-crystallization, chemical reactions), also glass transition temperature and heat capacity can be obtained [167]. In more details application of standard DSC will be discussed in further section.

3.5.7.2 Temperature-modulated differential scanning calorimetry

Temperature-modulated DSC (TMDSC or modulated-temperature DSC – MTDSC) is an extension of conventional DSC and was introduced in the early 1990s by Reading [173]. TMDSC is a software modification of standard DSC where perturbation is superimposed to the heating linear rise program [173-175]. In most cases the sinusoidal mode heating program is applied but sawtooth or other complex modulation may be used [176]. The simple sinusoidal modulation program, shown in Figure 13, can be expressed by equation:

$$T = T_0 + \beta t + A\sin(\omega t) \tag{12}$$

where T_0 is the starting temperature, β the heating/cooling rate, t time, A amplitude of modulated temperature and ω its angular frequency.

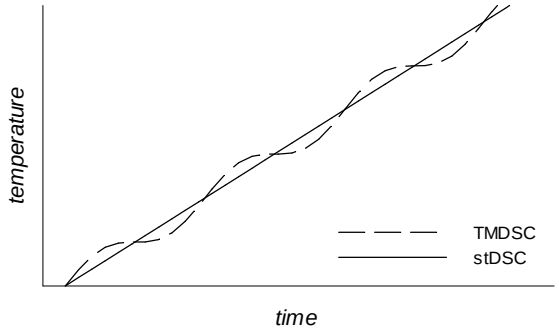

Figure 13. Plot of temperature as a function of time used in temperature programs for standard and temperature-modulated DSC.

As a result of the temperature modulation the obtained modulated heat-flow rate, $\Phi(T, t)$, into the sample can be described by the equation [177]:

$$\Delta\Phi_{\mathrm{RS}}(T,t) = \frac{\mathrm{d}Q}{\mathrm{d}t} = K\,(T_{\mathrm{R}} - T_{\mathrm{S}}) = \Phi_0 + A_{\Phi}\sin(\omega t - \varphi) \tag{13}$$

and can be divided into two parts and described by the equation:

$$\frac{\mathrm{d}Q}{\mathrm{d}t} = C_{\mathrm{p}}\,\frac{\mathrm{d}T}{\mathrm{d}t} + f(t,T) \tag{14}$$

where, K is the Newton's constant, A_{Φ} is the amplitude of modulated heat-flow rate, and φ is the phase shift, Q is the heat, C_{p} heat capacity, T the absolute temperature, t the time and $f(t,T)$ some function of time and temperature that governs the response associated with the physical or chemical transition. TMDSC software is designed to separate (or deconvolute) different types of sample thermal behaviours i.e. associated with $C_{\mathrm{p}}\,\mathrm{d}T/\mathrm{d}t$ and $f(t,T)$ terms of the above equation. The sample response to the linear heating is different to that of the sinusoidal heating. The term $C_{\mathrm{p}}\,\mathrm{d}T/\mathrm{d}t$ describes the modulated heat-flow rate associated with the material's heat capacity i.e. the heat-flow rate associated with energy stored in the molecular motions such as, for example, vibrations, rotations, conformations or translations. When the temperature is increased by for example 1 K, more energy is stored in these motions and when the temperature is decreased again by 1 K exactly the same amount of energy per mass unit is released by the material. This phenomenon is called *reversible process*. The term $f(t,T)$ corresponds to a thermal event such as chemical reaction or enthalpy recovery which are kinetically hindered events and are regarded as, however with some exceptions, *irreversible processes* [125, 167]. The example of the deconvolution of the temperature-modulated heat-flow rate is shown in Figure 14. The standard DSC would provide only a total heat-flow signal, the TMDSC procedure allowed for clear separation of non-reversing and reversing signals, Figure 14B. The separation of signals allows for observation of overlapped events such as a glass transition

process and enthalpy recovery or glass transition process and cross-linking reaction in a polymer [125, 172]. The glass transition is a change in heat capacity thus is a fully reversible process and depends only on C_p dT/dt term whereas the enthalpy recovery or cross-linking reaction are kinetically hindered events as the glassy system is in non-equilibrium state, and hence there will be a tendency for enthalpy reduction as a function of time toward the equilibrium and the chemical reaction is also time dependant event arises because of the formation of chemical bonds [125, 172] and thus are associated with $f(t,T)$ term of the equation (14).

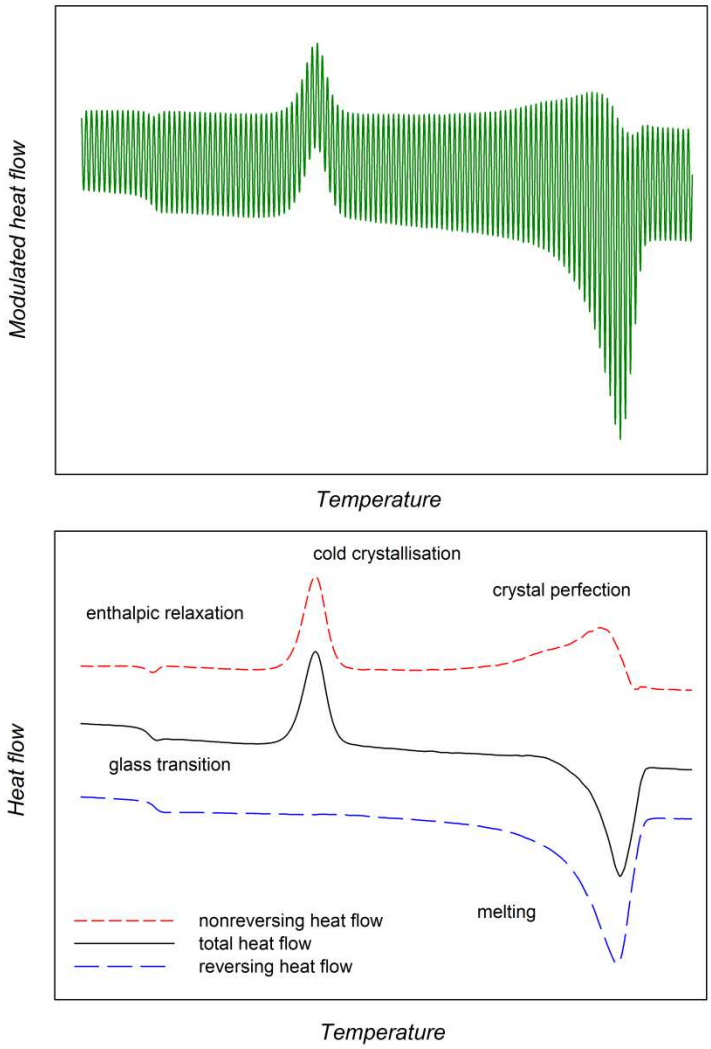

Figure 14. TMDSC (A) raw data and (B) results of deconvolution for quench-cooled polymeric material. Kinetic processes as enthalpy relaxation, cold crystallization or crystal perfection are separated from thermodynamic processes as glass transition or melting and appear on different signals. Modified from Ref. [177].

Another technique of TMDSC which allows for separation of kinetic and thermodynamic processes is quasi-isothermal TMDSC (Qi-TMDSC) [167, 177]. Technique is

especially useful for investigation of the glass and melting transitions in polymeric systems by measuring only their reversing heat capacities [178]. The Qi-TMDSC experiment involves running the instrument with an underlying heating rate of zero at a set temperature for a set a time period, then heating or cooling by an incremental amount [167, 177].

3.5.7.3 Pharmaceutical applications of differential scanning calorimetry

DSC is widely used in characterisation of pharmaceuticals, pure APIs or excipients and formulated products as well [125, 143]. The following thermal behaviour exhibited by single components can be measured by DSC: melting, crystallization, boiling, sublimation, dehydration/desolvation, glass transitions and polymorphic transitions. One of the most important pharmaceutical applications of DSC is detection and characterisation of polymorphs, solvates and hydrates. For example, AT_1 antagonist drug, losartan, was characterised by thermal methods [28, 179-181]. Two polymorphs were found – Form I and Form II. During heating of the Form I material converted into Form II followed by melting process, and decomposed immediately after melting, Figure 15.

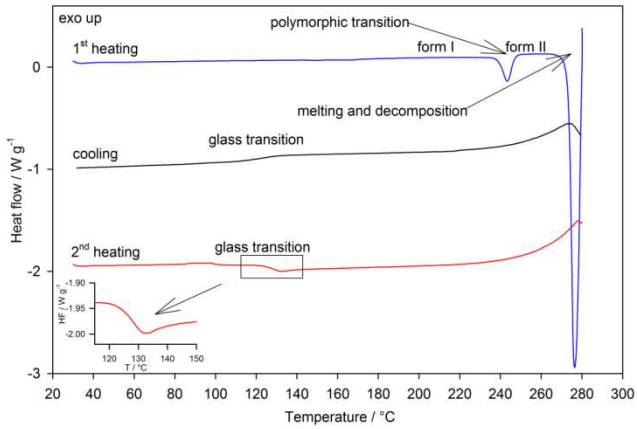

Figure 15. Standard DSC curves of crystalline losartan potassium showing 1st heating (polymorphic transition, melting and decomposition), cooling (glass transition of amorphised material) and 2nd heating (glass transition and decomposition). No crystallization is observed during heating or cooling run. Modified from Ref. [181].

The solid–solid polymorphic transition of Form I into Form II is seen on the non-reversing heat-flow rate, measured by TMDSC confirming irreversibility of the transition, Figure 16.

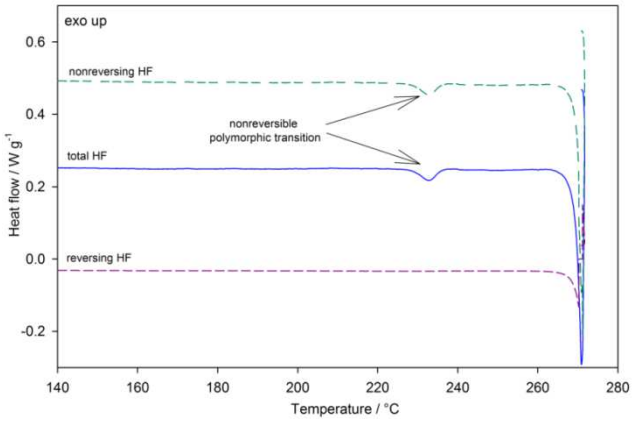

Figure 16. Temperature-modulated DSC thermogram of losartan shows non-contribution to the reversing heat-flow rate in the transition region of Form I – Form II. Modified from Refs. [180, 181].

Study by quasi-isothermal TMDSC confirmed irreversibility of the solid–solid transition and shows a small contribution of reversing heat capacity in the melting transition at much lower temperature than for standard DSC analysis, Figure 17.

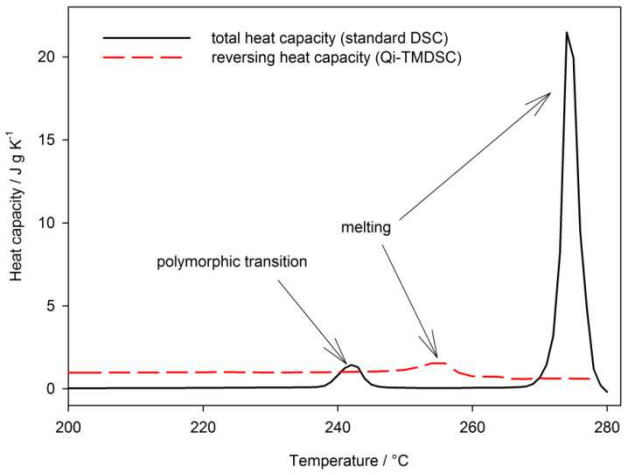

Figure 17. The comparison of the reversing heat capacity obtained from quasi-isothermal TMDSC with the total heat capacity obtained from standard DSC analysis for losartan potassium. Qi-TMDSC confirmed irreversible process of solid–solid transition and showed a small contribution of reversing heat capacity in the melting transition at much lower temperature than for standard DSC analysis. Modified from Ref. [181].

Calorimetric methods can also be employed for detection and characterisation of pharmaceutical glasses [49]. The most important parameters of the amorphous material are the glass transition temperature and change of heat capacity (ΔC_p) between the level of liquid heat capacity, C_p(liquid), and solid heat capacity, C_p(solid), at T_g. TMDSC is the method of choice for characterisation of the glass transition. The molecular mobility and physical ageing or annealing in the amorphous material i.e. structural relaxation towards thermodynamic equilibrium as a function of time [132], are also important phenomena from the pharmaceutical

sciences and industry point of view [6]. For example, Pyda and Wunderlich [182], studied glass transition of an polymeric excipient, poly(lactic acid) (PLA), by TMDSC. The kinetic and thermodynamic processes were separated in the glass transition region of an amorphous material. The total apparent heat capacity in the glass transition region results from an overlapping of the enthalpy relaxation and a step change in the heat capacity. In order to separate the two phenomena, the standard TMDSC was applied. Figure 18A–C display the results from TMDSC in the form of the total, reversing, and non-reversing heat capacities of poly(lactic acid), respectively. Figure 18A illustrates the total heat capacities, measured on heating for the samples with different thermal histories introduced by cooling from 373.15 to 283.15 K (100 to 10 °C) with cooling rates from 20 K min^{-1} to 0.1 K min^{-1}. The results show an overlapping of the simple changes of the heat capacity ongoing through the glass transition with changes due to the enthalpy relaxation. The total heat capacities were, next, separated into reversing and non-reversing heat capacities, using a deconvolution and results are presented in Figure 18B and C, respectively. The evolution of the glass transition temperature from the reversing heat capacity varies with the prior cooling rates is presented in Figure 18B. Figure 18B shows that the glass transition temperature of the annealed PLA samples shifts to higher temperature after cooling with a lower cooling rate. The enthalpy relaxation was evaluated from the non-reversing component, as presented in Figure 18C. The enthalpy relaxation peaks shift to a higher temperature for more slowly cooled PLA.

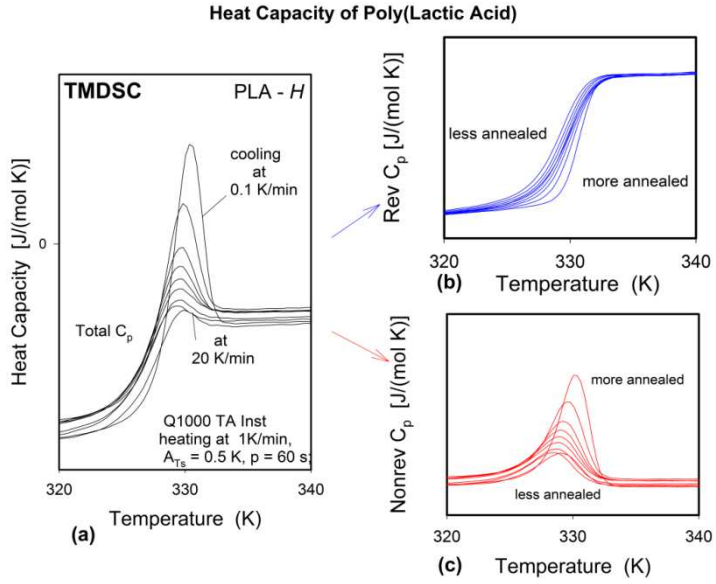

Figure 18. (a) The total, apparent, (b) reversing, and (c) non-reversing heat capacity of an amorphous poly(lactic acid) for standard TMDSC. Adapted from Ref. [182].

DSC is also used to study compatibilities between drug-drug and drug-excipient [41, 47, 51, 52]. This application has been briefly discussed in the chapter 3.6.

3.5.8 Nuclear magnetic resonance

Since the first observation of proton magnetic resonance in water [183] nuclear magnetic resonance (NMR) has grown from study of an interesting physical phenomenon to be the most powerful analytical method. The first high-resolution proton NMR spectrum of ethanol, published in 1951 [184], clearly demonstrated how the features of an NMR spectrum could be directly related to chemical structure, and since then NMR has been one of the most important tool for elucidation of molecular structure for organic chemists. Nowadays the NMR has been applied for a wide variety of fields such as chemistry, biology, pharmacy, physiology, food sciences or medicine [185-191].

3.5.8.1 Basic theory of NMR spectroscopy

In quantum mechanical terms an atomic nucleus is characterised by a nuclear spin number I referred to as *spin*. Nuclei can have integral, half-integral or zero spin quantum numbers. Nuclei with zero spin quantum number posses no nuclear spin and therefore cannot be observed by NMR. In this work only commonly observed NMR nuclei with $I = \frac{1}{2}$ such as ^{1}H, ^{13}C or ^{15}N will be discussed. A spinning charge with non-zero I results in generation of magnetic moment. There are only $2I + 1$ possible values of magnetic quantum number orientations, defined by the magnetic component quantum number (m_I). These are termed *spin states*. Outside a magnetic field ($\boldsymbol{B}_0 = 0$) both quantum states are equivalent. In the presence of magnetic field, the states have different energy as shown in Figure 19. The effect of the static field on the magnetic moment can be described in terms of classical mechanics. The magnetic moment has vector properties i.e. it has direction and magnitude. A static magnetic field applied to the nucleus causes it to precess at a rate dependent on the field strength ($\boldsymbol{B}_0$) and the magnetogyric ratio (γ) of the spin. The field is conventionally applied along the z-axis of a Cartesian co-ordinate frame and the motion of the nucleus represented as a vector moving on the surface of a cone. This motion is referred to as *Larmor precession*. The rate of the precession as defined by the angular velocity (ω in rad s^{-1} or ν in Hz), known as a *Larmor frequency* of the nucleus, and can be expressed as:

$$\omega_{\mathrm{NMR}} = -\gamma B_0 \tag{15}$$

or

$$\nu_{\mathrm{NMR}} = \frac{-\gamma B_0}{2\pi} \tag{16}$$

The nuclear magnetic resonance occurs when the spin changes the state, driven by the absorption of a quantum of energy. This energy is applied as an electromagnetic radiation,

whose frequency must match that of the Larmor precession for the resonance to occur. The energy required is:

$$\Delta E = h\nu_{\mathrm{NMR}} = \frac{h\gamma B_0}{2\pi} \tag{17}$$

where h is Planck's constant. The difference in an energy between two spins (ΔE) plays an important role in NMR spectroscopy. As seen in equation (17) increasing the applied field ($\boldsymbol{B}_0$) results in a greater ΔE and hence generates stronger NMR signal. For example, modern NMR spectrometers currently use field strengths up to 21.1 T which correspond to resonant frequencies up to 900, 226 and 91 MHz for ^{1}H, ^{13}C and ^{15}N nuclei, respectively.

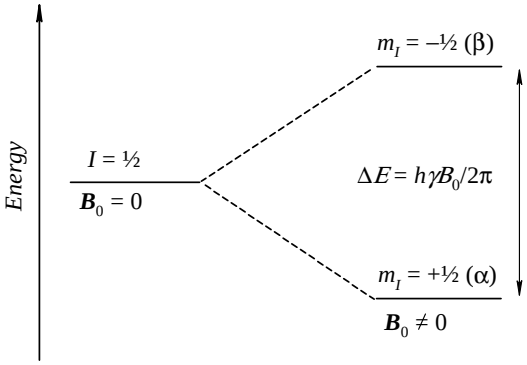

Figure 19. Energy levels of an isolated spin-$\frac{1}{2}$ states in the absence ($B_0 = 0$) and presence ($B_0 \neq 0$) of an external magnetic field (assumed $\gamma > 0$).

3.5.8.2 Solid-state NMR

Solution-state NMR spectra contain a series of very sharp, highly resolved signals due to the rapid molecular tumbling which averages anisotropic (orientation-dependant) NMR interactions. In solid-state NMR (SSNMR), spectra contain broad resonances as the molecular motions are very limited and anisotropic interactions are observed in the spectrum. The major causes of line broadening are dipolar couplings and chemical shift anisotropy (CSA). Furthermore, the lack of molecular motion results in long values of spin–lattice relaxation time (T_1) increasing the amount of time needed for experiment. A number of special techniques has been developed to overcome these difficulties.

3.5.8.2.1 Dipole-dipole interactions

Dipole-dipole interactions or dipolar couplings are interaction through space between two or more nuclear spin dipoles, Figure 20. The magnetic moment of one nucleus will affect the neighbouring magnetic field of another nucleus. In a solution, dipolar couplings are averaged to

their isotropic value, zero, by fast molecular motion. In a solid state these are a major cause of line broadening.

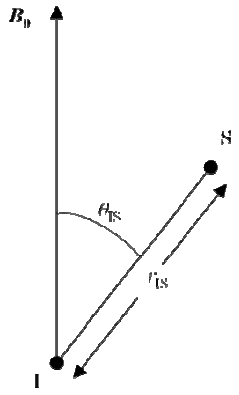

Figure 20. Interaction between two dipoles.

For a pair of two different spins at high magnetic field the dipolar energy can be expressed as:

$$h^{-1}E_{\mathrm{D}} = -D_{\mathrm{IS}} m_{\mathrm{I}}\, m_{\mathrm{S}} (3\cos^2\theta - 1) \tag{18}$$

where θ is the angle between the internuclear vector and the magnetic field, m_{I} and m_{S} are the magnetic quantum numbers, h is Planck's constant and D_{IS} is the dipolar coupling constant between spins I and S:

$$D_{\mathrm{IS}} = \gamma_{\mathrm{I}}\gamma_{\mathrm{S}} \left(\frac{h}{4\pi^2}\right)\left(\frac{\mu_0}{4\pi}\right) r_{\mathrm{IS}}^{-3} \tag{19}$$

where μ_0 is the vacuum permeability constant. It is seen from equation (18) that dipole-dipole interaction depends on the orientation of the dipoles. In a single crystal with one orientation of dipolar vectors a single set of resonances will be observed. In case of polycrystalline powders containing particles with all possible orientations of the dipole distance the spectra will be observed as the *Pake doublet*, Figure 21A.

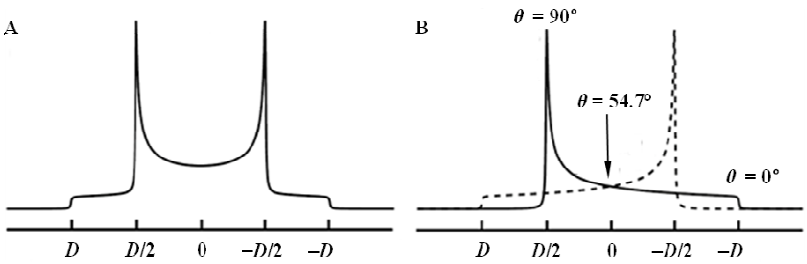

Figure 21. (A) A schematic heteronuclear dipolar powder pattern (Pake doublet) and (B) two powder patterns subspectra for different values of magnetic quantum number (m_I).

3.5.8.2.2 Chemical shift anisotropy

The nucleus of molecule placed in a magnetic field is magnetically shielded by the presence of the electrons, leading to a shielding field, $\boldsymbol{B}_S$ as expressed by the equation:

$$\boldsymbol{B}_S = -\boldsymbol{\sigma}\boldsymbol{B}_0 \tag{20}$$

where $\boldsymbol{B}_0$ is the applied magnetic field and $\boldsymbol{\sigma}$ is the shielding tensor. This secondary field contributes to the total field felt at the nucleus, and therefore affects the resonance frequency of the nucleus. This interaction depends on the orientation of the molecule with respect to magnetic field and is referred to as *chemical shift anisotropy* (CSA). In a solution, the rapid motion of molecules averages the CSA to zero and only a single isotropic chemical shift is observed. In the solid state molecules are relatively rigid and their orientation is fixed leading to a distribution of the chemical shifts known as a *powder patterns*, Figure 21B. The shielding anisotropy has an orientation dependence of $(3\cos^2\theta - 1)$.

3.5.8.2.3 Magic-angle spinning and high-power proton decoupling

Dipolar and chemical shielding interactions both are dependent on the orientation of the molecules. In solution, only the isotropic chemical shift is observed. In solid effects of dipolar coupling and chemical shift anisotropy give rise to line broadening. All of the internal NMR interactions depend on:

$$(3\cos^2\theta - 1) \tag{21}$$

Spinning the sample about an axis inclined at an angle β to the applied magnetic field, Figure 22, averages expression (21) to some extent and therefore allows for significant reduction of the orientation dependence of the solid [192, 193]. The average of $(3\cos^2\theta - 1)$ about the conical path for the vector $\boldsymbol{r}$ is given as:

$$\langle(3\cos^2\theta - 1)\rangle = \frac{1}{2}(3\cos^2\beta - 1)(3\cos^2\Theta - 1) \tag{22}$$

where β and Θ are defined in Figure 22. The contribution from the chemical shift anisotropy and dipolar coupling can be eliminated when expression (21) equals zero. This can be achieved when the value of a spinning angle β is 54.74°, the *magic angle*. Spinning sample at 54.74° with respect to applied magnetic field, $\boldsymbol{B}_0$ is termed as *magic-angle spinning* (MAS).

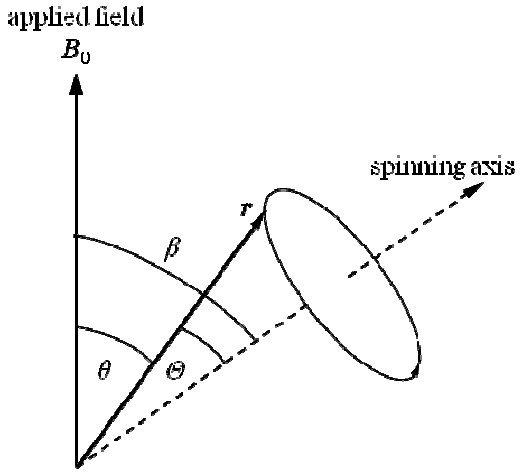

Figure 22. Schematic representation of the magic-angle experiment. The sample is spun in a rotor about a spinning axis orientated at the magic angle (β = 54.74°) with respect to the applied magnetic field (B_0). Adapted from Ref. [58].

The rate of the MAS must be equal to or greater than the magnitude of the anisotropic interaction to average it to zero. If the spinning rate is less than the magnitude of the interaction spinning sidebands becomes visible, separated by the rate of spinning, Figure 23. To remove these spinning sidebands artefacts, which can overlap with spectrum resonances and result in confusing spectra, different approaches are developed. One simple way to remove spinning sidebands is to increase the spinning rate. At the moment, speeds of 80 kHz are achievable with rotors of 1.0 mm diameter [194]. However, it is not always possible to spin sample at such high rate. Alternatively a pulse sequence developed by Dixon [195] known as TOtal Suppresion of Spinning Sidebands (TOSS) allows for effective suppression of the spinning sidebands. This method uses a series of 180° pulses at precisely placed points in a period prior to acquisition. Usually four 180° pulses are used with phase cycling to compensate for pulse imperfections.

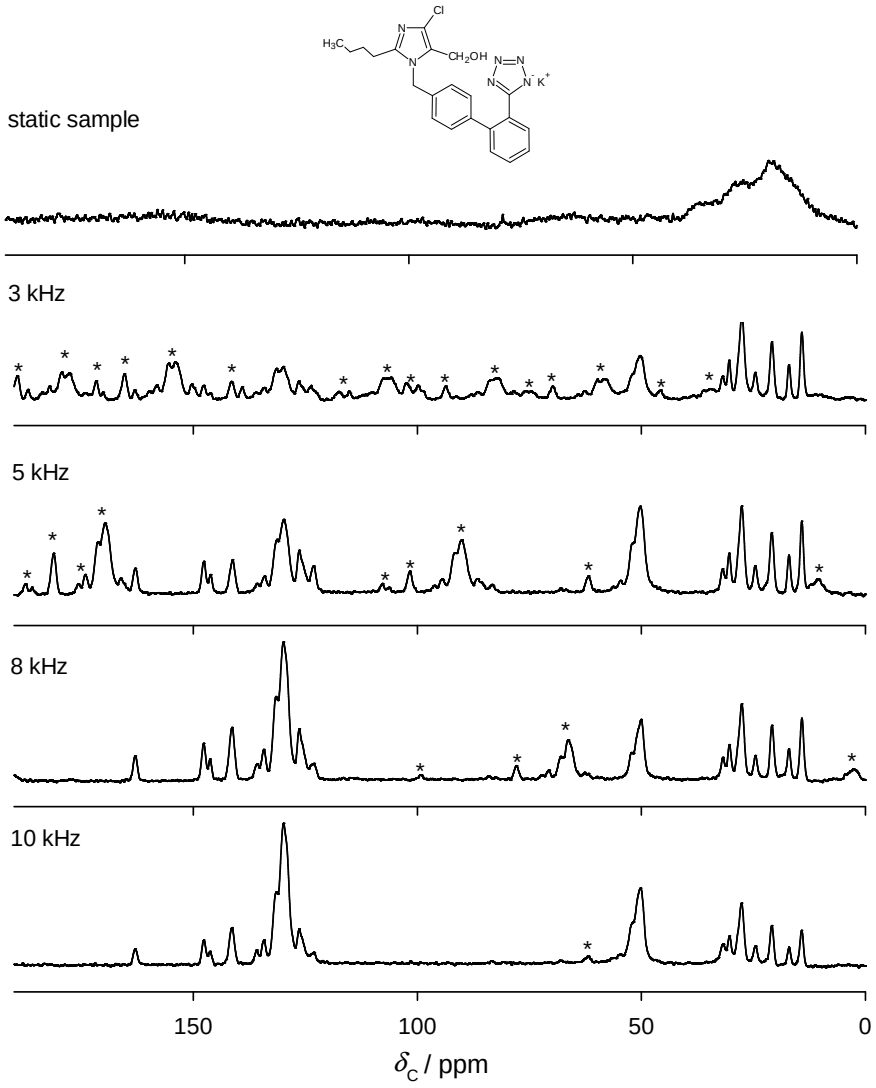

Figure 23. Solid-state ^{13}C NMR spectra of losartan potassium recorded with MAS at different spinning rate from 0 to 10 kHz. All spectra obtained at 125 MHz with cross-polarisation and high-power proton decoupling. 128 scans were acquired for each spectrum. Asterisks (*) denote spinning sidebands.

The homonuclear (^1H–^1H) and heteronuclear dipolar interactions (for example ^{13}C–^1H or ^{15}N–^1H) can be very strong, up to tens kHz. Thus dipole–dipole interactions cannot be fully removed by the MAS technique. Homonuclear ^1H–^1H dipolar couplings causes extensive line broadening when observing ^1H nucleus. The most observed nuclei by SSNMR in pharmaceuticals are ^{13}C and ^{15}N. Homonuclear ^{13}C–^{13}C and ^{15}N–^{15}N interactions are not an issue because of the improbability of two nuclei being close in space. However, the problem of heteronuclear $^{13}C(^{15}N)$–^1H dipolar couplings still remains. To overcome this interaction high-power proton decoupling (HPPD) technique is used [196, 197]. The radiofrequency (RF) pulses with a nutation frequency greater than the dipole interaction are applied on the proton channel, whilst acquiring on the carbon channel. The effect of the RF field will decouple the

proton from the carbon (nitrogen). Common decoupling required are continuous-wave (CW), two-pulse phase-modulated (TPPM) or SPINAL-64 decoupling pulse [58, 198, 199].

3.5.8.2.4 Relaxation times

The NMR spectrum is acquired by recording the response of bulk spin magnetisation to radiofrequency radiation. Pulses of radiation are used to excite range of frequencies. The resulting signal is a time response, termed as *free-induction decay* (FID) [58].

The magnetic field is applied in the *z* direction. The radiofrequency tilts the magnetisation towards *xy* plane, with detection also occurring in the *xy* plane. After excitation, the net magnetisation of the spins group (***M***) will return to its equilibrium state. The process of regaining equilibrium is referred to as *relaxation*. In a solid-state NMR two relaxation times are of particular interest i.e. *spin–lattice relaxation* and *spin–lattice relaxation in the rotating frame*.

Spin–lattice relaxation (or longitudinal) describes the process of regaining equilibrium of the *z* component of ***M*** after disruption. This process can be expressed by the following equation:

$$M_z(t) = [M_z(0) - M_0] \exp\left(\frac{-t}{T_1}\right) + M_0 \tag{23}$$

where M_0 is the equilibrium *z* magnetization, $M_z(0)$ is the magnetisation in the *z* direction after the disruption, T_1 is the time constant for the relaxation, Figure 24. The T_1 is referred to as the *longitudinal* or *spin–lattice relaxation time*. In homogenous systems spin–lattice relaxation process is generally mono-exponential. The T_1 relaxation time is sensitive to motion processes of the order of 100–500 MHz [200].

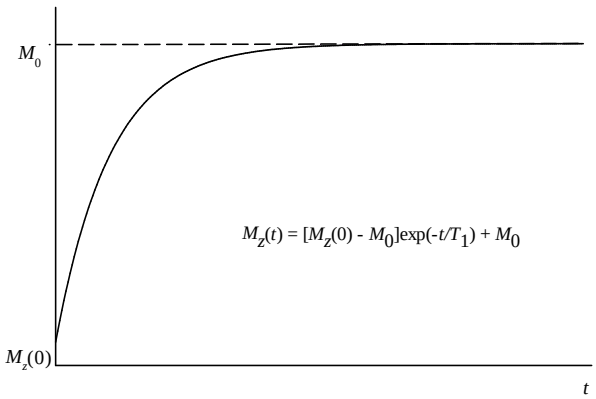

Figure 24. The *z*-magnetization change after a RF pulse as a function of time (*t*). The *z*-magnetization returns from $M_z(0)$ to M_0 following an exponential law. The time constant of the exponential function is T_1 referred to as the longitudinal or spin–lattice relaxation time.

Spin–lattice relaxation in the rotating frame describes the equilibration of transverse magnetisation along the radio-frequency field, $\boldsymbol{B}_1$, of an applied spin-locking pulse in the rotating frame of reference. The spin–lattice relaxation time in the rotating frame ($T_{1\rho}$) is similar to T_1 but it describes relaxation along the radio frequency field of the pulse (static in the rotating frame) rather than relaxation along $\boldsymbol{B}_0$. The $T_{1\rho}$ relaxation time reveals motion processes of the order 20–100 kHz [200].

3.5.8.3 Solid-state NMR experiments

3.5.8.3.1 Direct excitation

The simplest method for exciting nuclei and obtaining spectra in SSNMR is the experiment consisting of a 90° pulse followed by the detection of signal (acquisition). This method is known as a direct excitation (DE), direct polarisation (DP), pulse-acquire or single-pulse excitation (SPE). DE experiments allow for quick detection of mobile components by changing recycle delay. A long recycle delay applied shows all the species in a system whereas short recycle delay show only the species with shorter T_1 values i.e. mobile parts of the system. T_1 for some groups may be long thus DE experiments might be time-consuming due to long recycle delay required.

3.5.8.3.2 Cross-polarisation

The cross-polarisation (CP) is a technique which allows the transfer of magnetisation from abundant nuclei to dilute nuclei [58, 201, 202]. The natural abundance of the most common used nuclides is shown in Table I.

Table I. The spin properties of commonly used in pharmaceutical analysis spin-$\frac{1}{2}$ nuclides. The relative receptivity gives measures of the intensities to be expected relative to those for the proton. It is proportional to $\gamma^3 I(I+1)x$ [58].

Isotope	Natural abundance (x) [%]	Magnetogyric ratio (γ) [10^7 rad s^{-1} T^{-1}]	Relative receptivity vs. ^{1}H (D^p)
^{1}H	99.9885	26.7522128	1.000
^{13}C	1.07	6.728284	1.70×10^{-4}
^{15}N	0.368	–2.71261804	3.84×10^{-6}
^{19}F	100	25.18148	0.834
^{31}P	100	10.8394	6.65×10^{-2}

The CP experiment usually involves transfer of the magnetisation from abundant spin (I) (^{1}H or occasionally ^{19}F, ^{31}P) to rare nuclei (S) like ^{13}C or ^{15}N. The aim of this technique is to

improve the sensitivity and reduce waiting time between successive experiments. The signal enhancement is by a factor equal to magnetogyric factor (γ^H/γ^S) which is 4:1 and 10:1 for ^{1}H and ^{13}C and ^{1}H and ^{15}N nuclei, respectively. This allows for reduction time in experiment 16- or 100-fold, respectively, assuming 100% magnetisation transfer. The efficacy of cross-polarisation depends on sample nature and the experimental conditions. Because the magnetisation originates from ^{1}H nucleus, the recycle delay is limited by the recovery of the ^{1}H magnetisation and not that of the S spin (usually ^{13}C or ^{15}N). Therefore the pulse delay depends on spin–lattice relaxation T_1^H and not T_1^S. Usually $T_1^H << T_1^S$ thus the pulse sequence can be repeated faster than in DE experiment and increase the signal-to-noise ratio in the spectrum.

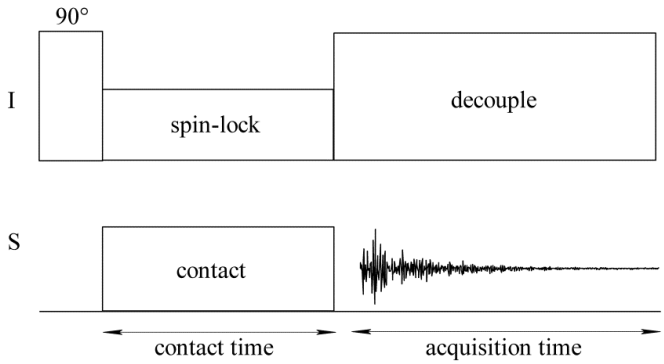

Figure 25. The cross-polarisation pulse sequence. Adapted from Ref. [58].

The CP pulse is shown in Figure 25. The initial 90° RF pulse is applied at the proton frequency rotates the ^{1}H magnetisation onto the *y* axis. Then the proton magnetisation is spin-locked in the *y* direction. During the spin-lock period RF is applied simultaneously at the S frequency. The time when these two pulses are applied is termed *contact time* (CT). To achieve the cross-polarisation ^{1}H and S RF fields must fulfil the Hartmann-Hahn match condition:

$$\gamma^H B_1^H = \gamma^S B_1^S \quad (24)$$

where B_1^H and B_1^S are magnetic field strengths applied to ^{1}H and to the S nuclei and γ^H and γ^S magnetogyric ratio of ^{1}H nucleus and the dilute spin, respectively.

The CP pulse sequence is generally used with MAS and HPPD which allows high-resolution spectra to be recorded.

3.5.8.3.3 Dipolar dephasing

The dipolar dephasing (DD, also known as an interrupted decoupling or non-quaternary suppression, NQS) pulse sequence is similar to CP sequence but contains a delay time (τ) where ^{1}H decoupling is turned off before acquisition, Figure 26 [58, 202, 203]. Turning off the decoupling connects the S (usually ^{13}C or ^{15}N) magnetisation of protonated nucleus to the large

proton spin bath. Thus any signal originating from species strongly coupled to proton decays faster than species weakly coupled to proton. The typical values of delay time for carbon are 40 µs and 200 µs for nitrogen. The DD experiment is used to distinguish quaternary carbons or tertiary nitrogens from protonated ones in the system. To avoid the need for large first-order phase correction the rotor synchronised 180° pulse on the X channel is applied, which refocuses the signal. DD technique is widely used to simplify the ^{13}C spectra, however it is not always efficient with ^{15}N [204] thus other spectral editing techniques might be more useful.

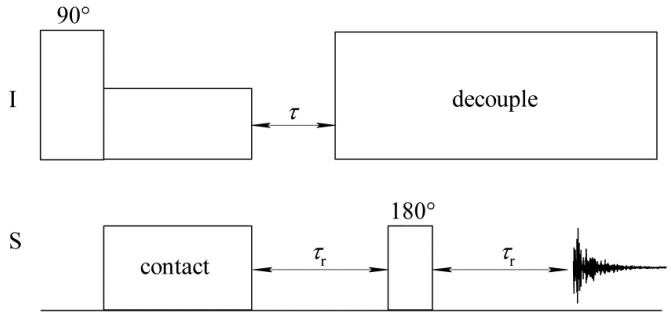

Figure 26. The dipolar dephasing pulse sequence; τ is the delay time (dephasing delay) and τ_r is the rotor period. Adapted from Ref. [58].

3.5.8.3.4 Inversion-recovery

The inversion-recovery (IR) technique allows nuclei (usually ^{13}C or ^{15}N) to be distinguished depending on their proton environment [205-207]. The only difference compared with the CP pulse sequence is the introduction of a phase inversion during the contact time, Figure 27. The dynamics of inversion during contact time depend strongly on the I–S dipolar coupling. As the abundant spins are usually protons, the sequence is very sensitive to the local proton environment and molecular motion. The main advantage over the dipolar dephasing experiment is that the magnetisation starts from an optimum value, then decreases and becomes negative with increasing inversion time (τ_i) thus it is easy to visualize the differently protonated nuclei in the system.

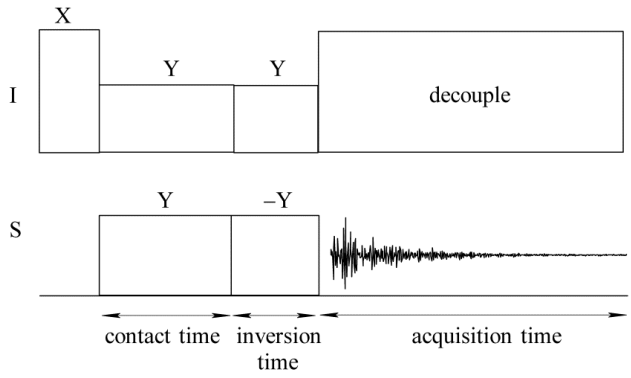

Figure 27. Inversion-recovery cross-polarisation pulse sequence. Adapted from Ref. [205].

3.5.8.3.5 Spin–lattice relaxation time experiments

For the spin–lattice relaxation in the laboratory frame, i.e. relaxation of magnetisation along the field $\boldsymbol{B}_{0,}$ there are four common methods:

- inversion-recovery,
- saturation-recovery,
- inversion-recovery with cross-polarisation,
- "Torchia" method [58, 208, 209].

The inversion-recovery method utilizes pulse sequence consisting of 180° pulse which rotates the magnetisation. Then at a time τ later, a 90° pulse creates an FID which is representative of the value of $M_z(\tau)$, Figure 28A. The magnetisation recovery is fitted to the equation:

$$M(\tau) = M_0\left[1 - 2\exp\left(\frac{-\tau}{T_1}\right)\right] \tag{25}$$

where $M(\tau)$ is the height of the selected peak after τ variable delay lengths, M_0 is the signal height where τ = 0. The inversion-recovery method provides a large signal range, from fully inverted to fully positive, but the disadvantage is that the recycle delay must be at least $5T_1$ to allow the system to fully relax between repetitions.

The saturation-recovery pulse sequence consists series of 90° pulses which saturates the spins. Then after a recovery time (τ), a further 90° pulse produces an FID, Figure 28B. The magnetisation recovery is fitted to the equation:

$$M(\tau) = M_0\left[1 - \exp\left(\frac{-\tau}{T_1}\right)\right] \tag{26}$$

This sequence is particularly useful when spin–lattice relaxation process is inefficient i.e. for long T_1 relaxation time values.

Inversion-recovery with cross-polarisation sequence measures T_1^H indirectly through an S nucleus spectrum, Figure 28C. The "Torchia" method also utilizes cross-polarisation and allows for measuring T_1^S, Figure 28D. The delay τ has to be usually extended to long time, but the advantage of using CP, making this method feasible for dilute and slow relaxing nuclei. The magnetisation recovery is usually fitted to the equation:

$$M(\tau) = M_0 \exp\left(\frac{-\tau}{T_1}\right) \tag{27}$$

However, as there is no ^{1}H decoupling applied during the variable delay to prevent damage to the probe, relaxation behaviour measured by this method may be non-exponential due to potential for cross-relaxation involving both ^{1}H and S nuclei, thus the analysis might be complex.

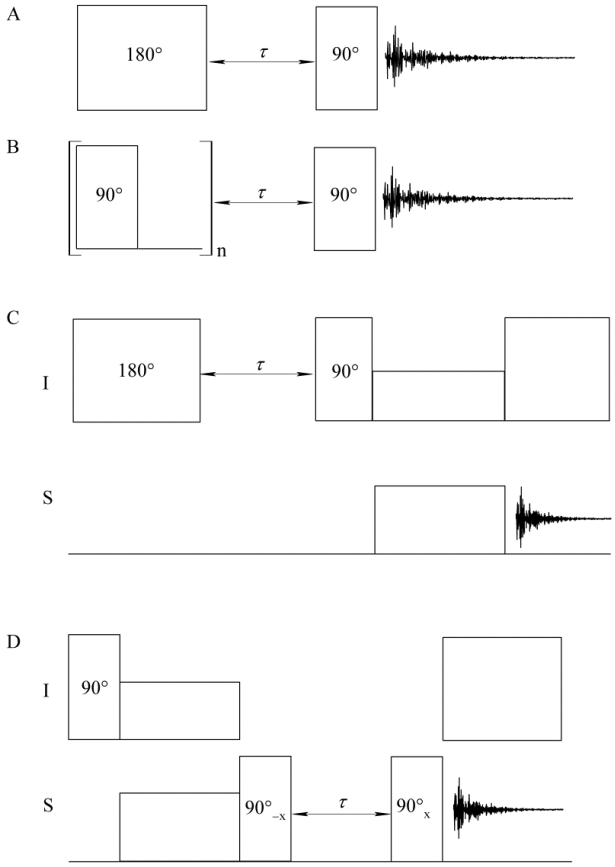

Figure 28. Pulse sequences used for measuring spin–lattice relaxation times: (A) inversion-recovery, (B) saturation-recovery, (C) inversion-recovery with cross-polarisation and (D) "Torchia" method. Adapted from Ref. [58].

3.5.8.3.6 Spin–lattice relaxation time in the rotating frame experiments

For the spin–lattice relaxation in the rotating frame ($T_{1\rho}$), there are three common methods:

- variable spin-lock,

- delayed contact,
- variable spin-lock with cross-polarisation preparation [58].

Variable spin-lock pulse sequence is shown in Figure 29A. In this method spectra are recorded as a function of the spin-lock time.

By incorporating a cross-polarisation step, $T_{1\rho}{}^{H}$ can be indirectly measured through an S nucleus spectrum. The method is known as a delayed contact and is shown in Figure 29B. Another method of measuring $T_{1\rho}{}^{S}$ using CP is to employ pulse sequence shown in Figure 29C, where a variable spin-lock RF field is used and an exponential decay curve will be observed as RF becomes longer in duration. Proton decoupling is not applied during the variable delay to prevent unwanted CP and thus cross relaxation may complicate data analysis.

The magnetisation decay in all pulses can be fitted to the following equation:

$$M(\tau) = M_0 \exp\left(\frac{-\tau}{T_{1\rho}}\right) \tag{28}$$

where M_0 is the initial magnetization and τ spin-lock time. With all $T_{1\rho}$ measurements it is important not to use too long spin-lock pulses as this may damage the probe.

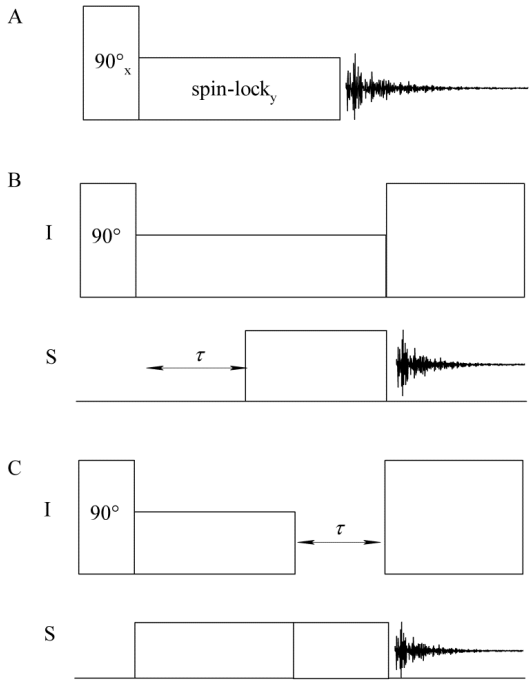

Figure 29. Pulse sequences used for measuring spin–lattice relaxation times in the rotating frame: (A) variable spin-lock, (B) delayed contact and (C) variable spin-lock with cross-polarisation preparation method. Adapted from Ref. [58].

3.5.8.3.7 Heteronuclear correlation experiments

To assign complex 1D spectra and/or to obtain further information about the structure of the system, 2D experiments can be performed. The Heteronuclear Correlation experiment (HETCOR) correlates the carbon or nitrogen spectrum with the high resolution proton spectrum [58, 210]. As ^{1}H spins are strongly coupled, obtaining useful resolution in the ^{1}H dimension may be difficult. Usually homonuclear decoupling is needed in order to narrow the abundant spin linewidths. Spin diffusion occurring during the cross-polarisation will also compromise the correlation information in the final spectrum. The correlation is obtained when ^{1}H and S nuclei are dipolar coupled; it is therefore a through-space correlation. Using a HETCOR experiment with short contact time, a 2D ^{1}H–S dipolar correlation map is obtained with correlations present between S resonances and the protons to which they are most strongly dipolar coupled. If longer contact time is used, more correlations will appear resulting from longer range dipolar couplings and ^{1}H spin diffusion. To reduce impact of spin diffusion on correlation experiments the Lee-Goldburg CP (LG-CP) sequence is often employed. LG-CP suppresses the homonuclear couplings while maintaining polarisation via the heteronuclear couplings. The HETCOR experiments are typically acquired with frequency switched Lee-Goldburg (FSLG) decoupling [211, 212] and during the S nucleus acquisition the protons are decoupled from S nuclei using TPPM decupling. The pulse sequence for FSLG HETCOR experiment is shown in Figure 30.

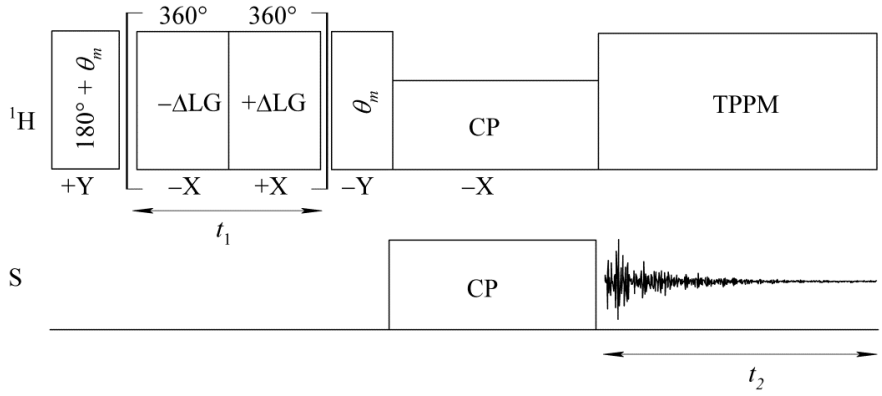

Figure 30. Pulse sequence used for FSLG HETCOR experiment. The sequence starts with with a $(180° + \theta_m)_y$ pulse on the protons, directly followed by a train of frequency- and phase-switched Lee-Goldburg pulses in the *xz* plane After the evolution period, the proton magnetization is turned back by a single magic angle (θ_m) *y* pulse, which will reverse any component perpendicular to the Lee-Goldburg pulse back into the *xy* plane, and which will bring the spin-locked component along the LG-pulse back to the *z* axis. Adapted from Ref. [211].

3.5.8.4 Pharmaceutical applications of solid-state NMR

Approximately 80–90% marketed drugs are solids and thus solid state characterisation of API, excipients and formulated products plays important role during both preformulation and formulation stages of drug development. SSNMR is a non-destructive, powerful technique for obtaining structural and dynamic information on solid pharmaceutical systems [58, 190, 191].

One of the most important pharmaceutical applications of SSNMR is characterisation of APIs polymorphs. Both crystalline and amorphous systems can be investigated. For example, Raghavan *et al*. investigated losartan potassium solid state forms using DSC, FT-IR, Raman spectroscopy, XRPD and SSNMR [28]. They found that losartan undergoes enantiotropic polymorphic transition during heating. The chemical shift on ^{13}C CP MAS NMR spectra of Form I, low-temperature stable form, and Form II, high-temperature stable form are significantly different, Figure 31. It was found that both forms have differences in molecular packing in the respective unit cell. In the Form I methyl of *n*-butyl signal splitting suggests the presence of more than one orientation for the *n*-butyl side chain in the unit cell whereas in the From II no such splitting is observed suggesting that in the unit cell only one crystallographically unique molecule existed.

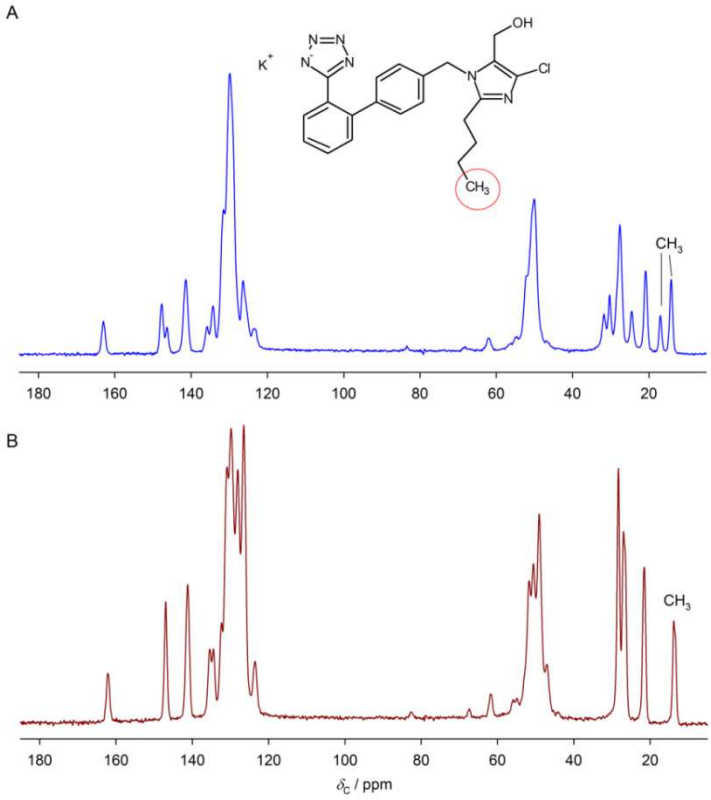

Figure 31. ^{13}C CPMAS spectra of losartan potassium, (A) Form I and (B) Form II.

Matsunaga *et al.* characterised by DSC, FT-IR, XRPD and SSNMR two polymorphs and an amorphous form of another sartan, candesartan cilexetil [29]. The ^{13}C CP MAS SSNMR spectra clearly distinguished these three forms. The ^{13}C resonances of amorphous form were significantly broader than those of crystalline forms, as a result of the distribution of local environments and hence dispersion of chemical shifts for each resonance. VT ^{13}C CP MAS SSNMR showed temperature-dependence of the terminal cyclohexanone ring of Form II, whereas those of Form I where scarcely affected. It was found that the cyclohexanone ring in the Form II existed as stable chair conformers. One chair form at lower temperature existed and the chair form–chair form conformational change occurred at higher temperatures. In the medium temperature cyclohexanone ring of Form II existed in the chair and boat conformations due to flip-flop motion.

Another example of successful SSNMR polymorph characterisation, is irbesartan, an example of configurational polymorphism [27]. Bauer *at al.* characterised two different crystal forms of irbesartan associated with tetrazole ring tautomerism, using one- and two-dimensional ^{13}C and ^{15}N CP MAS SSNMR as the main analytical tool. Carbon-13 CP MAS SSNMR spectra for forms A and B are not superimposable, Figure 32A and Figure 32B, reflecting substantial differences in the crystal structures. The difference is particularly significant for C-23 ($\Delta\delta_C$ = 8.6 ppm), clearly indicating that the tetrazole ring does not have the same structure in the two forms. Nitrogen-15 CP MAS SSNMR spectra confirmed existence of two tautomeric forms Figure 32C.

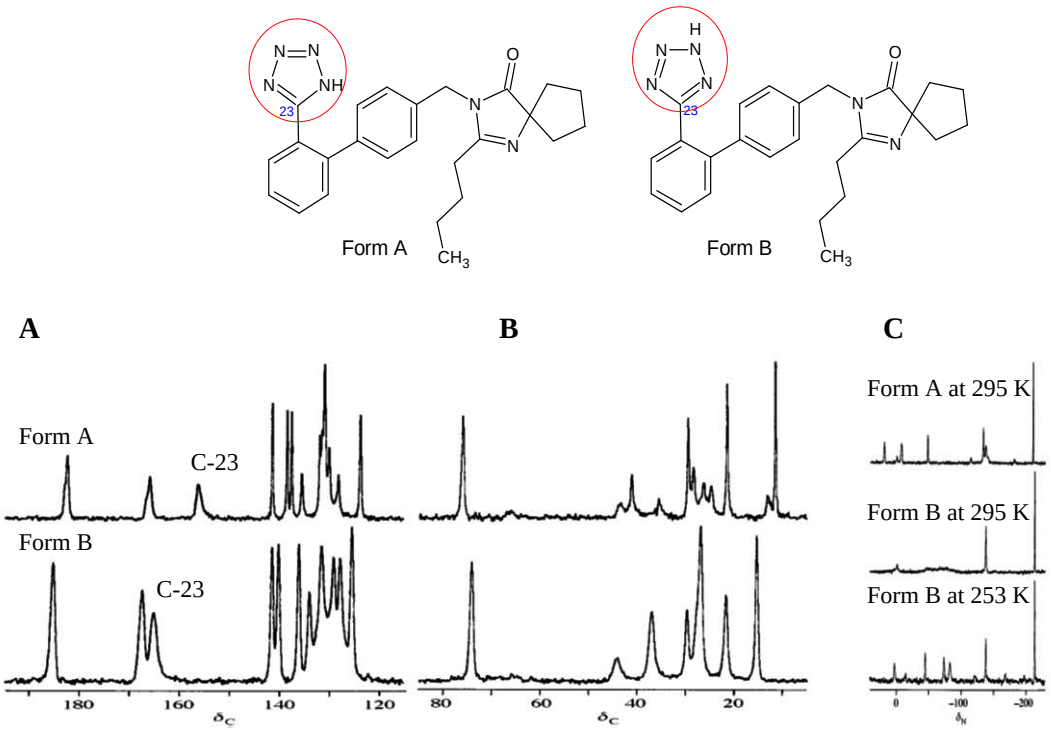

Figure 32. (A) High-frequency region and (B) low-frequency region of ^{13}C CPMAS spectra of irbesartan, Form A (top) and Form B (bottom) and (C) ^{15}N CPMAS spectra from Form A at 295 K (top), Form B at 295 K (middle) and Form B at 253 K (bottom) for irbesartan. Modified from Ref. [27].

SSNMR can also be employed to characterise solvates and hydrates. For example Othman *et al.* characterised solvates of drug used in treatment of benign prostatic hypertrophy – finasteride [213]. The crystal structures of the three finasteride solvates were found to be isomorphous as investigated by SCXRD and their XRPD patterns were almost indistinguishable. The solvates were clearly distinguished by the characteristic ^{13}C CPMAS NMR signals from the solvent clearly resolved from the finasteride peaks, Figure 33.

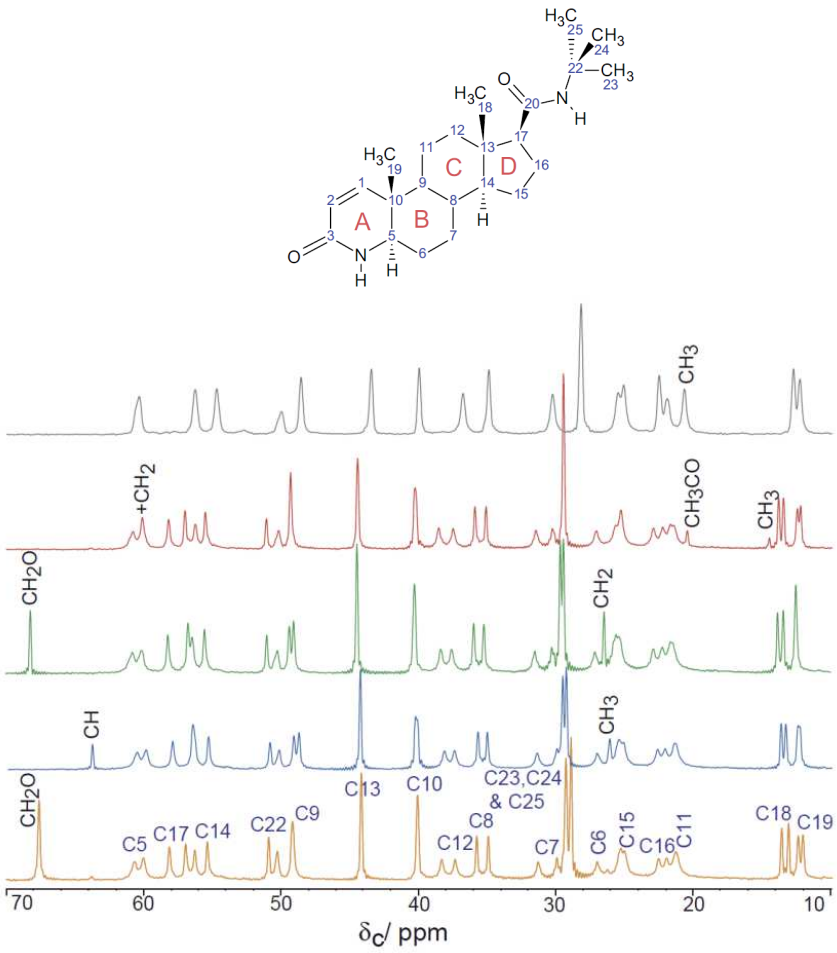

Figure 33. Carbon-13 CPMAS spectra of five solvates of finasteride (excluding the high-frequency part). Top to bottom: acetic acid; ethyl acetate hydrate; tetrahydrofuran solvate hydrate; isopropanol solvate hydrate; dioxane solvate hydrate. Assignments are indicated for the solvent peaks. Adapted from Ref. [213].

The physicochemical properties of a solid API are strongly related not only to its structural features but also to its molecular dynamics. Therefore, it is important to understand the dynamic of molecular motion occurring especially in a disordered, amorphous APIs,

because molecular relaxation takes place during storage of formulated amorphous drug. SSNMR has been widely used to study molecular dynamics in pharmaceutics [59, 191, 200, 214]. Luthra *et al.* studied changes in molecular dynamics of model drug systems during annealing by DSC [134] and ^{13}C NMR relaxation times [215]. They observed that in most cases annealing leads to longer T_1 and $T_{1\rho}$ NMR relaxation times, suggesting slowing of the local dynamics. This leaded to the expectation that chemical degradation processes that require molecular motion should be slowed down in aged glasses.

Another example of molecular dynamics studied by SSNMR relaxation times was reported by Gao [214]. A drug, delavirdine mesylate, in different crystalline and amorphous forms was characterised by ^{1}H T_1, ^{1}H $T_{1\rho}$ and ^{13}C T_1 SSNMR relaxation times. The values of measured relaxation times for different forms clearly indicated a very different molecular dynamic behaviour. The amorphous form, as expected, showed a higher degree of molecular mobility, and there were also significant differences in mobility between crystalline forms.

SSNMR can also be used for compatibility studies for characterising the interactions occurring between API and excipients [60-67].

3.6 Solid state drug-drug compatibility testing

The multi-ingredient drug products offer many benefits over the single ingredient drug products. It has been especially investigated in the case of CVD treatments. Combination therapy has been shown to reduce CVD complications by more than 80% [30], and strong interest has been expressed by the pharmaceutical industry to develop an all-in-one pill (multicomponent cardiovascular pill, MCCP or polypill) containing an angiotensin-converting enzyme (ACE) inhibitor, beta-blocker, aspirin and statin [33].

The simplest and the most economic approach to formulating a multi-ingredient dosage form is a blend or granulation containing all the active pharmaceutical ingredients. The combination of different agents in a single dosage form can, however, lead to interactions between APIs, potentially affecting the stability and bioavailability of either component [34-40]. Such interactions, termed incompatibilities, can be either physical or chemical in nature. Chemical interactions between APIs are well documented for FDCs intended for the treatment of tuberculosis, malaria or CVDs, conditions which usually require combination therapy [38-43]. For example, ternary and quaternary drug combinations containing rifampicin and isoniazid along with pyrazinamide and/or ethambutol hydrochloride were very unstable, showing up to 70% or 95% loss of rifampicin or isoniazid, respectively, due to chemical reaction [39]. Also, Kumar *et al.* reported incompatibility between polypill ingredients – atenolol, lisinopril, aspirin and statin due to chemical reactions [42, 43].

Solid-state reactions of API with excipient or API can include: transacylation, Maillard browning reactions and acid-base reactions [158]. As one of the most frequent approaches to improve physicochemical properties of an ionisable compound is to form a salt, and as formation of a free base/acid or new salt can significantly change physicochemical properties, acid-base reactions play an important role in formulation stability. Rohrs *et al.* reported decrease in dissolution rate for tablets of delavirdine mesylate following storage under accelerated stability conditions. This was found to result from formation of the less-soluble delavirdine free base due to acid-base reaction with excipient (croscarmellose sodium), as confirmed by FT-IR and SSNMR [67]. Zannou *et al.* found that maleate salt of a basic API showed a major loss in potency following stability testing, which again was attributed to conversion of the salt to the free base. The conversion strongly depended on microenviromental pH, and the formulation was successfully developed by acidification using citric acid as an excipient [216]. Guerrieri and Taylor investigated by FT-IR and Raman spectroscopy four model pharmaceutical salts (two APIs mesylate and napsylate salts) mixed with common basic excipients and exposed to moderate relative humidity [217]. They found that formation of free base depends on a number of factors such as pH_{max} of the salts (the pH of a solution where there is saturation of both ionized and unionized species), as well as the free base solubility. The conversion was also affected by excipient properties, including basicity, solubility, physical state and surface area.

Even in the absence of chemical reactions between components, the combination of two or more compounds (API-API or API-excipient) can result in physical interactions such as polymorphic transitions [44], amorphisation [45] or the formation of eutectic mixtures [46, 47]. These can cause problems during manufacturing [47, 48], with shelf life [49] or bioavailability [50]. For example, Bristol-Myers Squibb in 2010–11 recalled over 60 million tablets of an FDC product, Avalide®, containing an angiotensin receptor antagonist (irbesartan) and a diuretic (hydrochlorothiazide) due to appearance of a less-soluble irbesartan polymorph [96]. No such problems were observed with products containing irbesartan only. Zalac *et al.* have studied binary mixtures of antipyretic/analgesic drugs paracetamol and propyphenazone using DSC, XRPD and FT-IR spectroscopy [47]. Studies revealed physical interactions related to eutectic formation and a lower degree of crystallinity of both components in the physical mixture, with the formation of eutectic mixture having a significant impact on the physical stability of the formulation. Rawlinson *et al.* studied interaction between cross-linked polyvinylpyrrolidone (PVP-CL) and the poorly soluble crystalline drug compound, ibuprofen, by DSC, XRPD, Raman and FT-IR spectroscopy [45]. They reported a reduction in the crystallinity of ibuprofen

observed by XRPD on simple physical mixing with PVP-CL, with amorphisation increasing during storage of the physical mixtures at ambient conditions.

Clearly the identification of possible interactions between APIs is extremely important at an early stage of drug development process. Thermal analysis is frequently used to study the physicochemical properties of APIs and compatibilities between drug-drug and drug-excipient [41, 47, 51, 52]. DSC quickly provides information about possible interactions among the formulation components, according to the appearance, shift or disappearance of phase transition peaks and/or variations in the corresponding enthalpy or heat capacity values in thermal curves of drug-drug/excipient in physical mixtures [53, 54]. However, the interpretation of the thermal data is not always trivial, and the interactions observed at high temperatures may not always be relevant to ambient conditions. Therefore, the use of complementary analytical techniques, such as TGA, XRPD or FT-IR, is advisable, as shown in research papers [55, 56] and as reviewed in Ref. [57]. Isothermal microcalorimetry (IM) is other thermal method which also can be employed in compatibility screening [93, 218]. Solid-state nuclear magnetic resonance is another technique used to characterise pharmaceuticals [58, 59] and study physical or chemical interactions between APIs and excipients. It has been successfully used for characterising the physical interactions occurring between API and polymers [60-63], between API and β-cyclodextrin [64], and acid-base reactions between API and excipients [65-67], but SSNMR has not been widely used, however, in API–API compatibility studies.

In addition to the solid-state characterisation techniques, high-performance liquid chromatography or spectrophotometry can be used for the compatibility testing, however these techniques drawback is that the analysed sample must be stored under accelerated stability conditions for one to several weeks and then analysed using one of those techniques [158]. Also, the techniques do not provide information regarding physical incompatibilities.

4 RESEARCH OBJECTIVES

The aim of this study was to characterise two solid forms of valsartan to provide an insight into their structures and molecular mobilities and also to characterise two solid state forms of bisoprolol fumarate and to evaluate bisoprolol compatibility with amorphous valsartan employing multi-technique differential scanning calorimetry and solid-state NMR as a primary investigation tools supported by, where appropriate, particle size and shape analysis, HSM, TGA, solution-state NMR, FT-IR, XRPD and dissolution measurements.

The specific aims were:

- to obtain information about the solid state form of commercially available valsartan (AR form) and valsartan prepared by heating the AR form to 140 °C and rapidly cooled (AM form);
- to obtain information about molecular structure and molecular mobility of both valsartan forms;
- to characterise crystalline and amorphous forms of bisoprolol fumarate;
- to obtain information about compatibility of amorphous valsartan and crystalline bisoprolol fumarate.

5 EXPERIMENTAL PART

5.1 Materials

Pharmaceutical grade valsartan (VAL, AR form, as-received; Figure 34) was kindly obtained from Polpharma, Starogard Gdański, Poland and used without further treatment. Its fully amorphous form (form AM) was prepared immediately prior to experimental measurements in DSC pan in the instrument, in the NMR rotor in the probe, or on the hot stage of XRPD by heating sample to 140 °C, holding for 10–20 min then cooling with at least approximately 3 °C min^{-1} cooling rate to room temperature. Attempts to obtain crystalline material by re-crystallization based on previous published reports or patents [25, 26, 73, 75, 76] were unsuccessful.

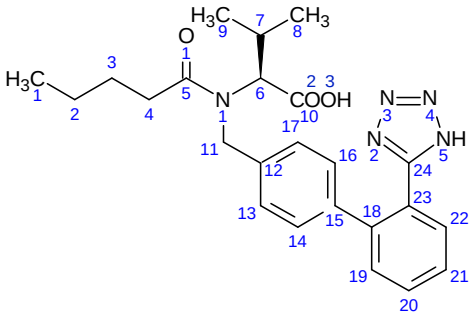

Figure 34. Chemical structure of valsartan with all atoms numbered.

Pharmaceutical grade crystalline bisoprolol fumarate (BISO; Figure 35) was kindly obtained from Biofarm, Poznań, Poland and used without further treatment. The amorphous form of bisoprolol was prepared immediately prior to experimental measurements in the DSC pan in the instrument, in the NMR rotor in the probe, or on the hot stage of XRPD by heating sample to 120 °C, holding for 5 min and then cooling with at least 10 °C min^{-1} cooling rate to –50 °C. Attempts to obtain diffraction-quality crystals by re-crystallization from water, methanol, ethanol and ethyl acetate solutions were unsuccessful.

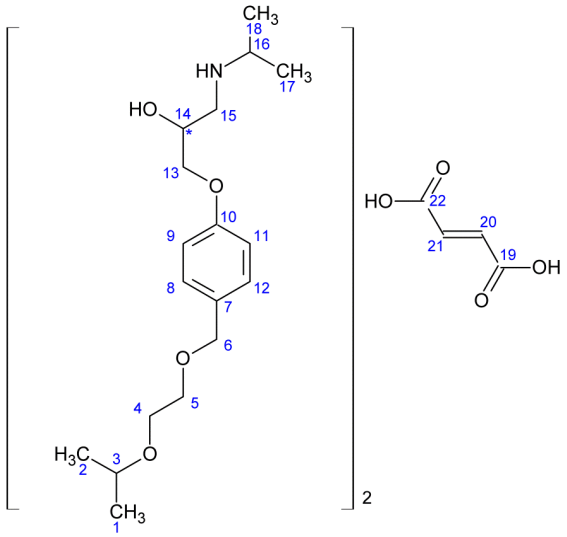

Figure 35. Chemical structures of bisoprolol fumarate or (*RS*)-1-((alpha-(2-isopropoxyethoxy)-p-tolyl)oxy)-3-(isopropylamino)-2-propanol fumarate (2:1) (M = 766.96 g mol^{-1}) with the carbons numbered. The chemical structure of bisoprolol fumarate is that of the neutral molecules, as conventionally given. The material is, however, expected to be in a salt form as a solid, with the fumaric acid present as a doubly de-protonated fumarate ion and with the bisoprolol assumed to be protonated at its NH site.

Physical mixtures of bisoprolol/valsartan in different concentrations from 10 to 95% (w/w) were prepared by mixing in a glass mortar for 20 min. Samples were used within 12 h. Melts were produced by heating of binary mixtures *in situ* in the DSC furnace, NMR probe or on the XRPD holder. The samples were melted at 120 °C and cooled to –50 °C with at least 10 °C min^{-1} cooling rate.

The purity of the provided and obtained materials was verified by solution ^{1}H and ^{13}C NMR. All other chemicals used were of analytical grade and were used as received.

5.2 Methods

5.2.1 Particle size and shape measurements

Valsartan, AR form particle size and shape analysis was determined using a Malvern Morphologi® G3 particle characterisation system (Malvern Instruments Ltd., Malvern, UK). Samples were dispersed using the automated sample dispersion unit and analysed in an episcopic (reflected) light, under 2.5X magnification. The following definitions of morphological parameters are used to describe the particles [219]:

- *Elongation* – expressed as:

$$Elongation = 1 - \frac{W}{L} \tag{29}$$

where *W* is a width and *L* is a length.

Values of *Elongation* ranges from 0 to 1, for example, a rod has a high *Elongation*.

- *CE (circle equivalent) Diameter* – the diameter of a circle with the same area as the projected area of the particle image.
- *HS (high sensitivity) Circularity* – the ratio of the object's projected area to the square of the perimeter of the object, expressed as:

$$HS\ Circularity = \frac{4\,\pi\,A}{P^2} \tag{30}$$

where *A* is an area and *P* is a perimeter. It is also sometimes termed *compactness*. A perfect circle has an *HS Circularity* of 1.0 while a narrow rod has an *HS Circularity* close to 0.

- *Convexity* – the perimeter of the convex hull of the object divided by its perimeter. The convex hull can be seen as the border created by an imaginary rubber band wrapped around the object. In the figure below B is the added "convexity area" of the particle A surrounded by the convex hull.

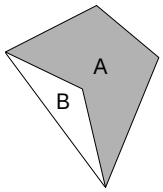

Figure 36. The particle area (A) and added "convexity area" (B).

The *Convexity* is expressed as:

$$Convexity = \frac{P_{\mathrm{A}} + P_{\mathrm{B}}}{P_{\mathrm{A}}} \tag{31}$$

where P_{A} and P_{B} perimeters of A and B, respectively The *Convexity* values are in the range 0 (least convex) to 1 (most convex). The *Convexity* is a measure of how "spiky" a particle is.

The CE *Diameter* results are provided on a volume basis, i.e. the contribution each particle makes is proportional to its volume – large particles dominate the distribution and sensitivity to small particles is reduced as their volume is so much smaller than the larger ones. The *Elongation*, *HS Circularity* and *Convexity* results are provided on a number basis, i.e. the contribution each particle makes to the distribution is the same; a very small particle has exactly the same 'weighting' as a very large particle.

The statistics of the distribution are calculated from the results using the derived diameters *D*[m,n] [219, 220]. *D*[n, 0.5], *D*[n, 0.1] and *D*[n, 0.9] are standard percentile readings from the analysis:

- D(n, 0.5) is the size at which 50% of the sample is smaller and 50% is larger;
- D(n, 0.1) is the size of particle below which 10% of the sample lies;
- D(n, 0.9) is the size of particle below which 90% of the sample lies.

The n or v in the expression refers to the number or volume distribution, respectively.

5.2.2 Thermogravimetric analysis

TGA curves were obtained using a Mettler-Toledo TGA/DSC1 instrument or a Perkin Elmer Pyris 1 TGA instrument under a nitrogen gas flow 60 mL min^{-1}. About 2–10 mg of powder samples were placed in an opened ceramic pan and heated at a rate of 10 °C min^{-1} from 25 to 600 °C.

5.2.3 Hot-stage microscopy

HSM analyses were performed using an Olympus SZH polarizing optical microscope equipped with Mettler-Toledo FP-82 hot-stage, a Mettle-Toledo FP80 programmable temperature-controller and Canon 20D DSLR camera. Samples were heated at 5 °C min^{-1} from room temperature to 140° C. Next, the samples were cooled down at about 1–2 °C min^{-1} to room temperature and reheated to 140 °C in a second run.

5.2.4 Differential scanning calorimetry

DSC curves were obtained using a DSC Q1000 TA Instrument Inc. (V9.9 Build 303) or a DSC 821 Mettler-Toledo instrument under a nitrogen gas flow of 50 and 60 mL min^{-1}, respectively. Sample powders (1–10 mg) were crimped in a standard or hermetic aluminium pan and heated with different rates (1, 5 or 10 °C min^{-1}) from –50 to 140 °C. Next, the samples were cooled down at 10, 20 or 50 °C min^{-1} to room temperature and reheated to 140 °C in a second run.

TMDSC curves were obtained using the DSC Q1000 TA Instrument Inc. instrument with an underlying heating rate 1 or 3 °C min^{-1} and a temperature modulation with amplitude of 0.5 or 1.5 °C, respectively, and period of 60 s (which is sometimes termed “standard TMDSC”) from –50 to 140 °C. The samples were then cooled at 10, 20 or 50 °C min^{-1} to –50 °C without modulation and reheated to 140 °C in a second run.

The enthalpy change after isothermal physical aging of AM valsartan form was determined as a function of aging time. Samples were first heated to 120 °C and held for several minutes to eliminate the effect of prior thermal history and then cooled at 25 °C min^{-1} to the aging temperature, T_a, which was 30, 40, 50 and 60 °C. The samples were maintained at the aging temperature for specified aging times ranging from 0 to 16 h, and after aging, samples were cooled at 25 °C min^{-1} to 25 °C. A subsequent heating scan at 3 °C min^{-1} to 120 °C

provides the data for the aged samples [182, 221]. The modulation parameters were the same as above.

Qi-TMDSC experiments with the underlying heating rate zero and a temperature modulation with amplitude of 0.5 °C and period of 60 s, were performed within the temperature range 25−130 °C at 1 °C increments with a 25 min measurements for each step.

The equipment was calibrated with indium (*m. p.* = 156.65 °C, ΔH_f = 28.45 J g^{-1}), and at least two tests were run on each sample. Melting, crystallization and relaxation events are quoted as an onset temperature. Glass transition temperatures are quoted as midpoints. The fictive temperature (Richardson) was calculated as the intersection of the pre- and post-transition enthalpy baselines according to Refs. [130, 131]. Values were determined using TA Universal Analysis 2000 V4.5A or Mettler-Toledo Star^e SW V10.0 software. Errors are quoted as one standard deviation.

5.2.5 Fourier transform infra-red measurements

FT-IR was carried out using an Alpha Bruker FT-IR spectrometer in KBr pellets. Spectra were recorded at room temperature from 4000 to 500 cm^{-1} collecting 64 scans and with a resolution of 2 cm^{-1}.

5.2.6 Solution-state nuclear magnetic resonance

Solution-state NMR experiments were carried out on a Varian VNMRS-700 machine with ^1H and ^{13}C frequencies of 699.73 and 175.97 MHz, respectively. Spectra of bisoprolol samples were measured in 0.5 mL of D_2O and [D_6]-DMSO. Spectra of valsartan and physical mixtures with bisoprolol were measured in 0.5 mL of [D_6]-DMSO. For each compound the full assignment was made using standard 2D techniques i.e.: ^1H–^1H correlation (COSY), one-bond ^1H–^{13}C single quantum correlation (HSQC) and long-range ^1H–^{13}C multiple-quantum correlation (HMBC). Standard conditions for COSY experiments were 1024 or 2048 data points with 256 increments in F_1 and 1 transient in F_2. For HSQC experiments 1024 or 2048 data points with 2 x 256 increments in F_1 and 8 transient in F_2 and for HMBC experiments 1024 or 2048 data points with 400 increments in F_1 and 8 transient in F_2. All measurements were performed at 25 °C.

The diffusion ordered spectroscopy (DOSY) experiments were measured at 25 °C on a 600 MHz Agilent spectrometer equipped with a probe with a *z*-gradient coil. The DBPPSTE (DOSY bipolar gradient pulses stimulated echo sequence) convection-compensated pulse sequence was used [222, 223] to acquire data sets in 31 min with 32 gradient amplitudes

ranging from 5 to 45 G cm^{-1} in equal steps of gradient squared, using 32 transients, a total diffusion-encoding gradient duration of 2.0 ms, and a diffusion time of 200 ms.

Data were processed using ACD/Spectrus Processor (Advanced Chemistry Development Inc., Canada) or Mnova NMR (Mestrelab Research, Spain) software.

5.2.7 Solid-state nuclear magnetic resonance

Carbon-13 solid-state NMR spectra were generally recorded with cross-polarization and magic-angle spinning using Varian VNMRS 400 and Varian Infinity Plus 500 spectrometers, operating at a ^{13}C frequency of 100.56 and 125.68 MHz, respectively. Probes using 5 and 6 mm diameter rotors made of zirconia were employed. Typical operating conditions used a CP contact time of 2 ms, a recycle delay of 2 s, 512 to 2048 transients and spin rate of 10 kHz. Carbon chemical shifts were referenced to the signal for tetramethylsilane via a replacement sample of solid adamantane (δ_C = 38.4 ppm for the high-frequency line). Variable-temperature experiments were performed from –20 °C to 120 °C, allowing samples to stabilize for 15–20 min before starting acquisition. All of the temperatures shown for ^{13}C SSNMR experiments are quoted with a correction of +16 °C above the displayed temperature, which is the estimated increase in sample temperature for a 5 mm rotor spinning at 10 kHz, based on previous calibration experiments using lead nitrate [224]. While the VT measurements are reproducible (performed at least in duplicate), and relative temperatures are accurate to within ±1 °C, the uncertainty on the absolute temperatures is estimated at ±4 °C. The very different sample conditions in the different techniques used, in any case, limits the transferability of temperature scales. Spinning sidebands were identified with the aid of spectra acquired with 14 kHz spinning rate.

Direct-excitation experiments were obtained using the Varian VNMRS 400 spectrometer operating at ^{13}C frequency of 100.56 MHz. A probe using 6 mm diameter rotor made of zirconia with Teflon® cap was employed. Typical operating conditions used a recycle delay of 1 s, 80 to 140 transients and spin rate of 6.8 kHz. Variable-temperature experiments were performed from 25 °C to 120 °C, allowing samples to stabilize for 15–20 min before starting acquisition. The temperatures for DE experiments were not calibrated.

^{13}C T_1 relaxation times were measured with cross polarisation using the “Torchia” method [209], although without ^{1}H decoupling during the relaxation period, using 21 recovery periods, τ, from 0.01 to 80 s, acquiring 64 transients per point. T_1 values were obtained by fitting the measured peak heights as function of τ to a simple mono-exponential decay. Molecular motions on the kHz time scale were probed by measuring ^{13}C spin–lattice relaxation times in the rotating frame, $T_{1\rho}$. Spin-locking pulse lengths were varied in 20 steps

from 1 to 20 ms, and the peak heights as a function of pulse length fitted to a mono-exponential decay. The error in T_1 and $T_{1\rho}$ values is due to this low signal-to-noise ratio and is expressed as the standard error in fitted values of T_1^C observed in nonlinear regression analysis.

Proton spectra were recorded using Varian Infinity Plus 500 spectrometer operating at a ^{1}H frequency of 499.70 MHz. A Bruker MAS probe using 1.3 mm diameter zirconia rotors was employed. Spectra were typically acquired using a recycle delay of 2 s, 4 to 64 transients and spin rates of 43, 53 and 67 kHz (for valsartan only). Data was also acquired at longer recycle delays (10 s) to verify that signals associated with slowly relaxing protons were not being missed. The estimated increase of the sample temperature with MAS rate of 53 kHz is estimated to be about 25 °C; identical results (but with lower spectral resolution) were obtained at the lower spin rate. Proton broadline NMR spectra for static samples were measured at 400.17 MHz using a Bruker Avance III HD spectrometer. A MAS probe using 5 mm diameter rotors made of zirconia was employed. A recycle delay of 5 s was used and 32 transients were acquired. Spectra were measured over a temperatures range from 25 to 120 °C, allowing at least 20 min for stabilization before acquisition.

Proton broadline NMR spectra and proton relaxation times (T_1^H and $T_{1\rho}^H$) for static samples were measured at 299.82 MHz using a Varian UnityPlus 300 spectrometer. Values of T_1 were derived from saturation-recovery experiments. $T_{1\rho}$ measurements were performed by varying a spin-lock time. Spectra were measured over a temperatures range from 25 to 120 °C, allowing at least 15 min for stabilization before acquisition.

Nitrogen-15 solid-state NMR spectra were recorded with CP and MAS using the Varian VNMRS 400 and the Varian InfinityPlus 500 spectrometers, operating at ^{15}N frequencies of 40.53 and 50.65 MHz respectively. Probes using 6 mm and 5 mm diameter rotors made of zirconia were employed respectively. Typical operating conditions used a CP contact time of 5 or 10 ms, a recycle delay of 1.5 or 2 s, 40000 to 150000 transients and spin rate of 6 or 10 kHz. Nitrogen chemical shifts were referenced using ^{15}N-enriched glycine at –347.4 ppm relative to the signal of neat nitromethane. Variable-temperature experiments were performed at 38, 80 and 110 °C, allowing samples to stabilize for 15–20 min before starting acquisition. All of the temperatures with 5 mm probe and 10 kH spinning rate shown for ^{15}N SSNMR experiments, unless otherwise stated, are quoted with a correction of +16 °C as for ^{13}C SSNMR experiments. Inversion-recovery CP MAS experiments were recorded with inversion time of 1 ms as described in Ref. [205].

The ^{1}H–^{13}C Heteronuclear Correlation (HETCOR) spectra were obtained at ambient temperature using the Varian VNMRS 400 spectrometer employing 4 or 6 mm rotors, with Frequency Switched Lee-Goldburg CP, two-pulse phase modulation decoupling, contact times

0.1 and 1.0 ms, 32 increments in the indirect dimension, 288 or 512 transients, recycle delays of 2 s and a spin rate of 10 kHz. A sample of glycine was employed for calibration.

Data were processed using gsim [225]. A Gaussian line broadening of 40 Hz was applied to the ^{13}C spectra and a "resolution enhancement" corresponding to an 80 Hz Gaussian function was applied to the ^{1}H MAS spectra.

5.2.8 First-principles computation

Gauge Including Projector Augmented Wave [226, 227] calculations were carried out with the CASTEP computer program for the crystalline valsartan given in Ref. [26]. Geometry optimisation was carried out both for the hydrogen atom positions only and for all atom positions (but with the unit cell dimensions fixed at the values determined from diffraction studies).

5.2.9 Powder X-ray diffractometry

X-ray diffraction patterns for most samples were obtained with a Bruker D8 ADVANCE instrument using a graphite bent-crystal monochromator (Cu $K_{\alpha,}$ λ = 0.1542 nm). Samples were placed on a hot-stage sample holder and scanned in reflection mode from 5° to 40° 2θ over a temperatures range from 0 to 120 °C in a step scan mode of 0.2° every second. Samples were allowed to stabilize for 10–15 min before starting acquisition.

Some of the patterns at the room temperatures were also obtained with a Phillips PW1830 generator operated at 40 kV and 45 mA, using nickel filtered Cu K_{α} radiation (λ = 0.1542 nm), and a diffracted beam graphite monochromator. The sample was placed either on Kapton^{TM} tape onto an aluminum holder or on a Silicon wafer and scanned in reflection mode from 5° to 40° 2 θ (for θ the half-scattering angle), at a step scan interval of 0.010 degrees per step, and holding time of 2.00 s/step.

X-ray diffraction patterns for bisoprolol/valsartan 70/30 (w/w) physical mixtures were obtained with a Bruker D8 ADVANCE instrument using a graphite monochromator (Mo K_{α}, λ = 0.0711 nm). Samples were placed in a capillary and scanned in reflection mode from 3° to 20° 2θ at 22, 60 and 80 °C. Samples were allowed to stabilize for 10–15 min before starting acquisition.

5.2.10 Intrinsic and apparent dissolution testing

The IDRs of both valsartan forms were measured by the rotating disc method using the Wood apparatus in an Erweka DT60 dissolution testing station (ERWEKA GmbH, Germany). The 8 mm diameter discs were compressed at 1300 psi and held for 40 s. Dissolution studies were

performed in 900 ml of deionised water maintained at a temperature of 37 ±0.2 °C and rotational speed of 100 rpm. Aliquots were withdrawn at predefined time points (120 points), replaced with dissolution medium, and analysed using a UV spectrophotometer at 250 nm. All measurements were performed in triplicates. IDR, the rate of mass transfer from solid to liquid state when conditions such as surface area, pH, ionic strength and stirring speed are kept constant, was determined using equation (7) [166].

The apparent dissolution tests of both valsartan forms were performed by the flow-through method in an USP apparatus 4 (CE 7 Smart, Sotax AG, Switzerland) [160]. Each cell was prepared by placing a 5-mm ruby bead in the apex of the cone to protect the inlet tube, and glass beads were added to the cone area to form a glass bead bed. Dissolution studies were performed in 1000 ml of deionised water maintained at a temperature of 37 ±0.2 °C with a flow rate of 8 mL min^{-1}. Aliquots were withdrawn at predefined time points (120 points), replaced with dissolution medium, and analysed using a UV spectrophotometer at 250 nm. All measurements were performed in triplicates.

5.3 Results

5.3.1 Valsartan

5.3.1.1 Particle size and shape analysis

AR valsartan form sample was tested by a morphology direct imaging microscopic method using a Morphologi® G3 apparatus. The analysed material shows particles with uneven shapes and wide array of diameters distribution ranging from 4 to 376 μm with a mean of about 170 μm. The elongation and circularity analysis indicated that the valsartan particles were more circular than elongated, Table II. The analysed material contains 97.5% unclassified shapes particles and only 2.5% fibres. Examples of the particles shapes and sizes are shown in Figure 37. The convexity was determined as low, indicating that the particles' edges are moderately even. The high circularity and low convexity would suggest that analysed valsartan probably has desirable powder flowability [228].

Table II. Particle size and shape reports for AR form of valsartan.

***CE Diameter* – volume distribution**	
CE Diameter minimum (μm): **4.13**	*CE Diameter D*[v, 0.1] (μm): **36.44**
CE Diameter maximum (μm): **376.35**	*CE Diameter D*[v, 0.5] (μm): **144.3**
CE Diameter mean (μm): **170.52**	*CE Diameter D*[v, 0.9] (μm): **304.6**
Particles counted: **50930**	*CE Diameter* standard deviation (μm): **11.86**
***Elongation* – number distribution**	
Elongation minimum (μm): **0.000**	*Elongation D*[n, 0.1] (μm): **0.183**
Elongation maximum (μm): **0.892**	*Elongation D*[n, 0.5] (μm): **0.407**
Elongation mean (μm): **0.402**	*Elongation D*[n, 0.9] (μm): **0.613**
Particles counted: **10849**	*Elongation* standard deviation (μm): **0.162**
***HS Circularity* – number distribution**	
HS Circularity minimum (μm): **0.217**	*HS Circularity D*[n, 0.1] (μm): **0.544**
HS Circularity maximum (μm): **0.976**	*HS Circularity D*[n, 0.5] (μm): **0.745**
HS Circularity mean (μm): **0.726**	*HS Circularity D*[n, 0.9] (μm): **0.876**
Particles counted: **10849**	*HS Circularity* standard deviation (μm): **0.128**
***Convexity* – number distribution**	
Convexity minimum (μm): **0.851**	*Convexity D*[n, 0.1] (μm): **0.962**
Convexity maximum (μm): **1.000**	*Convexity D*[n, 0.5] (μm): **0.982**
Convexity mean (μm): **0.982**	*Convexity D*[n, 0.9] (μm): **0.994**
Particles counted: **14117**	*Convexity* standard deviation (μm): **0.016**

A

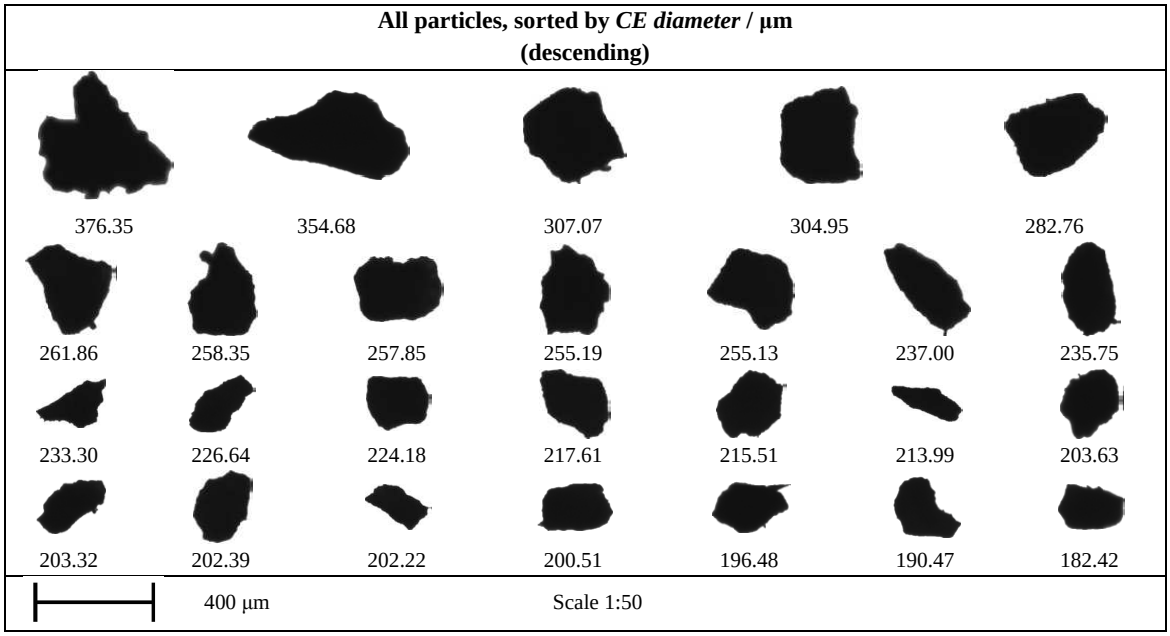

B

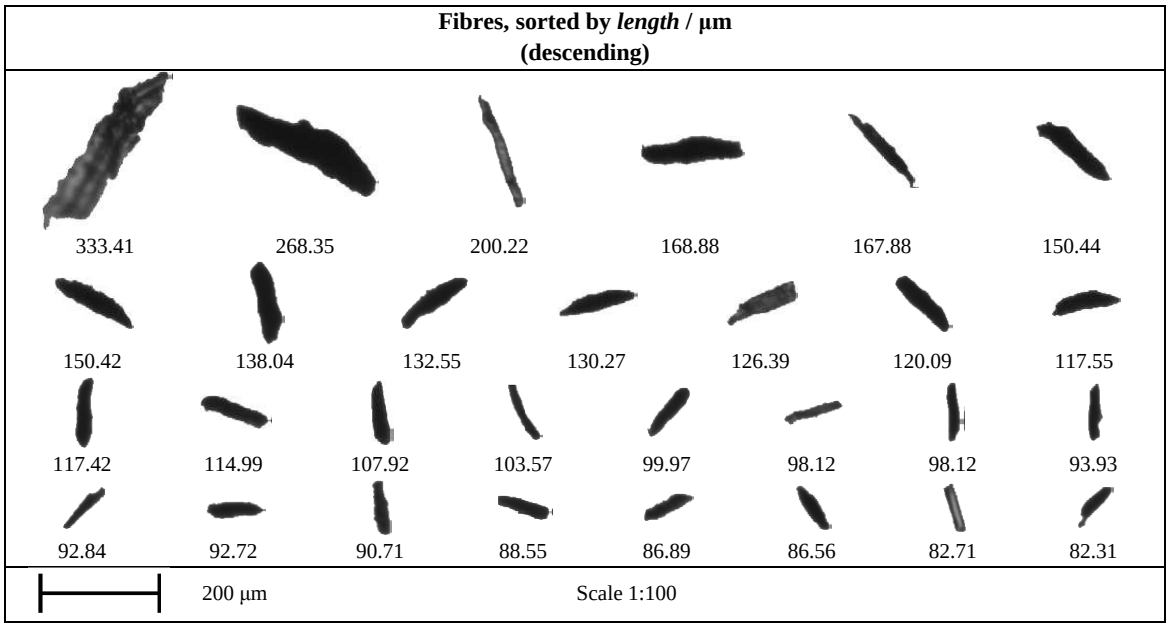

Figure 37. Particles images of AR valsartan form: (A) all particles and (B) fibers only.

5.3.1.2 Thermal analysis

The TGA curve of AR valsartan form shows three mass loss regions, Figure 38. The 1st occurs between 60–90 °C (1.3%), the 2nd between 160–300 °C (13.6%) and the 3rd between 300–580 °C (76.6%). The first step between 60–90 °C is due to loss of absorbed solvent, while the 2nd and 3rd steps are due to the thermal decomposition of valsartan.

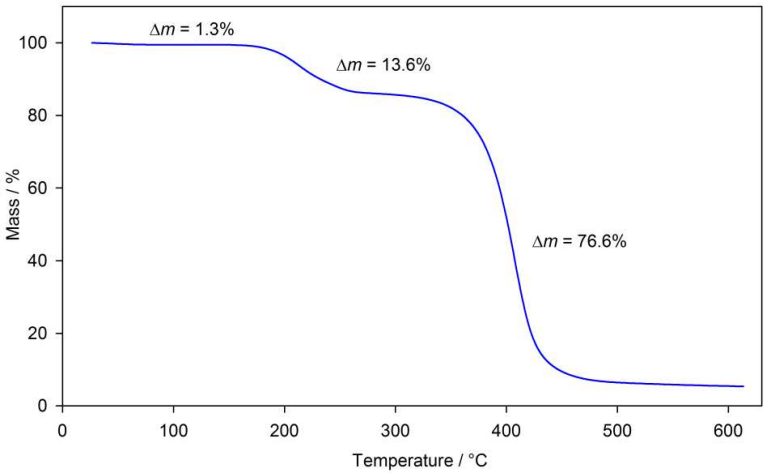

Figure 38. TGA curve of valsartan (AR form).

Figure 39 shows the heat-flow rate versus temperature measured by standard DSC on first heating with 10 °C min^{-1} rate, then on cooling from 140 °C with 10 °C min^{-1} rate to room temperature and the second heating again with heating rate at 10 °C min^{-1}. On the first heating DSC curve of AR valsartan form presents two endothermic events. A small broad peak around 60–90 °C (ΔH = 5 ±1 J g^{-1}) corresponds to a loss of solvent most likely water in the agreement with the results obtained from TGA, presented in Figure 38. The second event on this first heating is complex and at first glance may lead to a conclusion that the peak with a maximum at 100.6 °C (ΔH_{VAL} = 26 ±2 J g^{-1}) is due to melting. However, the diffractogram from X-ray measurements, Figure 45, does not indicate the occurrence of a crystalline form of the examined valsartan (AR form). The second transition with maximum peak temperature at 100.6 °C may correspond to a glass transition with high enthalpy relaxation peak overlapped with a change of heat capacity.

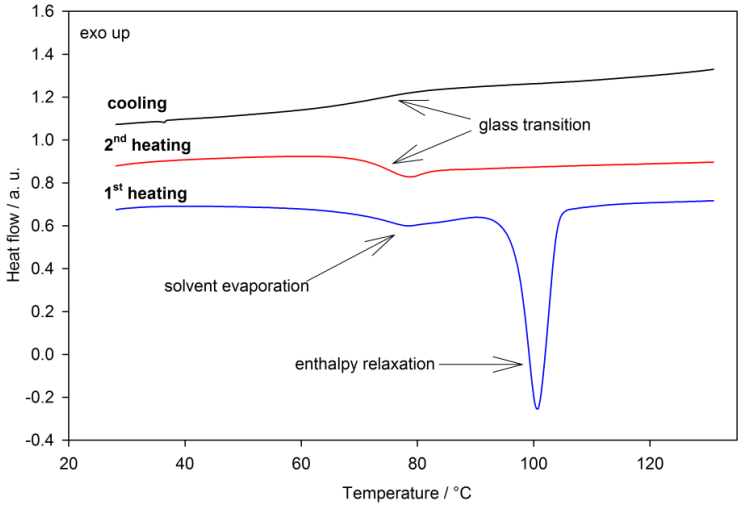

Figure 39. DSC curves of valsartan 1st (AR form) and 2nd (AM form) run on heating and cooling.

In order to evaluate the first heating results, the experiment by standard DSC on heating was repeated and divided into two steps: first, fresh valsartan (AR form) was heated from room temperature up to 90 °C in order to evaporate solvent, and then this sample was cooled to 25 °C and subsequently reheated up to 140 °C to observe more closely the process of the glass transition. The results of the two-step heating experiment are presented in Figure 40A. The evaluation of the glass transition process, resulting on second step heating and presented in Figure 40A curve III, is displayed in Figure 40B. The midpoint temperature of the fresh AR valsartan form sample was estimated as 93.6 °C with the increment of heat capacity (ΔC_p) as 0.68 ±0.02 J g^{-1} K^{-1}, Figure 40B, but the true glass transition temperature, of fresh valsartan (AR form) was defined as the fictive temperature with the value of $T_g^{Richardson}$ = 76.4 °C presented in Figure 40B.

The intensity of enthalpy recovery that occurs during the first heating scan, following an enthalpy relaxation process is probably due to some residual arrangement in the particles originating from creation of the fresh powder sample of valsartan and storage of the product at the room temperature and may be impacted by bonded solvent.

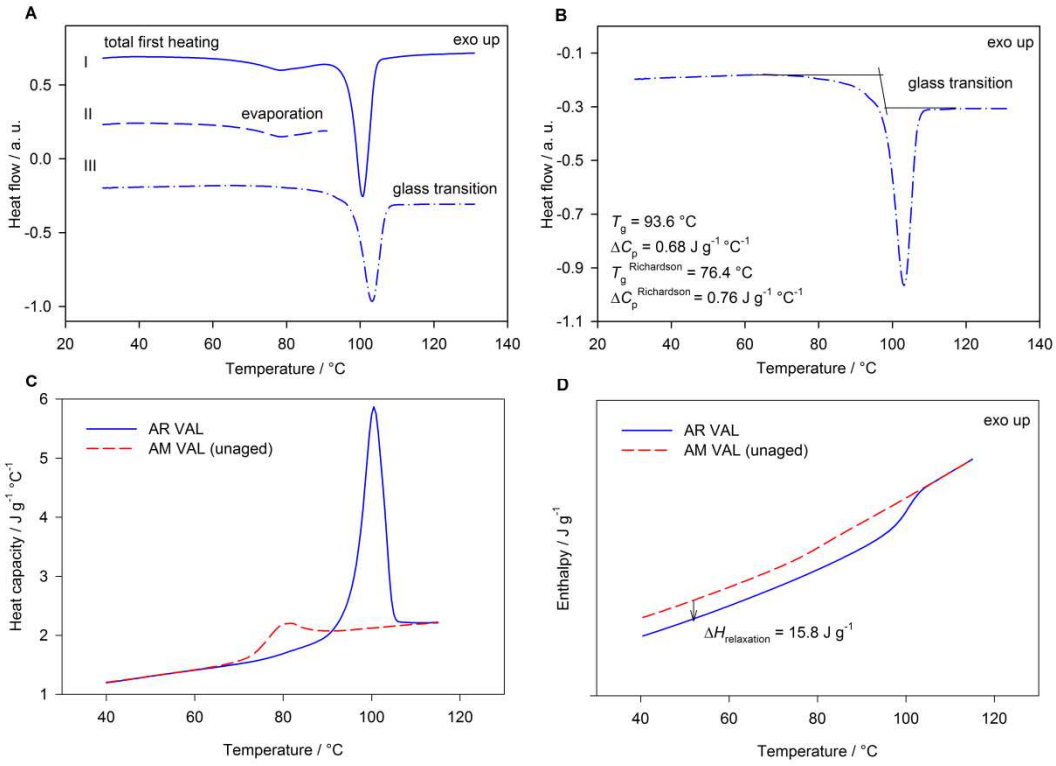

Figure 40. (A) DSC curves of valsartan (AR form) for the two-step heating experiment. (B) Evaluation of the glass transition from DSC curve of valsartan (AR form) from 2-step experiment (curve III). (C) The heat capacity of AR and AM almost unaged valsartan from standard DSC. (D) Evaluation of enthalpy relaxation from AR and AM unaged valsartan from first and second heating, respectively.

The enthalpy recovery that occurs during the first heating scan, following an enthalpy relaxation process, was determined by integrating the difference between the heat capacity (C_p) of the AR form and the unaged AM form of valsartan samples as illustrated in Figure 40C and D according to Ref. [229]. The heat capacity of fresh sample of valsartan, AR form, in Figure 40C was evaluated from heat-flow rate of second step of heating scan as presented in Figure 40A (curve III) and Figure 40B. The C_p of unaged amorphous valsartan sample (form AM) was converted from second heating scan as illustrated in Figure 39. Figure 40D shows enthalpy as the function of temperature for both samples resulting from the integration of the C_p. The enthalpy relaxation with a value of $\Delta H_{relaxation}$ = 15.8 J g^{-1} was obtained from the difference in enthalpies as illustrated in Figure 40D. Such unexpected high value, around 16 J g^{-1} of enthalpy relaxation, is probably related not only to the physical ageing process of amorphous sample but also due to the influence of solvent on this phase transition [230]. We can speculate that in this case the solvent probably does not act as a plasticizer but can nucleate for a better additional arranging of molecules sample during storage at room temperature, resulting in enthalpy value.

Figure 39 shows heat-flow rate of valsartan (form AM) versus temperature for a second run on heating, after cooling with 10 °C min^{-1} from 140 °C, where valsartan appears as a dry amorphous phase material with a glass transition at 73.9 ±0.5 °C and change of heat capacity (ΔC_p) 0.49 ±0.01 J g^{-1} K^{-1}. The change of heat capacity for amorphous valsartan on cooling was similar i.e.: 0.48 ±0.01 J g^{-1} K^{-1} with T_g at 72.8 ±0.5 °C. The difference between the glass transition (fictive temperature) of fresh valsartan, AR form, of around 76 °C and unaged valsartan, AM form, from second heating scan of around 74 °C is not significant when excluding influence of the enthalpy relaxation. The intensity and shift of endothermic peak of fresh sample results from overlapping of heat capacity changes and enthalpy relaxation process and these processes can be separated by TMDSC. TMDSC technique allowed for separation of the total heat-flow rate into reversing and non-reversing parts, as is presented in Figure 41 for the AR valsartan form. The non-reversing curve shows the enthalpy relaxation peak and the reversing curve shows the glass transition at around 94 °C.

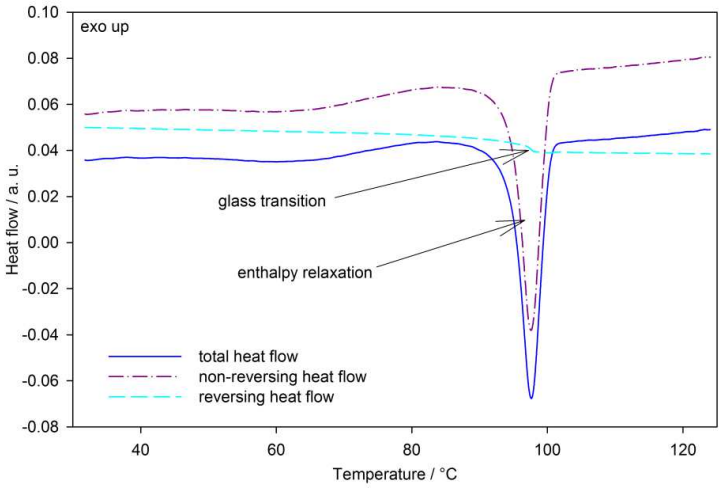

Figure 41. TMDSC curves of AR valsartan form for the first heating: total, reversing, and non-reversing heat-flow rate curves.

In the second heating, TMDSC allowed for separation of the glass transition from enthalpy of the relaxation process, Figure 42. T_g determined by TMDSC for AM form was found to be 77.7 ±0.9 °C. This difference might occur due to the ageing of the amorphous form during slow heating applied for TMDSC experiment (1 °C min^{-1}). It is known that the location of the glass transition temperature is a function of the experimental cooling rate and of the thermal history of the glassy material. Thus values determined by standard DSC and TMDSC might vary and even some variations are seen from experiment to experiment [128].

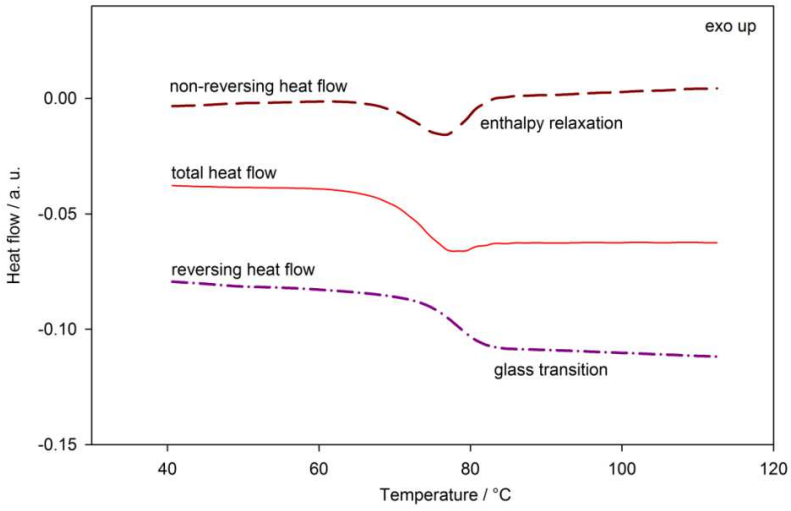

Figure 42. TMDSC response for dry amorphous valsartan (form AM), showing the total, reversing and non-reversing heat-flow signals.

Further confirmation of the amorphous nature of the AR valsartan form was provided by Qi-TMDSC, Figure 43. Qi-TMDSC provided reversing C_p characteristic of the sample and

change of the heat capacity at glass transition process can be clearly seen at around 83 °C. The glass transition temperature in the comparison to standard DSC and TMDSC results is lowered due to zero underlying heating rate.

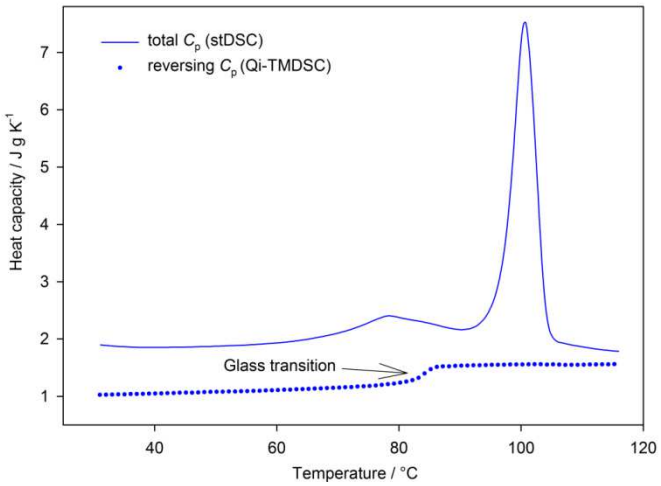

Figure 43. Comparison of the heat capacities for the 1st run for the AR valsartan form obtained from standard DSC and Qi-TMDSC. Qi-TMDSC shows glass transition process on the reversing heat capacity signal confirming amorphous nature of the AR valsartan form.

HSM analysis provided confirmation of information obtained from calorimetric methods. Figure 44A shows valsartan AR form polarized light photomicrographs at 30 °C. No birefringence is observed, indicating that the material is in the amorphous state. There were no changes observed between 30 and to about 98 °C. Although, second-order-like phase transitions are thought to be difficult to detect by optical methods, because of the small structural changes that occur [95], it was possible to observe glass transition process at around 100 °C for the as-received material, Figure 44B and C. Above the glass transition temperature sample exists in the liquid amorphous state, Figure 44D. In the 2nd heating run the glass transition process could not be observed under polarized light microscope (data not shown). No birefringence is observed in the freshly prepared AM form of valsartan after 24 h indicating that no crystallization had occurred (data not shown).

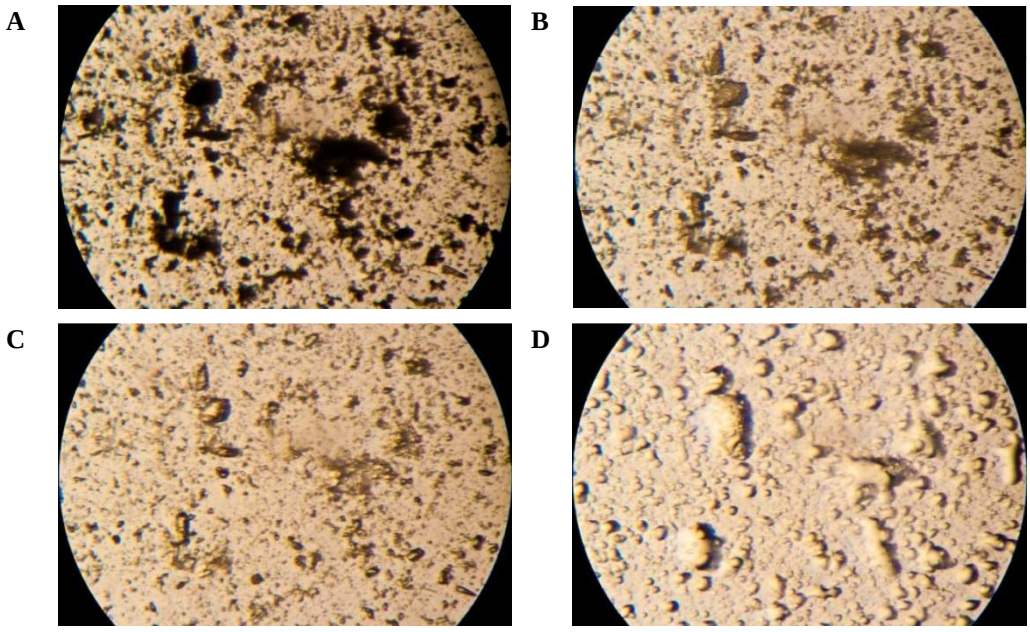

Figure 44. Polarized light photomicrographs of valsartan, AR form, at (A) 30 °C, showing lack of birefringence and indicating amorphous nature of the material (B) and (C) showing glass transition process at, 99 and 101 °C, respectively, and (D) material above the glass transition in the liquid amorphous state at 140 °C. Sample was heated with 5 °C min^{-1} rate.

5.3.1.3 X-ray powder diffractometry

Figure 45 shows room temperature X-ray powder diffraction measurements for a fresh sample of valsartan powder (blue curve, AR form) and the same sample after being treated by heating to 140 °C and cooling to room temperature (red curve, AM form). After heating, the powder readily consolidated to form a glassy thick film. X-ray patterns of both samples indicate their amorphous nature, however, some imitation of ordering in the AR form is observed.

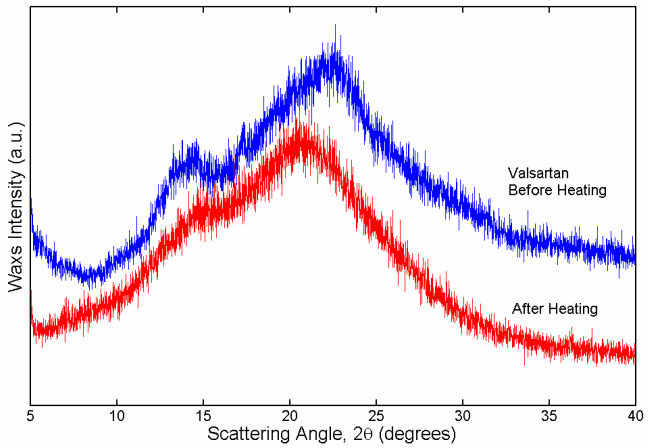

Figure 45. XRPD diagrams of valsartan (λ = 0.1542 nm) recorded at room temperature. Valsartan powder before (AR form) and after (AM form) heating to 140 °C.

It is known that the measured X-ray powder patterns of crystalline nanoparticles materials may exhibit the broad halos characteristic of X-ray amorphous material [231], however, the particle size analysis does not indicate the existence of nanocrystals, thus XRPD analysis confirmed the amorphous nature of the fresh powder sample of valsartan (AR form) as well as AM form.

5.3.1.4 Fourier transform infra-red spectroscopy

Figure 46 shows FT-IR spectra of both valsartan forms. The AR valsartan spectrum shows two carbonyl absorption bands at 1732.1 cm^{-1} and 1603.8 cm^{-1} assigned to carboxyl carbonyl (C-10) and amide carbonyl (C-5) stretching vibrations, respectively. These bands are of diagnostic value to elucidate changes in hydrogen bonds. There was no change in AM form in carboxyl carbonyl band (1732.1 cm^{-1}) whereas the C-5 carbonyl peak shifted towards higher wavenumber (1605.8 cm^{-1}) suggesting change in the environment of the carbonyl group associated with the amide moiety. This shifting of absorption band for the carbonyl group of amide to a higher wavenumber could be attributed to the breakdown of the intermolecular hydrogen bonds between C(5)O and the tetrazole N(5)H group similarly to that existed in the crystal [26], Figure 2, as well as *cis–trans* conformational changes in the fully amorphous form as discussed further. The complex region of 900–600 cm^{-1} represents bending and skeletal vibrations of aromatic rings in the compound, some small differences at this fingerprint region are also found, Figure 46 (inset). Also, there is an attenuation of broad peak with maximum at about 3436 cm^{-1} (N(5)H and/or OH) which is likely to be due to changes in the hydrogen bonds.

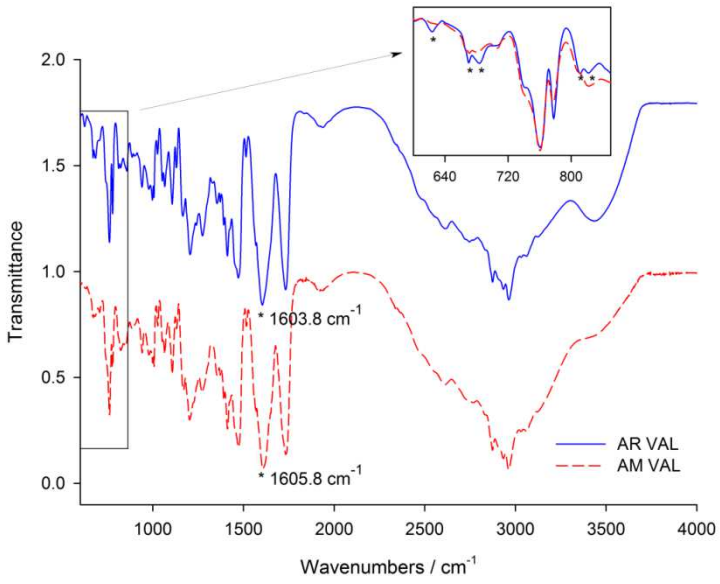

Figure 46. FT-IR spectra of two valsartan forms.

5.3.1.5 NMR analyses

5.3.1.5.1 Carbon-13 solid-state NMR

To distinguish molecular structures of valsartan forms ^{13}C CPMAS NMR was employed. Isotropic chemical shifts obtained from solids under MAS are similar to those obtained from solution, however in solids there is an absence of dynamic averaging which occurs readily in a solution. In solids the molecular conformations are “locked” in position due to “freezing” of the free rotation of bulky groups. Conformational (intramolecular) and crystal packing (intermolecular) interactions play important role in determining the magnetic field of individual nuclei in a solid state. Thus chemical shift is sensitive to changes in the immediate environment of the nucleus and provides specific and detailed diagnostic information [213, 214, 227]. Figure 47 shows ^{13}C CP MAS NMR spectra of both valsartan forms.

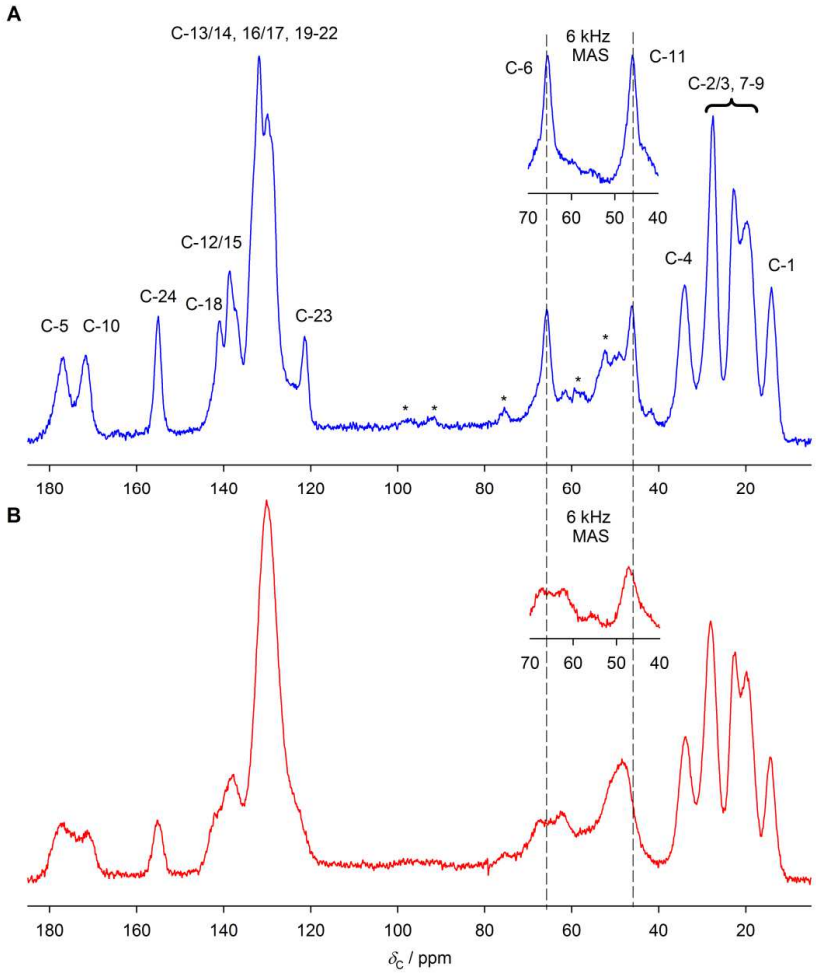

Figure 47. Carbon-13 CPMAS NMR spectra of (A) as-received and (B) fully amorphous valsartan recorded at 10 kHz spinning rate at room temperature. Insets show spectra at 40–70 ppm region not affected by spinning sidebands recorded at 6 kHz spinning rate. Asterisks (*) denote spinning sidebands.

The resonances were assigned based on ^{13}C solution-state NMR and by computational prediction of chemical shifts based on crystal structure given in Ref. [26]. Standard NMR techniques (COSY, HSQC and HMBC; appendices: Figure A 1, Figure A 2 and Figure A 3) were used to assign the solution-state spectrum. Table III lists the chemical shifts for two solid states of valsartan and compare them to corresponding solution-state and calculated values.

Table III. Solution-, solid-state and calculated NMR chemical shifts for valsartan at 25 °C (in [D_6]-DMSO) and 38 °C (solid state).

Carbon No	Solution-state NMR δ_C / ppm		Solid-state NMR δ_C / ppm		Calculated $\delta_{C(calc)}$ / ppm[a]
	Major conformer (M, *trans*)	Minor conformer (m, *cis*)	AR form	AM form	Crystalline form (*trans*)
1	14.16	14.25	14.1	14.3	11.8
8	18.25	18.93	19.8 22.6 27.6	19.8 22.6 28.0	22.3
2	22.12	22.27			24.7
9	20.59	19.84			25.2
3	27.26	27.45			27.9
7	28.00	28.04			29.8
4	32.90	32.94	34.1	33.8	34.3
11	49.15	45.90[b]	46.2	48.3	51.2
6	63.39	66.18	65.8	62.3, 67.3	73.1
23	123.84[c]	123.84[c]	121.3	121 – 139 with maxima at 130.1 138.0	129.7
19	130.98	131.05	123 – 139 with maxima at 129.7 131.8 138.5		135.5
21	128.14	128.01			136.2
16	129.24	128.73			136.2
14	129.24	128.73			136.9
13	126.72	127.37			137.4
17	126.72	127.37			138.5
20	130.98	131.05			139.0
22	131.51	131.51			142.7
12	138.22	137.55[b]			143.9
15	138.22	138.67			145.2
18	141.65	141.78	140.8	141.9	150.4
24	155.00[d]	155.00[d]	155.1	155.1	166.1
10	172.34	172.07	171.7	171.3	180.6
5	173.91	173.88	176.8	177.3	181.8

[a] $\delta_{C(calc)} = -(\sigma_{calc} - \sigma_{ref})$; where $\sigma_{ref} = 176.1$ ppm.

[b] Low and [c] very low intensity peaks. Low intensities will reflect long ^{13}C relaxation times of quaternary sites, but peaks may also be broadened by motional exchange.

[d] Not observed, data taken from Ref. [78].

The assignment of the resonances is somewhat difficult since non-equivalence of all carbons in the molecular skeleton is expected, there is severe overlapping in the regions 10–40 and 120–150 ppm and lines are broad due to amorphous nature of the material. The linewidths for the as-received valsartan (AR form) are relatively high which suggests the sample is not

crystalline, which is consistent with the thermal and XRPD analyses. The signals between 10 and 40 ppm arise from the aliphatic CHs, CH_2s and CH_3s. This region does not change dramatically after heating as-received form. The biggest difference in the AM form is for carbon resonances directly bonded to amide nitrogen (N-1) i.e.: at 46.2 ppm (C-11) and 65.8 ppm (C-6). In the fully amorphous material signal arises from C-11 is broadened and moves to higher chemical shift ($\Delta\delta_C$ = –2.1 ppm). The resonance arises from C-6 at 65.8 ppm is split to two broad signals with maxima at 62.3 and 67.3 ppm. This behaviour is similar to that observed in a solution where there are significant differences in C-11 and C-6 chemical shifts for *cis* and *trans* conformers (for C-11, δ_C^{cis} = 45.90, δ_C^{trans} = 49.15 ppm and for C-6, δ_C^{cis} = 66.18, δ_C^{trans} = 63.39 ppm). The results suggest that in the fully amorphous material valsartan exists as a mixture of *cis–trans* conformers, Figure 48.

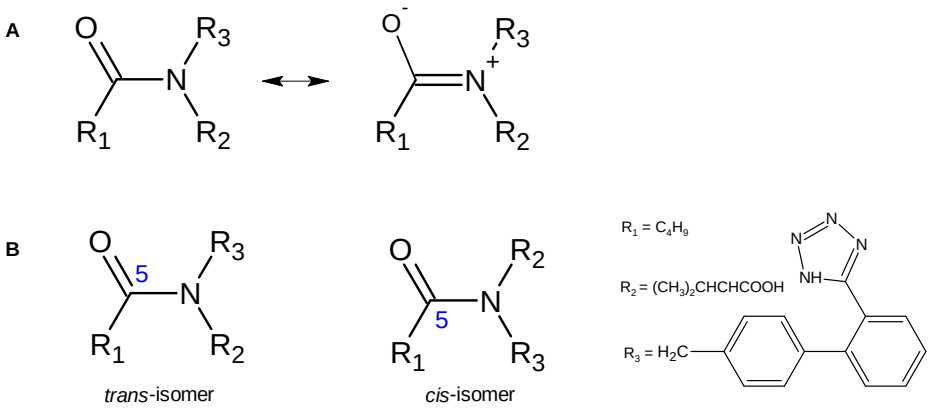

Figure 48. (A) The double bond character of amide bond and (B) possible conformations of valsartan in the liquid and solid state as a consequence of this phenomenon.

The signals between 120 and 150 ppm arise from the phenyl rings. These also broaden significantly in the fully amorphous material. The remaining signals at 155.1, 171.7 and 176.8 ppm come from the carbon in the tetrazole ring (C-24), the amide and acid carbons (C-5, C-10), respectively and all of these also broaden significantly. It has to be noted that there is no significant differences between solution-state NMR spectra between AR and AM valsartan forms, thus no degradation had occurred during heating the AR form. One can see from Figure 47 that the differences between two forms are immediately visible from ^{13}C CP MAS NMR spectra; fully amorphous form exhibits a general broadness of the ^{13}C resonances, resulting from the co-existence of a distribution of local environments and hence a dispersion of chemical shifts for each resonance. The broadness of the peaks obtained for the heated material (AM form) from compared to the as-received material (AR form) proved that valsartan treated by heating is in the amorphous form and is more disordered than as-received material as previously found by other methods.

In order to investigate the behaviour of both valsartan forms below and above the glass transition VT ^{13}C CP MAS NMR, Figure 49, were performed. Most of the chemical shifts for both forms were not affected by changing the temperature. A significant change for as-received valsartan is observed for C-6 at 110 °C i.e. above the glass transition, signal split into two resonances and for C-11 signal is broadened and shows chemical shift increase. These changes are most probably due to *cis–trans* isomerisation along the C(O)–N bond similarly to that in the solution [77, 78]. Over the analysed temperature range spectra show broad signals typical for amorphous material except for aliphatic carbons. If crystallization had occurred, sharp signals should be detected. VT experiments confirmed that no crystallization occurs during heating and cooling of both forms. There is also noticeable change in the aliphatic peak linewidth (C-1–C-4 and C-7–C-9) at 110 °C (sharpening) in both forms as the sample is going through the glass transition, the material is moving from glassy state to more mobile, liquid amorphous state. This sharpening of the lines is due to increased molecular mobility, as the wide array of potential orientations in glassy state begin to average similarly to that process in the solution state. In contrast the aromatic region in as-received material above glass transition had significantly broadened. It suggests different molecular mobility of aliphatic and aromatic groups in the material. As might be expected, the spectra of both materials above the glass transition at 110 °C are essentially identical.

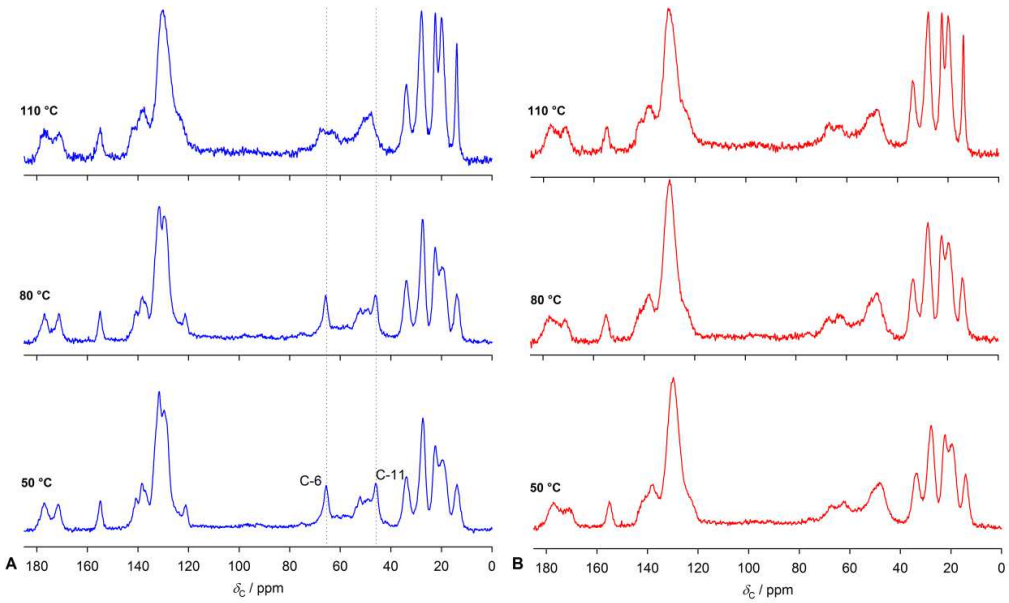

Figure 49. VT ^{13}C CPMAS spectra of (A) as-received (AR form) and (B) fully amorphous valsartan (AM form) before and after the glass transition process (T_g^{AR} = 94 °C and T_g^{AM} = 74 °C). It can be seen that the spectra of both forms recorded at 110 °C are essentially identical, most likely due to isomerisation of AR form above the glass transitions.

In order to obtain information about molecular mobility of both valsartan forms VT ^{13}C MAS direct-excitation NMR experiments were performed, Figure 49. Spectra display only the signals arising from fast-relaxing carbons i.e. methyls as well as methylenes and methines (C-1–C-4 and C-7–C-9) which indicate flexibility of alkyl chains. There is no signal observed from aliphatic carbons directly bonded to N-1 (C-6, C-11) and from carbonyl groups carbons (C-5, C-10). The very low intensity and broad resonance from aromatic carbons around 130 ppm is observed. The resonances are not observed even with long recycle delay up to of 60 s. These findings are consistent with VT ^{13}C CP MAS experiments results and suggest that the molecular mobility of aliphatic carbons (C-1–C-4 and C-7–C-9) is higher than the other ones.

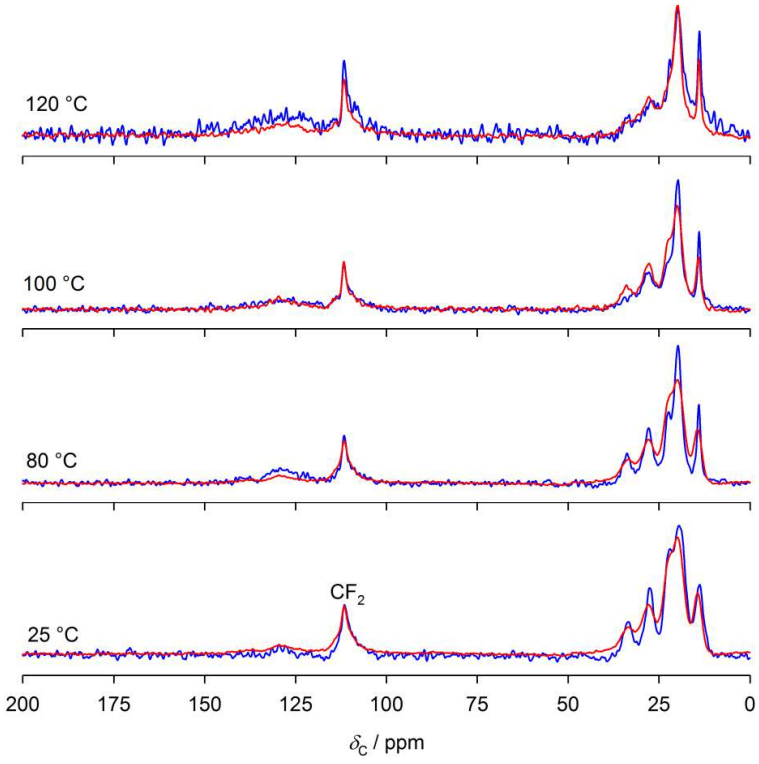

Figure 50. Carbon-13 spectra of AR (blue line) and AM (red line) valsartan obtained using direct-excitation experiment recorded at different temperatures with spinning rate at 6.8 kHz. Temperatures displayed are the set-up values not real samples temperatures. The signal at 110 ppm arises from the CF_2 carbon in the Teflon® used as a rotor cap.

5.3.1.5.2 Proton solid-state NMR

The static proton NMR measurements results in a single broad-line bandshape due to extensive ^{1}H–^{1}H dipolar coupling. Figure 51 shows ^{1}H static VT SSNMR spectra of both valsartan forms. As the temperature increases from 25 to 80 °C there are observed scarce changes in bandshapes for both forms. Rapid narrowing occurs at the temperature above 100 °C. These results show

a change in mobility above the glass transition. Below the glass transition, the amorphous state is glassy i.e. more rigid than for the state above glass transition where sample is in a liquid amorphous state. In the glassy state homonuclear dipolar coupling interactions cause substantial broadening of the line, and in the liquid amorphous state the increased molecular mobility implies substantial averaging of the dipolar interactions, producing sharper signal at 100 °C and above. As there are two different values of glass transition temperature estimated by standard DSC i.e. T_g^{AR} = 94 °C and T_g^{AM} = 74 °C one could expect differences in the spectra at 80 °C (i.e. sharper bandshape for fully amorphous sample), but the spectra look similarly. However, the fictive glass transition temperature for AR form is similar to that of the fully amorphous form i.e.: $T_g^{Richardson(AR)}$ = 76 °C, which explains spectra similarity. Nearly identical ^{1}H bandshapes suggest that two forms of valsartan have very similar molecular mobility on the timescale being probed.

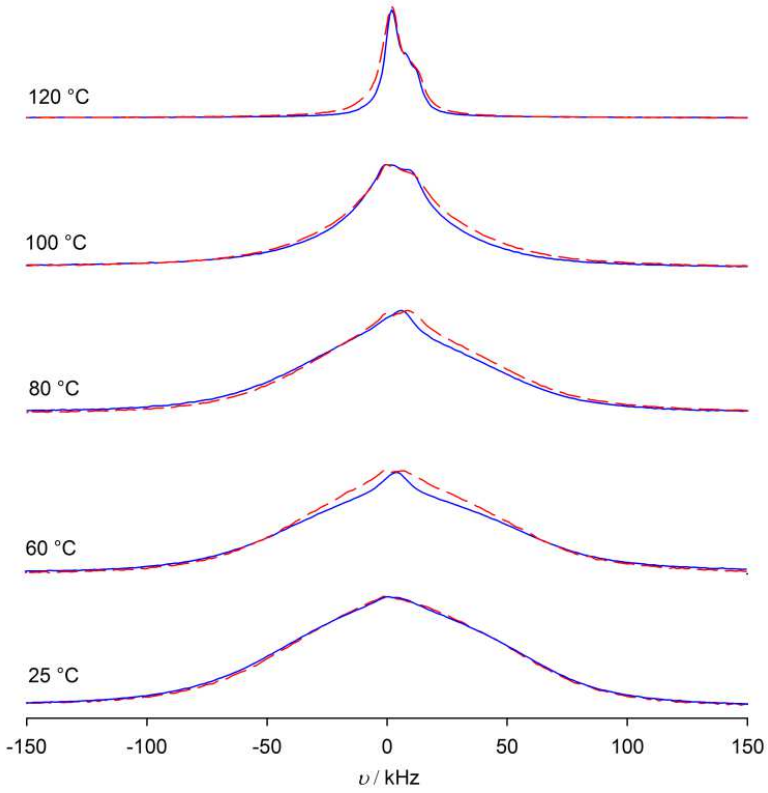

Figure 51. VT static ^{1}H NMR spectra of (A) AR (solid line) and (B) AM (dashed line) forms of valsartan. The sharpening of bandshapes is observed with the increase of temperature and is significant far above the glass transition temperatures (T_g^{AR} = 94 °C, $T_g^{Richardson(AR)}$ = 76 °C and T_g^{AM} = 74 °C) at 120 °C, where samples are in the liquid amorphous state.

To investigate the potential involvement of the C(5)O, C(10)OOH and N(5)H groups in the hydrogen bondings, ^{1}H MAS NMR studies were also performed using ultra-fast magic-angle spinning to reduce the line-broadening associated with the strong dipolar

interactions between ^{1}H spins. Five different resonances are clearly distinguishable in the ^{1}H spectrum of as-received valsartan at a spinning rate of 67 kHz, Figure 52, corresponding to alkyls (≈0.9 ppm), alkyls bonded with N-1 (≈5.6 ppm), aromatic (≈7.1 ppm), acidic (≈14.2 ppm) and tetrazole (≈16.4 ppm) protons. The signals arising from C-6 and C-11 in the AM form are less intense and are not resolved due to amorphisation and conformational changes. Furthermore, ^{1}H spectra of fully amorphous form show significant chemical shift displacement of tetrazole proton (N(5)H, $\Delta\delta_H$ = 1.1 ppm) suggesting involvement of tetrazole proton in hydrogen bonding. The acidic proton (C(10)OOH) is also broadened and moves to lower chemical shift but due to low resolution it was not possible to precisely estimate its chemical shift.

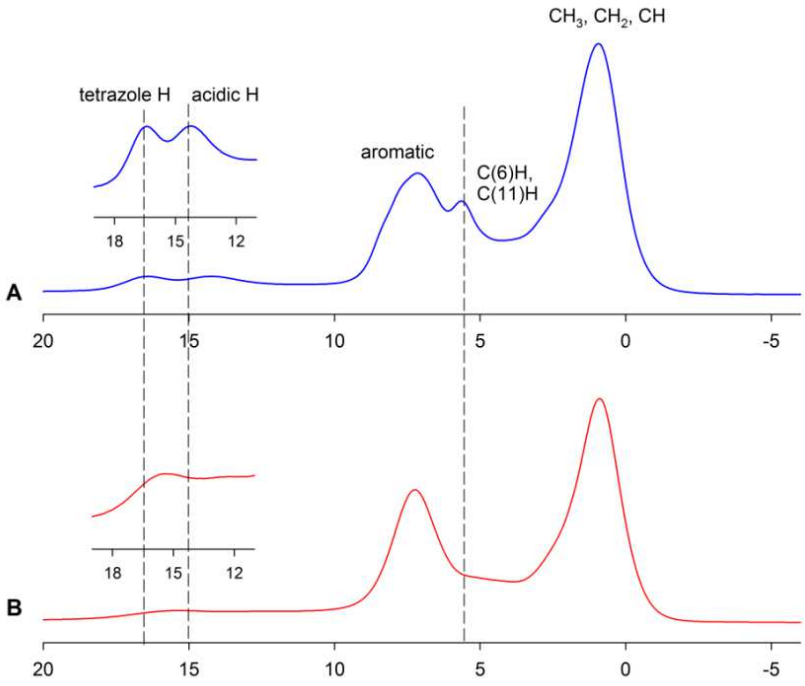

Figure 52. ^{1}H MAS NMR spectra of (A) as-received and (B) fully amorphous valsartan recorded at a MAS rate of 67 kHz.

5.3.1.5.3 Proton–carbon-13 heteronuclear correlation solid-state NMR

Additional information was obtained by heteronuclear correlation experiments. Using HETCOR experiments with short contact times, experiment gives 2D ^{1}H–^{13}C dipolar correlation maps with only correlations between carbon resonances and the protons to which they are most strongly dipolar coupled and if longer contact time is used, more correlations will appear resulting from longer range dipolar couplings and ^{1}H spin diffusion. The experiment with short contact time clearly showed cross-peaks from split C-6 in the AM valsartan form, Figure 53.

This splitting confirms ^{13}C experiment findings that AM form most likely exists as a mixture of *cis–trans* conformers. The experiment with long contact time did not reveal any new information about the systems.

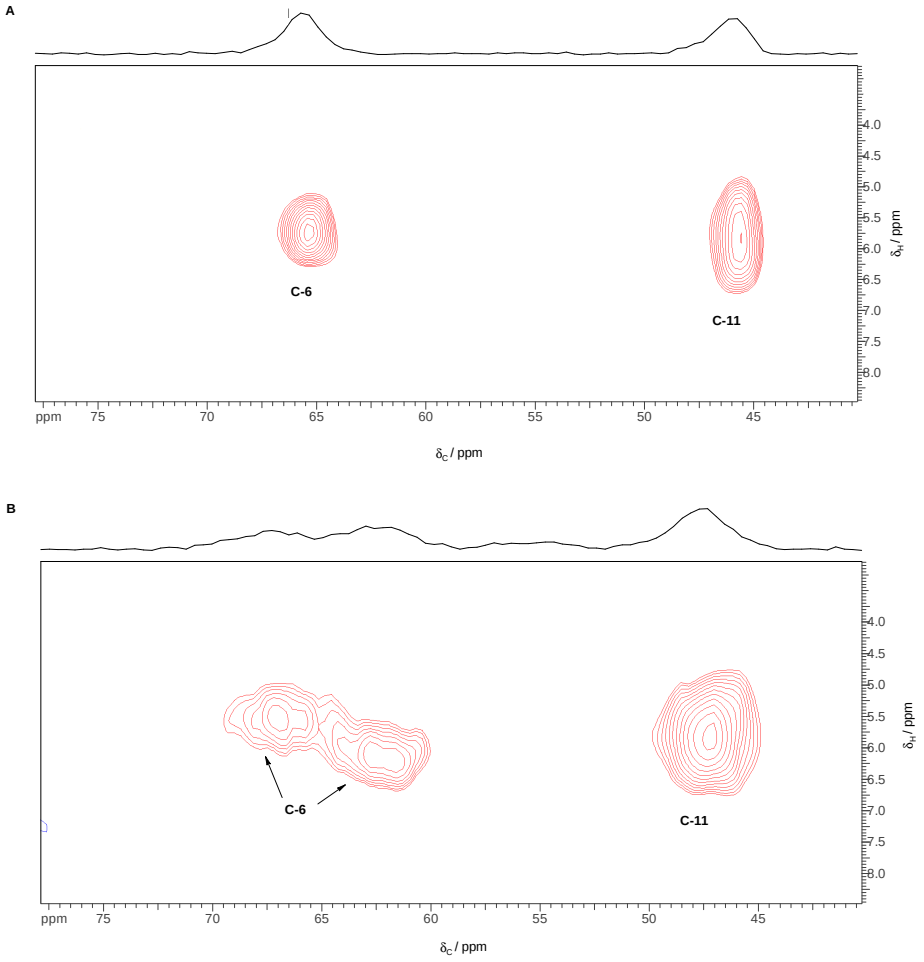

Figure 53. The 40–80 ppm region of ^{13}C–^{1}H HETCOR spectra of (A) as-received and (B) fully amorphous valsartan with 0.1 ms contact time showing directly bonded C-H links only. The fully amorphous form shows two split signals from C-6 suggesting valsartan existing as a mixture of *cis–trans* isomers.

5.3.1.5.4 Nitrogen-15 solid-state NMR

The ^{15}N CP MAS NMR was successfully employed to examine polymorphism of a closely related system irbesartan [27]. Valsartan in a solid state can theoretically exist in two tautomeric forms exhibited by tetrazole ring i.e. as 1,2,3,4-tetrazole or 1,2,3,5-tetrazole, Figure 54, similarly to that of irbesartan [27].

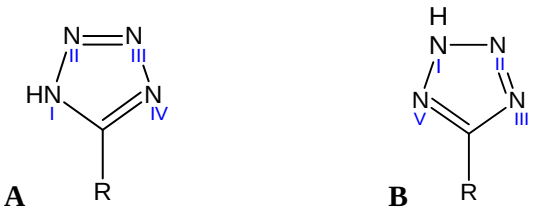

Figure 54. Possible tautomeric forms of valsartan: (A) 1,2,3,4- tautomeric form and (B) 1,2,3,5- tautomeric form.

Also, as previously mentioned, in a solution valsartan exists in two different conformations due to the hindered rotation of its amide bond [77, 78] and as suggested by ^{13}C CP MAS NMR results similar behaviour might be expected in the solid state in the AM form of valsartan. To investigate the possible tautomeric and conformational differences in valsartan forms, ^{15}N CP MAS NMR was employed.

Figure 55 shows ^{15}N CP MAS NMR spectra of both valsartan forms. As-received material gives 5 clear signals, as expected and weak signals at about –52, –160 and –255 ppm. The assignments are made by comparison with literature ^{15}N data for tetrazole-containing systems and computational prediction of chemical shifts for crystalline valsartan, Table IV and Figure 56. The signal at –247.3 ppm can be easily assigned to N-1. Assigning tetrazole peaks is not entirely trivial. To establish protonated nitrogen standard dipolar dephasing experiment was used, however, without success thus inversion-recovery (IR) CP MAS technique was then employed. IR CP MAS experiment confirmed that signal at –149.4 ppm arises from N-5, i.e. protonated nitrogen, Figure 55D. The signals at –13.2 and 10.3 ppm arise from N-4 and N-3, respectively. The signal at –71.2 ppm can be assigned to N-2. The assignment is in good agreement with irbesartan form A (except for N-2) and computational prediction of chemical shifts for crystalline valsartan, Table IV and Figure 56, and thus it can be concluded that valsartan in the solid state exists as a 1,2,3,4-tetrazole tautomer. The low intensity signal at –52 ppm was clearly observed on the spectrum at 80 °C and 110 °C (data not shown). The remaining low intensity signals at –160 and –255 ppm could not be resolved and also due to amorphous nature of material the experiments needed very long spectrometer time and thus it was not possible to obtain better signal-to-noise ratio spectra. The spectrum of AM valsartan shows general broadness of resonances and signal at –54 ppm is more intense and now can be clearly observed.

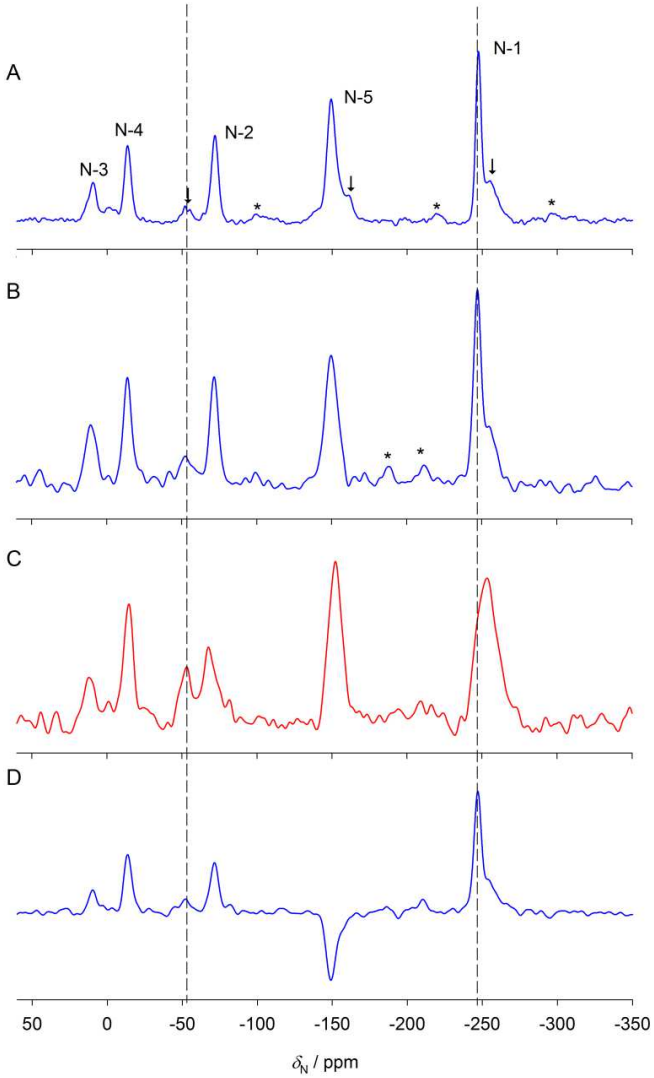

Figure 55. Nitrogen-15 CP MAS NMR spectra of AR VAL at (A) 6 kHz spinning rate (3 spectra added – 151 000 repetitions in total) (B) at 10 kHz spinning rate (30 000 repetitions in total), (C) AM VAL at 10 kHz spinning rate (40 000 repetitions) and (D) ^{15}N IR CPMAS NMR spectrum of AR VAL at 10 kHz spinning rate (2 spectra added – 331 000 repetitions in total). Arrows (↓) indicate signals arising most likely from other conformational isomer impurity in the AR form. All spectra recorded at room temperature. Asterisks (*) denote spinning sidebands.

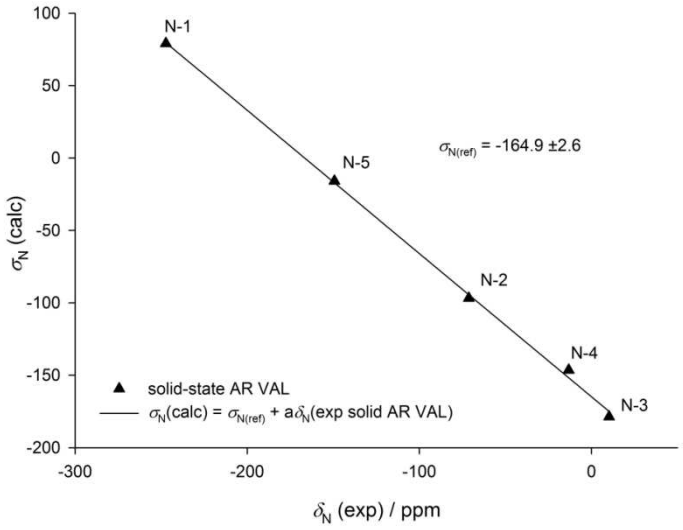

Figure 56. Plot of ^{15}N calculated chemical shielding crystalline valsartan vs. experimental chemical shifts for a main isomer of AR form for ^{15}N signal.

Table IV. Nitrogen-15 chemical shifts for valsartan and other related tetrazole systems.

Compound	State	δ_N / ppm					Ref.
		N-I[a]	N-II[a]	N-III[a]	N-IV[a]	N aliphatic	
Cis/trans isomers in AR valsartan[b] (1,2,3,4-tetrazole)	solid	–160.3, –149.4 (N-5)	–13.2 (N-4)	10.3 (N-3)	–51.7, –71.2 (N-2)	–254.9, –247.3 (N-1)	this work
Cis/trans isomers in AM valsartan[b] (1,2,3,4-tetrazole)	solid	–152.5 (N-5)	–15.2 (N-4)	11.5 (N-3)	–53.6, –67.8 (N-2)	–253.3 (N-1)	this work
Trans crystalline valsartan (calculated)[b,c] (1,2,3,4-tetrazole)	solid	–149.0 (N-5)	–18.4 (N-4)	13.8 (N-3)	–68.1 (N-2)	–244.1 (N-1)	this work
Irbesartan form A[d] (1,2,3,4-tetrazole)	solid	–143.4 (N-25)	–13.6 (N-26)	13.0 (N-27)	–54.2 (N-28)	–216.4 (N-1)	this work
5-phenyltetrazole (1,2,3,4-tetrazole)	solid	–153.2	–16.9	5.1	–78.0	-	[27]
Irbesartan form B[d] (1,2,3,5-tetrazole)	solid	–88.7 (N-26)	–3.2 (N-27)	–50.7 (N-28)	–79.3 (N-25)	–219.0 (N-1)[e]	[27]
1-methyl-1,2,3,5-tetrazole (1,2,3,5-tetrazole)	solution	–101.8	–0.8	–46.8	–72.8	-	[232]

[a] The nitrogen atom labelling used is the 1,2,3,4-tetrazole convention.
[b] The nitrogen atom labelling used is as in Ref. [26].
[c] $\delta_{iso} = -(\sigma_{iso}-\sigma_{ref})$, where σ_{ref} = –164.9 ppm.
[d] The nitrogen atom labelling used is as in Ref. [27].
[e] Originally chemical shift was reported with respect to nitrate resonance of solid external ammonium nitrate but here are reported relative to the signal of nitromethane to achieve consistency with other data.

5.3.1.6 Molecular mobility

By employing NMR it is possible to provide microscopic information about molecular mobility [59, 200, 214]. The differences in molecular mobility between fully amorphous and as-received valsartan were demonstrated based on different NMR relaxation times. Spin–lattice relaxation time (T_1) and spin–lattice relaxation time in the rotating frame ($T_{1\rho}$) were investigated by

^{1}H static SSNMR and ^{13}C CP MAS NMR in the temperature below and above the glass transition.

5.3.1.6.1 Spin–lattice relaxation time

Figure 57 shows the T_1^H as a function of temperature obtained for examined valsartan forms. The T_1 relaxation time is sensitive to motion processes of the order of 100–500 MHz [200]. The T_1^H measurements show a monotonic increase in the T_1 values with increasing temperature for both forms. The values of T_1^H at room temperature are significantly different for both forms i.e. $T_1^{H(AR)}$ = 0.99 ±0.02 ms (n = 2) and $T_1^{H(AM)}$ = 1.49 ±0.04 ms (n = 2). There is no sharp change in the T_1^H around the glass transition region, this suggests that rapid motions (e.g. methyl rotation) not change drastically when going by T_g [233]. The activation energy calculated from T_1^H plot was found to be significantly different i.e.: 7.4 for AR form and 3.7 kJ mol^{-1} for AM form.

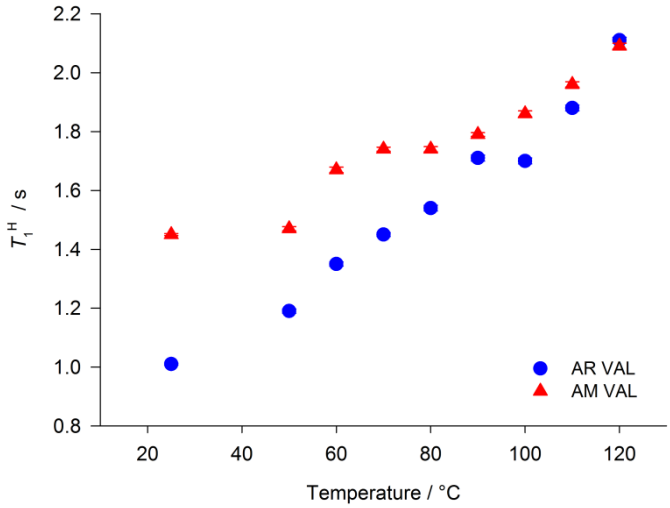

Figure 57. Static proton (A) T_1 for AR and AM valsartan forms.

These findings were confirmed by ^{13}C T_1 relaxation times, Figure 58. One of the basic advantages measurements of T_1^C versus T_1^H measurement is that the relaxation time of individual carbons can be measured and therefore may provide specific information with respect to the local motion (i.e. CH_3, CH_2, ring rotation etc.). In most cases the ^{13}C resonances intensity in this study can be fit to single exponential function to extract T_1^C values with the exception of the aliphatic carbons at 27.5 ppm which can be fitted to bi-exponential function. This bi-exponential behaviour most likely arises from the strong overlapping of the peaks in this region of the spectrum. The values of relaxation times for carbons at 14.0 ppm (C-1), 19.6 ppm and 22.6 ppm aliphatic carbons were about 1 s, for 22.9 ppm about 2 s and for aromatic carbons 40 and 48 s, the T_1^C for C-5, C-10, C-24 carbons were longer than 80 s and therefore too long to

measure. As in this case a longer T_1^C indicates slower molecular mobility of molecules in SSNMR the mobility of the phenyl rings, tetrazole ring and C-10, C-5 in carbonyl groups could be described as a slow rotation. In contrast the relaxation behaviour of signals for aliphatic carbons which are due to the side chain aliphatic carbons could be described as fast rotation. Most of the T_1^C values for aliphatic carbons of both valsartan forms are similar and within the measurement error, Table A I of appendices. The activation energies for both forms are identical within the measurement uncertainty, Figure 59. For example E_a for methyl carbon (C-1) was calculated to be 12.5 ±1.1 and 12.1 ±1.0 kJ mol^{-1} for AR and AM valsartan, respectively. Similarly aliphatic carbon at 19.6 ppm has E_a = 7.8 ±0.7 and 7.8 ±1.2 kJ mol^{-1} for AR and AM form, respectively. Slight difference was found for aliphatic carbon at 22.6 ppm E_a = 10.1 ±1.0 (AR form) and 7.4 ±1.1 kJ mol^{-1} (AM form) which is not fully understood. The behaviour of aromatic carbons is different than the aliphatic ones, Figure 58. The aliphatic carbons show a linear decrease of T_1^C values and do not show any significant change around the glass transition temperatures whereas aromatic carbons show sharp jump around the glass transition at around 80 °C suggesting that the increase in mobility above the glass transition is mainly due to change of aromatic rings mobility, Figure 58. The change around 80 °C suggest that NMR “can see” the fictive temperature for amorphous structure with high enthalpy relaxation peak as the change in the T_1 relaxation times seen is closer to the fictive glass transition temperature (76 °C) rather than the glass transition obtained by standard method (94 °C) for the AR form.

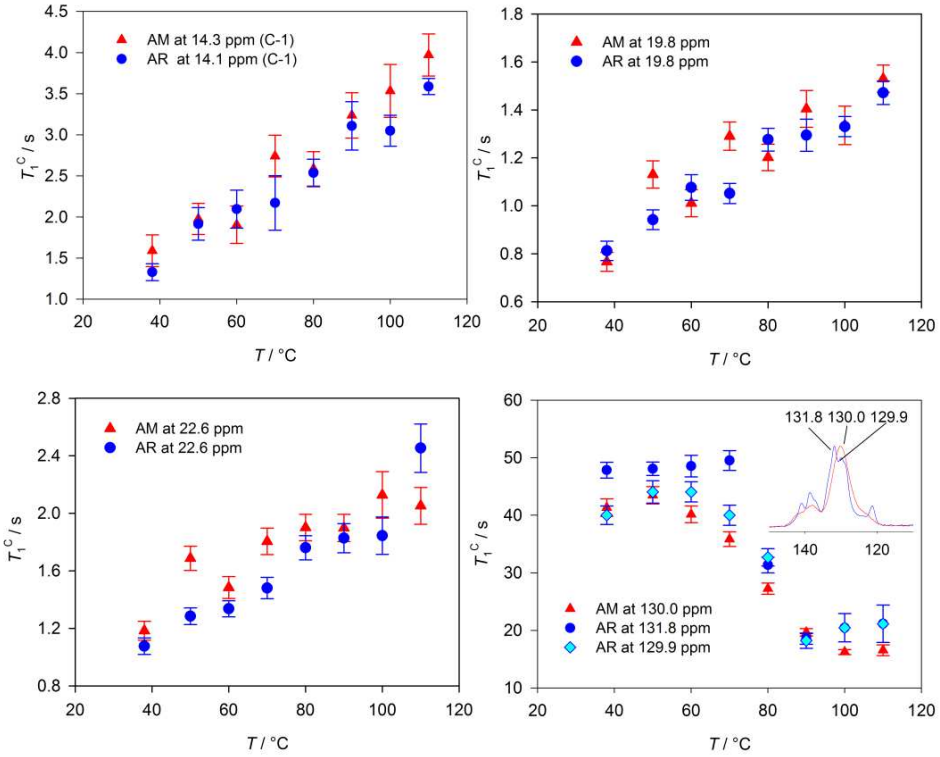

Figure 58. Examples of ^{13}C T_1 relaxation behaviour of AR and AM valsartan forms. Aliphatic carbons do not show any significant change around glass transition temperatures (T_g^{AR} = 94 °C, $T_g^{Richardson(AR)}$ = 76 °C and T_g^{AM} = 74 °C) whereas aromatic carbons show sharp jump around glass transition around 80 °C suggesting that the increase in mobility above the glass transition is mainly due to change of the aromatic rings mobility.

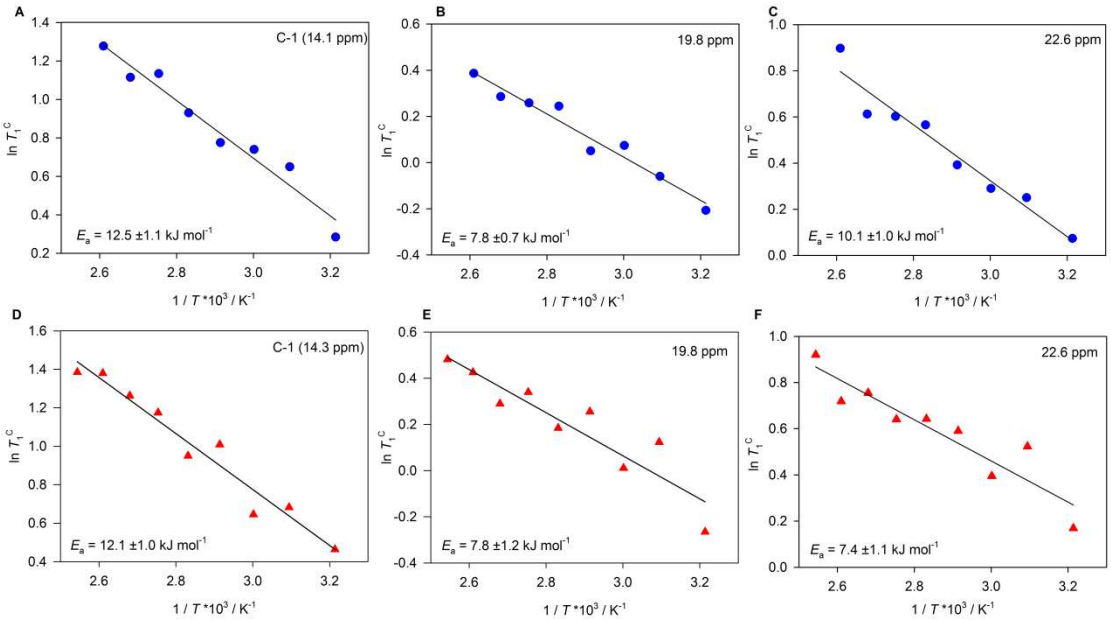

Figure 59. Selected T_1^C data as a function of reciprocal temperature for (A-C) as-received and (D-E) fully amorphous valsartan form and corresponding activation energies.

5.3.1.6.2 Spin–lattice relaxation time in the rotating frame

The $T_{1\rho}$ relaxation time is sensitive to the intermolecular interaction and may distinguish phase structures with different degree of order or crystallinity. The $T_{1\rho}$ relaxation time reveals motion processes of the order 20–100 kHz [200]. $T_{1\rho}{}^{H}$ was measured above and below glass transition temperature. Figure 60 shows the $T_{1\rho}{}^{H}$ as a function of temperature obtained for two forms of valsartan. As expected, $T_{1\rho}{}^{H}$ values below the glass transitions for as-received material are higher than for totally amorphous valsartan. The difference at ambient temperature is relatively low i.e. $T_{1\rho}{}^{H(AR)}$ = 15.2 ±0.3 (n = 2) and $T_{1\rho}{}^{H(AM)}$ = 11.7 ±0.1 ms (n = 2); previous study of small API relaxation times has shown higher differences in $T_{1\rho}$ between solid states i.e. in order of tens to hundreds ms [214], however the study compared crystalline versus amorphous form. The low difference suggests very similar molecular mobility of both forms and the results demonstrate that amorphisation makes valsartan more mobile after heating and suggests the disordered state, which is attributed to poor molecule packing resulting from the co-existence of multiple orientations. In the case of $T_1{}^{H}$ values there was no significant change around glass transition temperature, it can be seen that above T_g there is marked decrease in $T_{1\rho}{}^{H}$ values. As expected values above T_g in the liquid amorphous state for both materials are similar. Since the proton diffusion in solids is facilitated through the intermolecular interactions which is largely dependent upon the proximity of neighbouring hydrogen atoms and the local intermolecular interaction, decrease of $T_{1\rho}{}^{H}$ indicate reduction in short-range order [59, 214]. The findings indicate high sensitivity of $T_{1\rho}{}^{H}$ towards the short-range order in a solid state.

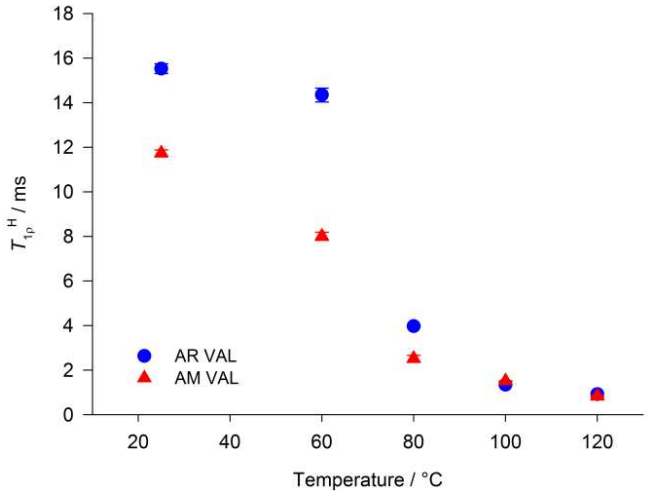

Figure 60. Static proton $T_{1\rho}{}^{H}$ data for AR and AM valsartan forms.

Also spin–lattice relaxation in the rotating frame on the specific carbon (^{13}C $T_{1\rho}{}^{H}$) were measured, Figure 61. The ^{13}C $T_{1\rho}{}^{H}$ relaxation showed mono-exponential behaviour. There is

a decrease in ^{13}C $T_{1\rho}{}^{H}$ values with increasing temperature in both forms; comparison of relaxation times does not clearly show significant differences in molecular mobility for both forms within analysed range of temperature. In opposite to the T_1 relaxation times, it is seen no significant difference between aliphatic and aromatic $T_{1\rho}{}^{H}$ relaxation times as the $T_{1\rho}$ is more sensitive to the overall molecular motion.

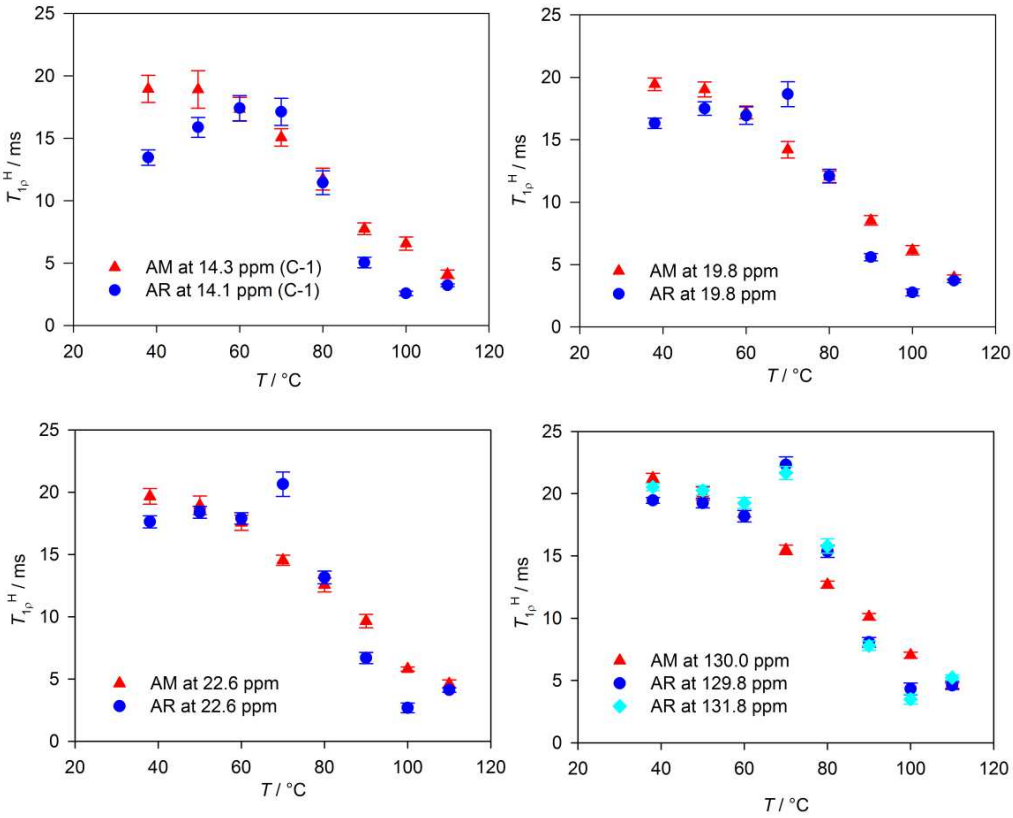

Figure 61. Selected plots of $T_{1\rho}{}^{H}$ measured via CP onto ^{13}C as a function of temperature for as-received and fully amorphous valsartan forms.

5.3.1.7 Molecular mobility in the annealed fully amorphous valsartan

5.3.1.7.1 Temperature-modulated differential scanning calorimetry

To investigate the impact of annealing at different temperatures below the glass transition on the glass transition temperature and enthalpy relaxation fully amorphous form (AM) was annealed at 30, 40, 50 and 60 °C for different length of time from 0 to 16 h and characterised by TMDSC. Figure 62 shows the total, reversing and non-reversing heat-flow rate obtained from TMDSC as a function of temperature for AM amorphous valsartan annealed at 50 °C for different lengths of time from 0 to 16 h. The enthalpy recovery peaks, Figure 62C, shown on non-reversing curve, increase and shift to higher temperatures as ageing time increases. Note that enthalpy relaxation peak can be observed in unannealed (no isothermal

ageing) sample which is due to annealing during cooling and heating DSC scans. On the reversing curve only glass transition is observed as ageing time increases the T_g moves towards higher temperature. The enthalpy relaxation and glass transition depends on the length of annealing time. For example the glass transition temperatures change from 76.7 to 77.3 °C, onset of enthalpy relaxation peak from 67.4 to 70.4 °C and ΔH from 2.8 to 7.4 J g^{-1} without and after 16 h of annealing for sample annealed at 50 °C. For comparison: the glass transition of AR valsartan sample was around 94 °C, onset of enthalpy relaxation peak 92 °C with ΔH = 26 J g^{-1}. The effect of annealing can be strongly observed for samples annealed at above 40 °C and is relatively low for sample annealed at 30 °C, Figure 63. As mentioned previously the location of the glass transition temperature is a function of the experimental cooling rate and of the thermal history of the glassy material [128]. Thus values reported for valsartan determined by standard DSC and TMDSC varies.

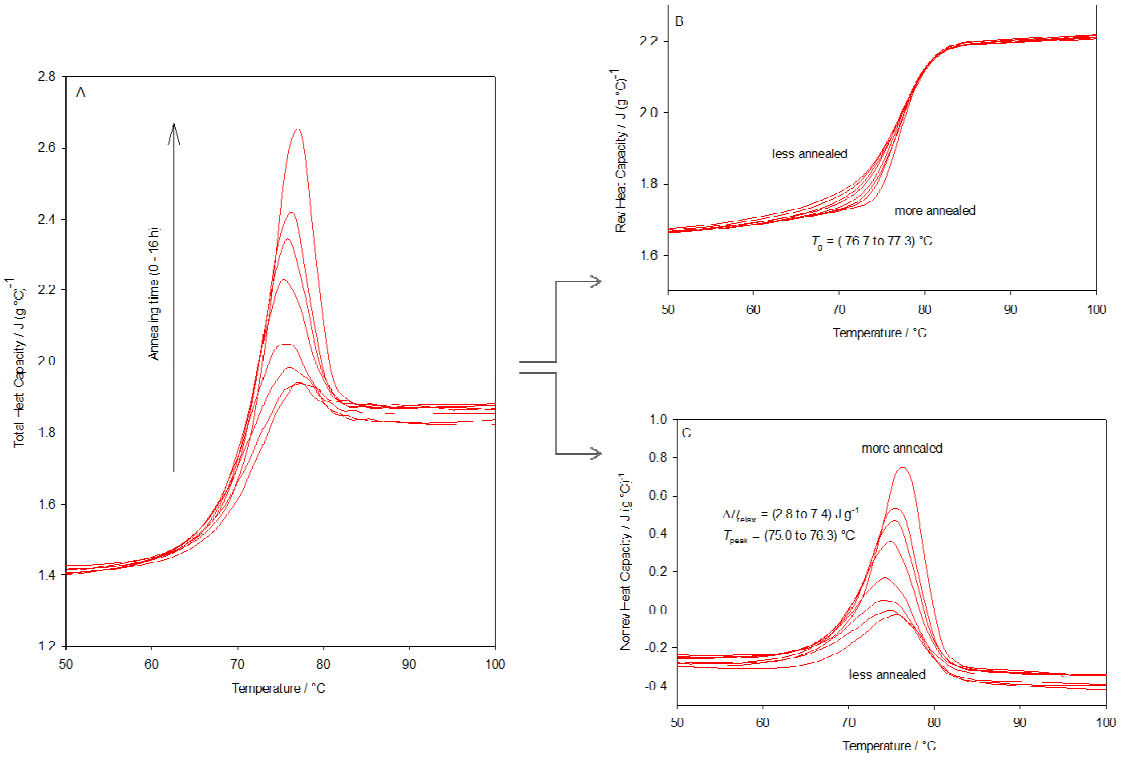

Figure 62. (A) Change of total, (B) reversing and (C) non-reversing heat capacity of AM valsartan annealed at 50 °C for different length of time from 0 to 16 h.

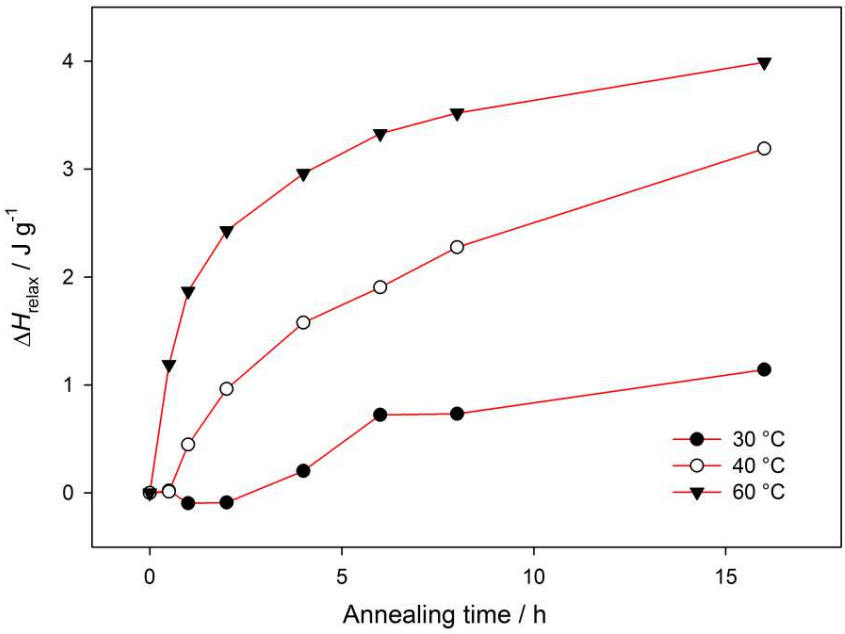

Figure 63. An enthalpy lost with time on structural relaxation of AM valsartan form annealed at 30, 40 and 60 °C. The value of enthalpy relaxation at T_a = 0 h was subtracted from values of enthalpies of annealed samples to exclude effect of thermal history during cooling/heating run. The relative standard deviations of enthalpy measurements were less than 10%.

5.3.1.7.2 The effect of annealing on the NMR relaxation times

To investigate the molecular mobility changes during annealing of fully amorphous form, T_1^H and $T_{1\rho}^H$ NMR relaxation times were measured, Table V. Duplicate measurements for T_1^H relaxation time in two different samples of unannealed AM form give following values 1.53 ±0.007 and ±1.45 ±0.003 s, where uncertainties listed are the standard errors in the parameters as determined from nonlinear regression analysis. Because of the spectrometer time needed for analyses, the replicates runs were not obtained for all the samples. The sample was annealed at 60 °C, i.e. around 14 °C below T_g, as determined by standard DSC. The T_1^H changed from 1.53 ±0.007 s to 1.25 ±0.014 s after 19 h of annealing, where the T_1^H for AR form was 0.97 ±0.004 s. These results suggest that annealing below T_g significantly reduces overall molecular mobility of amorphous material.

The $T_{1\rho}^H$ relaxation time in two different samples of unannealed AM form are as follow 11.64 ±0.11 and 11.74 ±0.14 ms. The $T_{1\rho}^H$ changed from 11.64 ±0.11 to 12.26 ±0.18 ms after 19 h of annealing in comparison the $T_{1\rho}^H$ for AR form was 14.86 ±0.21 ms. The behaviour of $T_{1\rho}^H$ suggests that annealing reduces molecular mobility on 20–100 kHz time scales as well.

Also the T_1^C relaxation times were measured for annealed material, however the results were within the error measurements and it was not possible to observe significant differences in the analysed materials.

Table V. Impact of annealing time on T_1^H and $T_{1\rho}^H$ relaxation times for fully amorphous valsartan form (AM form) annealed at 60 °C and recorded at 25 °C. The relaxation times for AR form are shown for comparison.

Annealing time / h	Relaxation time	T_1^H / s		$T_{1\rho}^H$ / ms	
	Form	AR	AM	AR	AM
0		0.97 ±0.004	1.53 ±0.007	14.86 ±0.21	11.64 ±0.11
1		N/A	1.28 ±0.027	N/A	11.69 ±0.16
3		N/A	1.33 ±0.009	N/A	11.48 ±0.13
19		N/A	1.25 ±0.014	N/A	12.26 ±0.18

5.3.1.8 Intrinsic and apparent dissolution rate measurements

The dissolution rate is a key parameter considered during preformulation drug development stage. As the API has to be dissolved before it can be absorbed, the dissolution profile can have an impact on both pharmacokinetic and pharmacodynamic parameters [234]. To understand how the subtle differences in amorphous state can affect the dissolution behaviour intrinsic dissolution and apparent dissolution tests were carried out. Intrinsic dissolution profiles for AR and AM valsartan in deionised water are shown in Figure 64A. IDR was calculated from slope of each curve for time period of 0–120 min. AR valsartan showed IDR value of 24.6 ±0.1 μg min^{-1} cm^{-2}. AM sample showed IDR value of 11.0 ±0.1 μg min^{-1} cm^{-2}, which was about twofold lower than the AR valsartan sample. Apparent dissolution tests from powdered drug in deionised water were also performed, Figure 64B. Results confirmed that the dissolution profiles are significantly different for examined amorphous solid states of valsartan. It is widely known that amorphous material has a higher free energy and usually presents a greater solubility and dissolution rate than its corresponding crystalline form [4-6]. Surprisingly, in these studies it was observed that less ordered, fully amorphous material (AM form) has lower dissolution rate than amorphous form with higher structure arrangement.

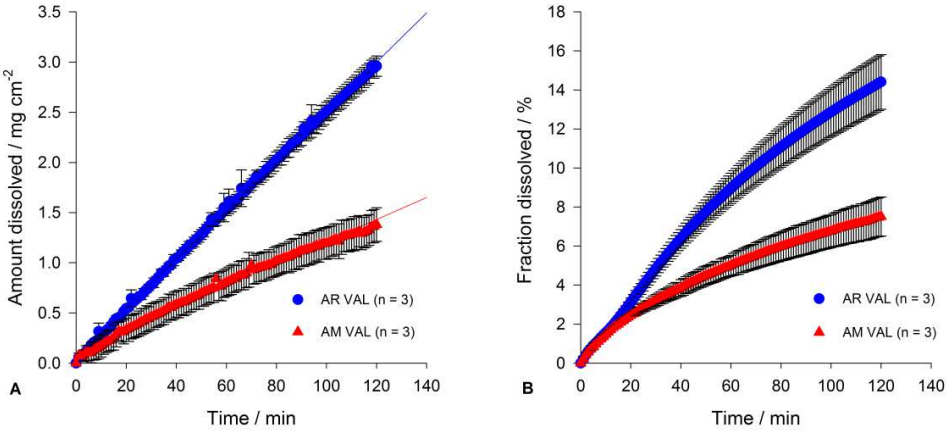

Figure 64. (A) Intrinsic and (B) apparent dissolution profiles of valsartan in different solid state forms in deionized water.

5.3.2 Valsartan and bisoprolol compatibility studies

5.3.2.1 Thermal analysis

Figure 65 shows the standard DSC traces of crystalline bisoprolol with 10 °C min^{-1} heating rate, cooling the sample to –50 °C at 10 °C min^{-1} and a second heating. On the first heating, the DSC curve shows one sharp endothermic peak with an onset at 102.3 ±0.3 °C and an enthalpy of fusion ΔH_{BISO} = 110 ±2 J g^{-1} due to melting. Three events are observed on the second run: a glass transition at –3.6 ±0.9 °C with a change of heat capacity (ΔC_p) of 0.51 ±0.02 J g^{-1} K^{-1}, followed by a cold crystallization exotherm at 24.2 ±0.6 °C (ΔH = 80 ±2 J g^{-1}) and a melting peak with onset at 95.4 ±1.4 °C (ΔH = 85 ±1 J g^{-1}). The lower values of the melting temperature and heat of fusion in the second heating may be due to differences in morphology in the re-crystallized phase of sample compared to the original crystalline material. There may be nanocrystalline domains present in the re-crystallized sample, which can lower the peak of melting, and/or the re-crystallization of the amorphous material may be incomplete. Both starting and re-crystallized material showed birefringence under polarized light microscopy, confirming their crystalline nature Figure 66A and E.

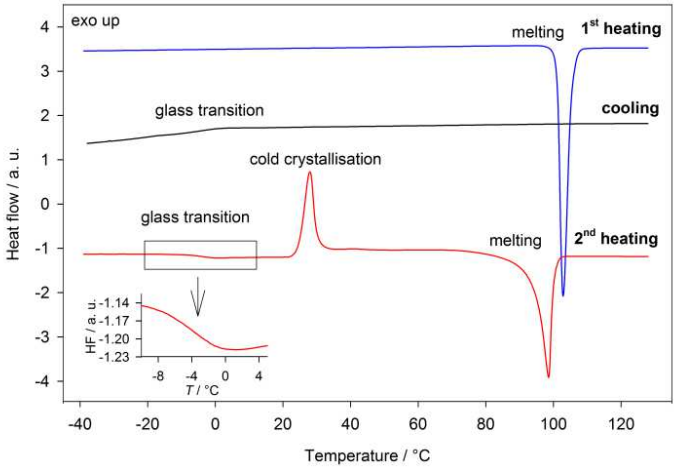

Figure 65. Standard DSC curves of crystalline bisoprolol showing 1st heating, cooling (glass transition of amorphised material) and 2nd heating (glass transition, cold crystallization, melting of re-crystallized material). All runs obtained at a 10 °C min^{-1} heating rate.

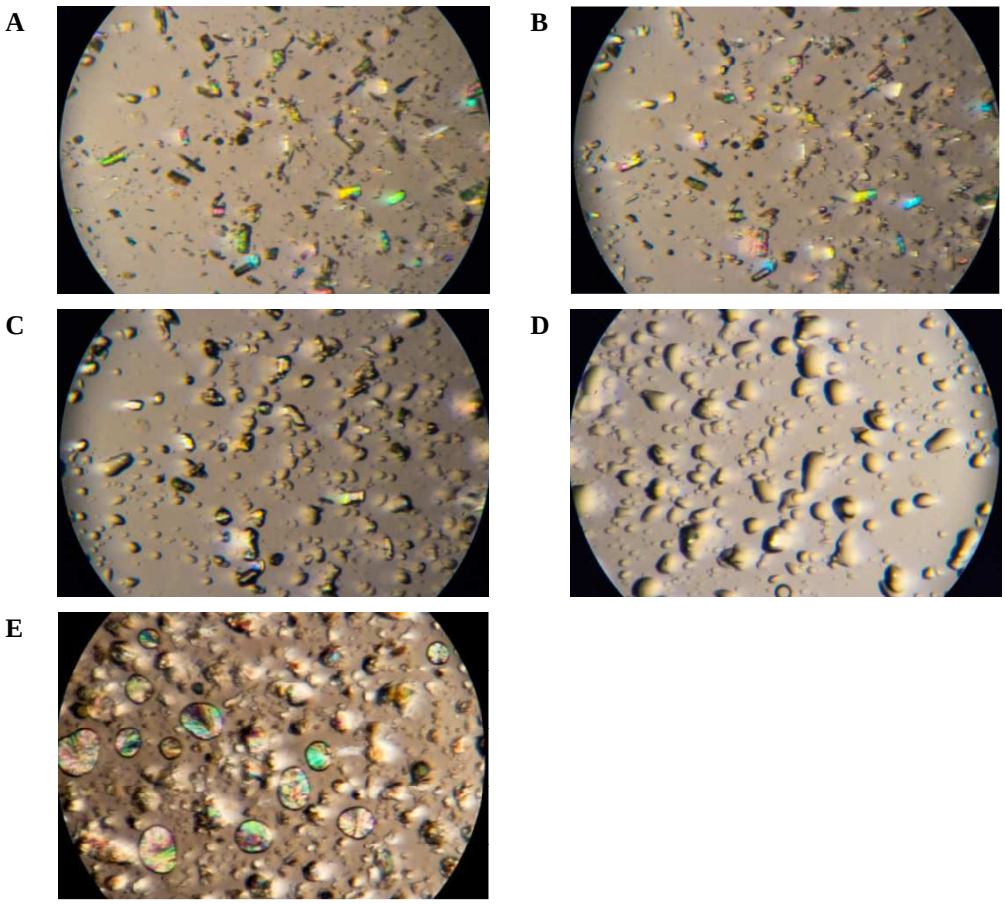

Figure 66. Polarized light photomicrographs of bisoprolol, at (A) 30 °C, showing birefringence indicating crystalline nature of the as-received material, (B) and (C) showing melting transition at, 100 and 101 °C, respectively, (D) fully melted material at 103 °C, and (E) material after cooling in the re-crystallized state, recorded at 30 °C. Re-crystallized material shows different crystal habit (spherulites). Sample was heated with 5 °C min^{-1} rate.

TGA curves, Figure 67, of the individual components and a 50/50 (w/w) bisoprolol/valsartan (AR form) physical mixture show that the ingredients change individually in the mixture, indicating that no degradation due to interaction of the components takes place.

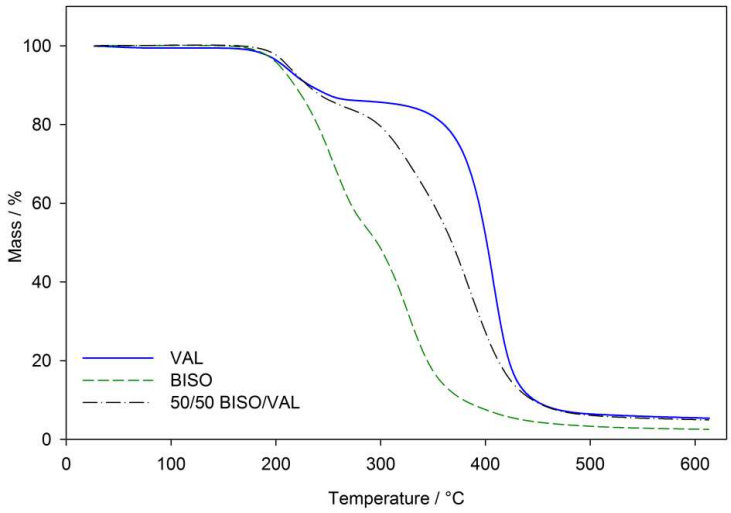

Figure 67. TGA curves for valsartan (AR form), crystalline bisoprolol and 50/50 (w/w) physical mixture of bisoprolol/valsartan (AR form), showing no evidence of mass loss before the degradation points of the individual components.

However, the DSC curve of the same physical mixture, Figure 68, does not show the expected sharp bisoprolol melting peak and instead shows overlapped broad endothermic peaks at around 60–100 °C, indicating some physical or chemical interaction has disrupted the crystal lattice of bisoprolol. The total enthalpy of this peak is estimated to be 51 ±5 J g^{-1}, which is lower than the weighted sum of the enthalpies of the individual components, $(\Delta H_{BISO} + \Delta H_{VAL})/2 \approx 68$ J g^{-1}, suggesting interaction. Two minima at about 77 and 100 °C are observed. The peak with minimum at around 100 °C can be ascribed to the enthalpy relaxation peak of valsartan (form AR). This is confirmed by the DSC trace of a physical mixture made with freshly prepared amorphous valsartan (form AM), which shows only the broad peak with one minimum at 77 °C, confirming that the peak at 100 °C arises from valsartan (form AR). The interaction observed by DSC is also seen in a simple micro- and macroscopic observation; powder samples mixed and heated on the hot-stage to about 60 °C convert into a more viscous state, and the material becomes sticky.

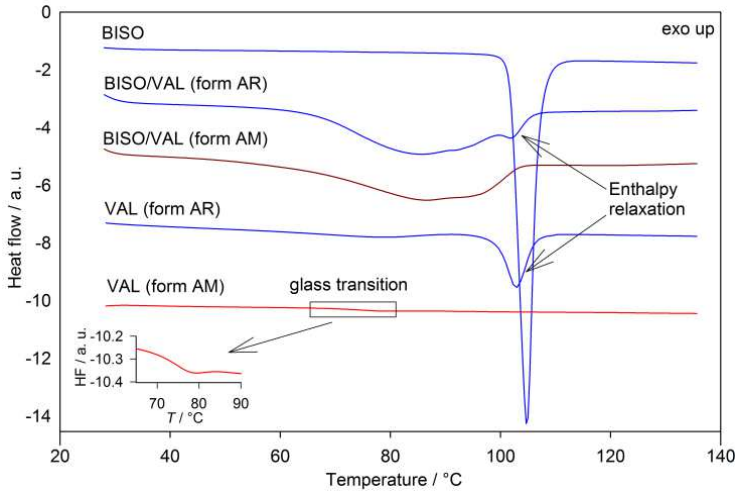

Figure 68. Standard DSC curves of the APIs and their 50/50 physical mixtures. The broad endothermic peak in the mixture indicates a significant physical or chemical interaction. All runs obtained at a 10 °C min^{-1} heating rate.

TMDSC was employed to separate the kinetic and thermodynamic processes during heating for a selected number of samples. Figure 69A shows the reversing and non-reversing heat-flow rates obtained from TMDSC as a function of temperature for the pure components and physical mixtures in 80/20, 50/50 and 20/80 (w/w) ratios. TMDSC separates the relaxation enthalpy of valsartan, observed in the non-reversing signal, from the change in heat capacity at glass transition observed in the reversing signal. The non-reversing curves for the 20/80 and 50/50 physical mixtures (solid lines) clearly show the enthalpy relaxation peak ascribed to valsartan (form AR) and a broad endotherm most probably due to physical or chemical change of bisoprolol fumarate. The enthalpy relaxation in the mixtures is difficult to estimate precisely due to peak overlap, but the values are approximately 70% and 50% lower than expected ($\Delta H_{50\%VAL}$ ~4 J g^{-1} compared to 50% ΔH_{VAL} = 13 J g^{-1}, and $\Delta H_{80\%VAL}$ ~11 J g^{-1} compared to 80% ΔH_{VAL} = 21 J g^{-1}). It was not possible to estimate the value of enthalpy relaxation for the 80/20 mixture. The reversing curves of the physical mixtures, dashed lines in Figure 69A, show only one event i.e. the glass transition. It is clear that there is a change in the glass transition temperature of valsartan in the 50/50 and 80/20 physical mixtures, and in its heat capacity in all mixtures.

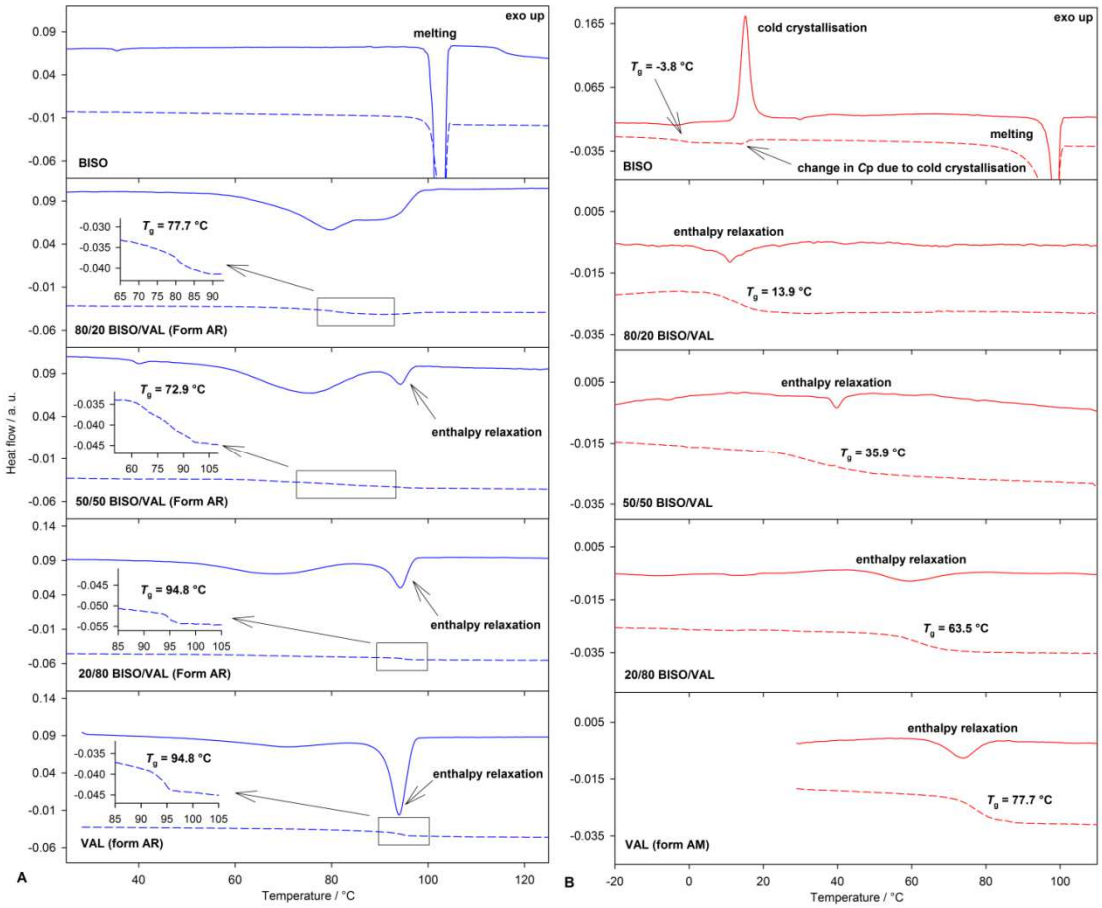

Figure 69. (A) 1st and (B) 2nd heating TMDSC experiments. Reversing (dashed line) signals show changes in glass transition and heat capacities. Non-reversing (solid line) signals show changes due to bisoprolol-valsartan interaction and enthalpy relaxation of valsartan (form AR), cold crystallization of bisoprolol, enthalpy relaxation of co-amorphous mixtures and valsartan (form AM).

Standard DSC experiments performed for twelve physical mixtures from 0 to 100% of bisoprolol show the same behaviour, Figure 70, as observed in TMDSC on the selected samples. In the physical mixtures with 90% bisoprolol by weight, the melting peak is broadened but can still be observed, while the melting peak was not identified with 80% or less bisoprolol in the mixture. The interaction was also observed under polarized light hot-stage microscopy, Figure 71.

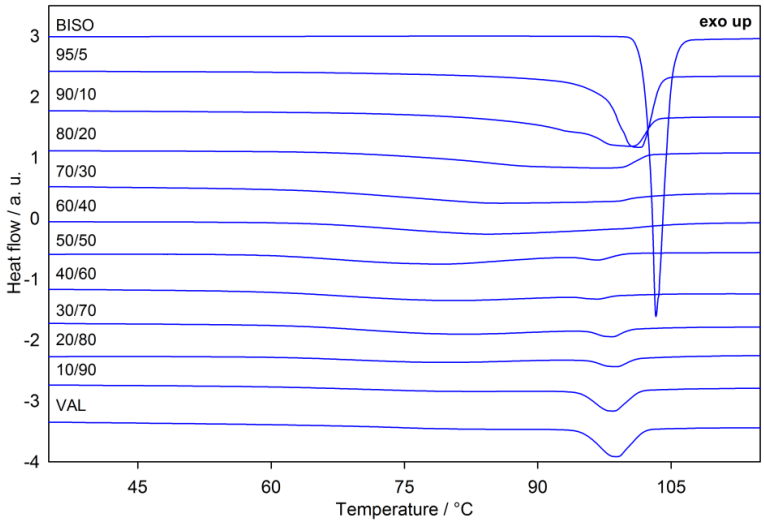

Figure 70. Standard DSC curves obtained at a 5 °C min^{-1} heating rate for APIs and their physical mixtures in a various weight ratios.

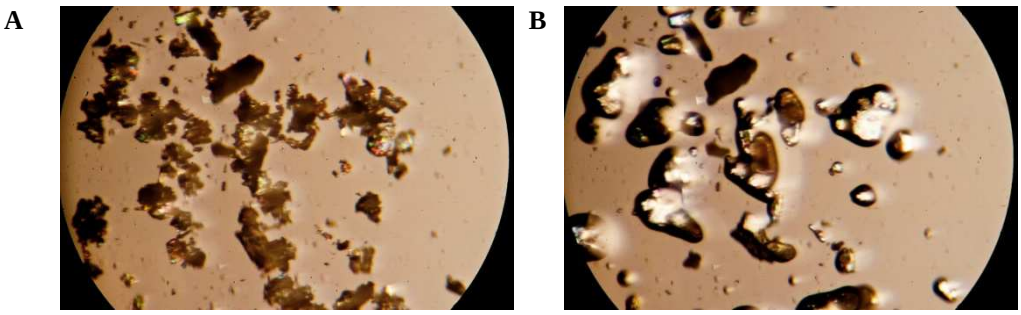

Figure 71. Polarized light photomicrographs of bisoprolol/valsartan 50/50 physical mixture at (A) 30 °C and (B) 85 °C showing interaction. Sample was heated with 5 °C min^{-1} rate.

In the second heating of the physical mixtures, both components are amorphous. The TMDSC reversing curves of quench-cooled bisoprolol, Figure 69B, show two thermodynamic processes: the glass transition and melting. As expected, the kinetically hindered cold crystallization process appears on the non-reversing curve. Neither melting nor cold crystallization is observed for co-melted 50/50 physical mixture; only a glass transition is observed. Compounds that are not miscible would show two separate glass transitions, one for each compound, while the co-melted bisoprolol/valsartan mixture only shows a single broad glass transition (T_g = 35.9 °C) at a temperature intermediate between the T_g of pure drugs, with the temperature depending on the composition. These findings suggest that valsartan and bisoprolol had dissolved each other to form a homogenous amorphous mixture [235]. Bisoprolol effectively lowers the T_g of valsartan thus affecting its stability.

5.3.2.2 NMR, Fourier transform infra-red and X-ray powder diffraction analyses

While DSC provides macroscopic information about the interaction between bisoprolol and valsartan, NMR and XRPD were used to probe the molecular basis for this behaviour.

Figure 72 shows the ^{13}C solution-state spectrum of bisoprolol and ^{13}C CP MAS NMR spectra of crystalline and quench-cooled (amorphous) bisoprolol. Due to the instability of the amorphous form at room temperature, spectra for both solid forms were acquired at –20 °C i.e. below the glass transition temperature. Standard NMR techniques (COSY, HSQC and HMBC; appendices: Figure A 4, Figure A 5 and Figure A 6) were used to assign the solution-state spectrum. The solid-state spectrum was assigned using solution-state NMR data and spectral editing techniques: interrupted decoupling (dipolar dephasing) and depolarization experiments (inversion times from 25 to 100 μs), Figure 73. The resulting assignments are presented in Table VI. The assignment of the solid-state spectra contains ambiguities due to its lower resolution and the differences in chemical shifts between the solution and solid state. Some of these ambiguities could, in principle, be resolved by computational prediction of chemical shifts given a crystal structure [227], but it was not possible to obtain diffraction quality crystal. Only one signal is observed for each site of bisoprolol and the two chemically distinct sites of the fumarate ion, indicating that the asymmetric unit cell contains a single bisoprolol molecule and a half molecule of fumarate. The spectrum of the crystalline material shows set of low intensity signals, denoted by arrows in Figure 72. Since there is no evidence from solution-state NMR of corresponding levels of chemical impurities, these signals could potentially arise from a second polymorphic form, or, more probably, enantiomeric “defects” (e.g. a *R*-molecule occupying a site otherwise occupied by *S* molecules). The low level of these signals (corresponding to about 1% of material) prevents further characterisation. The spectrum of the quench-cooled form exhibits the expected general broadness of the resonances due to the range of local environments. These spectra vary slightly from experiment to experiment, presumably reflecting differences in cooling rates used to obtain the amorphous form.

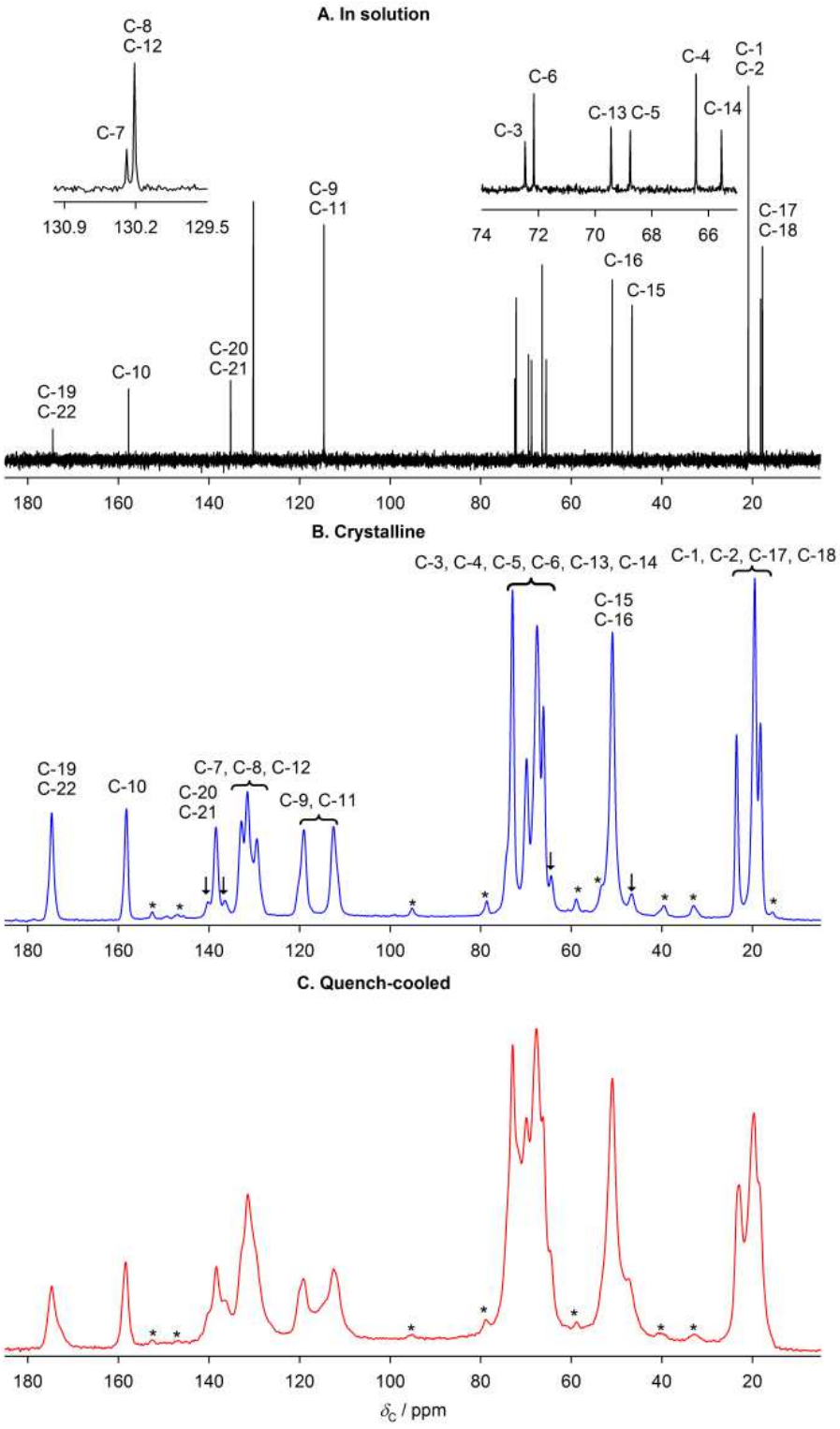

Figure 72. (A) ^{13}C solution-state NMR spectrum of bisoprolol in D_2O at 25 °C, ^{13}C CPMAS NMR spectra of (B) crystalline and (C) quench-cooled (amorphous) bisoprolol at –20 °C. Asterisks (*) denote spinning sidebands. Arrows (↓) denote signals that are thought to arise from polymorphic or enantiomeric impurities.

Table VI. Solution- and solid-state NMR chemical shifts for bisoprolol and 50/50 (w/w) bisoprolol/valsartan physical mixture at 25 °C (solution-state) and 38 °C (solid-state).

Carbon No	Bisoprolol					Bisoprolol/valsartan (after heating to 80 °C)	
	^{1}H solution-state NMR / ppm (D_2O)	^{1}H solution-state NMR / ppm ([D_6]-DMSO)	^{13}C solution-state NMR / ppm (D_2O)	^{13}C solution-state NMR / ppm ([D_6]-DMSO)	^{13}C CPMAS NMR / ppm (crystalline)	^{1}H solution-state NMR / ppm ([D_6]-DMSO)	^{13}C solution-state NMR / ppm ([D_6]-DMSO)
17, 18	1.22 (dd, 12H)	1.12 (dd, 12H)	17.79, 18.21	20.48, 20.82	18.4, 19.9, 20.6, 23.3	1.21	18.61, 18.62, 19.19, 19.21[a]
1, 2	1.03 (d, 12H)	1.06 (d, 12H)	20.93	22.49		1.06	22.48
15	3.10, 3.18 (2dd, 4H)	2.77, 2.92 (2dd, 4H)	46.63	48.65	51.2	2.93, 3.08	47.26, 47.28[a]
16	3.37 (sep, 2H)	3.04 (sep, 2H)	50.99	49.42		3.27	50.15
14	4.18 (m, 2H)	4.03 (m, 2H)	65.56	66.76	64.8 (CH_2), 66.5 (CH), 67.8, 70.2 (CH_2), 72.9, 73.6 (CH_2)	4.12	65.57, 65.58[a]
4	3.51 (m, 4H)	3.46 (m, 4H)	66.45	67.18		3.47	67.20
5	3.51 (m, 4H)	3.46 (m, 4H)	68.79	69.57		3.47	69.60
13	3.95, 4.03 (2d, 4H)	3.92 (m, 4H)	69.46	70.76		3.93	70.29
6	4.39 (s, 4H)	4.38 (s, 4H)	72.19	72.11		4.38	72.09
3	3.58 (sep, 2H)	3.52 (sep, 2H)	72.49	71.27		3.52	71.28
9, 11	6.90 (d, 4H)	6.90 (d, 4H)	114.65	114.67	113.1; 119.2	6.88, 6.90[a]	114.38
8, 12	7.25 (d, 4H)	7.22 (d, 4H)	130.24	129.59	131.8, 133.1[b]	7.22	129.59
7	-	-	130.32	131.02	130.4	-	131.23
20, 21	6.37 (s, 2H)	6.39 (s, 2H)	135.26	136.07	138.6	6.53	135.16
10	-	-	157.79	158.34	158.7	-	158.13
19, 22	-	-	174.51	169.73	175.1	-	167.83

[a] Resolution of signals most likely due to chiral centre and it is the subject of ongoing independent investigation. [b] At –20 °C

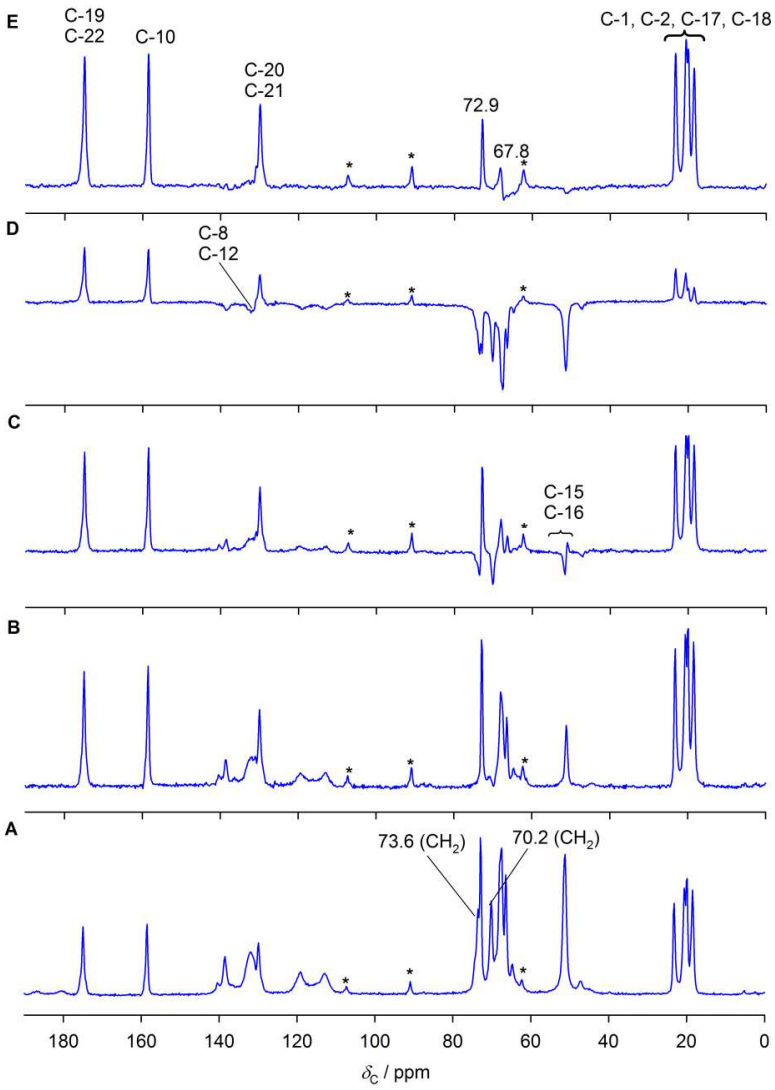

Figure 73. ^{13}C CPMAS NMR spectral editing experiments for crystalline bisoprolol recorded at room temperature at 6800 Hz spinning rate. (A) Conventional CP MAS, (B – D) CP depolarization with 25, 35 and 100 μs depolarisation time, respectively, and (E) interrupted decoupling spectrum with 40 μs delay time. The signal intensities for the CHs carbons are reduced, for the CH_2s are reduced or inverted and there is relatively little impact on the CH_3s and quaternary carbons in spectra with 25 and 35 μs inversion time (B and C). On spectrum D with 100 μs inversion time all the CHs and CH_2s are inverted leaving a small methyl signals and the quaternaries positive. Interrupted decoupling spectrum (E) shows methyl signals, the quaternary carbons and unexpectedly CHs and/or CH_2s carbons at 67.8 and 72.9 ppm suggesting some mobility in the molecule. Asterisks (*) denote spinning sidebands.

Figure 74A–E shows ^{13}C CP MAS spectra of crystalline bisoprolol as a function of temperature. At low temperature, distinct signals are observed for the phenyl carbons (C-9 and C-11) at 113.0 and 119.3 ppm, indicating that the two halves of the phenyl ring are not related by symmetry in the crystal structure. The phenyl resonances coalescence (at 116.0 ppm) above

60 °C corresponding to increased molecular mobility of phenyl ring. This is commonly observed in molecular solids e.g. Ref. [236] and references therein. Carbon C-8 and C-12 exhibit similar behaviour, although this is not clearly resolved due to overlap with the C-7 resonance. Subtle changes in the isopropyl signals (C-1, C-2, C-17 and C-18) are also observed, which are also consistent with increasing local mobility as the sample warms.

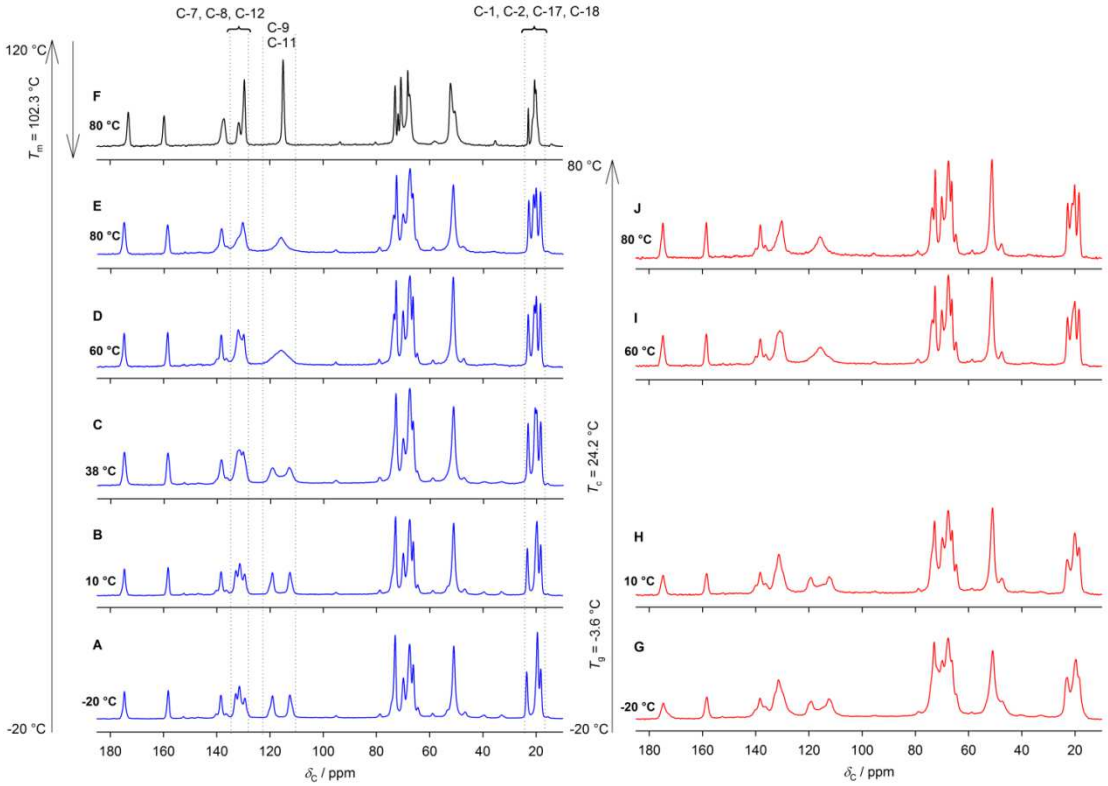

Figure 74. ^{13}C CPMAS NMR spectra of (A–E) crystalline, (F) melted then cooled to 80 °C in the liquid amorphous state and (G–J) quench-cooled bisoprolol as a function of calibrated temperature.

Figure 74F shows the ^{13}C CP MAS NMR spectrum of bisoprolol heated above the melting point (to 120 °C) and cooled to 80 °C, above both the glass transition and re-crystallization temperatures. The much sharper spectrum is consistent with the sample being in a liquid amorphous state, with a high degree of molecular mobility. As would be expected, the phenyl ring and isopropyl methyl carbon resonances are averaged in this state.

Figure 74G–J shows variable-temperature ^{13}C spectra of quench-cooled bisoprolol. As discussed above, the spectrum of quench-cooled bisoprolol at –20 °C is broad due to its glassy nature. At 10 °C, above the glass transition but below the cold crystallization temperature, the spectrum is slightly more resolved and sharper than at –20 °C, consistent with increased mobility and hence motional averaging in the liquid amorphous state. The appearance of relatively narrow signals at 60 and 80 °C shows that the bisoprolol has re-crystallized [59].

Figure 75 shows the ^{13}C NMR spectra of bisoprolol, valsartan and 70/30 and 50/50 physical mixtures at 38 and 80 °C. The spectra at 38 °C correspond to appropriately weighted combinations of the spectra of the pure drugs, showing no evidence of interactions between the components at ambient temperature. There are changes in the aromatic region (C-9, C-11) for the 70% bisoprolol/valsartan mixture, implying increased molecular mobility of phenyl ring. This observation is puzzling, and may simply reflect a strong sensitivity of this spectral feature to sample temperature. The spectrum of the 50/50 (w/w) physical mixture changes significantly at 80 °C, Figure 75H, with the peaks associated with the bisoprolol having much lower intensities. There are also some subtle changes in the valsartan resonances, e.g. some sharpening of the methyl carbon (C-1), suggesting an increase in mobility, and a slight decrease in intensity of C-11, but these are difficult to interpret with confidence. In contrast to the DSC results, there are no significant changes observed at 80 °C for the 70/30 and 80/20 physical mixtures in comparison to the pure drugs (data not shown).

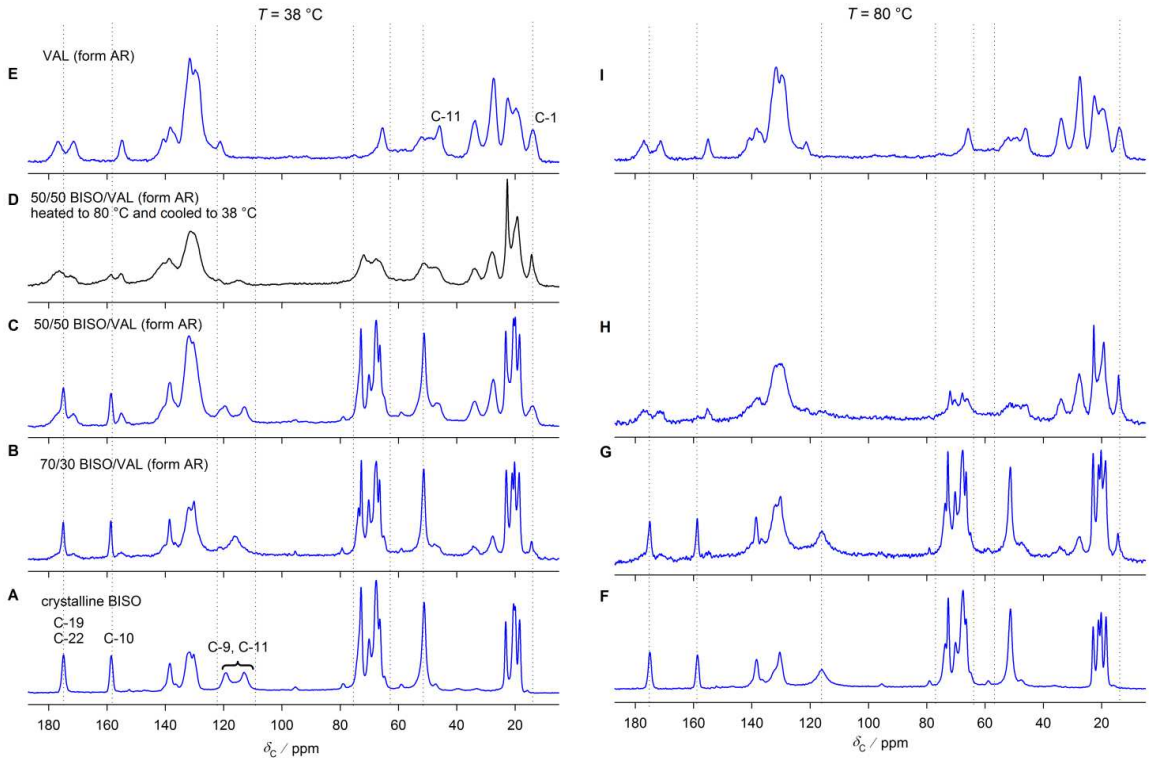

Figure 75. ^{13}C CPMAS NMR spectra of each API and physical mixtures in different concentrations at 38 and 80 °C.

Figure 75D shows the spectrum of the 50/50 (w/w) physical mixture of bisoprolol/valsartan heated to 80 °C and then cooled to 38 °C. The spectrum at 38 °C is similar to the spectrum at 80 °C, i.e. the reduction in intensities of the peaks associated with crystalline bisoprolol is irreversible. Experiments using longer recycle delays (up to 16 s) confirmed that the loss of these peaks was not an artefact of relaxation times – components with

long spin–lattice relaxation would be suppressed in experiments with short relaxation delays between scans. The loss of bisoprolol signals could also be associated with a dramatic increase in molecular mobility, which would selectively reduce the efficiency of cross-polarization for mobile components. However, direct excitation of the ^{13}C spectrum, using recycle delays of up to 50 s, did not reveal signals from mobile components that could be assigned to bisoprolol. To investigate the apparent disappearance of the bisoprolol signals in the 50/50 physical mixture spectrum, the intensities of the methyl (C-1, 14.1 ppm) resonance of valsartan and the alkyl signal at 72.9 ppm of bisoprolol in the binary mixture were measured as a function of the cross-polarization contact time, Figure 76. The slope of decaying part of the curve, which corresponds to $T_{1\rho}$ relaxation, is similar for both carbons. This is consistent with them being mixed at a molecular level or in domains smaller than 5 nm [58] and also shows that the weakness of the bisoprolol signals is not due to rapid $T_{1\rho}$ relaxation during cross-polarization. The bisoprolol signals are present, but just very weak and broad, presumably as a result of the distribution of local environments and hence dispersion of chemical shifts for each resonance due to amorphisation.

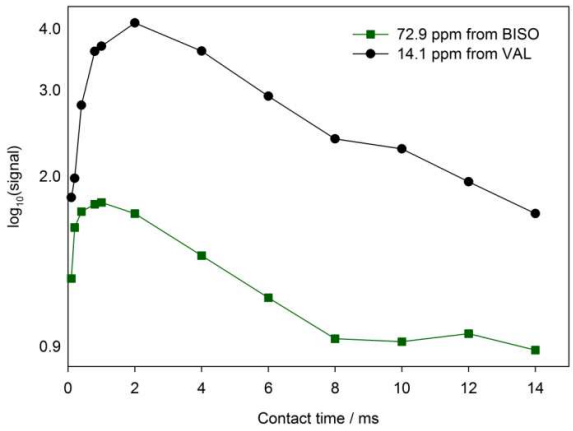

Figure 76. ^{13}C NMR signal intensity vs. cross-polarization contact time for the CH_3 at 14.1 ppm of valsartan and the alkyl signal at 72.9 ppm of bisoprolol in their 50/50 (w/w) physical mixture at 80 °C.

Figure 77 shows the X-ray diffraction patterns of crystalline and quench-cooled bisoprolol as a function of temperature. The diffraction patterns of the crystalline material at 60 and 80 °C show only modest changes of peak intensity and no significant changes in peak position, suggesting that there is no significant structural change during heating, which agrees with the DSC and NMR findings. XRPD of the quench-cooled bisoprolol at 0 °C, i.e. below the re-crystallization temperature, shows a characteristic halo pattern confirming its amorphous nature. At 60 °C, the material has re-crystallized into the same form as the starting material. However, the diffraction peaks are much weaker, suggesting a lower degree of crystallinity. This is consistent with the lower melting point of bisoprolol in the second heating and the

slightly broader and less-resolved NMR resonances of quench-cooled bisoprolol at 60 °C, Figure 74I.

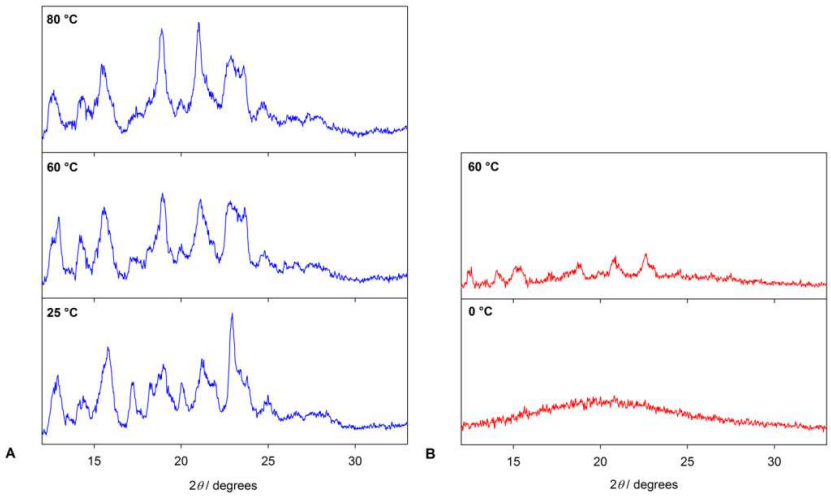

Figure 77. Variable-temperature X-ray diffractograms of (A) crystalline and (B) quench-cooled bisoprolol.

XRPD patterns of the 50/50 physical mixture, Figure 78, show peaks corresponding to bisoprolol at 25 °C. Although some studies suggest that the lack of observed interactions via XRPD at ambient temperature proves that DSC is a more sensitive technique [51, 237], variable-temperature XRPD experiments are necessary in order to meaningfully compare the two methods. A decrease of signal intensity from the crystalline bisoprolol component starts at about 60 °C (data not shown) and at 80 °C the XRPD pattern implies that the material is fully amorphous.

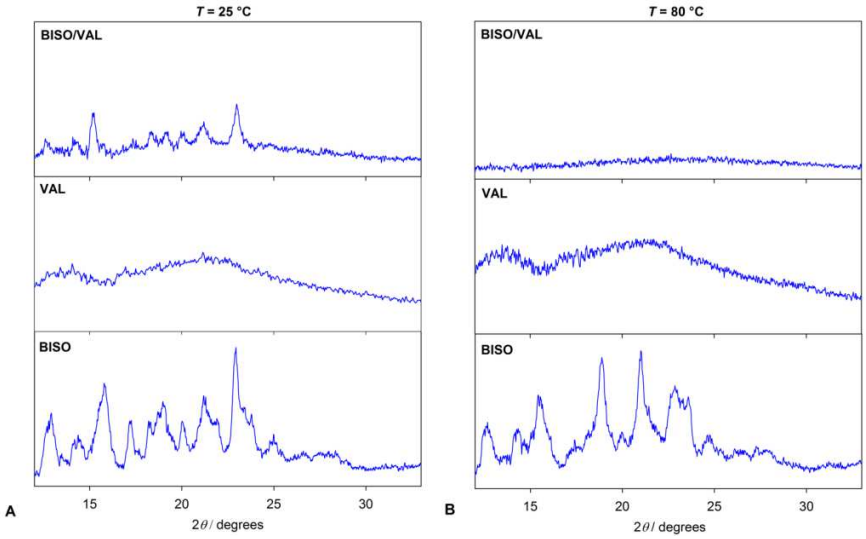

Figure 78. X-ray diffractograms of crystalline bisoprolol, amorphous valsartan (form AR) and a 50/50 (w/w) physical mixture of bisoprolol/valsartan (form AR) at (A) 25 °C and (B) 80 °C.

In the second heating, the amorphous halo observed from 0 to 60 °C confirms that the material remains amorphous, Figure 79, as found by other methods. In contrast to the solid-state NMR results on 70/30 and 80/20 mixtures, but in agreement with DSC, XRPD measurements on the 70/30 physical mixture showed only partial amorphisation of bisoprolol, with some of bisoprolol remaining in its crystalline state, Figure 80.

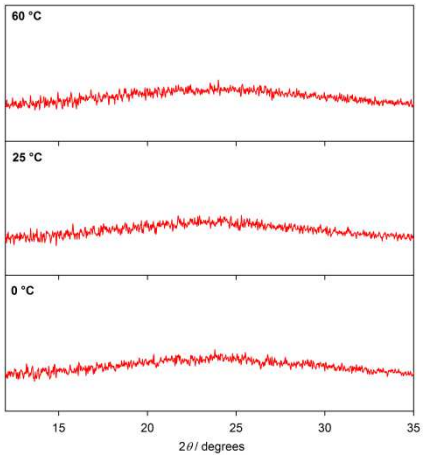

Figure 79. X-ray diffractograms of 50/50 (w/w) physical mixture of bisoprolol/valsartan recorded in the second heating run at 0, 25 and 60 °C. No crystallization is observed above cold crystallization temperature for pure bisoprolol (T_c = 24.2 °C) or glass transition process for the 50/50 (w/w) mixture (T_g = 35.9 °C). XRPD halo pattern is observed at all investigated temperatures confirming amorphous nature of the mixture and lack of tendency to crystallization.

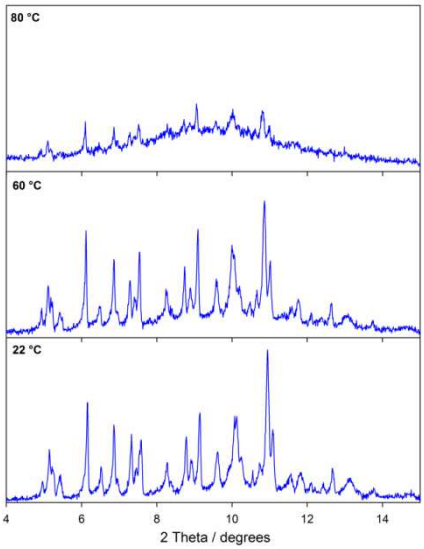

Figure 80. X-ray diffractograms of a 70/30 (w/w) bisoprolol/valsartan (form AR) physical mixture at 22, 60 and 80 °C. The results obtained at 80 °C clearly show only partial amorphisation of bisoprolol, with some of bisoprolol remaining in its crystalline state. Please note that the results are obtained from diffractometer operating at Mo K_α radiation in contrast to diffractograms shown on other Figures which were obtained using Cu K_α radiation.

To investigate the potential involvement of the COOH and NH groups in the interaction between the drugs, ^{1}H MAS NMR studies were also performed using very fast magic-angle spinning (53 kHz) to reduce the line-broadening associated with the strong dipolar interactions between ^{1}H spins [238]. Four different resonances are distinguishable in the fast MAS ^{1}H spectrum of bisoprolol, Figure 81A, corresponding to methyl (≈0.7 ppm), methylene, methine, hydroxyl, amine (2–5.5 ppm), aromatic (≈7 ppm) protons and also a low intensity signal at ≈10.4 ppm corresponding to an acid proton bonded to amine group. Figure 81D shows spectra of physical mixture of both APIs (solid line) and the sum of spectra of the pure materials (dashed line) The lines of physical mixture are slightly sharper than the sum spectrum confirming increased mobility at the onset of transition; increasing the spinning rate of the sample of untreated physical mixture to 63 kHz resulted in the sample volume expanding, presumably as the increased frictional heating triggered the interaction at about 60–80 °C. This volume expansion is consistent with the crystalline bisoprolol transforming into an amorphous form with lower density. Figure 81E shows the spectra of the physical mixture heated in an oven to 80 °C and cooled to room temperature. The lines are now significantly sharper than the spectrum of the pure materials, due to increased molecular mobility in the amorphised material. The spectrum also shows changes in the hydrogen bonding region i.e. in acidic and tetrazole protons signals arising from valsartan, which implies a change of hydrogen bonding due to amorphisation and/or deprotonation of these acidic carbons. The differences in overall mobility were confirmed by static ^{1}H NMR; the bandshape of untreated physical mixture is measurably broader ($\Delta\upsilon_{½}$ = 37.6 kHz) then that from the mixture heated to 80–85 °C and recorded at room temperature ($\Delta\upsilon_{½}$ = 28.9 kHz), consistent with increased motion in the amorphised material, Figure 82.

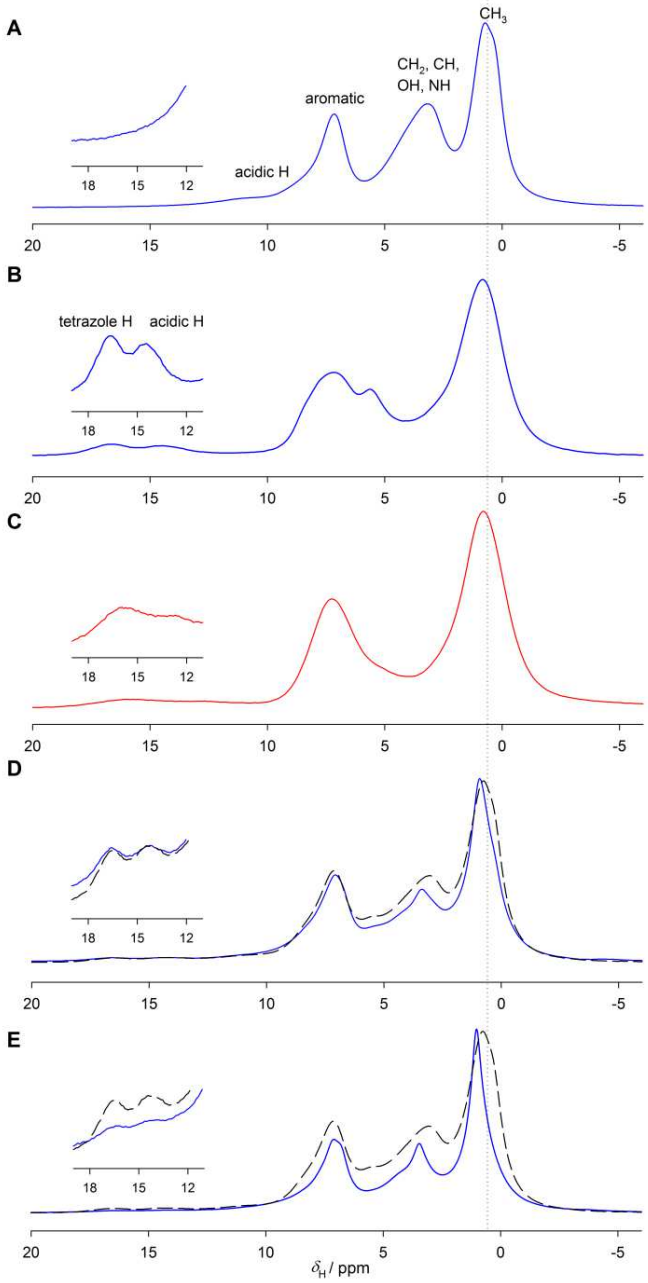

Figure 81. ^{1}H MAS NMR spectra of (A) bisoprolol, (B) valsartan (form AR), (C) valsartan (form AM), (D) 50/50 physical mixture of bisoprolol/valsartan (solid line) (E) 50/50 physical mixture of bisoprolol/valsartan heated to 80 °C (solid line). D and E show also the sum spectra of valsartan and bisoprolol (dashed line). Spectra were recorded at an MAS rate of 53 kHz. Sharper resonances in physical mixtures indicate increased mobility (amorphisation) of the mixture (D–E).

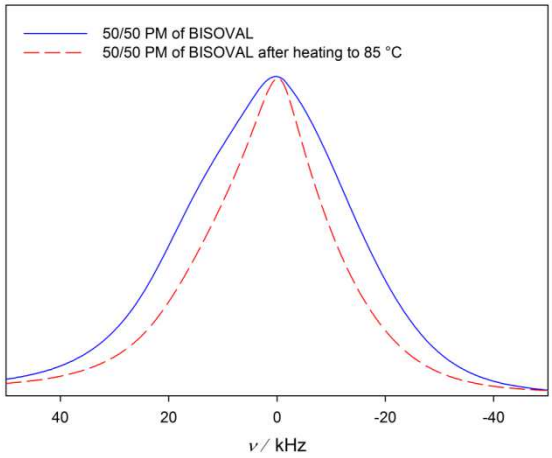

Figure 82. Proton static spectra of untreated (solid line) and heated to 85 °C (dashed line) 50/50 (w/w) bisoprolol/valsartan physical mixtures recorded at 25 °C. The bandshape of untreated physical mixture is measurably broader ($\Delta\upsilon_{½}$ = 37.6 kHz) then that from the mixture heated to 85 °C ($\Delta\upsilon_{½}$ = 28.9 kHz), implying increased motion in the amorphised material.

To further investigate the nature of the interactions, 1D and 2D solution-state NMR experiments were performed. Although there is a report related to degradation of bisoprolol in acidic environment [239], spectra of untreated and heated to 80 °C bisoprolol/valsartan physical mixtures do not show significant differences, indicating no significant degradation after heating the sample to the interaction temperature (80 °C) and holding the mixture at this temperature for 10–15 min. Comparing the spectra of bisoprolol fumarate in isolation and in its physical mixture reveals some significant differences in ^{1}H and ^{13}C chemical shifts, Table VI. These differences are largest for nuclei close to the amine group. For example, the methyl carbons (C-17, C-18) show increased shifts of 0.09 ppm for ^{1}H and 1.6–1.9 ppm for ^{13}C, while the methylene carbon (C-15) shift is 1.4 ppm lower in the mixture with valsartan. The fumarate carboxylic carbons (C-22, C-19) shifts also change significantly ($\Delta\delta_C$ = –1.9 ppm), implying a change in association of the fumarate ions. Comparing the valsartan spectra is more difficult due to the presence of two conformers in solution associated with hindered rotation of its amide bond, see Refs. [77, 78]. Changes are seen for the carbonyl group (C-5) and in the aromatic region (Table VII). These are associated with changes of conformational distribution of valsartan due to interaction with bisoprolol, and are not discussed further in this paper. There is also a noticeable change in shift of the carboxylic carbon (C-10, $\Delta\delta_C$ = –0.55 and –0.61 for the major and minor conformer, respectively). Similar information was provided by FT-IR spectroscopy, Figure 83.

Table VII. Solution-state NMR chemical shifts for valsartan and 50/50 (w/w) bisoprolol/valsartan physical mixture at 25 °C in [D_6]-DMSO. M and m denote major and minor conformers, respectively.

Carbon No	Valsartan				Bisoprolol/valsartan (after heating to 80 °C)			
	^{1}H shift / ppm		^{13}C shift / ppm		^{1}H shift / ppm		^{13}C shift / ppm	
	M	m	M	m	M	m	M	m
1	0.74	0.87	14.16	14.25	0.73	0.86	14.16	14.27
2	1.13	1.30	22.12	2.27	1.14	1.29	22.14	22.33
3	1.39	1.53	27.26	27.45	1.41	1.53	27.34	27.52
4	2.00, 2.18[a]	2.45, 2.50[a]	32.90	32.94	2.00, 2.18[a]	2.41, 2.50[a]	32.96	33.07
5	-	-	173.91	173.88	-	-	173.89	173.74
6	4.445	4.07	63.39	66.18	4.50	3.97	63.49	67.31
7	2.18	2.12	28.00	28.04	2.18	2.10	28.08	28.21
8	0.74	0.69	18.25	18.93	0.73	0.685	19.23	19.11
9	0.92	0.92	20.59	19.84	0.91	0.91	20.56	20.06
10	-	-	172.34	172.07	-	-	172.89	172.68
11	4.61	4.46	49.15	45.90[b]	4.56, 4.61[a]	4.45, 4.46[a]	48.81	45.90
12	-	-	138.22	137.55[b]	-	-	137.39	138.12
13	7.19	7.08	126.72	127.37	7.10	7.02	126.14	126.89
14	7.05	6.96	129.24	128.16	7.05	6.95	129.46	128.89
15	-	-	138.22	138.67	-	-	138.82	139.67
16	7.05	6.96	129.24	128.16	7.05	6.95	129.46	128.89
17	7.19	7.08	126.72	127.13	7.10	7.02	126.14	126.89
18	-	-	141.65	141.78	-	-	141.01	141.27
19	7.51	7.51	130.98	131.05	7.37, 7.41, 7.47, 7.55		129.16, 129.46 130.68, 131.04	
20	7.62	7.62	130.98	131.07				
21	7.55	7.55	128.14	128.01				
22	7.67	7.67	131.51	131.51				
23	-	-	123.84[c]	123.84[c]	-	-	Not detected	Not detected
24	-	-	Not detected	Not detected	-	-	Not detected	Not detected

[a] Chemical shift of nonequivalent protons of methylenes. [b] Low and [c] very low intensity peaks. Low intensities will reflect long ^{13}C relaxation times of quaternary sites, but peaks may also be broadened by motional exchange.

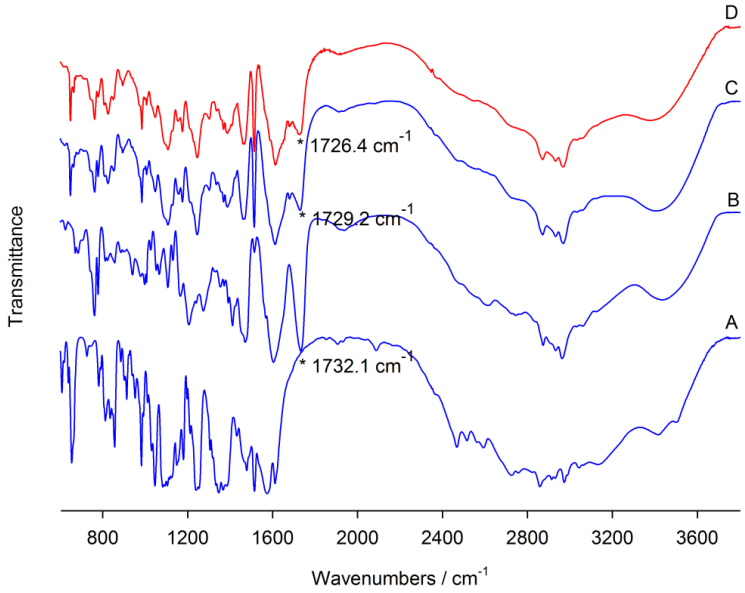

Figure 83. FT-IR spectra of (A) bisoprolol, (B) valsartan (form AR), (C) untreated and (D) heated to 80 °C 50/50 (w/w) bisoprolol/valsartan physical mixtures acquired at room temperature. Spectra show significant shift of the carbonyl group band of valsartan (C-10, $\upsilon_{C=O}$ = 1732.1 cm^{-1}), indicating the change in the local environment of carboxylic group. Due to peak overlap, it was not possible to obtain specific information about the interaction of bisoprolol in the physical mixture.

More direct evidence of interaction between valsartan and bisoprolol fumarate is provided by the diffusion ordered spectroscopy (DOSY) experiments, Figure 84. In D_2O solution, the fumarate species has a significantly faster diffusion rate (by a factor of 1.5) than the bisoprolol, as would be expected from its much smaller molecular mass and size, Figure 84A. In DMSO solution, however, the diffusion rates of fumarate and bisoprolol are similar (D_F = 1.746 (±0.006) × 10^{-10} m^2 s^{-1} and D_B = 1.865 (±0.005) × 10^{-10} m^2 s^{-1}), implying that they diffuse as an ion pair; this pairing is disrupted in D_2O solution, which allows the fumarate to diffuse more freely, Figure 84B. The presence of valsartan has a similar effect in the DMSO solution, Figure 84C; the valsartan and bisoprolol species migrate at the similar rate (D_B = 1.52 (±0.01) × 10^{-10} m^2 s^{-1} and D_{VAL} = 1.552 (±0.007) × 10^{-10} m^2 s^{-1}), with the fumarate diffusing 23% faster than bisoprolol. This strongly suggests that the valsartan and bisoprolol are preferentially associating, leaving the fumarate species to diffuse more quickly. Although the behaviour of molecules in solution cannot be directly compared to their behaviour in the solid state, these observations are consistent with the disruptive effects of valsartan on the crystalline bisoprolol fumarate.

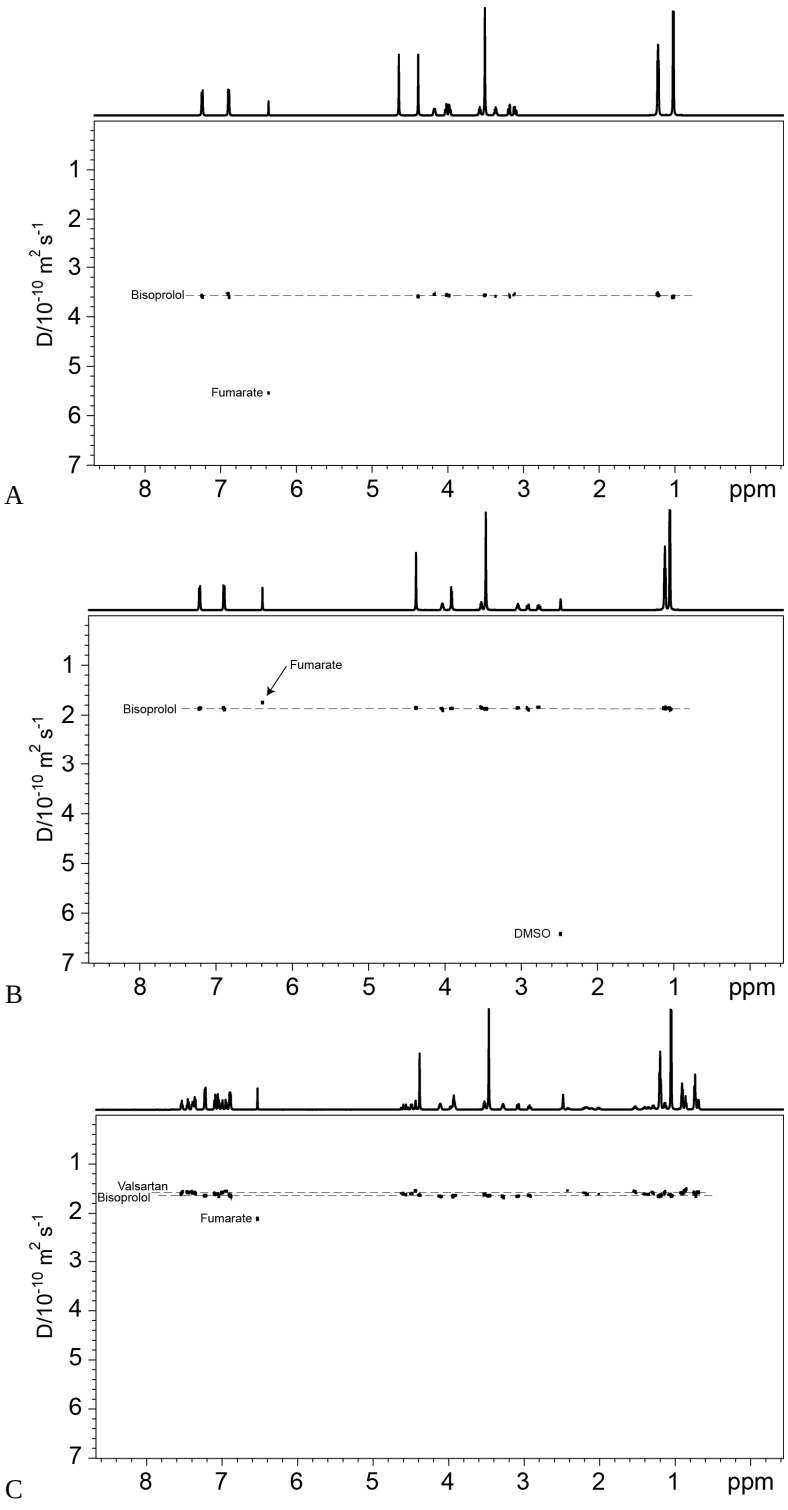

Figure 84. 2D-DOSY spectra of (A) bisoprolol fumarate in D_2O, (B) bisoprolol fumarate in [D_6]-DMSO and (C) 50/50 (w/w) physical mixture of bisoprolol/valsartan in [D_6]-DMSO. The diffusion coefficient of fumarate increases in presence of valsartan, suggesting competition of valsartan with fumarate.

5.4 Discussion

5.4.1 Valsartan

Two different solid state forms of valsartan were investigated by thermal methods and multi-technique solid-state NMR supported by particle size and shape analysis, solution-state NMR, FT-IR, XRPD and dissolution studies. The significant differences in local structures and physical properties for both amorphous forms were identified.

DSC experiments clearly showed differences between both analyzed forms. On the first heating DSC curve of AR valsartan form presents two endothermic events. The second event at the first glance may lead to a conclusion that the peak with a maximum at 100.6 °C (ΔH_{VAL} = 26 ±2 J g^{-1}) is due to melting as reported by some authors [23, 24]. Two-step standard DSC experiments confirmed that this endothermic event on this first heating is complex i.e. two processes: glass transition and enthalpy relaxation overlap. The DSC confirmed the amorphous nature of AR form of valsartan with the fictive glass transition temperature value at around 76 °C with a high value of enthalpy relaxation around 16 J g^{-1}. TMDSC allowed for the separation of the thermodynamic (glass transition) and kinetic (enthalpy relaxation) processes and provided clear signal for the glass transition in the AR form. Furthermore, Qi-TMDSC provided reversing C_p characteristic of the sample and change of the heat capacity at glass transition confirming amorphous nature of the as-received valsartan form. Both DSC and TMDSC confirmed amorphous nature of the AM valsartan form with the glass transition value at around 74 °C. HSM analyses also provided confirmation of amorphous nature of both forms.

X-ray diffraction measurements for both samples showed some subtle differences. For AR form there is some imitation of ordering, a broad peak around $2\theta = 14.4°$ (d = 0.62 nm), and a sharper but quite tiny peak at around $2\theta = 17.3°$ (d = 0.51 nm). Existence of additional broad peaks in the diffraction pattern suggests that in the fresh powder sample, some larger scale structures exist in addition to the broad amorphous halo. In contrast, this higher order of structure arrangement is diminished greatly in the sample of valsartan treated to 140 °C. In the AM form the X-ray intensity in this range of scattering angle is very much reduced. There is a distinct shift in the position of the peak maximum of the amorphous halo. This peak position can be used to estimate the average inter-atomic separation (d-spacing) of amorphous molecules of valsartan, by applying Bragg's Law. The sample heated to 140 °C has amorphous halo maximum occurring at d = 0.43 nm ($2\theta = 20.8°$) indicating an expansion of the average inter-atomic spacing of amorphous valsartan, to a value about 8% larger than that in the fresh powder sample which has a d = 0.40 nm ($2\theta = 22.3°$). It is observed that the valsartan structure

scattering at ~14° is greatly reduced after heating, suggesting that this structure may have been frozen-in by the thermal history during creation of the fresh powder sample. Further experiments would be necessary to determine the exact origin of this peak, and its possible relationship to bound solvent (water) content. Once the sample is heated above its glass transition temperature, structural rearrangement becomes possible, causing a reduction in amplitude of this scattering peak. XRPD confirmed amorphous nature of both materials, however with some higher level structure arrangement in the AR form.

FT-IR experiments showed only subtle differences in the characterised materials. There was a change in the amide carbonyl (C(5)O) stretching vibrations ($\upsilon_{C=O}{}^{AR}$ = 1603.8 cm^{-1}, $\upsilon_{C=O}{}^{AM}$ = 1605.8 cm^{-1}) consistent with a change in the environment of the carbonyl group associated with the amide moiety. This shifting of absorption band to a higher wavenumber could be attributed to the breakdown of the intermolecular hydrogen bonds between C(5)O and the tetrazole N(5)H group as well as *cis–trans* conformational changes around amide bond in the fully amorphous form.

Carbon-13 SSNMR experiments confirmed structural differences between both forms. Firstly, distinct linewidths broadening can be observed in fully amorphous form attributed to co-existence many different orientations which give rise in dispersion of chemical shifts for each resonance which confirms that the material is more disordered than as-received sample. Secondly, significant differences are noticed in the resonances arising from carbons directly bonded to amide bond nitrogen (N-1). By the comparison of resonances arising from C-11 and C-6 in the AR form with solution-state NMR and calculated spectrum is somewhat difficult to unambiguously claim the conformation of valsartan in the AR form. The comparison with solution-state could suggest that form AR exists mostly as a *cis* conformer i.e. in the solution: C-11, $\delta_C{}^{cis}$ = 45.90 ppm and C-6, $\delta_C{}^{cis}$ = 66.18 ppm whereas in the solid-state: C-11, $\delta_C{}^{AR}$ = 46.2 and C-6, $\delta_C{}^{AR}$ = 65.8 ppm. The calculated spectra based on crystal structure (*trans* isomer) are inconsistent with the solution-state data for C-11, $\delta_{C(calc)}{}^{trans}$ = 51.2 ±2.0 ppm (in solution $\delta_C{}^{trans}$ = 49.15) and C-6, $\delta_{C(calc)}{}^{trans}$ = 73.1 ±2.0 ppm (in solution $\delta_C{}^{trans}$ = 63.39 ppm). However, comparison of solution-state data as well as data based on crystal structure do not allow for AR form conformation confirmation as the changes in chemical shift due to packing in the solid state might be at least as large as the differences between *cis* and *trans* isomers for isolated molecules. The plot of calculated chemical shielding against experimental chemical shifts is shown in Figure 85.

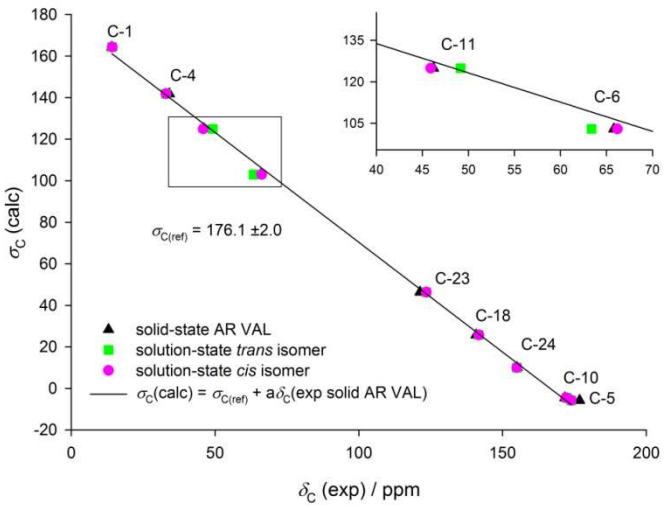

Figure 85. Plots of ^{13}C calculated chemical shielding crystalline valsartan vs. experimental chemical shifts for solid-state AR form and solution-state *trans* and *cis* conformers for ^{13}C. Only chemical shifts for carbons which could be resolved in solid-state for AR form are plotted. Carbon 24 is not observed in the solution thus data is taken from Ref. [78].

VT carbon-13 experiments revealed that AR valsartan form changes conformation going through the glass transition. Above the glass transition and after cooling to the room temperature carbons directly bonded to the N-1 shows broad signals at 48.3 ppm (C-11), 62.3 and 67.3 ppm (C-6). These results suggest that after phase transition valsartan changes conformation and probably exists as a mixture of *cis–trans* conformers. Similar behaviour in the solid state for crystalline API – captopril, was observed by Wang *et. al.* using VT FT-IR microscopy [240]. During the phase transition of crystalline captopril from solid- to liquid-state *cis–trans* isomerisation was observed. Furthermore, with increasing temperature in the liquid-state *cis* isomer was more favoured than *trans*. Also in the solid state *cis–trans* isomerisation was postulated as the origin of polymorphism in an ACE inhibitor fosinopril sodium [241].

Further differences in the structure between both forms were provided by ^{1}H ultra-fast MAS NMR. Five different resonances were clearly distinguished in the ^{1}H spectrum of as-received valsartan. The signals from protons bonded to C-6 and C-11 on the fully amorphous form spectrum are broadened due to amorphisation and conversion of one isomer into probably *cis–trans* mixture, furthermore, the signal of C-6 shows lower intensity due to split into two signals as seen in ^{13}C and HETCOR experiments. In the crystal structure of valsartan reported by Wang *et al.* the valsartan molecules are connected via two hydrogen bonds, both associated with the tetrazole ring, Figure 2 [26]. One hydrogen bond is generated between the carboxylic acid group (C-10) and the N-2 in the tetrazole ring, and the other one exists between the

carbonyl group (C-5) and the tetrazole ring at the N-5 position. ^{1}H spectra of fully amorphous form show significant decrease of chemical shift of tetrazole proton (N(5)H, $\Delta\delta_H$ = 1.1 ppm) suggesting involvement of tetrazole proton in hydrogen bonding. Acidic proton (C(10)OOH) is also broadened and shifted but due to low resolution it was not possible to precisely estimate its chemical shift. These finidings suggest that both tetrazole and acidic protons are involved in hydrogen bonding in the AR form, more ordered material, and might be formed similarly as in the crystalline form. Similar suggestions were reported by Taylor and Zografi for amorphous form of small API. It was found by X-ray diffraction, IR and Raman studies, that amorphous indomethacin appears to retain a local structure very similar to that of the crystal [242]. ^{1}H MAS experiments clearly showed the difference in the hydrogen bonding region between two amorphous forms.

Nitrogen-15 NMR experiments allowed to unambiguously confirm that both valsartan forms exist as an 1,2,3,4-tetrazole tautomer. The set of low intensity resonances in the nitrogen-15 experiments revealed that AR valsartan form exists predominantly as one probably conformational isomer with some other isomer impurity. The comparison of experimental data to the calculated ^{15}N spectra based on crystal structure (*S-trans* isomer) could suggest that AR form exists mostly as an *S-trans* isomer, Figure 56. However, ^{13}C data are ambiguous, thus it was not possible to ascertain in which conformation valsartan exist. The ^{15}N spectrum of AM form shows significant difference in comparison to untreated form and suggests that AM form is a mixture of isomers with the different ratio than AR form.

The differences in the molecular mobility between AR form and fully amorphous form were demonstrated based on DE ^{13}C SSNMR, ^{1}H static SSNMR and different NMR relaxation times. The spin–lattice relaxation time (T_1) and spin–lattice relaxation time in the rotating frame ($T_{1\rho}$) were investigated by ^{1}H static SSNMR and ^{13}C CP MAS NMR in the temperature below and above the glass transition. VT ^{13}C MAS DE NMR experiments indicated that alkyls (C-1–C-4 and C-7–C-9) are fast-relaxing carbons and aliphatic carbons directly bonded to N-1 (C-6, C-11) and carbonyl groups carbons (C-5, C-10) are slow-relaxing carbons suggesting different molecular mobility of aliphatic (C-1–C-4 and C-7–C-9) and the other ones. The VT ^{13}C MAS DE NMR did not reveal any differences in molecular mobility between two investigated forms, also static proton NMR measurements showed nearly identical ^{1}H bandshapes suggesting very similar molecular mobility. However, it was found that there is some significant difference in molecular mobility as measured by T_1^{H} and $T_{1\rho}^{H}$ relaxation times. The activation energy calculated from T_1^{H} plot was found to be significantly different i.e.: 7.4 for AR form and 3.7 kJ mol^{-1} for AM form. The differences in the T_1 and $T_{1\rho}$ measured on individual carbons for both forms are mostly within measurement error. However, T_1^{C}

measurements provided information about molecular motion behaviour of individual carbons during glass transition. Aliphatic carbons show linear decrease of T_1^C values and do not show any significant change around the glass transition temperatures whereas aromatic carbons show sharp jump around glass transition around 80 °C suggesting that the increase in mobility above glass transition is mainly due to change of aromatic rings mobility. The aromatic rings are main skeleton structure and the T_1^C data suggest that they are predominantly involved in glass transition of both valsartan forms. The low difference suggests very similar molecular mobility of both forms and the results demonstrate that amorphisation makes valsartan more mobile after heating and suggests the disordered state, which is attributed to poor molecule packing resulting from the co-existence of multiple orientations. In the case of T_1^H values there was no significant change around glass transition temperature. It can be seen that above T_g there is marked decrease in $T_{1\rho}^H$ values. As expected values above T_g in the liquid amorphous state for both materials are similar. Since the proton diffusion in solids is facilitated through the intermolecular interactions which is largely dependent upon the proximity of neighbouring hydrogen atoms and the local intermolecular interaction, decrease of $T_{1\rho}^H$ indicate reduction in short-range order [214].

AR form of valsartan and fully amorphous form characterised by DSC and TMDSC have different glass transition temperatures and large enthalpy relaxation for AR form. The amorphous systems formed by quench-cooling have an excess of thermodynamic properties (free energy, enthalpy and entropy) as compared to supercooled liquid state. During physical ageing at a particular temperature (T_a) an amorphous material looses excess of enthalpy as the system moves towards a more stable conformation. The amount of enthalpy lost during storage is recovered by the system during heating DSC run and is measured as an integral of enthalpy recovery peak which overlaps with glass transition. This phenomenon of enthalpy relaxation reflects the molecular mobility in the glassy state [128]. On the reversing curve only the glass transition is observed as ageing time increases the T_g moves towards higher temperature. TMDSC curves of valsartan storage at different temperature with different length of time did not show exothermic and/or endothermic behaviour due to crystallization and melting suggesting a lack of crystallization tendency of amorphous valsartan. The molecular mobility in aged amorphous forms of valsartan was characterised by T_1^H and $T_{1\rho}^H$ relaxation times. There was found significant difference between aged and unaged samples. The results suggest that annealing below T_g significantly reduces molecular mobility of amorphous material.

To understand how these structural and molecular mobility differences in the amorphous states can affect the dissolution behaviour, intrinsic and apparent dissolution tests were carried out. Both intrinsic and apparent dissolution profiles show significant difference for

examined amorphous solid states of valsartan. It is know that amorphous material has higher free energy and usually presents a greater solubility and dissolution rate than its corresponding crystalline form [4-6]. Surprisingly, in these studies it was found that less ordered, fully amorphous material (AM form) has a lower dissolution rate than amorphous form with higher structure arrangement (AR form). This behaviour could be due to observed *cis–trans* isomerisations after heating as-received material above the glass transition. It is known that *cis–trans* isomers can have different physical properties [243, 244]. Since *trans* isomers have more symmetry than *cis* isomers, *trans* isomers in most cases have lower solubility [245, 246] and in consequence bioavailability [244, 247]. Thus change in the concentration of valsartan isomers in AM form can have a significant impact on the dissolution rate. As it was not possible unambiguously ascertain from which isomer AR form exists it is not possible to discuss further this hypothesis.

From the pharmaceutical science and industry perspective characterisation of amorphous structure of glassy API is crucial. It has been speculated, that solids which have similar local structures in amorphous and crystalline state, should crystallize relatively easy, whereas crystallization of API with different local structures might be hindered [2]. Even though valsartan was approved by FDA in 1996 so far it has been marketed in its amorphous form which is usually less desirable due to low chemical and physical stability. The highly crystalline form was obtained and patented relatively very recently [25, 26]. It was also believed to be difficult to make highly crystalline form of valsartan. These studies suggest that both difficulties in obtaining crystalline form from solution and the high physical stability of amorphous form could be due to conformational diversity of the compound in both solution and in the glassy state. Similar hypotheses have been suggested and discussed in the literature for amorphous inorganic and organic compounds [2, 248-250]. Also the difference in the dissolution behaviour in both investigated forms was clearly showed this may have an impact on the final drug product bioavailability.

5.4.2 Valsartan and bisoprolol compatibility

Bisoprolol fumarate is found to have glass transition below room temperature (–3.6 °C) and to be unstable in amorphous form, undergoing re-crystallization upon heating to the same polymorphic form as starting material but probably with a lower degree of crystallinity. Knowing the glass-forming ability of APIs from their crystalline state is very important for development of the solid dosage form. Amorphous solid forms usually show improved solubility. The solubility improvement of amorphous form is not relevant to bisoprolol as it is freely soluble, but formation of amorphous API might increase the rate of chemical degradation

and cause problems during manufacturing [66, 251]. Baird *et al.* [252] divided the crystallization tendency of drug into 3 classes. Drugs showing only a crystallization peak (T_c) and no glass transition (T_g) signal during the 1st cooling of melted drug belong to class 1, those that do not undergo crystallization during the first cooling but become crystalline at above T_g during second heating, to class 2 and those that do not convert into crystalline form during cooling/heating/heating cycle, to class 3. Bisoprolol fumarate is found to belong to class 2. The crystalline form of valsartan could not be obtained, but the thermal behavior of its amorphous form indicates that it belongs to class 3.

Compatibility studies of crystalline bisoprolol fumarate and two amorphous forms of valsartan (free acid) were completed over a range of temperatures from room temperature to above the phase transitions of both APIs. DSC and TMDSC revealed the interaction of the APIs by the appearance of a new peak and the disappearance of the bisoprolol melting peak in the physical mixtures. Such lowering or shifting of the melting peak in mixtures might occur as a result of the formation of a eutectic mixture, which is a common phenomenon known for APIs [253]. However, eutectics are generally considered in terms of initially crystalline components, whereas in this case one of the materials is amorphous, having a T_g rather than a melting point. Moreover, the TMDSC reversing curve does not show an endothermic melting peak, suggesting no eutectic formation has occurred. Instead the new transition peak appears as a kinetic signal, confirming irreversibility of the process and indicating chemical or physical interaction. To the best my knowledge, this is the first report of API-API compatibility studies involving mixed solid states – crystalline and amorphous. The ^{13}C CP MAS NMR and XRPD measurements clearly show the interactions as the samples are heated to 80 °C. The ^{13}C NMR spectrum of the 50/50 physical mixture contained only broad and low intensity signals, suggesting that the bisoprolol has interacted with valsartan and amorphised. This is consistent with the picture from XRPD. The static ^{1}H bandshapes suggest increased overall mobility in the amorphised material, while the ^{1}H spectra obtained at ultra-fast MAS rates showed significant changes in the signals in the hydrogen bonding region arising from the acidic COOH and tetrazole hydrogens of valsartan.

A likely cause of the interaction is the competition between valsartan and fumarate for bisoprolol amine group. Valsartan has two acidic centres, the COOH group (pK_{a1} = 3.6) and the tetrazole ring (pK_{a2} = 4.7) [254], while bisoprolol is a salt of bicarboxylic fumaric acid (pK_{a1} = 3.0, pK_{a2} = 4.4) [114]. There is a possibility of H^+ exchange as valsartan has a lower pK_{a1} than pK_{a2} for fumaric acid. It is worth noting that valsartan as a free acid is successfully formulated with besylate salt API (Exforge®, amlodipine besylate), but benzenesulfonic acid is a much stronger acid (pK_a = 0.70) than valsartan, and so acid-base reaction is unlikely.

Although pK_a values describe equilibrium phenomena in solution, it is widely accepted that they can be a valuable tool for predicting acid-base interactions in solid-state [255]. It is possible that the dominant interaction in the solid state could be protonation of the doubly deprotonated fumarate in bisoprolol fumarate by the acidic proton of valsartan, corresponding to a 1:1 molar ratio of APIs. The mole ratios in the investigated 20/80, 50/50, 70/30 and 80/20 (w/w) bisoprolol/valsartan physical mixtures are as follows: 1:7.04, 1:1.76, 1:0.76, 1:0.44. ^{13}C CP MAS NMR measurement of 50/50 mixture revealed interaction, whereas the 70/30 and 80/20 spectra showed clear resonances from bisoprolol suggesting that a significant fraction of the bisoprolol fumarate was largely unchanged. The XRPD measurements indicated amorphisation of the mixture at 50/50 concentration, and experiments with the 70/30 mixture showed an increased halo pattern, confirming some amorphisation, but also some unaltered bisoprolol fumarate diffraction peaks. In the 50/50 mixture there is enough valsartan to displace one fumarate carboxylate, whereas in the 70/30 and 80/20 mixtures there is excess of bisoprolol fumarate, and thus crystalline bisoprolol can still be detected by NMR and XRPD. The TMDSC results show similar behavior with concentration; the non-reversing (kinetic) heat-flow rate shows an enthalpy relaxation peak corresponding to valsartan AR form in the 20/80 and 50/50 BISO/VAL physical mixtures but not in the 80/20 mixture, where all valsartan had “reacted”. The DSC shows evidence of the interaction over a wide range of concentrations; the melting peak is broadened but is observed in the physical mixtures with 90% bisoprolol concentration, while the melting peak was not identified with 80% or less of bisoprolol in the physical mixture. The results show that the addition of small amounts of valsartan (>10%) leads to major changes in the solid state of bisoprolol fumarate. In this respect, the DSC is more sensitive than XRPD and NMR, which both struggle to observe low fractions of amorphous content.

5.5 Conclusions

Two solid forms of valsartan were characterised by multi-technique DSC and solid-state NMR as a primary investigation tools supported by, where appropriate, particle size and shape analysis, HSM, TGA solution-state NMR, FT-IR, XRPD and dissolution measurements. The calorimetric methods, HSM, SSNMR and XRPD have revealed that both valsartan forms exist as the amorphous materials with some higher level of structure arrangement in the AR form. Some subtle differences between two forms could also be observed by FT-IR whereas 1D and 2D SSNMR clearly distinguished both forms at the molecular level. Furthermore, both forms had significantly different dissolution behaviour. In my best knowledge this is the first report where the more ordered API material showed greater dissolution rate than the fully disordered material. In more details, taking into account discussed results, it was possible to make following conclusions regarding valsartan:

- analysed valsartan samples exist in two different amorphous forms with some higher level of structure arrangement in the AR form;
- AR form exists mainly as one isomer, most likely due to the hindered rotation of its amide bond, with some impurity of the other isomer;
- AM form exists as a mixture of two, most likely, *cis–trans* isomers;
- both forms of analysed valsartan exist as 1,2,3,4-tetrazole tautomers;
- both forms are physically and chemically stable within analysed range of temperature and do not crystallize;
- molecular mobility of both forms is very similar, however some differences can be observed by T_1^H and $T_{1\rho}^H$ measurements suggesting more mobility in the AM form;
- based on T_1^C values it can be concluded that aliphatic carbons do not show any significant and sharp change around the glass transition temperatures, whereas aromatic carbons show sharp jump around glass transition around 80 °C suggesting that the increase in mobility above glass transition is mainly due to change of aromatic rings mobility in both forms;
- subtle changes in molecular mobility of annealed AM form can be observed by T_1^H and $T_{1\rho}^H$ NMR measurements, annealing significantly reduces overall molecular mobility of amorphous material;
- AR form had greater dissolution rate than the fully disordered AM form;
- studies stress the importance of amorphous sample preparation as the amorphous sample obtained from “crystallization” from solution (commercial AR form) can show

different physicochemical parameters than that obtained by rapid cooling from “melt” (AM form).

This contribution clearly demonstrated the importance of characterisation of amorphous pharmaceutical materials as there might be some types of order and/or conformational differences in that types of materials which might have significant influence on physicochemical properties and thus potentially on the pharmacological action of the final dosage form. It was proved that calorimetric methods and SSNMR spectroscopy offer a powerful tool for identification and characterisation of differently disordered amorphous forms of small APIs.

Furthermore, the crystalline and amorphous forms of bisoprolol and its compatibility with two amorphous forms of valsartan were analysed. Amorphous bisoprolol has low stability and re-crystallizes above the glass transition. The compatibility study has shown that simple blending of the APIs to produce a fixed-dose formulation of bisoprolol and valsartan is unsuitable due to physical and chemical reaction which causes amorphisation into a new bisoprolol/valsartan material at elevated temperatures, and potentially also under long-term storage. Thus, formulation of an FDC or polypill containing bisoprolol and valsartan would require physical separation of the ingredients to ensure a stable product. Similar problems might be expected with excipents or APIs containing carboxylic group, for example with aspirin or folic acid. It was demonstrated that thermal methods play a pivotal role in early detection of API-API interaction leading to incompatibilities. Solution- and solid-state NMR and XRPD provide information about the molecular nature of these interactions. Variable-temperature NMR and XRPD experiments are seen to be an ideal complement to thermal methods in the investigation of drug-drug incompatibilities as the kinetics of potential interactions may be too slow to be detected at ambient temperature.

6 LIST OF FIGURES AND TABLES

6.1 Figures

6.1.1 Main text

Figure 1. Chemical structure of valsartan, *N*-[*p*-(*o*-1*H*-tetrazol-5-ylphenyl)benzyl]-*N*-valeryl-L-valine (M = 435.52 g mol^{-1}). 16

Figure 2. The structure and hydrogen bonding of (*S*)-*trans* valsartan isomer adapted from Ref. [26]. Hydrogens are omitted for clarity. 17

Figure 3. The rennin angiotensin system with sites of blockade by ACE inhibitors and sartans. Modified from Ref. [82] 18

Figure 4. Chemical structure of bisoprolol base, ((*RS*)-1-((alpha-(2-isopropoxyethoxy)-p-tolyl)oxy)-3-(isopropylamino)-2-propanol), with chiral centre denoted by asterisk (*) (M = 325.44 g mol^{-1}). 20

Figure 5. Schematic representation of APIs solid forms. Modified from Refs. [94, 116]. 23

Figure 6. Schematic Gibbs free energy curves for a hypothetical single-component system that exhibits polymorphism, pseudopolyamorphism and polyamorphism. Crystals A, B and C correspond to polymorphs with melting temperatures, $T_{m,A}$, $T_{m,B}$ and $T_{m,C}$, respectively, and with a solid-solid polymorphic transition temperature ($T_{t,A\text{-}B}$). Liquid 1 and liquid 2 correspond to two liquids with first-order liquid-liquid true polyamorphic transition temperature (T_{ll}) with polyamorphs glass 1 and glass 2 with glass transitions temperatures, T_{g1} and T_{g2}, respectively. Glass 2 and 2′ describe glasses with different processing and/or storage history showing different glass transition temperatures, T_{g2} and $T_{g2'}$, respectively (pseudopolyamorphs). Modified from Refs. [2, 11]. 25

Figure 7. Changes of Gibbs free energy (G), enthalpy (H), entropy (S), volume (V) and heat capacity at constant pressure or volume (C_p and C_v) at (A) first- and (B) second-order phase transitions. The heat capacity has an infinite value at first-order phase transition temperature whereas at second-order phase transition, there is no discontinuity in H, S, V but a "jump" in the heat capacity is observed. Adapted from Ref. [127]. ... 26

Figure 8. Scheme of the critical manufacturing steps leading to final dosage formulation in which a solid state change might occur. Adapted from Ref. [141]. 28

Figure 9. Diagram of a flow-through apparatus used for determination of ADR. Modified from Refs. [88, 150, 164]. 34

Figure 10. Diagram of rotating disc batch-type apparatus for determination of IDR. Modified from Refs. [88, 150, 165]. 35

Figure 11. Plots showing (A) temperatures of sample (S) and reference (R) as a function of time in DSC experiment and (B) resulting from it changes of heat-flow rate as a function of temperature. Modified from Refs. [125, 167]. 36

Figure 12. Scheme of two types of DSC instruments: (A) heat flux DSC and (B) power compensation DSC. 1 = furnaces, 2 = thermocouple and 3 = platinum resistance thermometers. Modified from Ref. [125]. .. 37

Figure 13. Plot of temperature as a function of time used in temperature programs for standard and temperature-modulated DSC. 39

Figure 14. TMDSC (A) raw data and (B) results of deconvolution for quench-cooled polymeric material. Kinetic processes as enthalpy relaxation, cold crystallization or crystal perfection are separated from thermodynamic processes as glass transition or melting and appear on different signals. Modified from Ref. [177]. 40

Figure 15. Standard DSC curves of crystalline losartan potassium showing 1st heating (polymorphic transition, melting and decomposition), cooling (glass transition of amorphised material) and 2nd heating (glass transition and decomposition). No crystallization is observed during heating or cooling run. Modified from Ref. [181]. 41

Figure 16. Temperature-modulated DSC thermogram of losartan shows non-contribution to the reversing heat-flow rate in the transition region of Form I – Form II. Modified from Refs. [180, 181]. 42

Figure 17. The comparison of the reversing heat capacity obtained from quasi-isothermal TMDSC with the total heat capacity obtained from standard DSC analysis for losartan potassium. Qi-TMDSC confirmed irreversible process of solid–solid transition and showed a small contribution of reversing heat capacity in the melting transition at much lower temperature than for standard DSC analysis. Modified from Ref. [181]..... 42

Figure 18. (a) The total, apparent, (b) reversing, and (c) non-reversing heat capacity of an amorphous poly(lactic acid) for standard TMDSC. Adapted from Ref. [182]..... 43

Figure 19. Energy levels of an isolated spin-12 states in the absence ($B_0 = 0$) and presence ($B_0 \neq 0$) of an external magnetic field (assumed $\gamma > 0$)..... 45

Figure 20. Interaction between two dipoles..... 46

Figure 21. (A) A schematic heteronuclear dipolar powder pattern (Pake doublet) and (B) two powder patterns subspectra for different values of magnetic quantum number (m_I). 46

Figure 22. Schematic representation of the magic-angle experiment. The sample is spun in a rotor about a spinning axis orientated at the magic angle ($\beta = 54.74°$) with respect to the applied magnetic field (B_0). Adapted from Ref. [58]. 48

Figure 23. Solid-state ^{13}C NMR spectra of losartan potassium recorded with MAS at different spinning rate from 0 to 10 kHz. All spectra obtained at 125 MHz with cross-polarisation and high-power proton decoupling. 128 scans were acquired for each spectrum. Asterisks (*) denote spinning sidebands..... 49

Figure 24. The *z*-magnetization change after a RF pulse as a function of time (t). The *z*-magnetization returns from $M_z(0)$ to M_0 following an exponential law. The time constant of the exponential function is T_1 referred to as the longitudinal or spin–lattice relaxation time..... 50

Figure 25. The cross-polarisation pulse sequence. Adapted from Ref. [58]..... 52

Figure 26. The dipolar dephasing pulse sequence; τ is the delay time (dephasing delay) and τ_r is the rotor period. Adapted from Ref. [58]..... 53

Figure 27. Inversion-recovery cross-polarisation pulse sequence. Adapted from Ref. [205]. 54

Figure 28. Pulse sequences used for measuring spin–lattice relaxation times: (A) inversion-recovery, (B) saturation-recovery, (C) inversion-recovery with cross-polarisation and (D) “Torchia” method. Adapted from Ref. [58]. 55

Figure 29. Pulse sequences used for measuring spin–lattice relaxation times in the rotating frame: (A) variable spin-lock, (B) delayed contact and (C) variable spin-lock with cross-polarisation preparation method. Adapted from Ref. [58]. 56

Figure 30. Pulse sequence used for FSLG HETCOR experiment. The sequence starts with with a $(180° + \theta_m)_y$ pulse on the protons, directly followed by a train of frequency- and phase-switched Lee-Goldburg pulses in the *xz* plane After the evolution period, the proton magnetization is turned back by a single magic angle (θ_m) *y* pulse, which will reverse any component perpendicular to the Lee-Goldburg pulse back into the *xy* plane, and which will bring the spin-locked component along the LG-pulse back to the *z* axis. Adapted from Ref. [211]. 57

Figure 31. ^{13}C CPMAS spectra of losartan potassium, (A) Form I and (B) Form II..... 58

Figure 32. (A) High-frequency region and (B) low-frequency region of ^{13}C CPMAS spectra of irbesartan, Form A (top) and Form B (bottom) and (C) ^{15}N CPMAS spectra from Form A at 295 K (top), Form B at 295 K (middle) and Form B at 253 K (bottom) for irbesartan. Modified from Ref. [27]. 60

Figure 33. Carbon-13 CPMAS spectra of five solvates of finasteride (excluding the high-frequency part). Top to bottom: acetic acid; ethyl acetate hydrate; tetrahydrofuran solvate hydrate; isopropanol solvate hydrate; dioxane solvate hydrate. Assignments are indicated for the solvent peaks. Adapted from Ref. [213]. 60

Figure 34. Chemical structure of valsartan with all atoms numbered. 65

Figure 35. Chemical structures of bisoprolol fumarate or (*RS*)-1-((alpha-(2-isopropoxyethoxy)-p-tolyl)oxy)-3-(isopropylamino)-2-propanol fumarate (2:1) (M = 766.96 g mol^{-1}) with the carbons numbered. The chemical structure of bisoprolol fumarate is that of the neutral molecules, as conventionally given. The material is, however, expected to be in a salt form as a solid, with the fumaric acid present as a doubly de-protonated fumarate ion and with the bisoprolol assumed to be protonated at its NH site. 66

Figure 36. The particle area (A) and added “convexity area” (B)..... 67

Figure 37. Particles images of AR valsartan form: (A) all particles and (B) fibers only. 75

Figure 38. TGA curve of valsartan (AR form). 76

Figure 39. DSC curves of valsartan 1st (AR form) and 2nd (AM form) run on heating and cooling. 76

Figure 40. (A) DSC curves of valsartan (AR form) for the two-step heating experiment. (B) Evaluation of the glass transition from DSC curve of valsartan (AR form) from 2-step experiment (curve III). (C) The heat capacity of AR and AM almost unaged valsartan from standard DSC. (D) Evaluation of enthalpy relaxation from AR and AM unaged valsartan from first and second heating, respectively. 77

Figure 41. TMDSC curves of AR valsartan form for the first heating: total, reversing, and non-reversing heat-flow rate curves. 79

Figure 42. TMDSC response for dry amorphous valsartan (form AM), showing the total, reversing and non-reversing heat-flow signals. 79

Figure 43. Comparison of the heat capacities for the 1st run for the AR valsartan form obtained from standard DSC and Qi-TMDSC. Qi-TMDSC shows glass transition process on the reversing heat capacity signal confirming amorphous nature of the AR valsartan form. 80

Figure 44. Polarized light photomicrographs of valsartan, AR form, at (A) 30 °C, showing lack of birefringence and indicating amorphous nature of the material (B) and (C) showing glass transition process at, 99 and 101 °C, respectively, and (D) material above the glass transition in the liquid amorphous state at 140 °C. Sample was heated with 5 °C min^{-1} rate. 81

Figure 45. XRPD diagrams of valsartan (λ = 0.1542 nm) recorded at room temperature. Valsartan powder before (AR form) and after (AM form) heating to 140 °C. 81

Figure 46. FT-IR spectra of two valsartan forms. 82

Figure 47. Carbon-13 CPMAS NMR spectra of (A) as-received and (B) fully amorphous valsartan recorded at 10 kHz spinning rate at room temperature. Insets show spectra at 40–70 ppm region not affected by spinning sidebands recorded at 6 kHz spinning rate. Asterisks (*) denote spinning sidebands. 83

Figure 48. (A) The double bond character of amide bond and (B) possible conformations of valsartan in the liquid and solid state as a consequence of this phenomenon. 85

Figure 49. VT ^{13}C CPMAS spectra of (A) as-received (AR form) and (B) fully amorphous valsartan (AM form) before and after the glass transition process (T_g^{AR} = 94 °C and T_g^{AM} = 74 °C). It can be seen that the spectra of both forms recorded at 110 °C are essentially identical, most likely due to isomerisation of AR form above the glass transitions. 86

Figure 50. Carbon-13 spectra of AR (blue line) and AM (red line) valsartan obtained using direct-excitation experiment recorded at different temperatures with spinning rate at 6.8 kHz. Temperatures displayed are the set-up values not real samples temperatures. The signal at 110 ppm arises from the CF_2 carbon in the Teflon® used as a rotor cap. 87

Figure 51. VT static ^1H NMR spectra of (A) AR (solid line) and (B) AM (dashed line) forms of valsartan. The sharpening of bandshapes is observed with the increase of temperature and is significant far above the glass transition temperatures (T_g^{AR} = 94 °C, $T_g^{Richardson(AR)}$ = 76 °C and T_g^{AM} = 74 °C) at 120 °C, where samples are in the liquid amorphous state. 88

Figure 52. ^1H MAS NMR spectra of (A) as-received and (B) fully amorphous valsartan recorded at a MAS rate of 67 kHz. 89

Figure 53. The 40–80 ppm region of ^{13}C–^1H HETCOR spectra of (A) as-received and (B) fully amorphous valsartan with 0.1 ms contact time showing directly bonded C-H links only. The fully amorphous form shows two split signals from C-6 suggesting valsartan existing as a mixture of *cis–trans* isomers. 90

Figure 54. Possible tautomeric forms of valsartan: (A) 1,2,3,4- tautomeric form and (B) 1,2,3,5- tautomeric form. . 91

Figure 55. Nitrogen-15 CP MAS NMR spectra of AR VAL at (A) 6 kHz spinning rate (3 spectra added – 151 000 repetitions in total) (B) at 10 kHz spinning rate (30 000 repetitions in total), (C) AM VAL at 10 kHz spinning rate (40 000 repetitions) and (D) ^{15}N IR CPMAS NMR spectrum of AR VAL at 10 kHz spinning rate (2 spectra added – 331 000 repetitions in total). Arrows (↓) indicate signals arising most likely from other conformational isomer impurity in the AR form. All spectra recorded at room temperature. Asterisks (*) denote spinning sidebands. 92

Figure 56. Plot of ^{15}N calculated chemical shielding crystalline valsartan vs. experimental chemical shifts for a main isomer of AR form for ^{15}N signal. 93

Figure 57. Static proton (A) T_1 for AR and AM valsartan forms. 94

Figure 58. Examples of ^{13}C T_1 relaxation behaviour of AR and AM valsartan forms. Aliphatic carbons do not show any significant change around glass transition temperatures (T_g^{AR} = 94 °C, $T_g^{Richardson(AR)}$ = 76 °C and T_g^{AM} = 74 °C) whereas aromatic carbons show sharp jump around glass transition around 80 °C suggesting that the increase in mobility above the glass transition is mainly due to change of the aromatic rings mobility. 96

Figure 59. Selected T_1^C data as a function of reciprocal temperature for (A-C) as-received and (D-E) fully amorphous valsartan form and corresponding activation energies. 96

Figure 60. Static proton $T_{1\rho}^H$ data for AR and AM valsartan forms. 97

Figure 61. Selected plots of $T_{1\rho}^H$ measured via CP onto ^{13}C as a function of temperature for as-received and fully amorphous valsartan forms. 98

Figure 62. (A) Change of total, (B) reversing and (C) non-reversing heat capacity of AM valsartan annealed at 50 °C for different length of time from 0 to 16 h. 99

Figure 63. An enthalpy lost with time on structural relaxation of AM valsartan form annealed at 30, 40 and 60 °C. The value of enthalpy relaxation at T_a = 0 h was subtracted from values of enthalpies of annealed samples to exclude effect of thermal history during cooling/heating run. The relative standard deviations of enthalpy measurements were less than 10%. 100

Figure 64. (A) Intrinsic and (B) apparent dissolution profiles of valsartan in different solid state forms in deionized water 102

Figure 65. Standard DSC curves of crystalline bisoprolol showing 1st heating, cooling (glass transition of amorphised material) and 2nd heating (glass transition, cold crystallization, melting of re-crystallized material). All runs obtained at a 10 °C min^{-1} heating rate. 103

Figure 66. Polarized light photomicrographs of bisoprolol, at (A) 30 °C, showing birefringence indicating crystalline nature of the as-received material, (B) and (C) showing melting transition at, 100 and 101 °C, respectively, (D) fully melted material at 103 °C, and (E) material after cooling in the re-crystallized state, recorded at 30 °C. Re-crystallized material shows different crystal habit (spherulites). Sample was heated with 5 °C min^{-1} rate. 103

Figure 67. TGA curves for valsartan (AR form), crystalline bisoprolol and 50/50 (w/w) physical mixture of bisoprolol/valsartan (AR form), showing no evidence of mass loss before the degradation points of the individual components. 104

Figure 68. Standard DSC curves of the APIs and their 50/50 physical mixtures. The broad endothermic peak in the mixture indicates a significant physical or chemical interaction. All runs obtained at a 10 °C min^{-1} heating rate. 105

Figure 69. (A) 1st and (B) 2nd heating TMDSC experiments. Reversing (dashed line) signals show changes in glass transition and heat capacities. Non-reversing (solid line) signals show changes due to bisoprolol-valsartan interaction and enthalpy relaxation of valsartan (form AR), cold crystallization of bisoprolol, enthalpy relaxation of co-amorphous mixtures and valsartan (form AM). 106

Figure 70. Standard DSC curves obtained at a 5 °C min^{-1} heating rate for APIs and their physical mixtures in a various weight ratios. 107

Figure 71. Polarized light photomicrographs of bisoprolol/valsartan 50/50 physical mixture at (A) 30 °C and (B) 85 °C showing interaction. Sample was heated with 5 °C min^{-1} rate. 107

Figure 72. (A) ^{13}C solution-state NMR spectrum of bisoprolol in D_2O at 25 °C, ^{13}C CPMAS NMR spectra of (B) crystalline and (C) quench-cooled (amorphous) bisoprolol at –20 °C. Asterisks (*) denote spinning sidebands. Arrows (↓) denote signals that are thought to arise from polymorphic or enantiomeric impurities. 109

Figure 73. ^{13}C CPMAS NMR spectral editing experiments for crystalline bisoprolol recorded at room temperature at 6800 Hz spinning rate. (A) Conventional CP MAS, (B – D) CP depolarization with 25, 35 and 100 μs depolarisation time, respectively, and (E) interrupted decoupling spectrum with 40 μs delay time. The signal intensities for the CHs carbons are reduced, for the CH_2s are reduced or inverted and there is relatively little impact on the CH_3s and quaternary carbons in spectra with 25 and 35 μs inversion time (B and C). On spectrum D with 100 μs inversion time all the CHs and CH_2s are inverted leaving a small methyl signals and the quaternaries positive. Interrupted decoupling spectrum (E) shows methyl signals, the quaternary carbons and unexpectedly CHs and/or CH_2s carbons at 67.8 and 72.9 ppm suggesting some mobility in the molecule. Asterisks (*) denote spinning sidebands. 111

Figure 74. ^{13}C CPMAS NMR spectra of (A–E) crystalline, (F) melted then cooled to 80 °C in the liquid amorphous state and (G–J) quench-cooled bisoprolol as a function of calibrated temperature. 112

Figure 75. ^{13}C CPMAS NMR spectra of each API and physical mixtures in different concentrations at 38 and 80 °C. 113

Figure 76. ^{13}C NMR signal intensity vs. cross-polarization contact time for the CH_3 at 14.1 ppm of valsartan and the alkyl signal at 72.9 ppm of bisoprolol in their 50/50 (w/w) physical mixture at 80 °C. 114

Figure 77. Variable-temperature X-ray diffractograms of (A) crystalline and (B) quench-cooled bisoprolol..... 115

Figure 78. X-ray diffractograms of crystalline bisoprolol, amorphous valsartan (form AR) and a 50/50 (w/w) physical mixture of bisoprolol/valsartan (form AR) at (A) 25 °C and (B) 80 °C..... 115

Figure 79. X-ray diffractograms of 50/50 (w/w) physical mixture of bisoprolol/valsartan recorded in the second heating run at 0, 25 and 60 °C. No crystallization is observed above cold crystallization temperature for pure bisoprolol (T_c = 24.2 °C) or glass transition process for the 50/50 (w/w) mixture (T_g = 35.9 °C). XRPD halo pattern is observed at all investigated temperatures confirming amorphous nature of the mixture and lack of tendency to crystallization. 116

Figure 80. X-ray diffractograms of a 70/30 (w/w) bisoprolol/valsartan (form AR) physical mixture at 22, 60 and 80 °C. The results obtained at 80 °C clearly show only partial amorphisation of bisoprolol, with some of bisoprolol remaining in its crystalline state. Please note that the results are obtained from diffractometer operating at Mo K_α radiation in contrast to diffractograms shown on other Figures which were obtained using Cu K_α radiation..... 116

Figure 81. ^{1}H MAS NMR spectra of (A) bisoprolol, (B) valsartan (form AR), (C) valsartan (form AM), (D) 50/50 physical mixture of bisoprolol/valsartan (solid line) (E) 50/50 physical mixture of bisoprolol/valsartan heated to 80 °C (solid line). D and E show also the sum spectra of valsartan and bisoprolol (dashed line). Spectra were recorded at an MAS rate of 53 kHz. Sharper resonances in physical mixtures indicate increased mobility (amorphisation) of the mixture (D–E)..... 118

Figure 82. Proton static spectra of untreated (solid line) and heated to 85 °C (dashed line) 50/50 (w/w) bisoprolol/valsartan physical mixtures recorded at 25 °C. The bandshape of untreated physical mixture is measurably broader ($\Delta\upsilon_{½}$ = 37.6 kHz) then that from the mixture heated to 85 °C ($\Delta\upsilon_{½}$ = 28.9 kHz), implying increased motion in the amorphised material. 119

Figure 83. FT-IR spectra of (A) bisoprolol, (B) valsartan (form AR), (C) untreated and (D) heated to 80 °C 50/50 (w/w) bisoprolol/valsartan physical mixtures acquired at room temperature. Spectra show significant shift of the carbonyl group band of valsartan (C-10, $\upsilon_{C=O}$ = 1732.1 cm^{-1}), indicating the change in the local environment of carboxylic group. Due to peak overlap, it was not possible to obtain specific information about the interaction of bisoprolol in the physical mixture. 121

Figure 84. 2D-DOSY spectra of (A) bisoprolol fumarate in D_2O, (B) bisoprolol fumarate in [D_6]-DMSO and (C) 50/50 (w/w) physical mixture of bisoprolol/valsartan in [D_6]-DMSO. The diffusion coefficient of fumarate increases in presence of valsartan, suggesting competition of valsartan with fumarate. 122

Figure 85. Plots of ^{13}C calculated chemical shielding crystalline valsartan vs. experimental chemical shifts for solid-state AR form and solution-state *trans* and *cis* conformers for ^{13}C. Only chemical shifts for carbons which could be resolved in solid-state for AR form are plotted. Carbon 24 is not observed in the solution thus data is taken from Ref. [78]..... 125

6.1.2 Extended abstract in Polish

Rycina S 1. Krzywe TMDSC przedstawiające całkowity, odwracalny i nieodwracalny strumień ciepła w funkcji temperatury dla walsartanu (forma AR). Krzywe zarejestrowane z szybkością ogrzewania 1 °C min^{-1}. 152

Rycina S 2. XRPD formy AR (niebieska krzywa) i AM (czerwona krzywa) potwierdzające amorficzną strukturę obu form. 152

Rycina S 3. Widma ^{13}C CP MAS SSNMR (A) formy AR i (B) AM walsartanu. Widma zarejestrowane z MAS = 10 kHz. Wstawki pokazują region widma od 40 do 70 ppm zarejestrowany z MAS = 6 kHz. 154

Rycina S 4. (A) Specyficzna szybkość rozpuszczania i (B) dostępność farmaceutyczna form AR i AM walsartanu w H_20. 156

Rycina S 5. Krzywe DSC dla bisoprololu i dwóch form walsartanu oraz ich mieszanin z bisoprololem. Krzywe zarejestrowane z szybkością ogrzewania 10 °C min^{-1}. 157

Rycina S 6. Widma ^{13}C CP MAS NMR (A) bisoprololu, (B) 50/50 mieszaniny bisoprololu i walsartanu (C) 50/50 mieszaniny bisoprololu i walsartanu ogrzanej do temperatury interakcji (80 °C) i ochłodzonej do temperatury pokojowej i (D) formy AR walsartanu. 158

6.1.3 Appendices

Figure A 1. COSY spectrum of valsartan in [D_6]-DMSO recorded at room temperature. 169

Figure A 2. (A) Low-frequency and (B) high-frequency region of $^{1}H–^{13}C$ HSQC spectra of valsartan in [D_6]-DMSO recorded at room temperature. 170

Figure A 3. (A) Low-frequency and (B) high-frequency region of $^{1}H–^{13}C$ HMBC spectra of valsartan in [D_6]-DMSO recorded at room temperature. 171

Figure A 4. COSY spectrum of bisoprolol in [D_6]-DMSO recorded at room temperature. 173

Figure A 5. (A) Low-frequency and (B) high-frequency region of $^{1}H–^{13}C$ HSQC spectra of bisoprolol in [D_6]-DMSO recorded at room temperature. 174

Figure A 6. (A) Low-frequency and (B) high-frequency region of $^{1}H–^{13}C$ HMBC spectra of bisoprolol in [D_6]-DMSO recorded at room temperature. 175

6.2 Tables

6.2.1 Main text

Table I. The spin properties of commonly used in pharmaceutical analysis spin-12 nuclides. The relative receptivity gives measures of the intensities to be expected relative to those for the proton. It is proportional to $\gamma^3 I(I+1)x$ [55]. 51

Table II. Particle size and shape reports for AR form of valsartan. 74

Table III. Solution-, solid-state and calculated NMR chemical shifts for valsartan at 25 °C (in [D_6]-DMSO) and 38 °C (solid state). 84

Table IV. ^{15}N chemical shifts for valsartan and other related tetrazole systems. 93

Table V. Impact of annealing time on T_1^H and $T_{1\rho}^H$ relaxation times for fully amorphous valsartan form (AM form) annealed at 60 °C and recorded at 25 °C. The relaxation times for AR form are shown for comparison. 101

Table VI. Solution- and solid-state NMR chemical shifts for bisoprolol and 50/50 (w/w) bisoprolol/valsartan physical mixture at 25 °C (solution-state) and 38 °C (solid-state). 110

Table VII. Solution-state NMR chemical shifts for valsartan and 50/50 (w/w) bisoprolol/valsartan physical mixture at 25 °C in [D_6]-DMSO. M and m denote major and minor conformers, respectively. 120

6.2.2 Appendices

Table A I. Carbon-13 spin–lattice relaxation times (T_1) for AR and AM valsartan recorded at variable temperature and corresponding errors. 172

Table A II. Spin–lattice relaxation times in the rotating frame ($T_{1\rho}^H$) measured via CP onto ^{13}C for AR and AM valsartan recorded at variable temperature and corresponding errors. 172

7 LIST OF PUBLICATIONS AND PRESENTATIONS

7.1 Journal publications

1. **Skotnicki M**, Aguilar J, Pyda M, Hodgkinson P. *Bisoprolol and Bisoprolol-Valsartan Compatibility Studied by Differential Scanning Calorimetry, Nuclear Magnetic Resonance and X-Ray Powder Diffractometry*. Pharm Res. **2014**:1-16. DOI: 10.1007/s11095-014-1471-7. (**IF = 3.952**)
2. Magoń A, Wurm A, Schick C, Pangloli Ph, Zivanovic S, **Skotnicki M**, Pyda M. *Heat capacity and transition behavior of sucrose by standard, fast scanning and temperature-modulated calorimetry*. Thermochim Acta. **2014**:589(0), 183-196. (**IF = 2.105**)
3. Czerniecka A, Zarzyka I, **Skotnicki M**, Pyda M. *Zastosowanie metod analizy termicznej w badaniach polimorfizmu substancji leczniczych i pomocniczych*. Farm Pol. **2014**:70(3), 153-164. (**MNiSW = 3**)
4. **Skotnicki M**, Gawel A, Cebe P, Pyda M. *Thermal behavior and phase identification of Valsartan by standard and temperature-modulated differential scanning calorimetry*. Drug Dev Ind Pharm. **2013**:39(10), 1508-1514. (**IF = 2.006**)
5. **Skotnicki M**, Kaźmierska M, Pyda M. *Charakterystyka wybranych metod analizy termicznej stosowanych we współczesnej analizie i technologii farmaceutycznej*. Farm Pol. **2012**:68(2), 124-137. (**MNiSW = 3**)

7.2 Conference presentations

1. Kerr H, **Skotnicki M**, Hodgkinson P. *Solid-state nuclear magnetic resonance studies of disordered pharmaceutical materials*., SMARTER 4 (Structure elucidation by coMbining mAgnetic Resonance, compuTation modEling and diffRactions) Conference, University of Durham, Durham, UK, September **2014,** poster 19

2. **Skotnicki M**, Apperley DC, Pyda M and Hodgkinson P. *Characterisation of two amorphous Valsartan forms by multi-technique solid-state NMR*. Royal Society of Chemistry NMR Discussion Group Postgraduate Meeting 2013, School of Chemistry, University of Edinbrough, UK, May **2013**, p. 23, oral presentation.

3. Gaweł A, **Skotnicki M**, Grobelny P, Pyda M. *Compatibility studies between Valsartan, Aspirin and pharmaceutical excipients using Differential Scanning Calorimetry*. 6th Polish-German Symposium on Pharmaceutical Sciences "Perspectives for a new decade", Düsseldorf, Germany, May **2011**, p. 91

4. Wosicka H, Moritz M, Milanowski B, Cal K, **Skotnicki M**, Magoń A, Pyda M. *The experimental evidence of the glass transition of crystal by temperature modulated calorimetry*. 21st IUPAC International Conference on Chemical Thermodynamics ICCT-2010. Tsukuba, Japan, July **2010**, p. 279

5. **Skotnicki M**, Lulek J, Pyda M. *Wykorzystanie różnicowej kalorymetrii skaningowej w badaniach preformulacyjnych antagonistów receptora angiotensynowego AT_1*, Conference of Polish Academy of Sciences „The impact of technological processes on drug dissolution from solid oral dosage forms" Warsaw, Poland, November **2009**, p. 117

6. **Skotnicki M**, Pyda M. *Calorimetric methods for evaluating solid-solid transitions in sartans*, The 64th Calorimetry Conference CALCON 2009, Santa Fe, New Mexico, USA, June **2009**, p. 121

7. **Skotnicki M**, Magoń A, Pyda M.. *Thermal analysis of losartan potassium by temperature-modulated differential scanning calorimetry*, 5th German-Polish Symposium "New challenges for pharmaceutical sciences", Poznan, Poland, May **2009**, p. 59

8 ABSTRACT

Valsartan is an antihypertensive agent belonging to angiotensin II receptor antagonists class called sartans. Valsartan can be used alone or in combination with other antihypertensive drug. Combining drugs with synergistic mechanism of action in one dosage form has potential benefits, such as improved efficacy, reduced dosing, lower cost or enhanced patient compliance. Bisoprolol fumarate is a $beta_1$-selective (cardioselective) adrenoceptor blocking agent. Both valsartan and bisoprolol are used concomitantly in the treatment of cardiovascular diseases, however, there is no single dosage form currently on the market containing both agents.

Valsartan is marketed in a non-crystalline state form. It is estimated that approximately 80–90% of the active pharmaceutical ingredients (APIs) is formulated into solid dosage forms. An active pharmaceutical ingredient used in a solid dosage form can exist in crystalline or amorphous state. Amorphous active pharmaceutical ingredients have been used in the development of pharmaceutical solid formulations due to their advantages over crystalline forms such as increased solubility and dissolution rate. However, amorphous APIs are usually less stable than their crystalline counterparts.

The occurrence of polymorphism in crystal pharmaceuticals and its impact on physicochemical properties on API is well documented in the pharmaceutical literature. Polyamorphism has been reported for inorganic compounds but, it is believed that, there is no example of polyamorphism in pharmaceutics therefore investigation into the existence of polyamorphism in organic APIs is crucial. However, the differences in amorphous forms regarding stability and physicochemical properties, obtained by various preparation techniques have been reported for APIs. Despite a wide variety of analytical techniques available to characterise solid state such as differential scanning calorimetry (DSC), Fourier transform infra-red spectroscopy (FT-IR), solid-state nuclear magnetic resonance (SSNMR) or X-ray powder diffractometry (XRPD), the

structural characterisation of subtle differences between different amorphous forms of active pharmaceutical ingredients continues to be a challenge. The physicochemical properties of a solid API are strongly related not only to its structural features but also to its molecular dynamics. It is important to understand the dynamic of molecular motion occurring in an amorphous APIs, as molecular relaxation takes place during storage of formulated amorphous drug.

In this dissertation differential scanning calorimetry and solid-state NMR were used to characterise solid state of two amorphous valsartan forms (AR and AM) and crystalline and amorphous forms of bisoprolol fumarate, and also to evaluate their compatibility. Form AR of valsartan was the commercially available material and form AM was the material obtained by heating the AR form to 140 °C and rapidly cooled to a room temperature. The main analytical techniques were supported by, where appropriate, particle size and shape analysis, hot-stage microscopy (HSM), thermogravimetric analysis (TGA), solution-state NMR, FT-IR, XRPD, and dissolution studies. The study revealed that both valsartan forms exist as the amorphous materials with higher level of structure arrangement in the AR form. Both forms are physically and chemically stable within analysed range of temperature and do not crystallize. The DSC curve of AR form showed two endotherms, occurring around 80 °C and 100 °C, related to evaporation of solvent and an enthalpy relaxation with a high value around 16 J g^{-1}, respectively. The glass transition of AR valsartan form was found to be around 76 °C (fictive temperature) whereas for AM form at 74 °C. TMDSC allowed for separation of the total heat-flow rate into reversing and non-reversing parts showing overlapped thermodynamic and kinetic processes. The non-reversing curve corresponded to the enthalpy relaxation and the reversing curve clearly showed the glass transition in the AR form confirming its amorphous nature. XRPD confirmed that both forms exist in the amorphous state. Subtle differences between two forms could be observed by FT-IR whereas 1D and 2D SSNMR clearly distinguished both forms at the molecular level. It was possible to distinguish different structures in two amorphous

forms by ^{13}C and ^{15}N SSNMR i.e.: form AR exists nearly as a pure, conformational isomer and form AM as a mixture of isomers due to the hindered rotation of C(O)–N peptide bond.

Nitrogen-15 NMR experiments unambiguously confirmed that both valsartan forms exist as an 1,2,3,4-tetrazole tautomeric forms. Ultra-fast ^{1}H MAS NMR revealed differences in the hydrogen bonding in both forms. The subtle differences between both forms and in annealed AM form in molecular mobility were also found by NMR relaxation times. Moreover, the increase in the molecular mobility above the glass transition temperature for both forms was found to be mainly due to changes of mobility in the aromatic rings. Furthermore, both forms showed significantly different dissolution behaviour and surprisingly, more ordered form (AR form) material had greater dissolution rate than the fully disordered material (AM form).

Also the crystalline and amorphous forms of bisoprolol and its compatibility with two amorphous forms of valsartan were analysed. Amorphous bisoprolol has low stability and re-crystallizes above the glass transition (T_g = –3.6 °C). Thermal behaviour of crystalline and quench-cooled drug is presented. NMR experiments allowed the investigation of the conformational and dynamic properties of the pure bisoprolol fumarate. The physical mixtures of bisoprolol and valsartan with different concentrations were prepared and changes in thermal behaviour due to interaction were observed by DSC and TMDSC. The interactions between those drugs were further confirmed by XRPD, and the molecular-level nature of interactions was investigated by solution- and solid-state NMR. Strong interactions leading to incompatibility between bisoprolol and valsartan in the solid state were observed above 60 °C. XRPD and SSNMR indicate that the new material is in an amorphous state, and provided insight into the molecular nature of the incompatibility. In the solid state bisoprolol fumarate and valsartan react forming a new amorphous product. Therefore, formulation of a fixed-dose combination would require separate reservoirs for bisoprolol fumarate and

valsartan to prevent interactions between the components. Similar problems might be expected with excipients or APIs containing carboxylic groups.

This contribution clearly demonstrates the importance of characterisation of amorphous pharmaceutical materials as there might be some differences in order and/or conformations in that types of materials which might have an influence on physicochemical properties and thus potentially on the pharmacological action of the final dosage form. It was proved that calorimetric methods and SSNMR spectroscopy offer powerful tools for identification and characterisation of differently disordered amorphous forms of small APIs as well as for identification and characterisation of incompatibilities between API-API or API-excipient.

9 EXTENDED ABSTRACT IN POLISH

STRESZCZENIE

Charakterystyka walsartanu oraz badanie jego zgodności fizykochemicznej z bisoprololem z wykorzystaniem różnicowej kalorymetrii skaningowej i magnetycznego rezonansu jądrowego w fazie stałej

Nadciśnienie tętnicze należy obecnie do najczęstszych, przewlekłych chorób układu krążenia zarówno w Polsce jak i na świecie. Przewlekły charakter choroby sprawia, że pacjent zmuszony jest do przyjmowania leków do końca życia oraz znaczącej modyfikacji stylu życia. Niespełnienie tych warunków prowadzi do rozwoju groźnych dla życia powikłań sercowo-naczyniowych. Należą one do jednych z najczęstszych przyczyn umieralności w krajach zarówno rozwiniętych jak i rozwijających się. Pomimo stałego postępu, jaki dokonuje się w farmakoterapii nadciśnienia tętniczego, dane epidemiologiczne dotyczące tej choroby są wciąż niezadowalające.

Selektywne blokery receptorów angiotensyny II typu 1 (AT_1), zwane sartanami, to nowoczesna grupa leków stosowana w leczeniu nadciśnienia tętniczego. Wykorzystywane są one zarówno w monoterapii jak i w leczeniu skojarzonym z innymi lekami hipotensyjnymi. Do niewątpliwych korzyści wynikających ze stosowania sartanów należy zaliczyć: długotrwały efekt hipotensyjny, łagodny początek działania, brak odruchowej tachykardii, dawkowanie raz na dobę czy mniejszą częstość występowania nowych przypadków cukrzycy typu 2 w trakcie leczenia. Ze względu na korzystny profil farmakologiczny oraz wywoływanie niewielu działań niepożądanych (porównywalnych z placebo), w niedalekiej przyszłości ta grupa leków ma szanse na znaczące zwiększenie swojego udziału w terapii chorób sercowo-naczyniowych. Ponadto wyniki wieloośrodkowych badanń klinicznych z udziałem sartanów, mogą w istotny sposób wpłynąć na zmodyfikowanie obowiązujących standardów leczenia i poprawić rokowanie w grupie pacjentów z wysokim ryzykiem sercowo-naczyniowym. Jednym z przedstawicieli omawianej grupy leków jest walsartan. Aktywność farmakologiczną wykazuje jego enancjomer *S*, stąd też dostępne na rynku preparaty

zawierają wyłącznie ten enancjomer. Walsartan jest stosowany w postaci wolnego kwasu, którego dostępność biologiczna po podaniu doustnym nie przekracza 25%.

Bisoprolol to lek z grupy β-adrenolityków o największej wybiórczości w stosunku do receptorów β_1, pozbawiony wewnętrznej aktywności sympatykomimetycznej i właściwości stabilizujących błonę komórkową. Aktywność farmakologiczną wykazuje enancjomer *S*; dostępne preparaty zawierają mieszaninę racemiczną. Bisoprolol jest stosowany w postaci soli kwasu fumarowego. Po podaniu doustnym dostępność biologiczna bisoprololu wynosi około 90%. Jest on stosowany w leczeniu choroby niedokrwiennej serca, nadciśnieniu tętniczym czy zaburzeniach rytmu serca. Bisoprolol, podobnie jak walsartan, jest na ogół dobrze tolerowany przez pacjentów, a działania niepożądane są zwykle o średnim stopniu nasilenia.

Najbardziej powszechną i zarazem najwygodniejszą dla pacjenta drogą podania leku jest droga doustna. Obecnie najczęściej stosowaną postacią leku są tabletki, czyli postać leku w stanie stałym. Dzieje się tak ze względów terapeutycznych, technologicznych i ekonomicznych. Aktywne substancje farmaceutyczne (ang. *Active Pharmaceutical Ingredients*, APIs) w stanie stałym mogą występować w postaci krystalicznej lub bezpostaciowej – amorficznej. Struktura wewnętrzna substancji amorficznej, w przeciwieństwie do krystalicznej, nie jest uporządkowana, ale nie jest też zupełnie przypadkowa. Może posiadać uporządkowanie bliskiego zasięgu (ang. *short-range order*), ale brak jest uporządkowania dalekiego zasięgu (ang. *long-range order*). Z termodynamicznego punktu widzenia substancje amorficzne mają wyższą entalpię, entropię i energię swobodną od odpowiadających im kryształów. Walsartan jest obecny na rynku farmaceutycznym w postaci tabletek lub kapsułek, w których występuje on w postaci niekrystalicznej. Wprawdzie autorzy w niektórych doniesieniach naukowych klasyfikują postać walsartanu jako krystaliczną, jednak prezentowane przez nich wyniki analizy XRPD (ang. *X-ray powder diffractometry*) wskazują na amorficzność tego materiału.

Jak wcześniej wspomniano, forma amorficzna charakteryzuje się nieuporządkowaną strukturą wewnętrzną. Odmienna struktura ciał stałych jest przyczyną znacznych różnic we właściwościach fizykochemicznych substancji leczniczych, głównie temperatury topnienia, gęstości, twardości i szybkości rozpuszczalności, co ma bezpośredni wpływ na ich klasyfikację biofarmaceutyczną (ang. *Biopharmaceutics Classification System*, BCS). Szybkość rozpuszczania, wywiera bezpośredni wpływ na biodostępność substancji aktywnej, a tym samym decydują o jej skuteczności terapeutycznej. W związku z tym badanie uwalniania jest przyjęte jako jedna z metod oceny jakości preparatów na etapie rozwoju nowej formulacji, a po ich rejestracji staje się testem rutynowym, mającym udowodnić powtarzalność procesu produkcyjnego dla każdej serii preparatu. Służy ono również ocenie wpływu zamierzonych zmian składu formulacji, parametrów procesu produkcyjnego oraz warunków przechowywania na właściwości finalnego produktu. Badanie to może wykazać różnorodne zmiany właściwości leku, nawet te trudne do wykrycia innymi metodami. Wspomniany walsartan charakteryzuje się stosunkowo niską dostępnością biologiczną i jest zaliczany do II klasy systemu BCS (słabo rozpuszczalny ale dobrze przenikalny przez błony biologiczne). Forma amorficzna w porównaniu do postaci krystalicznej tej samej substancji, cechuje się zazwyczaj większą szybkością rozpuszczania. Większa szybkość rozpuszczania substancji leczniczej w formie amorficznej warunkuje skuteczność terapeutyczną przy niższej dawce niż w postaci krystalicznej, zmniejszając tym samym ryzyko wystąpienia działań niepożądanych. Stąd ostatnio wśród naukowców i producentów leków obserwuje się duże zainteresowanie postacią amorficzną. Substancje amorficzne można otrzymać różnymi metodami, np. przez szybkie schłodzenie stopionej substancji, kondensację pary, strącanie z roztworów, mielenie substancji krystalicznej czy liofilizację. Jednakże zastosowanie substancji amorficznych wiąże się z problemami wynikającymi z ich niskiej stabilności fizykochemicznej.

Zjawisko polimorfizmu jest powszechnie znane i szeroko dyskutowane w odniesieniu do krystalicznych odmian substancji farmaceutycznych. Natomiast, zjawisko wielopostaciowości substancji amorficznej zwane poliamorfizmem, zostało zaobserwowane i opisane jedynie dla substancji nieorganicznych. Na dzień dzisiejszy brak jest dostępnych danych na temat zaobserwowania tego zjawiska w odniesieniu do organicznych substancji farmaceutycznych. Stąd też zajęcie się tym zagadnieniem wydaje się być niezwykle istotne z punktu widzenia nauk farmaceutycznych, szczególnie, że ewentualne różnice w strukturze amorficznych ciał stałych mogą mieć wpływ na właściwości fizykochemiczne substancji aktywnej. W trakcie procesów technologicznych, w wyniku zmiany temperatury, ciśnienia, czy wilgotności może dojść do przejścia fazowego jednej formy ciała stałego w inną formę. Postać amorficzna jest mniej stabilna termodynamicznie, stąd będzie bardziej narażona na transformację podczas niektórych jednostkowych procesów technologicznych. Większość substancji amorficznych wykazuje tendencje do krystalizacji. Nieoczekiwane powstawanie lub znikanie określonej formy stanu stałego danej substancji leczniczej w trakcie jej przetwarzania może prowadzić do poważnych konsekwencji farmaceutycznych i terapeutycznych. Stąd też analiza odmian polimorficznych i amorficznych substancji farmaceutycznych oraz przejść fazowych w stanie stałym ma kluczowe znaczenie zarówno na etapie prac badawczo-rozwojowych nad nową formulacją, jak i podczas procesu produkcji.

Pomimo szerokiej gamy technik badawczych wykorzystywanych w analizie ciała stałego takich jak np. różnicowa kalorymetria skaningowa (ang. *differential scanning calorimetry*, DSC), spektroskopia w podczerwieni (ang. *Fourier transform infra-red spectroscopy*, FT-IR), magnetyczny rezonans jądrowy w fazie stałej (ang. *solid-state nuclear magnetic resonence*, SSNMR) czy proszkowa dyfrakcja rentgenowska (XRPD), charakterystyka ciał amorficznych wciąż pozostaje dużym wyzwaniem. Oprócz struktury ciała stałego, na właściwości fizykochemiczne ciał

amorficznych, może mieć wpływ dynamika molekularna, dlatego jej badanie wydaje się być istotnym elementem charakterystyki ciał amorficznych.

Zarówno walsartan jak i bisoprolol są stosowane łącznie w terapii chorób sercowo-naczyniowych. Obecnie na rynku farmaceutycznym nie istnieje preparat złożony zawierający obie te substancje aktywne. Warto zauważyć, że w fazie procedury rejestracyjnej do FDA (ang. *US Food and Drug Administration*) jest preparat złożony zawierający walsartan i inny beta-bloker – nebiwolol. Uważa się, że stosowanie preparatów złożonych umożliwia redukcję dawki, prowadzi do zwiększonej skuteczności leczenia czy też do lepszego przestrzegania zaleceń lekarskich przez pacjenta odnośnie regularnego przyjmowania leku. Terapia preparatami złożonymi przyczynia się do 80% obniżenia powikłań sercowo-naczyniowych. Stąd też przemysł farmaceutyczny jest wysoce zainteresowany wytworzeniem tzw. *polypill*, tj. preparatu zawierającego inhibitor ACE (ang. *angiotensin-converting enzyme*), beta-bloker, aspirynę i statynę. Najprostszym sposobem otrzymania preparatu złożonego jest zmieszanie substancji aktywnych z substancjami pomocniczymi i kompresja otrzymanej masy tabletkowej. Między substancjami leczniczymi i pomocniczymi wchodzącymi w skład leków może dochodzić do różnego rodzaju oddziaływań. Zachodzące interakcje mogą mieć wpływ pozytywny (np. prowadzić do zwiększenia stopnia rozpuszczalności i okresu trwałości substancji leczniczej) lub negatywny, prowadząc do nieprzewidzianych i niepożądanych zjawisk. W procesie tworzenia mieszanin substancji farmaceutycznych może dojść do interakcji pomiędzy jej składnikami i w efekcie do niezgodności farmaceutycznej, które mogą wpływać na właściwości fizykochemiczne API. To z kolei może spowodować zmiany dostępności biologicznej i wartości terapeutycznej preparatu leczniczego. Niezgodności w fazie farmaceutycznej mogą mieć charakter zjawisk chemicznych lub/i fizycznych. Niezgodności chemiczne są zazwyczaj wynikiem m.in. reakcji zobojętniania, hydrolizy, utleniania i redukcji, kompleksowania czy izomeryzacji. Natomiast niezgodności fizyczne występują w efekcie m.in. takich procesów jak absorpcja, adhezja, adsorpcja,

emulgowanie, rozdzielanie, rozpuszczanie, solubilizacja, solwatacja czy wilgotnienie. Przykładowo Bristol-Myers Squibb w latach 2010–11 wycofał ponad 60 milionów tabletek preparatu złożonego (Avalide®) zawierającego bloker receptorów AT_1 – irbesartan i lek diuretyczny – hydrochlorotiazyd z powodu pojawienia się formy irbesartanu o mniej pożądanym profilu uwalniania. Trzeba zauważyć, że sytuacja taka nie miała miejsca w przypadku preparatu zawierającego sam irbesartan. Badanie zgodności pomiędzy substancjami leczniczymi i pomocniczymi jest bardzo ważnym elementem etapu projektowania postaci leku, dlatego przeprowadza się je już na wczesnym etapie prac badawczo-rozwojowych. Metodą stosowaną do wykrywania interakcji między substancjami aktywnymi a substancją aktywną czy pomocniczą jest często DSC. Jest to szybka metoda wymagająca niewielkiej ilości substancji badanej, co jest niezwykle istotne szczególnie na początku prac nad nowym lekiem, gdzie ilość substancji jest zazwyczaj ograniczona. Interpretacja wyniku polega na zaobserwowaniu różnic w termogramach substancji aktywnej i mieszaniny substancji aktywnej z substancją badaną polegających na przesunięciu, zaniknięciu lub pojawieniu się piku endo- lub egzotermicznego. Jednak nie wszystkie zmiany w termogramie można uznać za interakcję. Stąd też jednoznaczna interpretacja wyników nie zawsze jest możliwa i dlatego w przypadku wątpliwości należy przeprowadzić badania dodatkowe z wykorzystaniem takich technik jak m.in. wysokosprawna chromatografia cieczowa, FT-IR czy XRPD. Magnetyczny rezonans jądrowy w fazie stałej nie jest rutynowo stosowany do wykrywania interakcji, jednak doniesienia na temat interakcji API z substancjami pomocniczymi są dostępne w piśmiennictwie.

Celem prowadzonych badań była charakterystyka fizykochemiczna dwóch amorficznych postaci walsartanu oraz krystalicznej i amorficznej postaci fumaranu bisoprololu a także badanie zgodności farmaceutycznej obu substancji. Głównymi zastosowanymi metodami badawczymi była różnicowa kalorymetria skaningowa i różnicowa kalorymetria skaningowa z modulacją temperatury (ang. *temperature-modulated DSC*, TMDSC) oraz magnetyczny rezonans jądrowy w fazie

stałej. Dodatkowo wykorzystano aparat do badania morfologii i wielkości cząstek, termomikroskopię, analizę termograwimetryczną (ang. *thermogravimetric analysis*, TGA) spektroskopię w podczerwieni, magnetyczny rezonans jądrowy w roztworze (NMR), proszkową dyfrakcję rentgenowską oraz badania specyficznej i pozornej szybkości rozpuszczania (ang. *intrinsic dissolution rate*, IDR; *apparent dissolution rate*, ADR). Scharakteryzowano dwie formy amorficzne walsartanu, tj.: próbkę handlową (forma AR) oraz próbkę otrzymaną przez ogrzanie formy AR do temperatury 140 °C i następnie jej szybkie schłodzenie do temperatury pokojowej (forma AM). Badania wykazały, że walsartan w stanie stałym występuje w dwóch różnych postaciach amorficznych. Forma handlowa walsartanu (AR), czasami błędnie opisywana w doniesieniach naukowych jako krystaliczna, charakteryzuje się większym uporządkowaniem cząsteczek niż forma amorficzna otrzymana poprzez ogrzanie materiału wyjściowego (AM). Obie formy odznaczają się stabilnością fizykochemiczną w analizowanych zakresach temperatury i nie ulegają krystalizacji podczas ogrzewania lub chłodzenia. Analiza termograwimetryczna ukazała trzy główne etapy straty masy podczas ogrzewania próbki. W pierwszym etapie w zakresie temperatury 60–90 °C strata masy jest związana z odparowaniem, rozpuszczalnika zawartego w materiale. Natomiast w drugim i trzecim etapie następuje rozkład cząsteczki walsartanu. Krzywa DSC formy AR ujawniła dwa endotermiczne sygnały, pierwszy związany z odparowaniem rozpuszczalnika około temperatury 80 °C i drugi związany z przejściem szklistym z dużą wartością entalpii relaksacji (16 J g^{-1}) około 100 °C. Temperaturę przejścia szklistego formy AR określono przez temperaturę fikcyjną (tzw. Richardsona), która wynosi około 76 °C. Dla formy AM zaobserwowano typowe przejście szkliste w temperaturze około 74 °C. Zastosowanie TMDSC pozwoliło rozdzielić procesy kinetyczne (entalpia relaksacji) od termodynamicznych (przejście szkliste) i jednoznacznie potwierdzić amorficzność materiału wyjściowego, Rycina S 1. Badania rentgenograficzne potwierdziły amorficzną strukturę obu form walsartanu

także wskazując na większy stopień uporządkowania cząsteczek w formie AR, Rycina S 2.

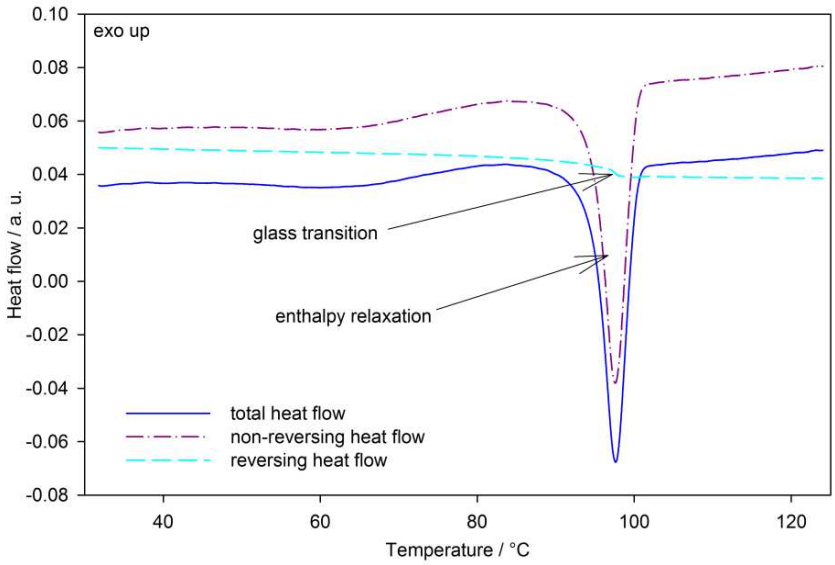

Rycina S 1. Krzywe TMDSC przedstawiające całkowity, odwracalny i nieodwracalny strumień ciepła w funkcji temperatury dla walsartanu (forma AR). Krzywe zarejestrowane z szybkością ogrzewania 1 °C min^{-1}.

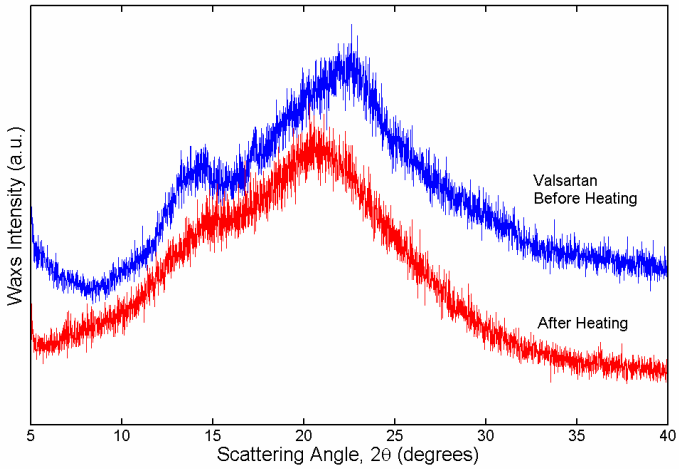

Rycina S 2. XRPD formy AR (niebieska krzywa) i AM (czerwona krzywa) potwierdzające amorficzną strukturę obu form.

Zastosowanie metody spektroskopii w podczerwieni pozwoliło zaobserwować subtelne różnice na poziomie molekularnym między dwoma formami walsartanu, tj. zauważono niewielkie przesunięcie pasma odpowiadającego grupie karbonylowej (C(5)O) wiązania amidowego w kierunku wyższej wartości długości fali w przypadku

formy AM. Przesunięcie to może być spowodowane rozerwaniem wiązań wodorowych w tej formie. Natomiast jedno- i dwuwymiarowe eksperymenty SSNMR jednoznacznie potwierdziły te różnice. Porównując widma ^{13}C SSNMR można zauważyć poszerzenie sygnałów dla formy AM w stosunku do materiału wyjściowego, co wskazuje na amorfizację materiału, Rycina S 3. Wartości przesunięć chemicznych dla większość sygnałów pozostają niezmienione. Istotne różnice można zauważyć dla węgli C-6 i C-11 czyli atomów bezpośrednio połączonych z azotem (N-1) grupy amidowej. W formie AM sygnał pochodzący od węgla C-11 ulega znacznemu poszerzeniu i przesunięciu ($\Delta\delta_C$ = –2,1 ppm). Natomiast sygnał pochodzący od węgla C-6 (65,8 ppm, forma AR) ulega rozszczepieniu na dwa sygnały (62,3 i 67,3 ppm). Analiza widm węglowych i azotowych pozwala przypuszczać, że forma AM występuje jako mieszanina izomerów *cis–trans*, natomiast forma AR jako, w większości, jeden izomer z niewielkim zanieczyszczeniem drugim izomerem. Izomeria najprawdopodobniej wynika z wiązania peptydowego (C(O)–N). To zjawisko występujące w stanie stałym jest podobne do zaobserwowanego w podczas analizy NMR roztworu walsartanu.

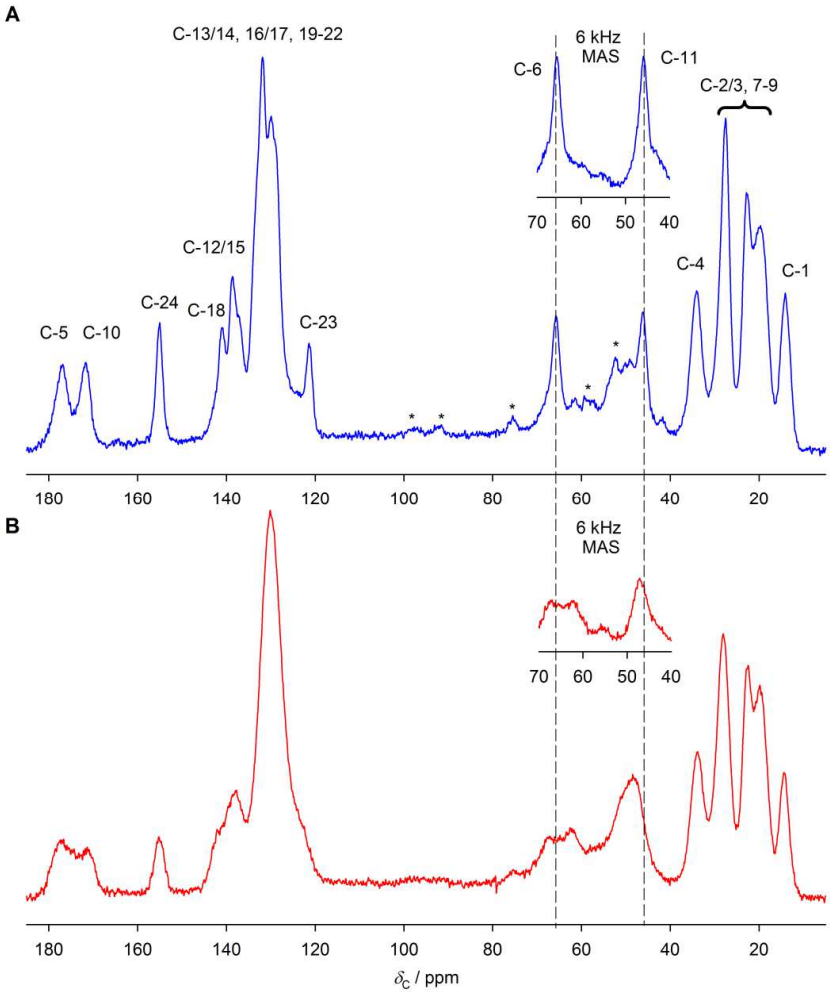

Rycina S 3. Widma ^{13}C CP MAS SSNMR (A) formy AR i (B) AM walsartanu. Widma zarejestrowane z MAS = 10 kHz. Wstawki pokazują region widma od 40 do 70 ppm zarejestrowany z MAS = 6 kHz.

Dane uzyskane z pomiarów zmienno-temperaturowych ^{13}C SSNMR sugerują, że do zmiany konformacji w formie AR dochodzi podczas przejścia szklistego. Natomiast dla formy AM nie zauważono znaczących zmian konformacyjnych poniżej i powyżej temperatury przejścia szklistego.

Jako, że walsartan, ze względu na występowanie w jego strukturze pierścienia tetrazolowego, w stanie stałym może teoretycznie istnieć w postaci dwóch tautomerów, dokonano analizy za pomocą ^{15}N SS NMR. Zjawisko takie zaobserwowano dla podobnego API – irbesartanu. Widma ^{15}N SS NMR formy AR ukazały pięć głównych sygnałów rezonansowych oraz sygnały pochodzące prawdopodobnie od zanieczyszczenia drugim izomerem. W formie AM piki te

wyraźnie zwiększyły swoją intensywność co sugeruje izomeryzację, podobnie jak w przypadku pomiarów za pomocą ^{13}C SSNMR. Azot związany z protonem (N-5) w formie AR został zidentyfikowany przy pomocy eksperymentu ^{15}N IR (ang. *inversion-recovery*) CP MAS NMR (–149,4 ppm). Eksperymenty te potwierdziły występowanie obu form walsartanu w postaci 1,2,3,4-tetrazolowego tautomeru.

W celu analizy wiązań wodorowych w obu formach zastosowano technikę ^{1}H MAS NMR. Wyniki analizy wskazują wyraźnie na różnice w wiązaniach wodorowych między dwoma formami. Zostało zaobserwowane pięć różnych sygnałów rezonansowych, tj. protony alkilowe (≈0,9 ppm), protony alkilowe węgla C-6 i C-11 związane z atomem azotu N-1 (≈5,6 ppm), protony aromatyczne (≈7,1 ppm), proton grupy karboksylowej (≈14,2 ppm) i proton pierścienia tetrazolowego (≈16,4 ppm). Sygnały pochodzące od protonów C-6 i C-11 w formie AM wykazują mniejszą intensywność co może sugerować amorfizację i zmiany konformacyjne zaobserwowane za pomocą ^{13}C i ^{15}N SSNMR. Ponadto widma formy całkowicie amorficznej ukazują znaczącą zmianę przesunięcia chemicznego dla protonu pierścienia tetrazolowego (N(5)H, $\Delta\delta_H = 1{,}1$ ppm) sugerując jego zaangażowanie w tworzeniu wiązania wodorowego. Sygnał pochodzący od protonu grupy karboksylowej (C(10)OOH) ulega poszerzeniu i zmienia się wartość jego przesunięcia chemicznego, jednakże z powodu niskiej rozdzielczości nie było możliwe oszacowanie jego wartości tego przesunięcia. Powyższe wyniki sugerują, że wiązania wodorowe w formie amorficznej AR mogą być podobne do tych występujących w postaci krystalicznej walsartanu.

Dzięki zastosowaniu pomiarów czasów relaksacji NMR zostały zaobserwowane niewielkie różnice w dynamice molekularnej badanych form oraz starzonej formy AM. Ponadto, wykazano, że różnice w mobilności molekularnej podczas przejścia szklistego wynikają prawdopodobnie głównie ze zmiany mobilności pierścieni aromatycznych.

Różnice w budowie na poziomie mikroskopowym dwóch form przekładają się na różnice profilach rozpuszczania badanych materiałów. Wykazano, że bardziej

uporządkowany materiał odznacza się prawie dwukrotnie większą specyficzną szybkością rozpuszczania niż materiał całkowicie amorficzny (dla formy AR IDR = 24,6 ±0,1 μg min^{-1} cm^{-2}, a dla formy AM IDR = 11,0 ±0,1 μg min^{-1} cm^{-2}), Rycina S 4A. Istotne różnice zaobserwowano również w pozornej szybkości rozpuszczania obu materiałów, Rycina S 4B.

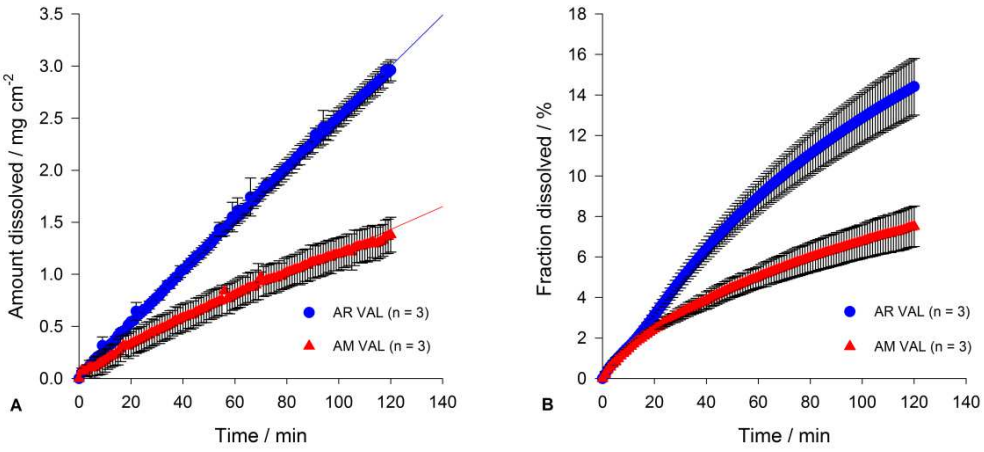

Rycina S 4. (A) Specyficzna szybkość rozpuszczania i (B) pozorna szybkość rozpuszczania form AR i AM walsartanu w H_20.

Ponadto w pracy przedstawiono charakterystykę formy krystalicznej i amorficznej fumaranu bisoprololu oraz zbadano jego zgodność farmaceutyczną z walsartanem. Na podstawie analizy DSC stwierdzono, że krystaliczny bisoprolol ulega topnieniu w temperaturze około 102 °C. W trakcie drugiego podgrzewania zaobserwowano trzy procesy: przejście szkliste (T_g = –3,6 °C), zimną krystalizację (24,2 °C) oraz topnienie w temperaturze około 95 °C. Obniżenie temperatury topnienia bisoprololu podczas drugiego ogrzewania może wynikać z różnic w morfologii materiału po rekrystalizacji. Badanie wykazało niestabilność amorficznego bisoprololu, który ulega rekrystalizacji powyżej temperatury przejścia szklistego. Analiza NMR pozwoliła na zbadanie zmian konformacyjnych i dynamiki molekularnej bisoprololu. Mieszaniny fizyczne bisoprololu z walsartanem w różnych stosunkach wagowych składników zostały zanalizowane za pomocą metod termicznych. Wyniki analizy TGA nie ujawniły interakcji pomiędzy składnikami mieszaniny. Natomiast zastosowanie

standardowej DSC pozwoliło na stwierdzenie interakcji przejawiającej się zanikiem piku endotermicznego związanego z procesem topnienia bisoprololu i pojawieniem się szerokiego piku w zakresie około 60–100 °C, Rycina S 5. Analiza TMDSC potwierdziła interakcję między bisoprololem i walsartanem w temperaturze powyżej 60 °C. TMDSC umożliwiła rozdzielenie zjawisk kinetycznych i termodynamicznych ukazując proces przejścia szklistego mieszaniny bisoprololu i walsartanu w różnych stosunkach wagowych składników. W większości przypadków T_g znacznie różniły się od temperatury przejścia szklistego czystych substancji.

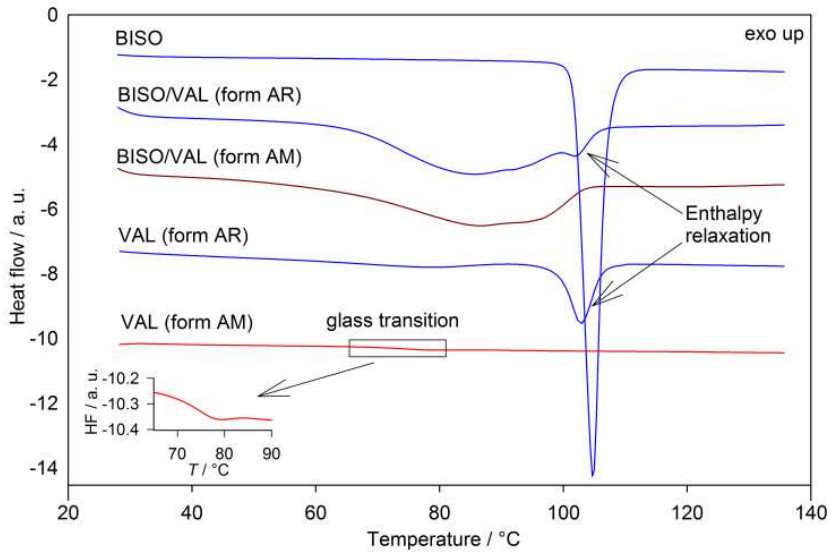

Rycina S 5. Krzywe DSC dla bisoprololu i dwóch form walsartanu oraz ich mieszanin z bisoprololem. Krzywe zarejestrowane z szybkością ogrzewania 10 °C min^{-1}.

Z kolei analiza dyfraktometryczna (XRPD) mieszaniny bisoprololu z walsartanem ujawniła, że w wyniku interakcji dochodzi do amorfizacji bisoprololu. NMR w fazie stałej i w roztworze dostarczyły informacji o naturze interakcji. Widmo ^{13}C SSNMR ukazało znaczne poszerzenie pików pochodzących od bisoprololu w mieszaninie z walsartanem potwierdzając niezgodność prowadzącą do amorfizacji materiału, Rycina S 6.

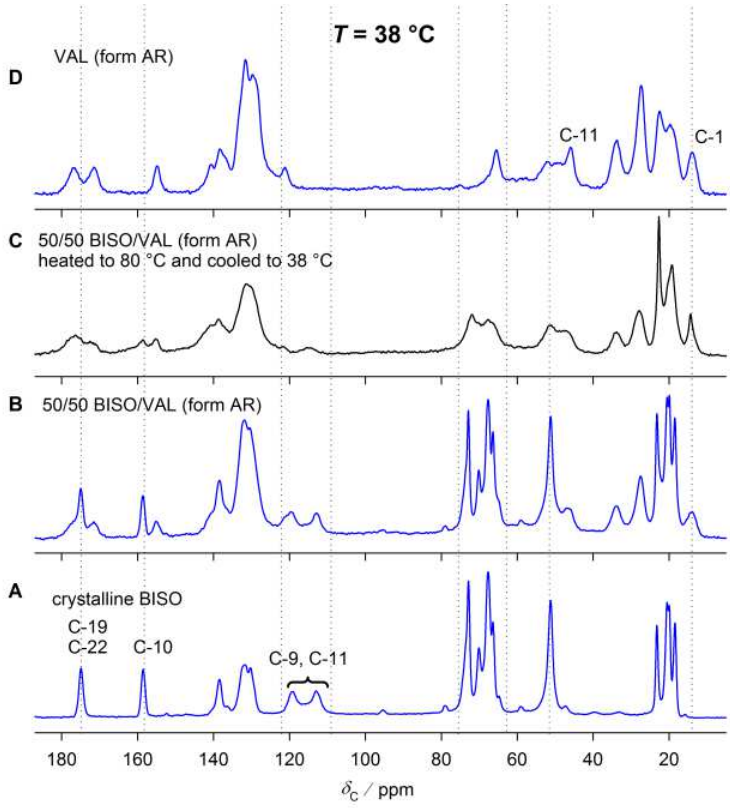

Rycina S 6. Widma ^{13}C CP MAS NMR (A) bisoprololu, (B) 50/50 mieszaniny bisoprololu i walsartanu (C) 50/50 mieszaniny bisoprololu i walsartanu ogrzanej do temperatury interakcji (80 °C) i ochłodzonej do temperatury pokojowej i (D) formy AR walsartanu.

Eksperymenty DOSY (ang. *diffusion ordered spectroscopy*) sugerują, że interakcja wynika z współzawodnictwa walsartanu z resztą kwasu fumarowego o grupę aminową bisoprololu. Mimo, że nie można jednoznacznie odnosić zjawisk zachodzących w roztworze do zjawisk zachodzących w ciele stałym, wyniki analizy DOSY są zgodne z zaobserwowaną amorfizacją kryształu bisoprololu wykrytych za pomocą innych technik. Wyniki badania zgodności w fazie farmaceutycznej wskazują, że przy projektowaniu procesu technologicznego wytwarzania tabletek zawierających bisoprolol i walsartan należałoby uwzględnić brak możliwości zastosowania bezpośredniego mieszania obu substancji leczniczych z substancjami pomocniczymi z następującą kompresją masy tabletkowej. W technologii złożonego produktu niezbędne byłoby fizyczne oddzielenie od siebie obu substancji aktywnych. Ponadto podobnej

interakcji z fumaranem bisoprololu można spodziewać się w przypadku substancji aktywnych czy pomocniczych zawierających grupę karboksylową.

W wyniku przeprowadzonych badań stwierdzono, że walsartan występuje w postaci dwóch różnych form amorficznych istotnie różniących się profilami rozpuszczalności. Różnice te mogą znacząco wpływać na skuteczność terapeutyczną finalnego preparatu leczniczego. Stąd też wyniki badań zawarte w pracy jednoznacznie wskazują na ważność charakterystyki substancji amorficznych, jako że różnice w strukturze materiałów amorficznych mogą wpływać na właściwości fizykochemiczne API. Potwierdzono, że metody kalorymetryczne są użytecznymi narzędziami do identyfikacji i charakterystyki materiałów amorficznych oraz do badania niezgodności farmaceutycznych między substancjami aktywnymi czy też substancjami aktywnymi i pomocniczymi. Szczególnie użytecznym narzędziem do charakterystyki substancji amorficznych okazała się być temperaturow-modulowana DSC, która pozwala na rozdzielenie pików pochodzących od różnych procesów nakładających się, tj. przejścia szklistego i relaksacji materiału amorficznego. Wykazano również użyteczność SSNMR do charakterystyki amorficznych ciał stałych na poziomie molekularnym. Metoda ta pozwala na wykrycie subtelnych różnic pomiędzy formami amorficznymi. SSNMR jest również użyteczną metodą w badaniu niezgodności w fazie farmaceutycznej pomiędzy składnikami preparatów farmaceutycznych. Przeprowadzone badania wskazują również na konieczność stosowania pomiarów zmienno-temperaturowych zarówno SSNMR jaki XRPD w celu wykrycia interakcji prowadzących do niezgodności, jako że interakcja może nie zostać wykryta w temperaturze pokojowej.

10 REFERENCES

1. Hillery AM, Lloyd AW, Swarbrick J. Drug Delivery and Targeting: For Pharmacists and Pharmaceutical Scientists. London: Taylor & Francis; 2003.
2. Shalaev E, Zografi G. The concept of 'structure' in amorphous solids from the perspective of the pharmaceutical sciences. In: Levine H, editor. Amorphous Food and Pharmaceutical Systems. Cambridge: The Royal Society of Chemistry; 2002. p. 11-30.
3. Petit S, Coquerel G. The Amorphous State. In: Hilfiker R, editor. Polymorphism: in the Pharmaceutical Industry. Weinheim: Wiley-VCH Verlag GmbH & Co. KGaA; 2006. p. 259-285.
4. Hancock BC, Parks M. *What is the True Solubility Advantage for Amorphous Pharmaceuticals?* Pharm Res. 2000;17(4):397-404.
5. Babu NJ, Nangia A. *Solubility Advantage of Amorphous Drugs and Pharmaceutical Cocrystals*. Cryst Growth Des. 2011;11(7):2662-2679.
6. Craig DQM, Royall PG, Kett VL, Hopton ML. *The relevance of the amorphous state to pharmaceutical dosage forms: glassy drugs and freeze dried systems*. Int J Pharm. 1999;179(2):179-207.
7. Gardner CR, Walsh CT, Almarsson O. *Drugs as materials: valuing physical form in drug discovery*. Nat Rev Drug Discov. 2004;3(11):926-934.
8. Brittain HG. Polymorphism in pharmaceutical solids. New York: Informa Healthcare; 2009.
9. Morris KR, Griesser UJ, Eckhardt CJ, Stowell JG. *Theoretical approaches to physical transformations of active pharmaceutical ingredients during manufacturing processes*. Adv Drug Del Rev. 2001;48(1):91-114.
10. Vippagunta SR, Brittain HG, Grant DJW. *Crystalline solids*. Adv Drug Del Rev. 2001;48(1):3-26.
11. Rodríguez-Spong B, Price CP, Jayasankar A, Matzger AJ, Rodríguez-Hornedo Nr. *General principles of pharmaceutical solid polymorphism: A supramolecular perspective*. Adv Drug Del Rev. 2004;56(3):241-274.
12. Brus J, Urbanova M, Sedenkova I, Brusova H. *New perspectives of ^{19}F MAS NMR in the characterization of amorphous forms of atorvastatin in dosage formulations*. Int J Pharm. 2011;409(1–2):62-74.
13. Savolainen M, Heinz A, Strachan C, Gordon KC, Yliruusi J, Rades T, *et al. Screening for differences in the amorphous state of indomethacin using multivariate visualization*. Eur J Pharm Sci. 2007;30(2):113-123.
14. Patterson JE, James MB, Forster AH, Lancaster RW, Butler JM, Rades T. *The influence of thermal and mechanical preparative techniques on the amorphous state of four poorly soluble compounds*. J Pharm Sci. 2005;94(9):1998-2012.
15. Graeser KA, Strachan CJ, Patterson JE, Gordon KC, Rades T. *Physicochemical Properties and Stability of Two Differently Prepared Amorphous Forms of Simvastatin*. Cryst Growth Des. 2008;8(1):128-135.
16. Mishima O, Calvert LD, Whalley E. *`Melting ice' I at 77 K and 10 kbar: a new method of making amorphous solids*. Nature. 1984;310(5976):393-395.
17. Grimsditch M. *Polymorphism in Amorphous SiO_2*. Phys Rev Lett. 1984;52(26):2379-2381.
18. Aasland S, McMillan PF. *Density-driven liquid-liquid phase separation in the system AI_2O_3-Y_2O_3*. Nature. 1994;369(6482):633-636.
19. Hancock BC, Shalaev EY, Shamblin SL. *Polyamorphism: a pharmaceutical science perspective*. J Pharm Pharmacol. 2002;54(8):1151-1152.
20. Zhang GGZ, Law D, Schmitt EA, Qiu Y. *Phase transformation considerations during process development and manufacture of solid oral dosage forms*. Adv Drug Del Rev. 2004;56(3):371-390.
21. Bhattacharya S, Suryanarayanan R. *Local mobility in amorphous pharmaceuticals—characterization and implications on stability*. J Pharm Sci. 2009;98(9):2935-2953.
22. Volpe M. *Preventing cardiovascular events with angiotensin II receptor blockers: a closer look at telmisartan and valsartan*. Expert Rev Cardiovasc Ther. 2012;10(8):1061-1072.
23. Tran TT, Tran PH, Park JB, Lee BJ. *Effects of solvents and crystallization conditions on the polymorphic behaviors and dissolution rates of valsartan*. Arch Pharm Res. 2012;35(7):1223-1230.
24. Shrivastava AR, Ursekar B, Kapadia CJ. *Design, optimization, preparation and evaluation of dispersion granules of valsartan and formulation into tablets*. Curr Drug Del. 2009;6(1):28-37.
25. Burgbacher J, Hahn BT, Rampf FA, Schneeberger R. Highly crystalline valsartan. WO2012016969 A1 2012
26. Wang J-R, Wang X, Lu L, Mei X. *Highly Crystalline Forms of Valsartan with Superior Physicochemical Stability*. Cryst Growth Des. 2013;13(7):3261-3269.
27. Bauer M, Harris RK, Rao RC, Apperley DC, Rodger CA. *NMR study of desmotropy in Irbesartan, a tetrazole-containing pharmaceutical compound*. J Chem Soc, Perkin Trans 2. 1998(3):475-482.
28. Raghavan K, Dwivedi A, Campbell GC, Jr., Johnston E, Levorse D, McCauley J, *et al. A spectroscopic investigation of losartan polymorphs*. Pharm Res. 1993;10(6):900-904.
29. Matsunaga H, Eguchi T, Nishijima K, Enomoto T, Sasaoki K, Nakamura N. *Solid-state characterization of candesartan cilexetil (TCV-116): Crystal structure and molecular mobility*. Chem Pharm Bull. 1999;47:182-186.

30. Wald NJ, Law MR. *A strategy to reduce cardiovascular disease by more than 80%*. BMJ. 2003;326(7404):1419.
31. *Bisoprolol-another cardioselective beta blocker*. Drug Ther Bull. 1989;27(14):55-56.
32. Forest Laboratories Submits a New Drug Application for Nebivolol and Valsartan Combination in Hypertension. Forest Laboratories, Inc.; 2014 24.07.2014. Available from: http://investor.frx.com/press-release/product-news/forest-laboratories-submits-new-drug-application-nebivolol-and-valsartan-.
33. Rodgers A, Patel A, Berwanger O, Bots M, Grimm R, Grobbee DE, *et al. An international randomised placebo-controlled trial of a four-component combination pill ("polypill") in people with raised cardiovascular risk*. PLoS One. 2011;6(5):e19857.
34. Guglietta A, Guerrero M. *Issues to consider in the pharmaceutical development of a cardiovascular polypill*. Nat Clin Pract Cardiovasc Med. 2009;6(2):112-119.
35. Kumar V, Prasad B, Singh S. *Pharmaceutical issues in the development of a polypill for the treatment of cardiovascular diseases*. Drug Discov Today Ther Strateg. 2008;5(1):63-71.
36. Singh S, Mariappan TT, Sharda N, Singh B. *Degradation of Rifampicin, Isoniazid and Pyrazinamide from Prepared Mixtures and Marketed Single and Combination Products Under Acid Conditions*. Pharm Pharmacol Commun. 2000;6(11):491-494.
37. Singh S, Mohan B. *A pilot stability study on four-drug fixed-dose combination anti-tuberculosis products*. Int J Tuberc Lung Dis. 2003;7(3):298-303.
38. Singh S, Mariappan TT, Sharda N, Kumar S, Chakraborti AK. *The Reason for an Increase in Decomposition of Rifampicin in the Presence of Isoniazid under Acid Conditions*. Pharm Pharmacol Commun. 2000;6(9):405-410.
39. Bhutani H, Singh S, Jindal KC, Chakraborti AK. *Mechanistic explanation to the catalysis by pyrazinamide and ethambutol of reaction between rifampicin and isoniazid in anti-TB FDCs*. J Pharm Biomed Anal. 2005;39(5):892-899.
40. Shishoo CJ, Shah SA, Rathod IS, Savale SS, Vora MJ. *Impaired bioavailability of rifampicin in presence of isoniazid from fixed dose combination (FDC) formulation*. Int J Pharm. 2001;228(1–2):53-67.
41. Okwelogu C, Clark B, de Matas M, Ifudu D, Igwilo C, Silva B, *et al. Design of a fixed-dose paediatric combination of artesunate and amodiaquine hydrochloride*. Int J Pharm. 2010;387(1–2):19-25.
42. Kumar V, Shah RP, Singh S. *LC and LC-MS methods for the investigation of polypills for the treatment of cardiovascular diseases. Part 1. Separation of active components and classification of their interaction/degradation products*. J Pharm Biomed Anal. 2008;47(3):508-515.
43. Kumar V, Malik S, Singh S. *Polypill for the treatment of cardiovascular diseases part 2. LC-MS/TOF characterization of interaction/degradation products of atenolol/lisinopril and aspirin, and mechanisms of formation thereof*. J Pharm Biomed Anal. 2008;48(3):619-628.
44. Forni F, Coppi G, Iannuccelli V, Vandelli MA, Cameroni R. *The grinding of the polymorphic forms of chloramphenicol stearic ester in the presence of colloidal silica*. Acta Pharm Suec. 1988;25(3):173-180.
45. Rawlinson CF, Williams AC, Timmins P, Grimsey I. *Polymer-mediated disruption of drug crystallinity*. Int J Pharm. 2007;336(1):42-48.
46. Chadwick K, Davey R, Cross W. *How does grinding produce co-crystals? Insights from the case of benzophenone and diphenylamine*. CrystEngComm. 2007;9(9):732-734.
47. Zalac S, Khan MZI, Gabelica V, Tudja M, Mestrovic E, Romih M. *Paracetamol-propyphenazone interaction and formulation difficulties associated with eutectic formation in combination solid dosage forms*. Chem Pharm Bull (Tokyo). 1999;47(3):302-307.
48. Serajuddin AT. *Solid dispersion of poorly water-soluble drugs: early promises, subsequent problems, and recent breakthroughs*. J Pharm Sci. 1999;88(10):1058-1066.
49. Yu L. *Amorphous pharmaceutical solids: preparation, characterization and stabilization*. Adv Drug Del Rev. 2001;48(1):27-42.
50. Bauer J, Spanton S, Henry R, Quick J, Dziki W, Porter W, *et al. Ritonavir: an extraordinary example of conformational polymorphism*. Pharm Res. 2001;18(6):859-866.
51. Peres-Filho M, Gaeti M, Oliveira S, Marreto R, Lima E. *Thermoanalytical investigation of olanzapine compatibility with excipients used in solid oral dosage forms*. J Therm Anal Calorim. 2011;104(1):255-260.
52. Oliveira GGG, Ferraz HG, Matos JSR. *Thermoanalytical study of glibenclamide and excipients*. J Therm Anal Calorim. 2005;79(2):267-270.
53. Stulzer HK, Rodrigues PO, Cardoso TM, Matos JSR, Silva MAS. *Compatibility studies between captopril and pharmaceutical excipients used in tablets formulations*. J Therm Anal Calorim. 2008;91(1):323-328.
54. Tajber L, Corrigan OI, Healy AM. *Physicochemical evaluation of PVP–thiazide diuretic interactions in co-spray-dried composites—analysis of glass transition composition relationships*. Eur J Pharm Sci. 2005;24(5):553-563.
55. Bruni G, Amici L, Berbenni V, Marini A, Orlandi A. *Drug-Excipient Compatibility Studies. Search of interaction indicators*. J Therm Anal Calorim. 2002;68(2):561-573.
56. Bruni G, Berbenni V, Milanese C, Girella A, Marini A. *Drug-excipient compatibility studies in binary and ternary mixtures by physico-chemical techniques*. J Therm Anal Calorim. 2010;102(1):193-201.
57. Bharate SS, Bharate SB, Bajaj AN. *Incompatibilities of Pharmaceutical Excipients with Active Pharmaceutical Ingredients: A Comprehensive Review*. J Excipients and Food Chem. 2010;1(3):3-26.

58. Apperley DC, Harris, RK., Hodgkinson, P. Solid-state NMR basic principles & practice. New York,: Momentum Press; 2012.
59. Apperley DC, Forster AH, Fournier R, Harris RK, Hodgkinson P, Lancaster RW, *et al. Characterisation of indomethacin and nifedipine using variable-temperature solid-state NMR*. Magn Reson Chem. 2005;43(11):881-892.
60. Mollica G, Geppi M, Pignatello R, Veracini C. *Molecular Properties of Flurbiprofen and its Solid Dispersions with Eudragit RL100 Studied by High- and Low-Resolution Solid-State Nuclear Magnetic Resonance*. Pharm Res. 2006;23(9):2129-2140.
61. Geppi M, Guccione S, Mollica G, Pignatello R, Veracini CA. *Molecular properties of ibuprofen and its solid dispersions with Eudragit RL100 studied by solid-state nuclear magnetic resonance*. Pharm Res. 2005;22(9):1544-1555.
62. Pignatello R, Ferro M, De Guidi G, Salemi G, Vandelli MA, Guccione S, *et al. Preparation, characterisation and photosensitivity studies of solid dispersions of diflunisal and Eudragit RS100® and RL100®*. Int J Pharm. 2001;218(1–2):27-42.
63. Aso Y, Yoshioka S. *Molecular mobility of nifedipine–PVP and phenobarbital–PVP solid dispersions as measured by ^{13}C-NMR spin-lattice relaxation time*. J Pharm Sci. 2006;95(2):318-325.
64. Braga SS, Gonçalves IS, Herdtweck E, Teixeira-Dias JJC. *Solid state inclusion compound of S-ibuprofen in β-cyclodextrin: structure and characterisation*. New J Chem. 2003;27(3):597-601.
65. Chen X, Griesser UJ, Te RL, Pfeiffer RR, Morris KR, Stowell JG, *et al. Analysis of the acid–base reaction between solid indomethacin and sodium bicarbonate using infrared spectroscopy, X-ray powder diffraction, and solid-state nuclear magnetic resonance spectroscopy*. J Pharm Biomed Anal. 2005;38(4):670-677.
66. Byrn SR, Xu W, Newman AW. *Chemical reactivity in solid-state pharmaceuticals: formulation implications*. Adv Drug Del Rev. 2001;48(1):115-136.
67. Rohrs BR, Thamann TJ, Gao P, Stelzer DJ, Bergren MS, Chao RS. *Tablet Dissolution Affected by a Moisture Mediated Solid-State Interaction Between Drug and Disintegrant*. Pharm Res. 1999;16(12):1850-1856.
68. Nabel EG. *Cardiovascular disease*. N Engl J Med. 2003;349(1):60-72.
69. Alwan A. Global status report on noncommunicable diseases 2010: World Health Organization; 2011.
70. Mathers CD, Loncar D. *Projections of global mortality and burden of disease from 2002 to 2030*. PLoS Med. 2006;3(11):e442.
71. Vyas VK, Ghate M. *Substituted benzimidazole derivatives as angiotensin II-AT1 receptor antagonist: A review*. Mini-Rev Med Chem. 2010;10(14):1366-1384.
72. Bühlmayer P, Furet P, Criscione L, de Gasparo M, Whitebread S, Schmidlin T, *et al. Valsartan, a potent, orally active angiotensin II antagonist developed from the structurally new amino acid series*. Biorg Med Chem Lett. 1994;4(1):29-34.
73. Bühlmayer P, Ostermayer F, Schmidlin T. Acyl compounds. US5399578 A 1995
74. Koltai T, Malachi O, Sasson N, Gold A. Process for preparing amorphous valsartan. WO2006076561 A1 2006
75. Reguri B, Sunkari S. Cardiovascular disorders; hypotensive agents. US20040072886 A1 2004
76. Rukhman I, Flyaks E, Koltai T, Aronhime J. Polymorphs of valsartan. US7105557 B2 2006
77. Li F, Zhang H, Jiang L, Zhang W, Nie J, Feng Y, *et al. Dynamic NMR study and theoretical calculations on the conformational exchange of valsartan and related compounds*. Magn Reson Chem. 2007;45(11):929-936.
78. Potamitis C, Zervou M, Katsiaras V, Zoumpoulakis P, Durdagi S, Papadopoulos MG, *et al. Antihypertensive drug valsartan in solution and at the AT_1 receptor: conformational analysis, dynamic NMR spectroscopy, in silico docking, and molecular dynamics simulations*. J Chem Inf Model. 2009;49(3):726-739.
79. Burnier M, Brunner H. *Angiotensin II receptor antagonists*. Lancet. 2000;355(9204):637-645.
80. Abdel-Rahman EM, Unger T, Schölkens BA. Angiotensin Vol. II. Berlin: Springer-Verlag; 2004.
81. van Zwieten P. *Angiotensin II receptor antagonists (AT_1-blockers, ARBs, sartans): similarities and differences*. Neth Heart J. 2006;14(11):381.
82. Schmieder RE. *Mechanisms for the clinical benefits of angiotensin II receptor blockers*. Am J Hypertens. 2005;18(5):720-730.
83. Csajka C, Buclin T, Brunner H, Biollaz J. *Pharmacokinetic-Pharmacodynamic Profile of Angiotensin II Receptor Antagonists*. Clin Pharmacokinet. 1997;32(1):1-29.
84. Michel MC, Foster C, Brunner HR, Liu L. *A systematic comparison of the properties of clinically used angiotensin II type 1 receptor antagonists*. Pharmacol Rev. 2013;65(2):809-848.
85. Okopski JV. *Recent advances in pharmaceutical chemistry--review. III. A new wave of beta-blockers*. J Clin Pharm Ther. 1987;12(6):369-388.
86. Lin GQ, You QD, Cheng JF. Chiral Drugs: Chemistry and Biological Action. Hoboken: John Wiley & Sons; 2011.
87. Charoo NA, Shamsher AAA, Lian LY, Abrahamsson B, Cristofoletti R, Groot DW, *et al. Biowaiver Monograph for Immediate-Release Solid Oral Dosage Forms: Bisoprolol Fumarate*. J Pharm Sci. 2014;103(2):378-391.

88. European Pharmacopoeia 6.0: Council Of Europe; Strasbourg; 2007.
89. McGavin JK, Keating GM. *Bisoprolol: a review of its use in chronic heart failure*. Drugs. 2002;62(18):2677-2696.
90. Brayfield A. Martindale: The Complete Drug Reference 38th Ed.: Pharmaceutical Press; 2014.
91. Fixed Dose Combination of Bisoprolol and Amlodipine in the Treatment of Hypertension. U.S. National Institutes of Health. 2014 21.08.2014. Available from: http://clinicaltrials.gov/show/NCT01977794.
92. Fahlman B. Solid-State Chemistry. In. Materials Chemistry. Dordrecht: Springer Science & Business Media; 2011. p. 13-156.
93. Storey RA, Ymén I. Solid State Characterization of Pharmaceuticals. Chichester: John Wiley & Sons; 2011.
94. Hilfiker R. Polymorphism: In the Pharmaceutical Industry. Weinheim: Wiley-VCH Verlag GmbH & Co. KGaA; 2006.
95. Bernstein J. Polymorphism in Molecular Crystals. Oxford: Oxford University Press; 2002.
96. Lee AY, Erdemir D, Myerson AS. *Crystal polymorphism in chemical process development*. Annu Rev Chem Biomol Eng. 2011;2(1):259-280.
97. Blagden N, de Matas M, Gavan PT, York P. *Crystal engineering of active pharmaceutical ingredients to improve solubility and dissolution rates*. Adv Drug Del Rev. 2007;59(7):617-630.
98. Hammond RB, Pencheva K, Roberts KJ, Auffret T. *Quantifying solubility enhancement due to particle size reduction and crystal habit modification: Case study of acetyl salicylic acid*. J Pharm Sci. 2007;96(8):1967-1973.
99. Modi SR, Dantuluri AKR, Puri V, Pawar YB, Nandekar P, Sangamwar AT, *et al. Impact of Crystal Habit on Biopharmaceutical Performance of Celecoxib*. Cryst Growth Des. 2013;13(7):2824-2832.
100. York P. *Solid-state properties of powders in the formulation and processing of solid dosage forms*. Int J Pharm. 1983;14(1):1-28.
101. Houson I. Process Understanding: For Scale-Up and Manufacture of Active Ingredients. Weinheim: Wiley-VCH Verlag GmbH & Co. KGaA; 2011.
102. Brittain HG. *Polymorphism and solvatomorphism 2010*. J Pharm Sci. 2012;101(2):464-484.
103. Yu L, Reutzel-Edens SM, Mitchell CA. *Crystallization and Polymorphism of Conformationally Flexible Molecules: Problems, Patterns, and Strategies*. Org Process Res Dev. 2000;4(5):396-402.
104. Price CP, Grzesiak AL, Lang M, Matzger AJ. *Polymorphism of Nabumetone*. Cryst Growth Des. 2002;2(6):501-503.
105. Reutzel-Edens SM, Bush JK, Magee PA, Stephenson GA, Byrn SR. *Anhydrates and Hydrates of Olanzapine: Crystallization, Solid-State Characterization, and Structural Relationships*. Cryst Growth Des. 2003;3(6):897-907.
106. Holzer W, Claramunt RM, López C, Alkorta I, Elguero J. *A study in desmotropy*. Solid State Nucl Magn Reson. 2008;34(1–2):68-76.
107. Seddon KR. *Pseudopolymorph: A Polemic*. Cryst Growth Des. 2004;4(6):1087-1087.
108. Shete G, Puri V, Kumar L, Bansal A. *Solid State Characterization of Commercial Crystalline and Amorphous Atorvastatin Calcium Samples*. AAPS PharmSciTech. 2010;11(2):598-609.
109. Zupančič V, Ograjšek N, Kotar-Jordan B, Vrečer F. *Physical characterization of pantoprazole sodium hydrates*. Int J Pharm. 2005;291(1–2):59-68.
110. Vishweshwar P, McMahon JA, Bis JA, Zaworotko MJ. *Pharmaceutical co-crystals*. J Pharm Sci. 2006;95(3):499-516.
111. Vishweshwar P, McMahon JA, Peterson ML, Hickey MB, Shattock TR, Zaworotko MJ. *Crystal engineering of pharmaceutical co-crystals from polymorphic active pharmaceutical ingredients*. Chem Commun. 2005(36):4601-4603.
112. Miroshnyk I, Mirza S, Sandler N. *Pharmaceutical co-crystals – an opportunity for drug product enhancement*. Expert Opin Drug Deliv. 2009;6(4):333-341.
113. Petruševski G, Naumov P, Jovanovski G, Ng SW. *Unprecedented sodium–oxygen clusters in the solid-state structure of trisodium hydrogentetravalproate monohydrate: A model for the physiological activity of the anticonvulsant drug Epilim®*. Inorg Chem Commun. 2008;11(1):81-84.
114. Stahl PH, Wermuth CG. Pharmaceutical salts: Properties, selection, and use. Zurich: VHCA : Wiley-VCH; 2002.
115. Aakeröy CB, Fasulo ME, Desper J. *Cocrystal or Salt: Does It Really Matter?* Mol Pharm. 2007;4(3):317-322.
116. Lu J, Rohani S. *Polymorphism and Crystallization of Active Pharmaceutical Ingredients (APIs)*. Curr Med Chem. 2009;16(7):884-905.
117. Hancock BC, Zografi G. *Characteristics and significance of the amorphous state in pharmaceutical systems*. J Pharm Sci. 1997;86(1):1-12.
118. Hancock BC, Carlson GT, Ladipo DD, Langdon BA, Mullarney MP. *Comparison of the mechanical properties of the crystalline and amorphous forms of a drug substance*. Int J Pharm. 2002;241(1):73-85.
119. Sheskey PJ, Hendren J. *The Effects of Roll Compaction Equipment Variables, Granulation Technique, and HPMC Polymer Level on Controlled-Release Matrix Model Drug Formulation*. Pharm Technol. 1999;23:90-107.

120. Al-Angari A, Kennerley J, Newton J. *The compaction properties of polyethylene glycols*. J Pharm Pharmacol. 1985;37(3):151-153.
121. Rowe RC, Sheskey PJ, Cook WG, Association AP, Fenton ME. Handbook of Pharmaceutical Excipients. London: Pharmaceutical Press; 2012.
122. Brown ME. Handbook of Thermal Analysis and Calorimetry: Principles and Practice. Amsterdam: Elsevier Science; 1998.
123. Kauzmann W. *The Nature of the Glassy State and the Behavior of Liquids at Low Temperatures*. Chem Rev. 1948;43(2):219-256.
124. Hancock B, Shamblin S, Zografi G. *Molecular Mobility of Amorphous Pharmaceutical Solids Below Their Glass Transition Temperatures*. Pharm Res. 1995;12(6):799-806.
125. Craig DQM, Reading M. Thermal analysis of pharmaceuticals. Boca Raton, FL: CRC Press/Taylor & Francis; 2007.
126. Blundell SJ, Blundell KM. Concepts in Thermal Physics. Oxford: Oxford University Press; 2010.
127. Roos YH. Phase Transitions in Foods. San Diego: Academic Press; 1995.
128. Hancock BC, Shamblin SL. *Molecular mobility of amorphous pharmaceuticals determined using differential scanning calorimetry*. Thermochim Acta. 2001;380(2):95-107.
129. Cheng SZ. Handbook of Thermal Analysis and Calorimetry: Applications to Polymers and Plastics. Amsterdam: Elsevier Science; 2002.
130. Richardson MJ, Savill NG. *Derivation of accurate glass transition temperatures by differential scanning calorimetry*. Polymer. 1975;16(10):753-757.
131. Hutchinson JM. *Determination of the glass transition temperature*. J Therm Anal Calorim. 2009;98(3):579-589.
132. Hutchinson JM. *Physical aging of polymers*. Prog Polym Sci. 1995;20(4):703-760.
133. Abdul-Fattah AM, Dellerman KM, Bogner RH, Pikal MJ. *The effect of annealing on the stability of amorphous solids: chemical stability of freeze-dried moxalactam*. J Pharm Sci. 2007;96(5):1237-1250.
134. Luthra SA, Hodge IM, Pikal MJ. *Investigation of the impact of annealing on global molecular mobility in glasses: Optimization for stabilization of amorphous pharmaceuticals*. J Pharm Sci. 2008;97(9):3865-3882.
135. McMillan PF. *Polyamorphic transformations in liquids and glasses*. J Mater Chem. 2004;14(10):1506-1512.
136. Aitipamula S, Banerjee R, Bansal AK, Biradha K, Cheney ML, Choudhury AR, *et al. Polymorphs, Salts, and Cocrystals: What's in a Name?* Cryst Growth Des. 2012;12(5):2147-2152.
137. Baird JA, Taylor LS. *Evaluation of amorphous solid dispersion properties using thermal analysis techniques*. Adv Drug Deliv Rev. 2012;64(5):396-421.
138. Shayanfar A, Jouyban A. *Drug–Drug Coamorphous Systems: Characterization and Physicochemical Properties of Coamorphous Atorvastatin with Carvedilol and Glibenclamide*. J Pharm Innov. 2013;8(4):218-228.
139. Löbmann K, Laitinen R, Grohganz H, Gordon KC, Strachan C, Rades T. *Coamorphous Drug Systems: Enhanced Physical Stability and Dissolution Rate of Indomethacin and Naproxen*. Mol Pharm. 2011;8(5):1919-1928.
140. Löbmann K, Strachan C, Grohganz H, Rades T, Korhonen O, Laitinen R. *Co-amorphous simvastatin and glipizide combinations show improved physical stability without evidence of intermolecular interactions*. Eur J Pharm Biopharm. 2012;81(1):159-169.
141. Giron D. *Contribution of thermal methods and related techniques to the rational development of pharmaceuticals—Part 1*. Pharm Sci Technolo Today. 1998;1(5):191-199.
142. Haines PJ. Principles of Thermal Analysis and Calorimetry. Cambridge: Royal Society of Chemistry; 2002.
143. Giron D. *Applications of Thermal Analysis and Coupled Techniques in Pharmaceutical Industry*. J Therm Anal Calorim. 2002;68(2):335-357.
144. Bugay DE. *Characterization of the solid-state: spectroscopic techniques*. Adv Drug Del Rev. 2001;48(1):43-65.
145. Heinz A, Strachan CJ, Gordon KC, Rades T. *Analysis of solid-state transformations of pharmaceutical compounds using vibrational spectroscopy*. J Pharm Pharmacol. 2009;61(8):971-988.
146. Vankeirsbilck T, Vercauteren A, Baeyens W, Van der Weken G, Verpoort F, Vergote G, *et al. Applications of Raman spectroscopy in pharmaceutical analysis*. TrAC, Trends Anal Chem. 2002;21(12):869-877.
147. Chadha R, Bhandari S. *Drug–excipient compatibility screening — Role of thermoanalytical and spectroscopic techniques*. J Pharm Biomed Anal. 2014;87(0):82-97.
148. McGoverin CM, Rades T, Gordon KC. *Recent pharmaceutical applications of raman and terahertz spectroscopies*. J Pharm Sci. 2008;97(11):4598-4621.
149. Brittain HG. *X-ray diffraction III: pharmaceutical applications*. Spectroscopy. 2001;16:7.
150. Brittain HG. Physical Characterization of Pharmaceutical Solids. London: Taylor & Francis; 1995.
151. Carlton RA. Pharmaceutical Microscopy. New York: Springer; 2011.
152. Amelinckx S, van Dyck D, van Landuyt J, van Tendeloo G. Handbook of Microscopy: Applications in Materials Science, Solid-State Physics, and Chemistry. Methods II. Weinheim: VCH; 2008.
153. Amelinckx S, van Dyck D, van Landuyt J, van Tendeloo G. Handbook of Microscopy, Methods I. Weinheim: VCH; 1997.

154. Mosharraf M, Nyström C. *The effect of particle size and shape on the surface specific dissolution rate of microsized practically insoluble drugs*. Int J Pharm. 1995;122(1–2):35-47.
155. Liversidge GG, Cundy KC. *Particle size reduction for improvement of oral bioavailability of hydrophobic drugs: I. Absolute oral bioavailability of nanocrystalline danazol in beagle dogs*. Int J Pharm. 1995;125(1):91-97.
156. Automated imaging advanced particle characterization. Malvern Instruments Ltd. 2014 24.06.2014. Available from: http://www.malvern.com/Assets/MRK1900-02_Morpholo_G3_Sysmex%20Imaging_LRA4.pdf.
157. Ulusoy U, Kursun I. *Comparison of different 2D image analysis measurement techniques for the shape of talc particles produced by different media milling*. Miner Eng. 2011;24(2):91-97.
158. Adeyeye MC, Brittain HG. Preformulation in Solid Dosage Form Development. London: Taylor & Francis; 2008.
159. Higuchi T, Shih F-ML, Kimura T, Rytting JH. *Solubility determination of barely aqueous-soluble organic solids*. J Pharm Sci. 1979;68(10):1267-1272.
160. The United States Pharmacopeia USP 37. The National Formulary NF 32. Rockville: The United States Pharmacopeial Convention; 2013.
161. Qiu Y, Chen Y, Zhang GGZ, Liu L, Yu L, Rao V, *et al.* Developing Solid Oral Dosage Forms: Pharmaceutical Theory & Practice: Academic Press; 2009.
162. Hörter D, Dressman JB. *Influence of physicochemical properties on dissolution of drugs in the gastrointestinal tract*. Adv Drug Del Rev. 2001;46(1–3):75-87.
163. Dressman JJ, Kramer J. Pharmaceutical Dissolution Testing. London: Taylor & Francis; 2005.
164. Fotaki N. *Flow-through cell apparatus (USP Apparatus 4): Operation and features*. Dissolution Technol. 2011;18(4):46-49.
165. Viegas TX, Curatella RU, Van Winkle LL, Brinker G. *Measurement of intrinsic drug dissolution rates using two types of apparatus*. Pharm Technol. 2001;25(6):44-53.
166. Nogami H, Nagai T, Suzuki A. *Studies on Powdered Preparations. XVII. Dissolution Rate of Sulfonamides by Rotating Disk Method*. Chem Pharm Bull (Tokyo). 1966;14(4):329-338.
167. Wunderlich B. Thermal Analysis of Polymeric Materials. Berlin: Springer-Verlag; 2005.
168. Watson ES, O'Neill MJ, Justin J, Brenner N. *A Differential Scanning Calorimeter for Quantitative Differential Thermal Analysis*. Anal Chem. 1964;36(7):1233-1238.
169. Gill P, Moghadam TT, Ranjbar B. *Differential scanning calorimetry techniques: applications in biology and nanoscience*. J Biomol Tech. 2010;21(4):167-193.
170. Kaletunç G. Calorimetry in Food Processing: Analysis and Design of Food Systems. Ames: Wiley-Blackwell; 2009.
171. Bruylants G, Wouters J, Michaux C. *Differential Scanning Calorimetry in Life Science: Thermodynamics, Stability, Molecular Recognition and Application in Drug Design*. Curr Med Chem. 2005;12(17):2011-2020.
172. Menczel JD, Prime RB. Thermal Analysis of Polymers, Fundamentals and Applications. Hoboken: John Wiley & Sons; 2009.
173. Reading M. *Modulated differential scanning calorimetry — a new way forward in materials characterization*. Trends Polym Sci. 1993;1(8):248-253.
174. Coleman NJ, Craig DQM. *Modulated temperature differential scanning calorimetry: A novel approach to pharmaceutical thermal analysis*. Int J Pharm. 1996;135(1–2):13-29.
175. Simon SL. *Temperature-modulated differential scanning calorimetry: theory and application*. Thermochim Acta. 2001;374(1):55-71.
176. Wunderlich B, Androsch R, Pyda M, Kwon YK. *Heat capacity by multi-frequencies sawtooth modulation*. Thermochim Acta. 2000;348(1–2):181-190.
177. Pyda M. Temperature-Modulated Differential Scanning Calorimetry. In.Encyclopedia Of Polymer Science and Technology. On-line: John Wiley & Sons; 2014. p. 1-31.
178. Wunderlich B. *Quasi-isothermal temperature-modulated differential scanning calorimetry (TMDSC) for the separation of reversible and irreversible thermodynamic changes in glass transition and melting ranges of flexible macromolecules*. Pure Appl Chem. 2009;81(10):1931-1952.
179. Wu L-S, Gerard C, Hussain MA. *Thermal analysis and solution calorimetry studies on losartan polymorphs*. Pharm Res. 1993;10(12):1793-1795.
180. Rabel S, Jona J, Maurin M. *Applications of modulated differential scanning calorimetry in preformulation studies*. J Pharm Biomed Anal. 1999;21(2):339-345.
181. Czerniecka A, Zarzyka I, Skotnicki M, Pyda M. *Zastosowanie metod analizy termicznej w badaniach polimorfizmu substancji leczniczych i pomocniczych*. Farm Pol. 2014;70(3):153-164.
182. Pyda M, Wunderlich B. *Reversing and Nonreversing Heat Capacity of Poly(lactic acid) in the Glass Transition Region by TMDSC*. Macromolecules. 2005;38(25):10472-10479.
183. Bloch F, Hansen WW, Packard M. *Nuclear Induction*. Phys Rev. 1946;69(3-4):127-127.
184. Arnold JT, Dharmatti SS, Packard ME. *Chemical Effects on Nuclear Induction Signals from Organic Compounds*. J Chem Phys. 1951;19(4):507-507.
185. Claridge TDW. High-resolution NMR Techniques in Organic Chemistry. Amsterdam: Elsevier; 1999.

186. Wawer I, Diehl B, Holzgrabe U. NMR Spectroscopy in Pharmaceutical Analysis. Oxford: Elsevier Science; 2008.
187. Gillies RJ. NMR In Physiology and Biomedicine. San Diego: Academic Press; 1994.
188. Spyros A, Dais P. NMR Spectroscopy in Food Analysis. Cambridge: Royal Society of Chemistry; 2012.
189. Hausser KH, Kalbitzer HR. NMR in Medicine and Biology: Structure Determination, Tomography, in Vivo Spectroscopy. Berlin: Springer-Verlag; 2012.
190. Harris RK. *Applications of solid-state NMR to pharmaceutical polymorphism and related matters*. J Pharm Pharmacol. 2007;59(2):225-239.
191. Geppi M, Mollica G, Borsacchi S, Veracini CA. *Solid-State NMR Studies of Pharmaceutical Systems*. Appl Spectrosc Rev. 2008;43(3):202-302.
192. Lowe IJ. *Free Induction Decays of Rotating Solids*. Phys Rev Lett. 1959;2(7):285-287.
193. Andrew ER, Bradbury A, Eades RG. *Removal of Dipolar Broadening of Nuclear Magnetic Resonance Spectra of Solids by Specimen Rotation*. Nature. 1959;183(4678):1802-1803.
194. Nishiyama Y, Endo Y, Nemoto T, Utsumi H, Yamauchi K, Hioka K, *et al. Very fast magic angle spinning ^{1}H-^{14}N 2D solid-state NMR: Sub-micro-liter sample data collection in a few minutes*. J Magn Reson. 2011;208(1):44-48.
195. Dixon WT. *Spinning-sideband-free and spinning-sideband-only NMR spectra in spinning samples*. J Chem Phys. 1982;77(4):1800-1809.
196. Sarles LR, Cotts RM. *Double Nuclear Magnetic Resonance and the Dipole Interaction in Solids*. Phys Rev. 1958;111(3):853-859.
197. Bloch F. *Theory of Line Narrowing by Double-Frequency Irradiation*. Phys Rev. 1958;111(3):841-853.
198. Bennett AE, Rienstra CM, Auger M, Lakshmi KV, Griffin RG. *Heteronuclear decoupling in rotating solids*. J Chem Phys. 1995;103(16):6951-6958.
199. Fung BM, Khitrin AK, Ermolaev K. *An Improved Broadband Decoupling Sequence for Liquid Crystals and Solids*. J Magn Reson. 2000;142(1):97-101.
200. Carignani E, Borsacchi S, Geppi M. *Detailed characterization of the dynamics of ibuprofen in the solid state by a multi-technique NMR approach*. Chemphyschem. 2011;12(5):974-981.
201. Hartmann SR, Hahn EL. *Nuclear Double Resonance in the Rotating Frame*. Phys Rev. 1962;128(5):2042-2053.
202. Duer MJ. Solid State NMR Spectroscopy: Principles and Applications. Oxford: Blackwell Science; 2002.
203. Opella SJ, Frey MH. *Selection of nonprotonated carbon resonances in solid-state nuclear magnetic resonance*. JACS. 1979;101(19):5854-5856.
204. Tatton AS, Pham TN, Vogt FG, Iuga D, Edwards AJ, Brown SP. *Probing intermolecular interactions and nitrogen protonation in pharmaceuticals by novel ^{15}N-edited and 2D ^{14}N-^{1}H solid-state NMR*. CrystEngComm. 2012;14(8):2654-2659.
205. Gervais C, Babonneau F, Maquet J, Bonhomme C, Massiot D, Framery E, *et al. ^{15}N cross-polarization using the inversion–recovery cross-polarization technique and ^{11}B magic angle spinning NMR studies of reference compounds containing B—N bonds*. Magn Reson Chem. 1998;36(6):407-414.
206. Hirschinger J, Hervé M. *Cross-polarization dynamics and spin diffusion in some aromatic compounds*. Solid State Nucl Magn Reson. 1994;3(3):121-135.
207. Babonneau F, Maquet J, Bonhomme C, Richter R, Roewer G, Bahloul D. *^{29}Si and ^{13}C NMR Investigation of the Polysilane-to-Poly(carbosilane) Conversion of Poly(methylchlorosilanes) Using Cross-Polarization and Inversion Recovery Cross-Polarization Techniques*. Chem Mater. 1996;8(7):1415-1428.
208. McBrierty VJ, Packer KJ. Nuclear Magnetic Resonance in Solid Polymers. Cambridge: Cambridge University Press; 2006.
209. Torchia DA. *The measurement of proton-enhanced carbon-13 T_1 values by a method which suppresses artifacts*. J Magn Reson. 1978;30(3):613-616.
210. Burum DP, Bielecki A. *An improved experiment for heteronuclear-correlation 2D NMR in Solids*. J Magn Reson (1969). 1991;94(3):645-652.
211. van Rossum BJ, Förster H, de Groot HJM. *High-Field and High-Speed CP-MAS ^{13}C NMR Heteronuclear Dipolar-Correlation Spectroscopy of Solids with Frequency-Switched Lee–Goldburg Homonuclear Decoupling*. J Magn Reson. 1997;124(2):516-519.
212. Lee M, Goldburg WI. *Nuclear-Magnetic-Resonance Line Narrowing by a Rotating rf Field*. Phys Rev. 1965;140(4A):A1261-A1271.
213. Othman A, Evans JS, Evans IR, Harris RK, Hodgkinson P. *Structural study of polymorphs and solvates of finasteride*. J Pharm Sci. 2007;96(5):1380-1397.
214. Gao P. *Characterization of three crystalline forms (VIII, XI, and XII) and the amorphous form (V) of delavirdine mesylate using ^{13}C CP/MAS NMR*. Pharm Res. 1998;15(9):1425-1433.
215. Luthra SA, Pikal MJ, Utz M. *Solid state ^{13}C NMR investigation of impact of annealing in lyophilized glasses*. J Pharm Sci. 2008;97(10):4336-4346.
216. Zannou EA, Ji Q, Joshi YM, Serajuddin ATM. *Stabilization of the maleate salt of a basic drug by adjustment of microenvironmental pH in solid dosage form*. Int J Pharm. 2007;337(1–2):210-218.
217. Guerrieri P, Taylor L. *Role of Salt and Excipient Properties on Disproportionation in the Solid-State*. Pharm Res. 2009;26(8):2015-2026.

218. Schmitt EA, Peck K, Sun Y, Geoffroy J-M. *Rapid, practical and predictive excipient compatibility screening using isothermal microcalorimetry*. Thermochim Acta. 2001;380(2):175-184.
219. Morphologi G3 User Manual. In. Malvern: Malvern Instruments Ltd.; 2008.
220. BS 2955: 1993 (98) Glossary of Terms Relating to Particle Technology. In. London: British Standards Institute; 1998.
221. Kawakami K, Pikal MJ. *Calorimetric investigation of the structural relaxation of amorphous materials: Evaluating validity of the methodologies*. J Pharm Sci. 2005;94(5):948-965.
222. Wu DH, Chen AD, Johnson CS. *An Improved Diffusion-Ordered Spectroscopy Experiment Incorporating Bipolar-Gradient Pulses*. J Magn Reson Ser A. 1995;115(2):260-264.
223. Jerschow A, Müller N. *Suppression of Convection Artifacts in Stimulated-Echo Diffusion Experiments. Double-Stimulated-Echo Experiments*. J Magn Reson. 1997;125(2):372-375.
224. Mildner T, Ernst H, Freude D. *^{207}Pb NMR detection of spinning-induced temperature gradients in MAS rotors*. Solid State Nucl Magn Reson. 1995;5(3):269-271.
225. Zorin V. Gsim – a visualisation and processing program for solid-state NMR. 2013.06.11. Available from: http://gsim.sourceforge.net.
226. Pickard CJ, Mauri F. *All-electron magnetic response with pseudopotentials: NMR chemical shifts*. Phys Rev B. 2001;63(24):245101.
227. Harris RK, Hodgkinson P, Pickard CJ, Yates JR, Zorin V. *Chemical shift computations on a crystallographic basis: some reflections and comments*. Magn Reson Chem. 2007;45:S174-S186.
228. You-lin Z, Shi-ping F. *The flowability of ground powders and the comminuting mechanism of mills*. J Wuhan Univ Technol, Mater Sci Ed. 2004;19(4):13-16.
229. Cowie JMG, Ferguson R. *Physical aging studies in poly(vinylmethyl ether). I. Enthalpy relaxation as a function of aging temperature*. Macromolecules. 1989;22(5):2307-2312.
230. Airaksinen S, Karjalainen M, Shevchenko A, Westermarck S, Leppänen E, Rantanen J, *et al. Role of water in the physical stability of solid dosage formulations*. J Pharm Sci. 2005;94(10):2147-2165.
231. Bates S, Zografi G, Engers D, Morris K, Crowley K, Newman A. *Analysis of Amorphous and Nanocrystalline Solids from Their X-Ray Diffraction Patterns*. Pharm Res. 2006;23(10):2333-2349.
232. Stefaniak L, Roberts JD, Witanowski M, Webb GA. *A ^{15}N NMR study of some azoles*. Orgn Magn Res. 1984;22(4):215-220.
233. Aso Y, Yoshioka S, Kojima S. *Relationship between the crystallization rates of amorphous nifedipine, phenobarbital, and flopropione, and their molecular mobility as measured by their enthalpy relaxation and (1)H NMR relaxation times*. J Pharm Sci. 2000;89(3):408-416.
234. Hörter D, Dressman JB. *Influence of physicochemical properties on dissolution of drugs in the gastrointestinal tract*. Adv Drug Del Rev. 1997;25(1):3-14.
235. Kalichevsky MT, Jaroszkiewicz EM, Blanshard JMV. *A study of the glass transition of amylopectin—sugar mixtures*. Polymer. 1993;34(2):346-358.
236. Apperley DC, Markwell AF, Frantsuzov I, Ilott AJ, Harris RK, Hodgkinson P. *NMR characterisation of dynamics in solvates and desolvates of formoterol fumarate*. PCCP. 2013;15(17):6422-6430.
237. Marini A, Berbenni V, Moioli S, Bruni G, Cofrancesco P, Margheritis C, *et al. Drug-excipient compatibility studies by physico-chemical techniques; The case of Indomethacin*. J Therm Anal Calorim. 2003;73(2):529-545.
238. Zorin VE, Brown SP, Hodgkinson P. *Origins of linewidth in ^{1}H magic-angle spinning NMR*. J Chem Phys. 2006;125(14):144508.
239. Dulin WA. *Degradation of Bisoprolol Fumarate in Tablets Formulated with Dicalcium Phosphate*. Drug Dev Ind Pharm. 1995;21(4):393-409.
240. Wang S-L, Lin S-Y, Chen T-F, Chuang C-H. *Solid-state trans–cis isomerization of captopril determined by thermal Fourier transform infrared (FT-IR) microspectroscopy*. J Pharm Sci. 2001;90(8):1034-1039.
241. Brittain HG, Morris KR, Bugay DE, Thakur AB, Serajuddin ATM. *Solid-state NMR and IR for the analysis of pharmaceutical solids: Polymorphs of fosinopril sodium*. J Pharm Biomed Anal. 1993;11(11–12):1063-1069.
242. Taylor L, Zografi G. *Spectroscopic Characterization of Interactions Between PVP and Indomethacin in Amorphous Molecular Dispersions*. Pharm Res. 1997;14(12):1691-1698.
243. Smith MB, March J. Advanced organic chemistry: reactions, mechanisms, and structure. New York: John Wiley & Sons; 2006.
244. Boileau AC, Merchen NR, Wasson K, Atkinson CA, Erdman JW. *Cis-Lycopene Is More Bioavailable Than Trans-Lycopene In Vitro and In Vivo in Lymph-Cannulated Ferrets*. J Nutr. 1999;129(6):1176-1181.
245. Smith MB, March J. Stereochemistry. In. March's Advanced Organic Chemistry. New York: John Wiley & Sons; 2006. p. 136-233.
246. Schoen BW, Lira CT, Lee A. *Separation and Solubility of Cis and Trans Isomers in Nanostructured Double-Decker Silsequioxanes*. J Chem Eng Data. 2014.
247. Boileau TW-M, Boileau AC, Erdman JW. *Bioavailability of all-trans and cis-Isomers of Lycopene*. Exp Biol Med. 2002;227(10):914-919.

248. Ishii K, Nakayama H, Koyama K, Yokoyama Y, Ohashi Y. *Molecular Conformation of Butanenitrile in Gas, Liquid, Glass, and Crystalline States: In Relation to the Stability of the Glass State*. Bull Chem Soc Jpn. 1997;70(9):2085-2091.
249. Jarmelo S, Maria TMR, Leitao MLP, Fausto R. *The low temperature crystalline and glassy states of methyl α-hydroxy-isobutyrate*. PCCP. 2001;3(3):387-392.
250. Turnbull D. *Relation of crystallization behavior to structure in amorphous systems*. Ann N Y Acad Sci. 1976;279(1):185-185.
251. Yoshioka S, Aso Y. *Correlations between molecular mobility and chemical stability during storage of amorphous pharmaceuticals*. J Pharm Sci. 2007;96(5):960-981.
252. Baird JA, Van Eerdenbrugh B, Taylor LS. *A classification system to assess the crystallization tendency of organic molecules from undercooled melts*. J Pharm Sci. 2010;99(9):3787-3806.
253. Cherukuvada S, Nangia A. *Eutectics as improved pharmaceutical materials: design, properties and characterization*. Chem Commun. 2014;50(8):906-923.
254. Tosco P, Rolando B, Fruttero R, Henchoz Y, Martel S, Carrupt P-A, *et al. Physicochemical Profiling of Sartans: A Detailed Study of Ionization Constants and Distribution Coefficients*. Helv Chim Acta. 2008;91(3):468-482.
255. Childs SL, Stahly GP, Park A. *The Salt−Cocrystal Continuum: The Influence of Crystal Structure on Ionization State*. Mol Pharm. 2007;4(3):323-338.

11 APPENDICES

11.1 2D solution-state NMR spectra of valsartan

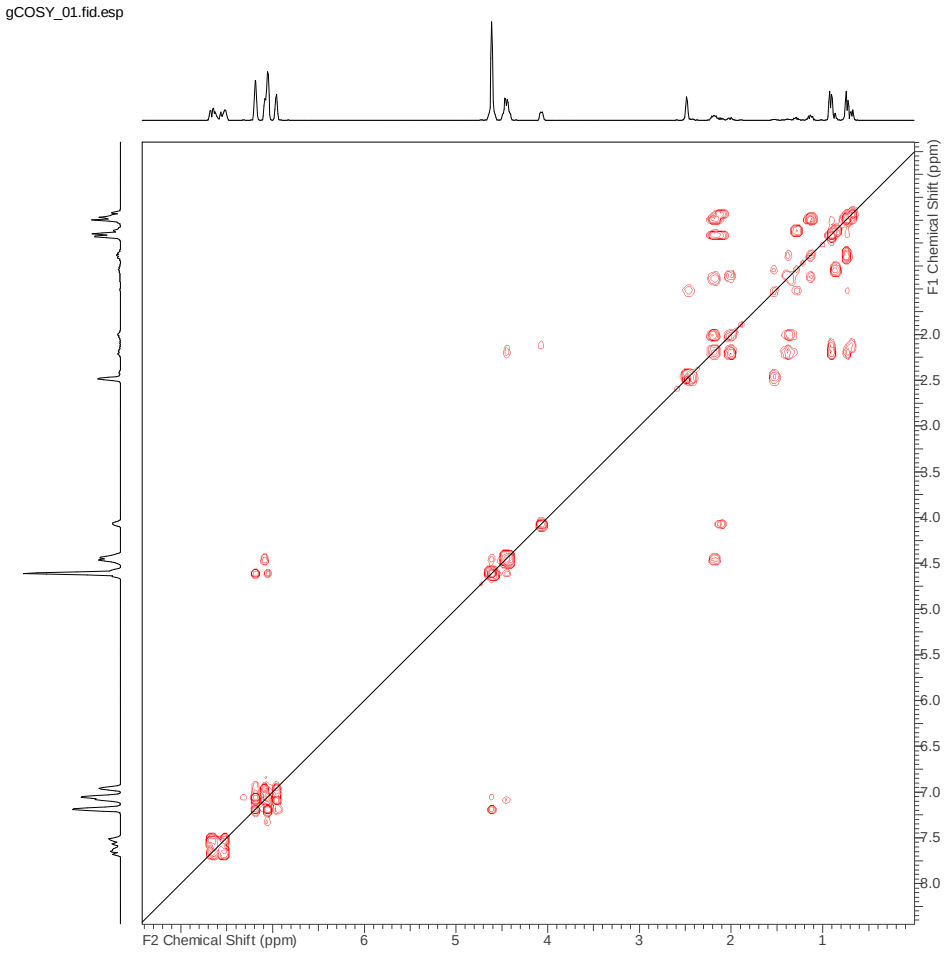

Figure A 1. COSY spectrum of valsartan in [D_6]-DMSO recorded at room temperature.

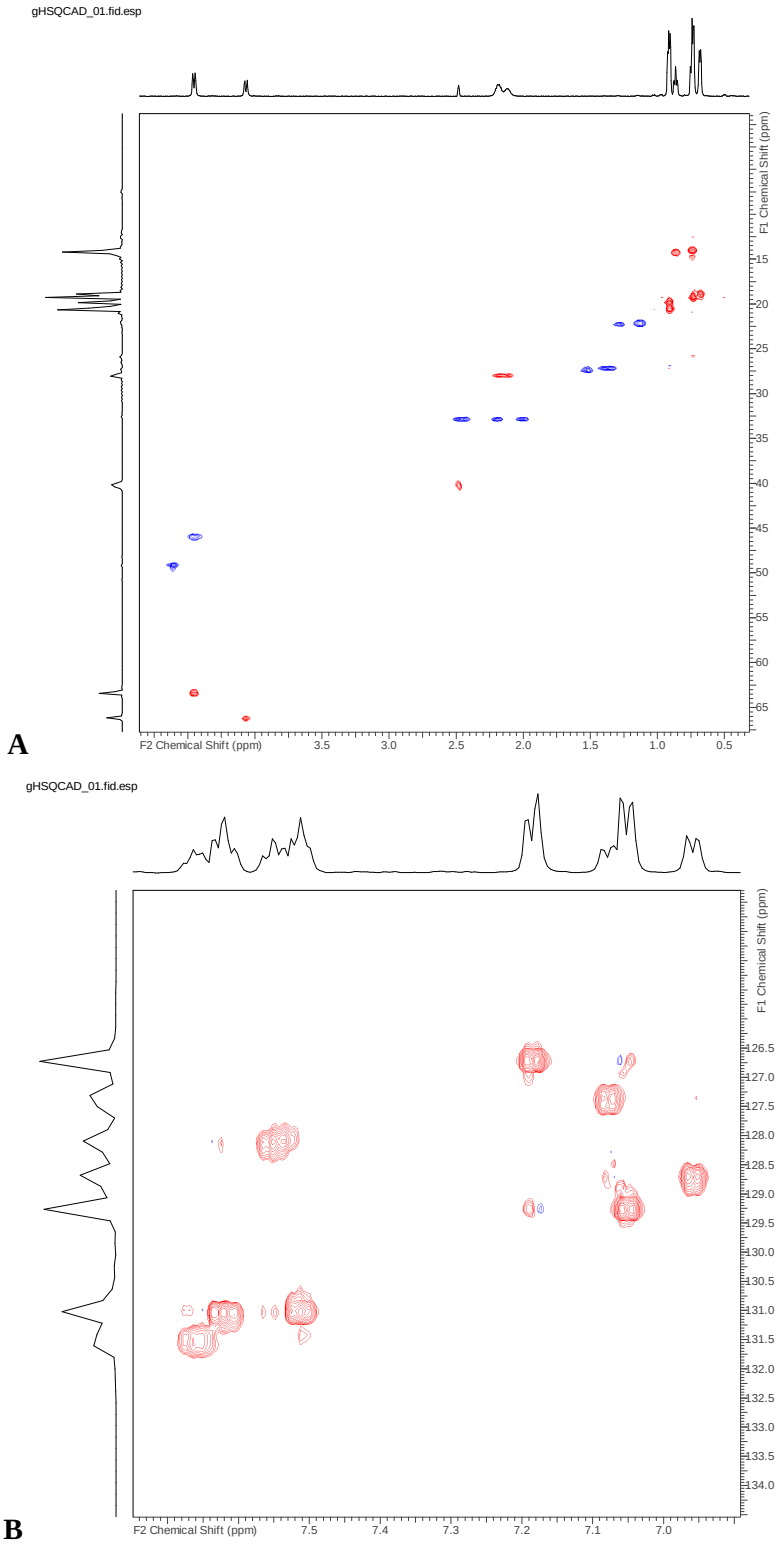

Figure A 2. (A) Low-frequency and (B) high-frequency region of $^{1}H–^{13}C$ HSQC spectra of valsartan in [D_6]-DMSO recorded at room temperature.

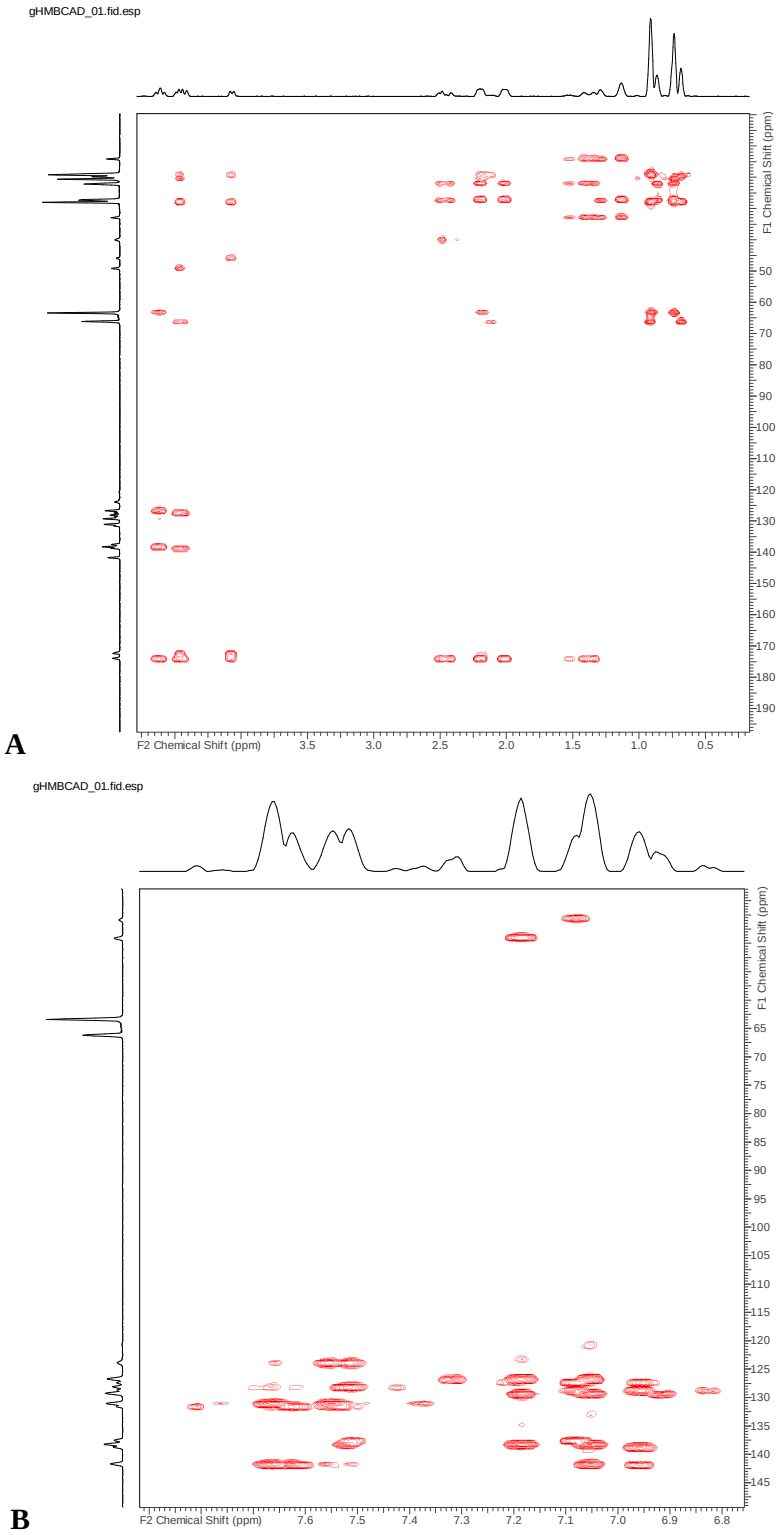

Figure A 3. (A) Low-frequency and (B) high-frequency region of ^{1}H–^{13}C HMBC spectra of valsartan in [D_6]-DMSO recorded at room temperature.

11.2 Relaxation times for valsartan forms

Table A I. Carbon-13 spin–lattice relaxation times (T_1) for AR and AM valsartan recorded at variable temperature and corresponding errors.

T / °C	T_1 / s									
	Signal / ppm	**14.1**	**14.3**	**19.8**		**22.6**		**129.9**	**131.8**	**130.0**
	Form	**AR**	**AM**	**AR**	**AM**	**AR**	**AM**	**AR**	**AR**	**AM**
38		1.33 ±0.10	1.59 ±0.19	0.81 ±0.04	0.77 ±0.04	1.08 ±0.06	1.18 ±0.07	40.0 ±1.60	47.85 ±1.37	41.32 ±1.54
50		1.92 ±0.20	1.98 ±0.19	0.94 ±0.04	1.13 ±0.06	1.28 ±0.06	1.69± 0.08	44.05 ±1.94	48.08 ±1.16	43.48 ±1.51
60		2.10 ±0.23	1.91 ±0.23	1.08 ±0.05	1.01 ±0.06	1.34 ±0.06	1.48 ±0.08	44.05 ±1.75	48.54 ±1.89	40.16 ±1.45
70		2.17 ±0.33	2.74 ±0.25	1.05 ±0.04	1.29 ±0.06	1.48 ±0.07	1.81 ±0.09	40.00 ±1.76	49.51 ±1.72	35.84 ±1.29
80		2.54 ±0.17	2.59 ±0.21	1.28 ±0.05	1.20 ±0.06	1.76 ±0.08	1.90 ±0.09	32.68 ±1.49	31.35 ±1.38	27.25 ±0.97
90		3.11 ±0.29	3.24 ±0.27	1.30 ±0.07	1.40 ±0.08	1.83 ±0.1	1.90 ±0.1	18.22 ±1.33	18.52 ±0.93	19.65 ±0.66
100		3.05 ±0.19	3.53 ±0.32	1.33 ±0.04	1.34 ±0.08	1.84 ±0.13	2.13 ±0.16	20.45 ±2.47[a]		16.23 ±0.45
110		3.59 ±0.10	3.97 ±0.26	1.47 ±0.05	1.53 ±0.06	2.45 ±0.17	2.05 ±0.13	21.14 ±3.26[a]		16.56 ±0.93

[a] Only one signal was observed at around 131 ppm at 100 and 110 °C.

Table A II. Spin–lattice relaxation times in the rotating frame ($T_{1\rho}{}^{H}$) measured via CP onto ^{13}C for AR and AM valsartan recorded at variable temperature and corresponding errors.

T / °C	$T_{1\rho}{}^{H}$ / ms													
	Signal / ppm	**14.1**	**14.3**	**19.8**		**22.6**		**27.6**	**28.0**	**34.1**	**33.8**	**129.7**	**131.8**	**130.1**
	Form	**AR**	**AM**	**AR**	**AM**	**AR**	**AM**	**AR**	**AM**	**AR**	**AM**	**AR**	**AR**	**AM**
38		13.5 ±0.6	19.0 ±1.1	16.3 ±0.4	19.4 ±0.5	17.6 ±0.5	19.7 ±0.6	19.7 ±0.4	20.8 ±0.8	19.8 ±0.9	19.5 ±1.3	19.5 ±0.2	20.5 ±0.3	21.3 ±0.4
50		15.9 ±0.8	18.9 ±1.5	17.5 ±0.5	19.0 ±0.6	18.4 ±0.5	19.0 ±0.8	19.6 ±0.5	20.2 ±0.9	18.2 ±0.8	20.1 ±1.6	19.2 ±0.4	20.3 ±0.4	20.0 ±0.5
60		17.4 ±1.0	17.3 ±1.0	16.9 ±0.7	17.2 ±0.5	17.9 ±0.5	17.6 ±0.6	18.6 ±0.4	18.1 ±0.6	20.3 ±1.1	17.9 ±1.2	18.2 ±0.5	19.3 ±0.4	18.4 ±0.3
70		17.1 ±1.1	15.1 ±0.7	18.7 ±1.0	14.2 ±0.7	20.6 ±1.0	14.5 ±0.4	21.2 ±0.6	16.4 ±0.7	20.2 ±1.3	16.1 ±1.6	22.3 ±0.6	21.7 ±0.5	15.5 ±0.4
80		11.5 ±1.0	11.7 ±0.9	12.1 ±0.6	12.0 ±0.5	13.2 ±0.5	12.6 ±0.6	14.6 ±0.3	13.6 ±0.5	16.1 ±1.2	11.8 ±1.0	15.4 ±0.5	15.8 ±0.6	12.7 ±0.3
90		5.05 ±0.4	7.8 ±0.5	5.6 ±0.3	8.5 ±0.4	6.7 ±0.4	9.7 ±0.5	7.8 ±0.4	9.1 ±0.3	9.9 ±1.5	9.7 ±0.9	8.1 ±0.4	7.8 ±0.4	10.1 ±0.3
100		2.6 ±0.2	6.6 ±0.5	2.8 ±0.3	6.2 ±0.4	2.7 ±0.4	5.8 ±0.2	3.0 ±0.3	7.2 ±0.4	3.3 ±0.7	6.9 ±1.1	4.3 ±0.5	3.5 ±0.4	7.0 ±0.2

11.3 2D solution-state NMR spectra of bisoprolol

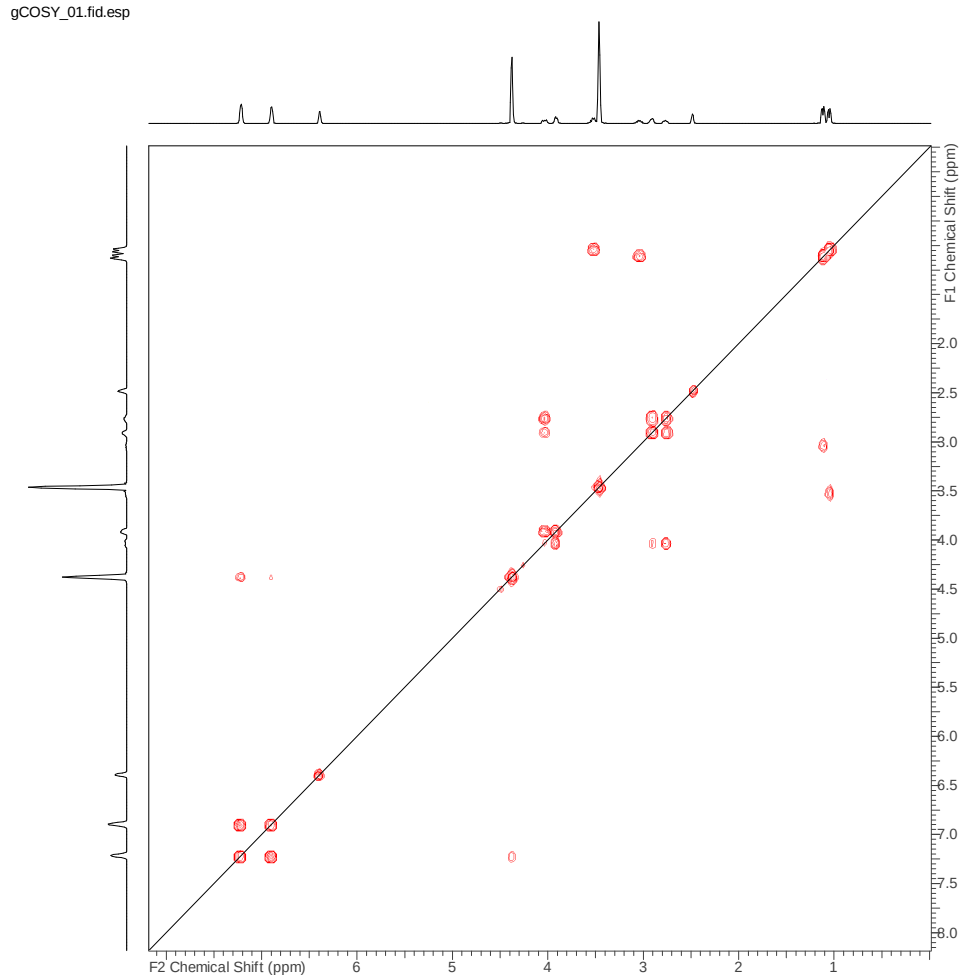

Figure A 4. COSY spectrum of bisoprolol in [D_6]-DMSO recorded at room temperature.

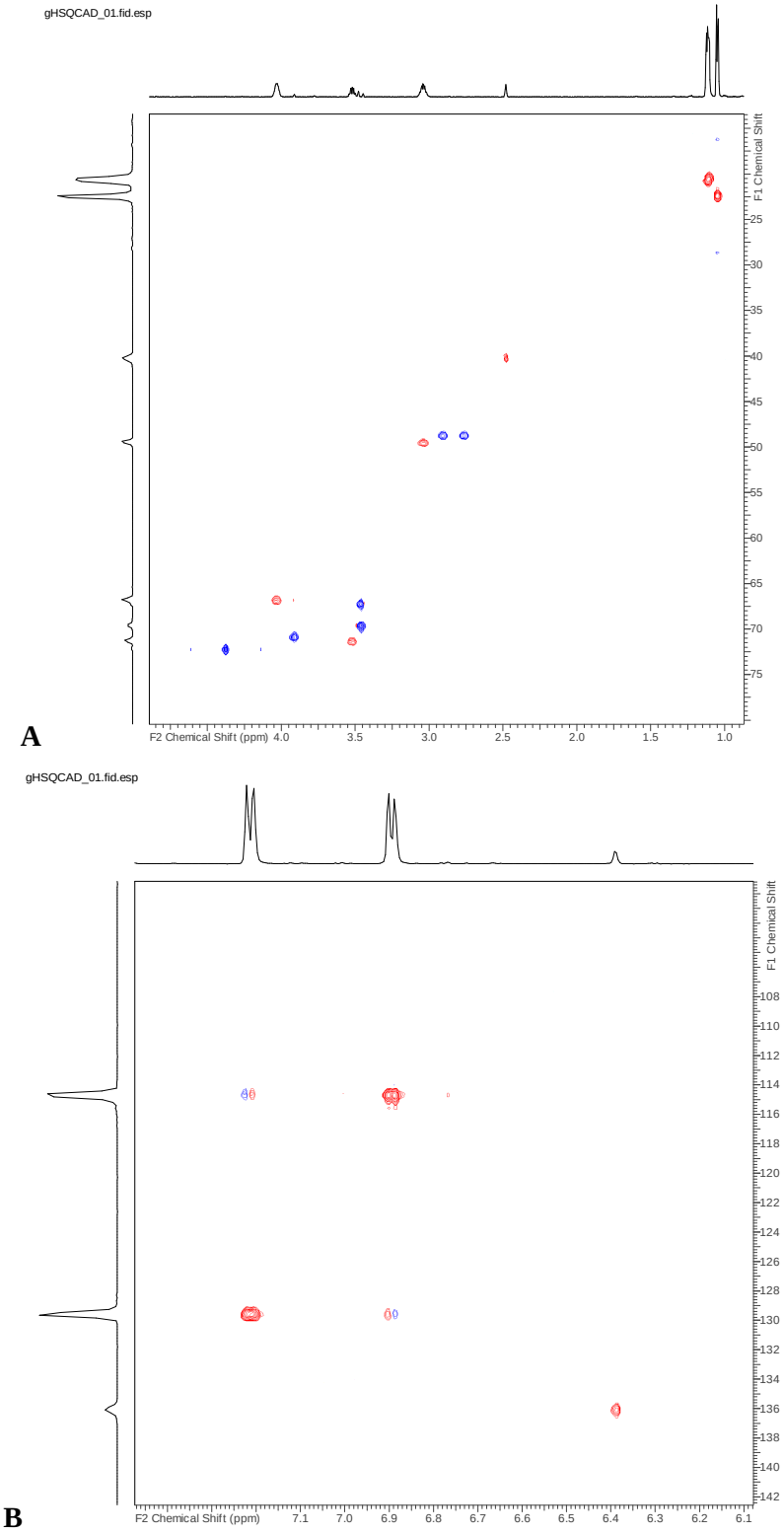

Figure A 5. (A) Low-frequency and (B) high-frequency region of ^{1}H–^{13}C HSQC spectra of bisoprolol in [D_6]-DMSO recorded at room temperature.

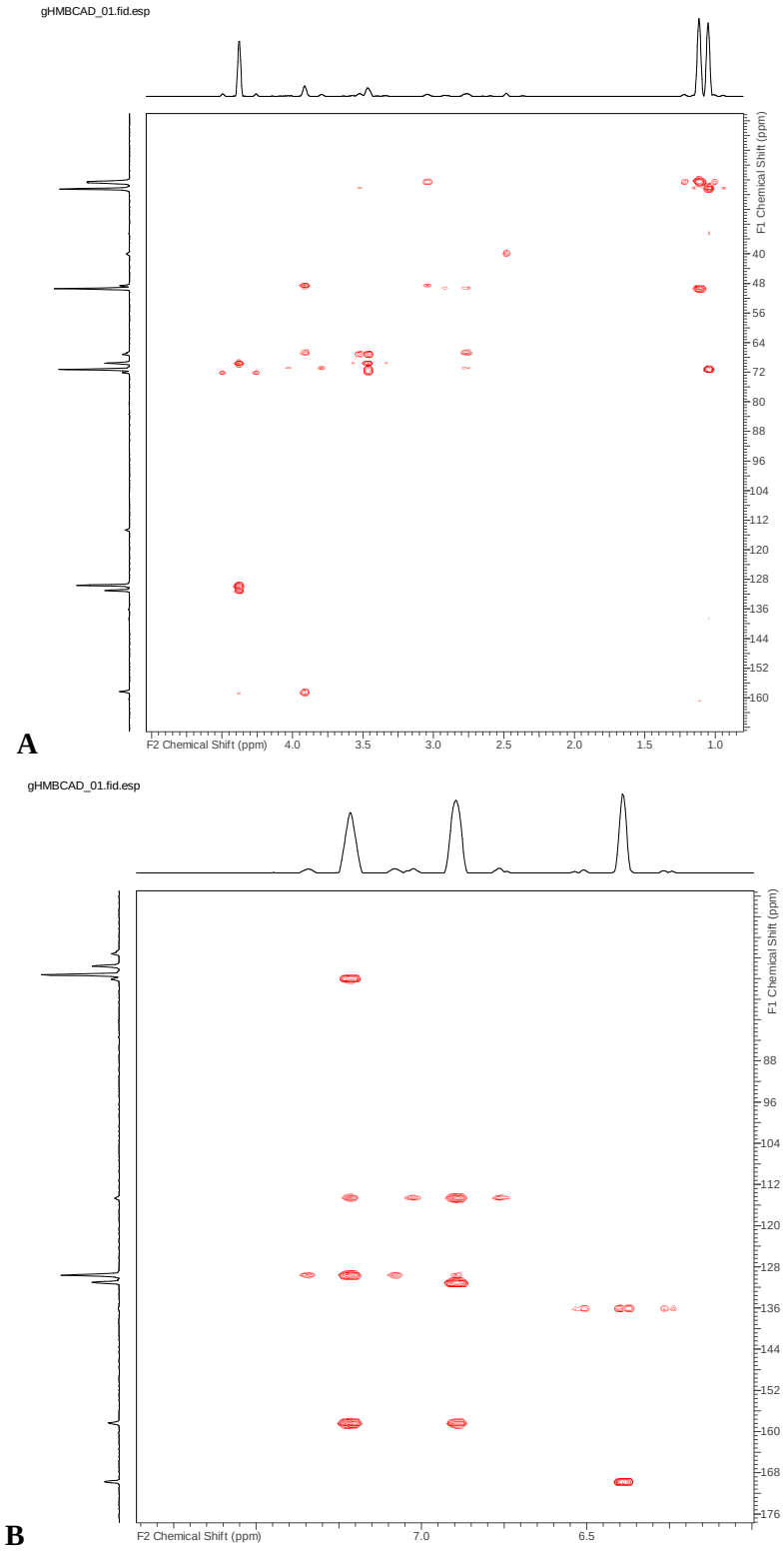

Figure A 6. (A) Low-frequency and (B) high-frequency region of ^{1}H–^{13}C HMBC spectra of bisoprolol in [D_6]-DMSO recorded at room temperature.

12 OŚWIADCZENIA

OŚWIADCZENIE

Niniejszym oświadczam, iż jestem autorem pracy doktorskiej p.t.:

"**Characterisation of valsartan and its compatibility with bisoprolol studied by differential scanning calorimetry and solid-state nuclear magnetic resonance**"

"**Charakterystyka walsartanu oraz badanie jego zgodności fizykochemicznej z bisoprololem z wykorzystaniem różnicowej kalorymetrii skaningowej i magnetycznego rezonansu jądrowego w fazie stałej**".

Praca ta została przeze mnie napisana samodzielnie (bez jakiegokolwiek udziału osób trzecich), przy wykorzystaniu wykazanej w pracy literatury przedmiotu i materiałów źródłowych, stanowi ona pracę oryginalną, nie narusza praw autorskich oraz dóbr osobistych osób trzecich i jest wolna od jakichkolwiek zapożyczeń.

Oświadczam również, że wymieniona praca nie zawiera danych i informacji, które zostały uzyskane w sposób niedozwolony prawem oraz nie była dotychczas przedmiotem żadnej urzędowej procedury związanej z uzyskaniem stopnia naukowego: doktor nauk farmaceutycznych, a złożona przeze mnie dyskietka/płyta CD zawiera elektroniczny zapis przedstawionej przeze mnie pracy.

Jednocześnie oświadczam, że nieodpłatnie udzielam Uniwersytetowi Medycznemu im. Karola Marcinkowskiego w Poznaniu licencji do korzystania z wyżej wymienionej pracy bez ograniczeń czasowych i terytorialnych w zakresie obrotu nośnikami, na których pracę utrwalono przez: wprowadzanie do obrotu, użyczenie lub najem egzemplarzy w postaci elektronicznej a nadto upoważniam Uniwersytet Medyczny im. Karola Marcinkowskiego w Poznaniu do przechowywania i archiwizowania pracy w zakresie wprowadzania jej do pamięci komputera oraz do jej zwielokrotniania i udostępniania w formie elektronicznej oraz drukowanej.

Marcin SKOTNICKI

……

Data, podpis

OŚWIADCZENIE

Wyrażam zgodę na udostępnienie mojej rozprawy doktorskiej w Czytelni Naukowej Biblioteki Głównej Uniwersytetu Medycznego im. K. Marcinkowskiego w Poznaniu oraz w formie elektronicznej w Wielkopolskiej Bibliotece Cyfrowej (www.wbc.poznan.pl).

Poznań, dnia.....

.....

(podpis)